Technische Universität München
TUM School of Natural Sciences

TUM

Size-Selected Pt Clusters on Fe_3O_4(001): How Cluster-Support Interactions Dominate Morphology, Stability and Reactivity

Sebastian Dominik Kaiser

Vollständiger Abdruck der von der TUM School of Natural Sciences der Technischen

Universität München zur Erlangung eines

Doktors der Naturwissenschaften (Dr. rer. nat.)

genehmigten Dissertation.

Vorsitz: Prof. Dr. Barbara Lechner

Prüfer*innen der Dissertation:

       1.   Priv.-Doz. Dr. Friedrich Esch
       2.   Prof. Dr. Klaus Köhler
       3.   Prof. Dr. Gareth S. Parkinson

Die Dissertation wurde am 30.08.2023 bei der Technischen Universität München eingereicht

und durch die TUM School of Natural Sciences am 13.10.2023 angenommen.

Acknowledgement

First and foremost, I want to thank Friedrich Esch and Barbara Lechner for their supervision during the last few years. Thank you for always being available, even on Sunday evenings, sharing your scientific and technical knowledge, continuously pushing me out of my comfort zone, and especially Friedrich for your never-ending enthusiasm and motivation. Furthermore, great thanks are due to Ueli Heiz, who gave me the opportunity and liberty to pursue my own research interests in his amazing group while always being available for discussions and scientific input and encouraging a friendly and productive work atmosphere.

I would like to thank all the colleagues I had the pleasure to share a lab with: Johanna Reich, Matthias Krinninger, and Florian Kraushofer. Thanks for generating such a nice and cooperative environment. It was incredibly fun to work with you. Big thanks also to Robert Spitzenpfeil and Christian Schmid, our technicians/Ph.D. student babysitters for keeping everything running, and also to the mechanics and electronics workshops for realizing all the weird plans I came up with. Furthermore, I want to thank the entire Heiz group and functional nanomaterials group. I really enjoyed being part of the team, the personal atmosphere, the technical and scientific support from everybody, and especially all the group activities, cakes, and barbecues.

There were and still are a lot of fruitful scientific collaborations that significantly contributed to the success of this thesis. First, I would like to thank Gianfranco Pacchioni, Sergio Tosoni, and Farahnaz Maleki for providing, explaining, and discussing the DFT calculations in the lattice oxygen reverse spillover project. I also greatly appreciate Wolfgang Harbich, who shared his knowledge about how to operate and troubleshoot a sniffer setup. Thank you also to Andrey Shavorskiy and Suyun Zhu, who stayed up all night with us during our remote beamtime, in which we investigated the SMSI effect on clusters. Nicolas Bock, thank you for introducing me to the beautiful world of carbon nitrides. I Would also like to thank Aras Kartouzian and the Nanocat crew, Kevin Bertrang and Tobias Hinke, for inviting me to join their countless synchrotron adventures, where we investigated some surprisingly interesting Ta clusters on Pt(111). In this regard, also big thanks to Alessandro Baraldi, his entire group, and Paolo Lacovig. Further thanks are due to my colleagues from the bright side of catalysis, Martin Tschurl, Philip Petzoldt, and Lucia Mengel, for letting me be part of another project where we are investigating the SMSI effect on clusters on r-TiO_2.

Finally, I want to thank my partner, Katharina, for her love, patience, and support during the last couple of years and especially during the writing of this thesis.

Abstract

Reducible oxides are characterized by particular electron, oxygen, and cation buffering capabilities that lead to their manifold use as active redox catalysts in industry. They are also promising support materials for catalytically active metal nanoparticles, whereby particle-support interactions, such as the activation of lattice oxygen, can steer the catalyst's morphology, stability, and reactivity. Instead of nanoparticles, our experimental setup offers the exciting possibility of generating size-selected sub-nanometer clusters that exhibit a unique reactivity due to their physical and electronic structure. Depositing these on reducible oxides allows us to explore cluster-support interactions under full particle size control at the lower end of the size scale in the non-scalable regime of matter. This thesis investigates such cluster-support interactions, specifically annealing-induced ones, for Pt_5, Pt_{10} and Pt_{19} clusters on $Fe_3O_4(001)$. A combined experimental approach, consisting of scanning tunneling microscopy(STM), x-ray photoelectron spectroscopy (XPS), temperature programmed desorption (TPD), and pulsed reactivity measurements allows disentangling redox-induced surface dynamics, e.g., encapsulation and spillover processes. Complementary density functional theory (DFT) calculations, performed by our collaborators in the group of Gianfranco Pacchioni, provide access to their energetic details.

All investigated cluster sizes can be deposited size-selected and intact at room temperature, where the system remains stable and no degradation is observed. Upon annealing to 473-623 K and independent of their size, the Pt clusters catalyze CO oxidation, involving lattice oxygen in a metal-assisted Mars-van Krevelen mechanism. Separating the reaction steps and tracing the oxygen transport elucidates the precise nature of the involved oxygen species: In a lattice oxygen reverse spillover mechanism, lattice oxygen atoms migrate from the $Fe_3O_4(001)$ support onto the Pt clusters, where they can be accumulated, and readily participate in the CO oxidation. Concomitantly, starting at 523 K, strong metal-support interaction (SMSI) induces an encapsulation of the Pt clusters by an FeO-like layer, resulting in a loss of CO adsorption capacity. While well-explored for nanoparticles, SMSI-induced encapsulation was hitherto unclear whether also occurring in the non-scalable size regime. In the same temperature range, STM measurements show a decrease in apparent cluster height caused by (i) a restructuring of the clusters due to lattice oxygen reverse spillover and (ii) a hypothesized change in electronic structure due to SMSI. Cluster sintering starts simultaneously; the specific onset temperatures scale with the cluster footprint and are thus size-dependent. Pt_5 and Pt_{10} sinter via cluster diffusion and coalescence; for Pt_{19}, only Ostwald ripening is observed. Remarkably, the diffusion of small Pt clusters at the verge of encapsulation is still possible. At the same time, the encapsulat-

ing layer successfully suppresses atom detachment and thus Ostwald ripening up to 823 K, which is 200 K above the thermodynamic cluster stability limit (Hüttig temperature). Finally, above 1000 K, a distribution of square-shaped, crystalline nanoparticles results.

The scientific results presented in this thesis have been made possible by various technical developments and improvements. A UHV transfer suitcase was constructed to transport highly susceptible cluster samples to other measurement facilities, enabling, e.g., the synchrotron measurements in the SMSI project. The optimization of the XPS and the commissioning of a new sniffer setup, with the development of measurement routines and a detailed pulsed evaluation software required for the lattice oxygen reverse spillover project resulted in a powerful toolbox ideally suited for investigating model catalysts with integral measurements, complementary to the local STM studies. The full capabilities of this toolbox are exemplified in a side project of this thesis, the bottom-up synthesis and characterization of carbon nitride films, included in the appendix. In parallel but not included in this thesis, an STM-based technique for tracking the diffusion path of atoms or clusters with a time resolution of 10 ms and below was implemented. It will soon be used to investigate the diffusion paths and energies of supported clusters at elevated temperatures.

Kurzfassung

Reduzierbare Oxide besitzen besondere Elektronen-, Sauerstoff- und Kationenpufferfähigkeiten, aufgrund derer sie in der Industrie als aktiver Redoxkatalysator vielfache Verwendung finden. Sie sind des Weiteren vielversprechende Trägermaterialien für katalytisch aktive Metallnanopartikel, wobei Partikel-Träger-Wechselwirkungen, wie z.B. die Aktivierung von Gittersauerstoff, die Morphologie, Stabilität und Reaktivität des Katalysators definieren können. Unser experimenteller Aufbau erlaubt es anstelle von Nanopartikeln größenselektierte Cluster im Sub-Nanometer Bereich zu verwenden, welche aufgrund ihrer physikalischen und elektronischen Struktur eine einzigartige Reaktivität aufweisen. Durch Aufbringen dieser Cluster auf reduzierbaren Oxiden ist es möglich die Wechselwirkungen zwischen den Clustern und dem Trägermaterial am untersten Ende der Größenskala, im nicht skalierbaren Regime, und unter vollständiger Größenkontrolle zu erforschen. In Rahmen dieser Dissertation werden solche Cluster-Träger-Wechselwirkungen, insbesondere temperaturinduzierter Natur, für Pt_5, Pt_{10} und Pt_{19} Cluster auf $Fe_3O_4(001)$ untersucht. Dabei ermöglicht ein kombinierter experimenteller Ansatz, bestehend aus Rastertunnelmikroskopie (STM), Röntgenphotoelektronenspektroskopie (XPS), temperaturprogrammierter Desorption (TPD) und gepulsten Reaktivitätsmessungen die Entwirrung von miteinander verwobenen, redox-induzierte Oberflächendynamiken, wie z.B. Einkapselungs- und Spillover-Prozesse. Deren energetische Details werden durch ergänzende quantenphysikalische Berechnungen mittels Dichtefunktionalitätstheorie (DFT), durchgeführt von unseren Kooperationspartnern um Gianfranco Pacchioni, zugänglich.

Bei Raumtemperatur können alle untersuchten Clustergrößen größenselektiert und intakt deponiert werden, das resultierende System ist stabil. Wird das System auf 473-623 K erhitzt, so katalysieren die Pt Cluster unabhängig von ihrer Größe die CO Oxidation. Dabei folgt die Reaktion einem metallunterstützten Mars-Van Krevelen Mechanismus, bei dem der Gittersauerstoff des Trägeroxids eine entscheidende Rolle spielt. Durch eine Trennung der Reaktionsschritte und das Nachverfolgen des Sauerstofftransports lässt sich die genaue Natur der beteiligten Sauerstoffspezies aufklären: In einem umgekehrten Spillover Mechanismus (lattice oxygen reverse spillover) wandern Gittersauerstoffatome vom $Fe_3O_4(001)$ Träger auf die Pt Cluster, was zur Anreicherung von hochreaktivem Sauerstoff führt, der dann für die CO Oxidation zur Verfügung steht. Gleichzeitig führt ab 523 K die starke Metall-Träger Wechselwirkung (strong metal-support interaction, SMSI) zu einer Einkapselung der Pt Cluster. Die einkapselnde Schicht besitzt eine FeO ähnliche Stöchiometrie und manifestiert sich in einer Reduktion der CO Adsorptionskapazitäten der Cluster. Während diese SMSI-induzierte Einkapselung bei Nanopartikeln gut erforscht ist, war bisher unklar, ob sie auch

im nicht skalierbaren Größenbereich auftritt. Im selben Temperaturbereich zeigen STM Messungen eine Verringerung der scheinbaren Clusterhöhe. Die Ursachen dieses Effekts sind (i) eine Strukturänderung der Cluster aufgrund des umgekehrten Spillovers von Gittersauerstoff und (ii) eine vermutete Änderung der elektronischen Struktur durch SMSI. Gleichzeitig setzt in diesem Temperaturbereich das Sintern der Cluster ein, wobei die spezifischen Anfangstemperaturen mit der Grundfläche der Cluster skalieren und somit größenabhängig sind. Pt_5 und Pt_{10} Cluster sintern durch Clusterdiffusion und Koaleszenz; für Pt_{19} Cluster wird lediglich Ostwald-Reifung beobachtet. Bemerkenswerterweise ist demnach die Diffusion von kleinen Pt Clustern am Rande der Einkapselung noch möglich. Gleichzeitig unterdrückt die einkapselnde Schicht erfolgreich das Abdampfen von Atomen, und damit die Ostwald-Reifung, bis zu einer Temperatur von 823 K, welche 200 K über der Hüttig Temperatur, dem thermodynamischen Stabilitätslimit der Cluster liegt. Oberhalb von 1000 K ergibt sich schließlich eine Verteilung von viereckigen, kristallinen Nanopartikeln.

Die in dieser Dissertation vorgestellten wissenschaftlichen Ergebnisse wurden durch eine Reihe technologischer Entwicklungen und Verbesserungen ermöglicht. So wurde ein UHV-Transferkoffer konstruiert, der den Transport hochempfindlicher Clusterproben zu anderen Messeinrichtungen erlaubt, wodurch z.B. die Synchrotronmessungen im SMSI-Projekt ermöglicht wurden. Durch Optimierung des XPS und Inbetriebnahme des neuen Sniffer-Aufbaus, zusammen mit der Entwicklung von Messroutinen und einer detaillierten Auswertesoftware für gepulste Messungen, die im Spillover-Projekt benötigt wurde, wurde, ergänzt durch das STM, eine leistungsstarke experimentelle Plattform geschaffen, die ideal für die Untersuchung von Modelkatalysatoren geeignet ist. Die volle Leistungsfähigkeit dieser Plattform wird in einem Nebenprojekt dieser Arbeit, der Bottom-up-Synthese und Charakterisierung von Carbonitridfilmen, veranschaulicht (siehe Anhang). Parallel dazu wurde eine STM-basierte Technik zur Verfolgung des Diffusionspfades von Atomen oder Clustern mit einer Zeitauflösung von 10 ms und darunter implementiert, die jedoch nicht in diese Arbeit aufgenommen wurde. Sie wird demnächst zur Untersuchung der Diffusionspfade und -energien von geträgenen Clustern bei erhöhten Temperaturen eingesetzt werden.

Contents

List of Figures

List of Tables

1 Introduction

The European Union intends to become climate-neutral by 2050, which means a net emission of greenhouse gases of zero.[1] To achieve this ambitious goal, the use of fossil fuels for energy generation has to be reduced significantly and sustainable, "green" energy sources have to be developed instead. This change not only affects electricity generation, but also transport, and while cars and trains can be operated electrically, another energy source has to be found for planes and ships. As of today, high hopes are focused on hydrogen, or hydrogen-based synthetic fuels.[2] The production of hydrogen, however, is still mainly based on fossil energy sources, like for example steam reforming of natural gas, and synthetic fuels are far from being produced and used on a sufficiently large scale. Furthermore, the reduction of fossil energy carriers also affects the entire production industry, as processes have to be more and more energy efficient. This challenges in particular the chemical industry that not only has a high fossil fuel use and overall energy consumption, but also is responsible for developing and synthesizing sustainable alternatives. As a consequence, old procedures have to be reworked, and new synthesis routes have to be found to meet the upcoming demands for new materials, whereby energy efficiency and sustainability are the ultimate goal. One approach to this problem is the development of new and/or improved catalysts. These can reduce the energy demand of (existing) chemical processes significantly, increase their sustainability via improved catalyst selectivity and stability and establish synthesis routes for new materials.

In the majority of all industrial chemical processes (i.e. 85-90%), a catalyst is used, out of which 80 to 85% are catalyzed heterogeneously.[3] Prominent examples include the ammonia synthesis (about 2% of the world's energy consumption), sulphuric acid production or fuel refining, and not to forget the automotive exhaust gas treatment catalyst in every vehicle with a combustion engine. Heterogeneous catalysts are usually in a solid state, while the reactants are either gases (typical for base chemicals or refineries) or liquids (fine chemical synthesis).[4] Thus, reactions can only occur at the surface of the catalyst, and generally a large surface area is desired in catalyst development. As a consequence, these catalysts typically consist of catalytically active material, which can be either a metal or a metal oxide that is finely dispersed on a chemically rather inert, high surface carrier material such as amorphous carbon, SiO_2 or Al_2O_3.[3,5] To optimize surface area and thus material efficiency, the catalytically active material itself is utilized in the form of nanometer sized particles,[6] which is even more important when the catalyst is based on expensive noble metals like Pt, Pd or Rh. Traditionally, new heterogeneous catalysts are found experimentally mostly by trial and error. Due to the seemingly endless amount of tuning parameters, this process can be incredibly time consuming. One prominent example is the Haber-Bosch process for NH_3 synthesis, where about 20000 experiments on 3000 different cat-

alysts were necessary to develop the first industrially usable catalyst formulation.[7] However, due to the ever increasing demand for new and more efficient catalysts for increasingly specific and complex reactions, a more rational approach is highly desired. The current procedure is "catalyst by design", which aims at including all available experimental and computational fundamental insights into the development of new catalysts. Sadly, even today this strategy is rarely applicable, as the prediction of the behaviour of a heterogeneous catalyst is still very challenging. Besides the intrinsic complexity of catalytic systems, rendering a computational approach almost impossible, one main reason is the lack of knowledge about exact reaction mechanisms and structure-reactivity relationships on the atomic scale.[5]

The surface science approach tries to access fundamental insights by drastically reducing the complexity of a catalyst, using simple model systems that are well defined and can be prepared reproducibly.[8,9] To precisely control the number and types of adsorbates, investigations are conducted under ultra high vacuum (UHV) conditions. Atomically flat single crystals or thin films with known crystalline facets and well-defined adsorption sites provide suitable supports for catalytically active particles. Note that these model systems are too far from real applied catalysts and industrially relevant environments to provide directly applicable technical solutions; a problem typically referred to as pressure and complexity gaps. Thus, the surface science approach rather aims at providing a library of general, fundamental concepts, which can then in turn be used in more applied catalyst development. Local techniques as for example scanning tunneling microscopy (STM) provide structural information for each individual particle and can help to link structure and catalytic activity. Integral, mass spectrometry based techniques, such as temperature programmed desorption (TPD) or pulsed reactivity measurements, investigate adsorption and reaction pathways as well as the overall activity of the system. Finally, integral spectroscopic techniques such as X-ray photoelectron spectroscopy (XPS) give insights into chemical composition and oxidation state and thus binding motifs of the surface atoms, before, during and after a catalytic reaction. By combining all the information obtained by these techniques, a fundamental picture of the catalytic reaction emerges, which can then be applied to understand reaction pathways on real catalysts. Chemical processes tend to be highly dynamic on the atomic scale. Thus, apart from the reaction mechanism itself, surface science methods are also used to study the stability and evolution of a catalyst on a certain support as a function of temperature, pressure or gas phase composition, increasing the complexity of the system step by step.

As introduced above, heterogeneous catalysts typically consist of a catalytically active material on a support. In this thesis, size-selected metal clusters have been used as active catalysts, which add another dimension of complexity, but also an additional tuning parameter to the system, namely the particle size, defined precisely to the number of atoms. Clusters are defined as atom agglomerates between 2 and 100 atoms, larger particles are referred to as nanoparticles. Note that the expression "cluster", however, is used variably in the scientific community and particles ranging from a few atoms,[10–13] up to hundreds or thousands of atoms are sometimes considered clusters.[14,15] Here, the more strict definition was chosen, since it covers the non-scalable size regime, where the cluster properties start to differ from extended bulk materials and physical as well as chemical properties are only

predictable as a general trend, but not for each individual cluster size.[16] Especially towards the lower size limit, the clusters increasingly behave more like "super" atoms or molecules rather than metallic particles, and the reactivity of a cluster can change tremendously from atom to atom. This enables an entirely new approach to heterogeneous catalyst development and improvement: Due to their unique, size-dependent electronic structure, clusters have the potential to access different reaction pathways, beyond that accessible with classic, nanoparticle based catalysts, e.g. the molecular activation of O_2.[17–19]

Although clusters can be dosed in a single size, they still exhibit a high structural complexity, as clusters typically have a large number of structural isomers energetically close to the ground state.[20–22] As a consequence, a variety of cluster geometries can co-exist simultaneously, leading to a continuous restructuring of the clusters, referred to as dynamic structural fluxionality.[16,20,23,24] This is especially true in the gas phase, but even supported clusters, even though they typically exhibit fewer energetically accessible isomers, can still transform their structure fluxionally, as for example observed for Pd clusters on h-BN.[25] This fluxionality is often responsible for the unique chemical reactivity of the clusters.[26] Apart from their high structural fluxionality, the unique size-dependent properties of clusters can also result from their electronic structure.[27,28] Similar to molecules, clusters exhibit discrete electronic states that can be altered significantly by the addition of just a single atom.[29–32] When increasing the cluster size, these discrete states continuously evolve into the bulk band structure, thus strong size-effects preferably occur towards the lower end of the cluster size regime.[31] These electronic effects manifest themselves as discontinuities in the size dependence of observables, such as electron affinity (EA) and ionization potential (IP),[33,34] which cease when going to increasingly larger particle sizes.[31,35]

Clusters have been shown to exhibit special properties across a wide range of materials and observables, whereby the impact of the cluster size on the chemical and physical properties of matter is manifold: Firstly, size-dependent stability islands are observed when investigating a distribution of noble gas or s-metal clusters in the gas phase.[36–38] Van der Waals clusters, such as noble gas clusters, prefer specific geometries that maximize the inter-atomic interaction and are stabilized upon geometric shell closure, whereas electronic effects dominate for clusters with shared valence electrons (e.g. s-metals) that are stabilized upon electronic shell closure. Both effects lead to an improved stability of specific cluster sizes ("magic numbers").[39–41] Also the overall metallicity can change, as for example observed for Pt clusters that exhibit a non-metallic behaviour for small cluster sizes.[42] Furthermore, magnetism can have a strong size-dependence: Fe, Ni and Co clusters have been shown to exhibit a higher magnetic moment per atom than the corresponding bulk materials,[43,44] with size dependent minima at closed geometric shells for Ni,[45] and Rh which is non-magnetic in the bulk state shows superparamagnetism in the cluster regime.[46,47]

Adsorption and desorption energies and processes can also be size-dependent, highly relevant for catalytic purposes. CO desorption from Pt or Pd clusters, for example, is different from the corresponding bulk materials, and desorption temperatures (and thus poisoning effects) vary with cluster size.[48,49] The chemical activity and reactivity of clusters can differ significantly with the addition or

removal of a single atom, which for example is observed when investigating CO oxidation on Pt clusters,[11,12,50] or ethylene hydrogenation where the cluster size effect additionally depends on the support acidity.[51] Interestingly, materials that are non reactive in the bulk state can become active as clusters. Au for example, which is nearly inert as bulk material, becomes a highly active and selective redox catalyst in the cluster regime,[52–55] and Au_8 has been shown to exhibit a significantly higher activity in CO oxidation than Au_9 or especially Au_7.[17,56] Another example is Ta and its oxides, which are only capable of CO_2 and methane activation in the cluster size regime, whereby again the reactivity changes with cluster size on the scale of atoms.[57–59]

The main issue with employing clusters as active catalysts in real catalysis is their stability: Clusters are intrinsically metastable and prone to ripening or sintering, which results in a loss of size-selection.[23,60–63] There are two fundamental particle sintering mechanisms that have also been observed for clusters: Ostwald and Smoluchowski ripening.[64,65] In the former, cluster growth is based on atom detachment from one cluster, followed by diffusion and reattachment to another cluster. The latter describes diffusion and coalescence of entire clusters. Due to the high vapour pressure of the typically strongly under-coordinated cluster surface and the small footprint, clusters tend to sinter already at lower temperatures compared to nanoparticles.[66,67] Thus, cluster stabilization is crucial for their use in any catalytic application and a variety of methods for sintering suppression have been explored or proposed, e.g. alloying with stabilizing metals,[68,69] interface control via defects or encapsulation.

Overall, size-selected clusters deposited on single crystalline substrates result in some of the most well-defined model catalytic systems and allow to explore reaction mechanisms and especially catalyst-support interactions on a fundamental level. It has to be kept in mind, however, that due to the strong size-dependence, results obtained for clusters cannot necessarily be applied to real, nanoparticle based catalysts. Nevertheless, the research of supported clusters contributes to a library of various possible effects and reactions, that can be taken into account when investigating more realistic, but less defined industrial catalysts. Furthermore, certain cluster sizes can exhibit a much higher catalytic activity than corresponding nanoparticles.[70] Cluster research can help to find an stabilized those specific sizes and thus also directly contribute to the development of new catalysts.

1.1 Reducible Metal Oxide Supports in (Model) Catalysis

In metal oxides, reducibility describes the ability of the material to release oxygen under reducing conditions. To remove a neutral oxygen atom from a surface, the original O^{2-} ions of the oxide have to be oxidized, yielding two excess electrons per oxygen atom that have to be taken up by the corresponding metal cations. On non-reducible oxides, the empty states of the metal (conduction band) are energetically too high above the Fermi level to easily accommodate these excess electrons.[71] Thus the metal cations exhibit an intrinsic reluctance to undergo reduction and therefore refuse to release oxygen easily. Typically, non-reducible oxides are formed by main group metals, such as SiO_2 or MgO; they are chemically inert and are characterized by a large bandgap of > 3 eV. Reducible metal

oxides, on the other hand, have low lying empty states close to the Fermi level that are formed by metal d-band orbitals.[71] Thus, excess electrons originating from oxygen removal can easily be distributed in the conduction band, leading to the formal reduction of the corresponding metal cations. Reducible oxides are typically transition metal oxides with a small bandgap of $< 3eV$, for which a semiconductor-like behaviour is observed. However, the transition between reducible and non-reducible metal oxides is smooth, and there are intermediate metal oxides, such as ZnO or Nb_2O_5 where a reducible behaviour is expected under certain conditions.[72] In contrast to non-reducible oxides, reducible ones can be an integral part of a chemical reaction, where they act as an electron and/or oxygen buffer. This leads to a different way of redox reaction control, giving the opportunity to separate individual steps in a chemical reaction.

When we look at the chemical industry, reducible metal oxides are actually used in some of the most important catalytic processes. V_2O_5 supported on SiO_2, for example, is used in the large scale oxidation of SO_2 to SO_3 necessary for sulphuric acid production(contact process).[4] The oxidation either takes place via an in-situ formed $[(VO)_2O(SO_4)_4]^{4-}$ complex, to which first O_2 is attached followed by the consecutive oxidation of two SO_2 molecules, or, via a Mars-van Krevelen reaction mechanism, whereby SO_2 is oxidized to SO_3, while the V^{5+} is reduced to V^{4+}.[73,74] The catalyst is subsequently re-oxidized with O_2, completing the catalytic cycle. Fe_3O_4 finds its use in the NH_3 synthesis catalyst, as a precursor for the catalytically active iron species, obtained after in-situ reduction.[75,76] A variety of mixed, reducible transition metal oxides are used for the selective oxidation of propylene,[5] whereby the desired product defines which catalyst is used: A mixed Bi, Mo oxide for example results in the formation of Acrolein.[77,78] Another example is the removal of CO in fuel cell feed gas using a mixed Cu, Ce oxide PROX-catalyst,[79,80] or the removal of nitrous oxides from exhaust gases by selective catalytic reduction where catalysts based on V, Cr, or Mo oxides supported on TiO_2 can be used.[81] Overall reducible metal oxides are widely spread active catalysts, but are only rarely appearing catalyst support materials. This is not surprising considering that common non-reducible support materials such as SiO_2 or Al_2O_3 are abundant, cheap and chemically stable under harsh reaction conditions. Thus the question arises why it might be interesting to also investigate reducible oxides as potential support materials for catalysts.

The first advantage of reducible oxides is their ability to act as an electron buffer. Thus charge transfer is comparably easy, and metal nanoparticles or clusters supported on a reducible oxide are quite commonly (partially) charged.[82–86] This is in stark contrast to non reducible oxides, where polarization effects dominate and no charge transfer is observed.[51,83] The charged particles can now enable different reaction pathways hardly possible on non-reducible oxides, whereby the particle charge can also change during a reaction, exploiting the full electron buffering capabilities of the support. This was for example shown by Wang et al. in a theoretical investigation of the CO oxidation on Au_{20} clusters supported on r-TiO_2(110) (rutile):[82] Upon adsorption, the clusters become negatively charged, however as soon as O_2 is co-adsorbed, the charge is transferred to the oxygen molecules via the reducible substrate, resulting in the activation of molecular oxygen. When more O_2 molecules are adsorbed

(up to 3 per cluster), the Au clusters become even positively charged. Subsequently CO is adsorbed, which almost has no effect on the cluster charge, and the reaction with the O_2^{2-} occurs at the cluster perimeter, leading to the desorption of CO_2, wherby the original negative charge on the cluster is restored.

Apart from supported particles, reducible oxides also facilitate charge transfer to various adsorbates, which can be crucial for adsorbate diffusion processes. One classic example is the charge transfer induced diffusion of O_2 molecules on r-TiO_2, investigated by Wahlström et al.:[87] An oxygen molecule adsorbed on top of a Ti site gets randomly charged by thermal excitation, whereby its equilibrium adsorption position changes to a bridging site, in between the original adsorption site on one Ti and the next one. When the O_2 molecules get discharged again, the equilibrium position changes back, either to its original position or moving to the next Ti site, resulting in charging-induced diffusion. Another very prominent surface diffusion example for adsorbates on reducible oxides concerns hydrogen atoms, as e.g. investigated by Karim et al. by comparing irreducible Al_2O_3 with reducible anatase TiO_2 amorphous film supports:[88] They placed multiple pairs of Pt and iron oxide nanoparticles with varying distances on the respective support and introduced H_2 into the gas phase, which adsorbs dissociatively on the Pt and spills over to the support, where it may diffuse to the iron oxide that is subsequently reduced. Whereas the iron oxide on Al_2O_3 was only significantly reduced when in direct contact with the Pt, indicating almost no H diffusion on the support, on TiO_2 the degree of iron oxide particle reduction was independent of the distance, showing that here hydrogen diffusion is possible over a long range. They attribute this to a combined electron-proton mobility in TiO_2, whereby the electron is transferred between neighbouring Ti cations in the substrate simultaneously to the proton diffusion at the surface. Similar observations have been made on CeO_2, where H diffusion can occur in the μm space range.[89] All these diffusion effects offer additional possibilities of reaction control when using reducible oxides as catalyst support, always in combination with the fact that single redox reaction steps can be separated. This has been exploited in a series of studies investigating the photocatalytic oxidation of alcohols on a r-TiO_2(110) surface with the help of Pt clusters as a co-catalyst:[90–92] The alcohols dissociatively adsorb at oxygen vacancies, are subsequently oxidized by photo-holes generated upon illumination and consecutively desorb as aldehydes. The reducible support facilitates the diffusion of the resulting H atoms to the Pt clusters where they can recombine and desorb, thus avoiding a poisoning of the surface by H atoms.

The second advantage of reducible oxide supports is their ability to supply oxygen: One parameter commonly used to characterize the reducibility of an oxide is the oxygen vacancy formation energy that determines how energetically costly the removal of a surface oxygen atom would be.[71,72,93] Interestingly, when looking at metal clusters and nanoparticles supported on oxide surfaces, there is a general trend that the oxygen vacancy formation energy is reduced in close proximity to the nanoparticle, e.g. at its perimeter, both for reducible and non-reducible oxide supports.[71,94] Thus, metal particles on an oxide support facilitate the removal of oxygen atoms, increasing its reducibility, and can activate oxygen atoms to react in a Mars-van Krevelen (MvK) mechanism. In a classical Mars-

van Krevelen catalytic cycle, the oxidation of an adsorbed reactant is facilitated by the extraction of a lattice oxygen atom from the reducible oxide; the missing oxygen is subsequently replaced by re-oxidizing the catalyst with molecular oxygen from the gas phase.[95] In a metal-assisted Mars-van Krevelen mechanism, metal particles deposited on a reducible oxide facilitate the extraction of surface oxygen, thus leading to a higher catalytic activity at lower temperatures. This was for example beautifully shown by Widmann et al., who investigated the CO oxidation on Au particles on TiO_2 at 80°C with a series of pulsed experiments:[96] CO molecules from the gas phase adsorb at the Au particles and are consecutively oxidized with lattice oxygen from the Au-TiO_2 interface, whereby the CO_2 formation decreases over time, since the lattice oxygen reservoir at the particle perimeter is depleted. Consecutive dosage of oxygen could re-oxidize the TiO_2 and thus, regenerate the catalyst. This example nicely shows how the oxygen buffering ability of a reducible oxide allows to separate a chemical reaction into two individual subsequent steps. Furthermore, in a different study from the same group, the authors compare the CO_2 formation of samples with the same Au loading but different particle sizes, where they could observe an increase in CO_2 with decreasing particles size, thus increasing cumulative particle perimeter.[97] This confirms that the reaction only occurs at the interface, following a metal-assisted Mars-van Krevelen mechanism, whereby the activity strongly depends on the reducibility of the underlying support, as also shown by Widmann et al. in a different study:[98] Here, the CO oxidation activity of Au nanoparticles was investigated by simultaneous pulses of CO and O_2, whereby a much higher CO conversion was observed for TiO_2 supported Au particles compared to Al_2O_3 supported ones, and the conversion on oxides with intermediate reducibility (ZrO_2 and ZnO) was in between. In the case of ZrO_2, a classical non-reducible oxide, it was later shown by Puigdollers et al. that Au particles can actually reduce the oxygen vacancy formation energy at the interface significantly, thus CO oxidation becomes exothermic at the interface while being strongly endothermic on the bare ZrO_2.[99] This is a nice example of how metal particles can actually influence reducibility and turn a non-reducible oxide into a reducible one, indicating that a strict separation into reducible and non-reducible oxides may be a bit oversimplified and the transition is indeed a smooth one.

When focusing on catalysis, apart from CO oxidation, the activation of interface oxygen also plays a crucial role in the water-gas shift (WGS) reaction, where a higher catalytic activity for Pt and Rh particles was reported when deposited on CeO_2/Al_2O_3 compared to pure Al_2O_3.[100] Investigating a similar system, namely Pt/TiO_2, Kalamaras et al. confirmed in a kinetic and mechanistic ^{18}O isotopic exchange study the crucial role of activated lattice oxygen in the WGS mechanism:[101] CO from the gas phase adsorbs on the Pt particles, where it is oxidized with oxygen atoms from the TiO_2 support at the metal-oxide interface. After CO_2 desorption, the resulting oxygen vacancy is consecutively filled by a H_2O molecule and the hydrogen atoms recombine at the Pt particles, forming H_2. In a theoretical study on Pt clusters TiO_2(110) by Ammal et al., this redox pathway was confirmed to be the dominant one, at temperatures between 473 and 673 K. Notably, an additional spectator CO molecule adsorbed on the Pt cluster led to a further enhancement of the catalytic activity.[102, 103]

On certain metal oxide supports, of which the best understood example is CeO_2, activation of lattice

oxygen atoms at the metal-oxide interface can occur via migration of oxygen atoms from the interface onto the metal particles, a process generally referred to as reverse spillover, yielding highly active oxygen atoms on the particles.[71, 104, 105] This mechanism was shown several years ago by Zafiris et al. based on a series of CO TPD experiments on Rh/CeO_2:[104] In a first CO TPD run, only a high temperature CO_2 feature appearing at the high temperature end of the CO desorption is observed, however consecutive runs give rise to another CO_2 feature at lower temperatures, which the authors assigned to the migration and accumulation of lattice oxygen on the Rh particles. Similar to TiO_2, the removal of oxygen by CO oxidation eventually led to a depletion of the oxygen atoms in proximity to the Rh particles, resulting in a more and more reduced CO oxidation activity. It could be restored by replenishing the interface oxygen by annealing to higher temperatures, inducing higher oxygen mobility in the CeO_2 bulk. This was also shown later by directly comparing Rh particles supported on near-stoichiometric and reduced CeO_2 films, where the lack of available oxygen on the more reduced film resulted in a suppression of oxygen reverse spillover.[106] In a different study, Happel et al. provided evidence for the migration of lattice oxygen on $Pt/CeO_2(111)/Cu(111)$ via infra-red absorption spectroscopy:[107] After annealing, a blue shift in the stretching frequency of adsorbed CO hints towards oxygen atoms that have migrated on, and slightly oxidized the Pt surface. When it comes to clusters, oxygen reverse spillover is mainly investigated theoretically, but the experimental literature on the topic is rather scarce. DFT calculations for Pt_8/CeO_2 indicate that oxygen reverse spillover is energetically possible and can facilitate oxygen vacancy formation at the cluster perimeter;[108, 109] when the clusters are supported on CeO_2 nanoparticles, lattice oxygen migration onto the Pt even becomes exothermic, as shown by Vayssilov et al..[108] Another DFT study by Negreiros et al. suggests a change in morphology of $Pt_{3-6}/CeO_2(111)$ as a consequence of oxygen reverse spillover, whereby the clusters adapt a more 2D-shape.[110] Additionally, the migration of lattice oxygen atoms onto Ru_{10} and Ni_{10} clusters has been investigated theoretically for an anatase $TiO_2(101)$ and a tetragonal zirconia $ZrO_2(101)$ surface, whereby oxygen reverse spillover appears to be only slightly endothermic for all combinations.[111, 112]

When it comes to the catalytic application, oxygen reverse spillover has been proposed to play a crucial role in the mechanism of methanol steam reforming on $Cu/CeO_2/Al_2O_3$:[113, 114] In a first step, CeO_2 lattice oxygen migrates on the Cu particles, partially oxidizing them, followed by methanol and water adsorption at the $Cu-CeO_2$ interface. CO_2 and H_2 are formed in the consecutive surface reaction, involving the spillover oxygen atoms, whereby the oxygen that originates from the water fills the interface oxygen vacancy and thus completes the catalytic cycle.

As described above, the degree of reducibility has a huge impact on the surface chemistry of an oxide, especially in combination with adsorbed metal particles and clusters, and the ability of a reducible oxide to act as an electron and oxygen buffer results in a richer surface chemistry, when compared to non-reducible oxide supports. The removal of oxygen from reducible oxides leads to the formation of oxygen vacancies, which on some oxides, as for example CeO_2, can dominate the surface chemistry.[115–117] Furthermore, the removal of oxygen atoms inevitably results in the reduction of the lattice

cations that can sometimes, as for example in the case of Fe_3O_4, exhibit a higher mobility and may diffuse from the surface into the bulk and vice versa, especially at elevated temperatures. Thus, the surface chemistry of a reducible oxide can either be governed by an interplay of oxygen vacancies and lattice cation interstitials, as for example in TiO_2,[118–120] or be completely dominated by cation interstitials, as observed in the case of Fe_3O_4.[13,121–123] In the latter case, if the interstitial diffusion is fast enough, the reducible oxide can furthermore act as a cation buffer, and dynamically react to changes in its redox environment, which can have a huge impact on the appearance and reactivity of supported particles.

Arguably one of the most important concepts, where cation interstitials alter the entire appearance, reactivity and stability of metals deposited on reducible metal oxides, is strong metal support interaction (SMSI). This phenomenon was initially discussed in a pioneering work by Tauster et al., investigating noble metal particles supported on TiO_2.[124] Upon annealing to 500°C in H_2, they observed a significant decrease in CO and H_2 uptake, which they later could relate to the growth of a thin TiO_x layer on top of the metal particles.[125] In a more general picture, SMSI describes the encapsulation of group VIII metals on reducible oxides upon annealing in reducing atmosphere (e.g. hydrogen or UHV). The encapsulating thin film is typically a reduced version of the support material and is postulated to be of self-limiting thickness and defined stoichiometry. This was further confirmed a few years later, when Dulub et al. directly imaged the encapsulating layer formed on top of large Pt nanoparticles grown on $TiO_2(110)$ by means of STM.[126] They discovered a complex, two layered zigzag structure covering the particles, with an overall film stoichiometry of $TiO_{1.1}$. Scanning tunneling spectroscopy (STS) measurements revealed a change in the electronic structure of the particles resulting in a more semiconductor like behaviour upon encapsulation.

There is still an on-going discussion about whether the encapsulation can be reversed under oxidizing conditions, and while earlier publications suggests such a reversal,[124,127,128] more recent results rather point towards a further growth of the encapsulating layer in O_2.[129–131] For $Pt/TiO_2(110)$, Petzoldt et al. showed a high SMSI layer growth rate in 1.3 x 10^{-5} mbar O_2, while at 0.13 mbar a much slower growth due to the formation of less reactive PtO_x species was observed.[129] Thus, catalytically active, metallic Pt seems to be beneficial for the encapsulating layer growth. In an impressive transmission electron microscopy (TEM) study on Pt/TiO_2, Beck et al. resolved the formation of an encapsulating TiO_x layer around a particle in 1 bar of H_2 at 600°C, separated from the Pt particle core by a Pt-Ti alloy layer.[130] When replacing the hydrogen with 1 bar of oxygen, a de-alloying of the intermediate layer leading to the growth of the SMSI layer was observed, indicating the dynamic nature of the SMSI layer stability and growth.

Currently, there are two main hypotheses about the underlying mechanism of SMSI formation, based on all these observations.[132,133] For both, the overall thermodynamic driving force is the surface energy minimization, meaning a high surface free energy metal particle on a low surface free energy oxide support is prone to encapsulation by a reduced oxide film, as the formation of an oxide-metal interface is energetically favoured. The first mechanism, introduced by Fu et al.,[134] describes the migration of the encapsulating layer on the metal as a three step process, assuming the metal to have

a larger work function and surface free energy than the oxide: (i) Negative polarization and electron transfer from the support to the metal due to its higher work function, (ii) consecutive diffusion of M^+ ions to the surface, and (iii) migration of a thin suboxide layer on top of the metal particle. The second theory, shown recently by Beck et al.,[130] introduces an alloy formation between reduced metal atoms from the oxide support and the metal nanoparticle as a competing mechanism to that of the migration of the reduced support oxide. This proposed mechanism consists of the reduction of the support oxide at the metal interface and alloying, followed by segregation and oxidation to form the encapsulating film.[133] Both mechanisms of SMSI formation may appear concomitantly in the experiment, leading to a more complicated, collective mechanism.[132,133] They rely on a sufficiently high ion mobility in the reducible oxide substrate, which is achieved at elevated temperatures. The temperature at which the encapsulation process sets in is controversially discussed - for Pd/TiO_2 temperatures as low as 473 K have been reported.[135] Besides the temperature, the SMSI effect and encapsulation rate has also been shown to depend on the crystal phase,[136,137] facet,[138] and morphology of the underlying support.[132] Although most of the fundamental work was performed on Pt or Pd on TiO_2, SMSI has been described for many more metals on a large variety of reducible oxide surfaces including Fe_3O_4,[139,140] CeO_2,[141] Nb_2O_5,,[142,143] and MoO_3.[144,145] More recently, it was even reported that an SMSI-like encapsulation state on non-reducible support materials can be achieved, but under rather specific reaction conditions:[146–148] The encapsulation of Au nanoparticles on MgO, for example, could be achieved in a CO_2 atmosphere via the formation of $MgCO_3$ species, which then migrate onto the particle.[148]

As described above, SMSI has been extensively studied for metal nanoparticles on reducible oxide supports. However, only little is known about SMSI in the sub-nanometer cluster size regime. The absence of crystalline structures, the high fluxionality, curvature and intrinsic metastability of clusters rises the question whether classical SMSI appears at such small scale, and how it can be differentiated from an alloy. Kaden et al. have investigated size-selected Pd clusters deposited on $TiO_2(110)$ and observed the deactivation of the CO oxidation activity, as well as a loss in CO adsorption sites following consecutive temperature programmed reaction (TPR) experiments to 500 K.[149] Combining the TPR and ion scattering experiments, they identified cluster encapsulation due to SMSI as the reason for their observations. In a different study, Wu et al. compared non size-selected sub-nanometer Pt clusters with larger nanoparticles, both on $TiO_2(110)$.[150] In their samples, the nanoparticles showed a loss in CO adsorption capability combined with a decrease in Pt intensity in ion scattering spectra upon annealing, which they attributed to encapsulation. They argue, that the cluster samples show no such behaviour, and SMSI does not occur in the cluster size regime. However, both studies mention the lack of microscopy experiments, which would be necessary to exclude morphology changes or cluster sintering during the annealing. Thus SMSI in the cluster regime remains a largely unexplored territory.

While SMSI is nowadays an established concept in surface science (i.e. most commonly under UHV conditions), it has recently experienced a remarkable renaissance in fundamental catalysis research, where catalytic systems are investigated in gaseous or liquid environments. Employing SMSI to improve catalytic particle stabilization, as well as engineer selectivity and activity is a new and promising

approach to catalyst development. Transmission electron microscopy (TEM) studies on Pt nanoparticles on TiO_2 at 600°C revealed that the encapsulating layer stabilizes the particles against sintering: An SMSI layer, originally formed in an O_2 atmosphere, disappears in an $O_2 + H_2$ mixture, leading to restructuring and diffusion of the particle.[151] After removing the hydrogen, a new encapsulating layer grows, that stabilizes the particle again. An SMSI related catalyst particle stabilization has also been observed in a variety of industrially relevant reactions, including methanol steam reforming,[152, 153] water-gas shift reaction,[154] low temperature CO oxidation,[155] and the electrochemical hydrogen oxidation reaction.[156, 157]

Apart from particle stabilization, SMSI is able to influence or alter the activity and/or selectivity of a catalyst. The impact of SMSI may be manifold and various hypotheses are being discussed, ranging from the encapsulating layer being only permeable for certain small molecules, to the formation of new, specific reaction sites within the layer. An enhanced catalytic activity was for example observed for CO oxidation,[158, 159] or Fischer-Tropsch synthesis,[160, 161] due to the hypothesized generation of additional metal-support interface sites as a consequence of encapsulation. In a recent example, Zhang et al. discovered a significant enhancement in Fischer-Tropsch activity on partially encapsulated Ru particles on TiO_2.[160] They attributed this observation to the activation of the CO dissociation, due to adsorption of the oxygen atom at oxygen vacancies at the encapsulating TiO_x film-Ru interface. The consecutive C-C coupling happens on the Ru sites. SMSI is also exploited to improve and control product selectivity in several reactions: In CO_2 hydrogenation reaction, the product selectivity switches almost entirely to CO after encapsulation, while CH_4 formation is suppressed.[145, 162, 163] Guo et al. recently achieved improved ethylene selectivity in the catalytic hydrogenation of acetylene on Pd/CeO_2 and Pd/TiO_2, employing the SMSI effect with a twist:[164, 165] In a system containing Pd nanoparticles (bad ethylene selectivity) as well as Pd single atoms (good ethylene selectivity), they could successfully encapsulate only the larger nanoparticles, which subsequently were inactive for hydrogenation, yielding a single atom catalyst with high ethylene selectivity.

All the examples and concepts presented in this section nicely illustrate, how a reducible oxide support can influence the stability, morphology and reactivity of catalytically active metal nanoparticles, by its electron, oxygen and sometimes cation buffering capabilities. This is especially crucial, when it comes to sub-nanometer clusters without clear crystalline facets, which are expected to be strongly influenced by the reducible oxide and, due to their metastable nature, might benefit from a potentially stabilizing effect, such as SMSI. As a consequence, the reducible oxide is clearly not only a spectator of the catalytic reaction, but an integral part of the catalytic cycle, and has to be chosen with care. In this work, a $Fe_3O_4(001)$ support was selected, as it is known to maintain its surface stoichiometry via cation exchange with the bulk, and its high cation mobility may also have a significant impact on deposited clusters.

1.2 Magnetite Fe$_3$O$_4$ and its (001) Surface

Making up 5.63% of the continental crust, iron is one of the most ubiquitous, accessible chemical elements on the earth, present especially as a variety of oxides.[166] Magnetite (Fe$_3$O$_4$), although thermodynamically only metastable under ambient conditions, is an abundant, naturally occurring iron mineral, industrially mainly used for the production of crude iron. Magnetite crystallizes in an inverse spinel crystal structure with the general formula AB$_2$O$_4$, and can thus be written as Fe^{2+}(Fe^{3+})$_2$(O^{2-})$_4$: The O^{2-} anions are forming an fcc lattice with the Fe^{2+} cations occupying a quarter of the octahedral sites, and the Fe^{3+} cations occupying a quarter of the octahedral sites and an eighth of the tetrahedral sites (in contrast to a "normal" spinel where the A^{2+} ions occupy an eighth of the tetrahedral sites and the B^{3+} ions half of the octahedral ones).[167,168] This bulk crystal structure is shown in figure 1.1 (a).
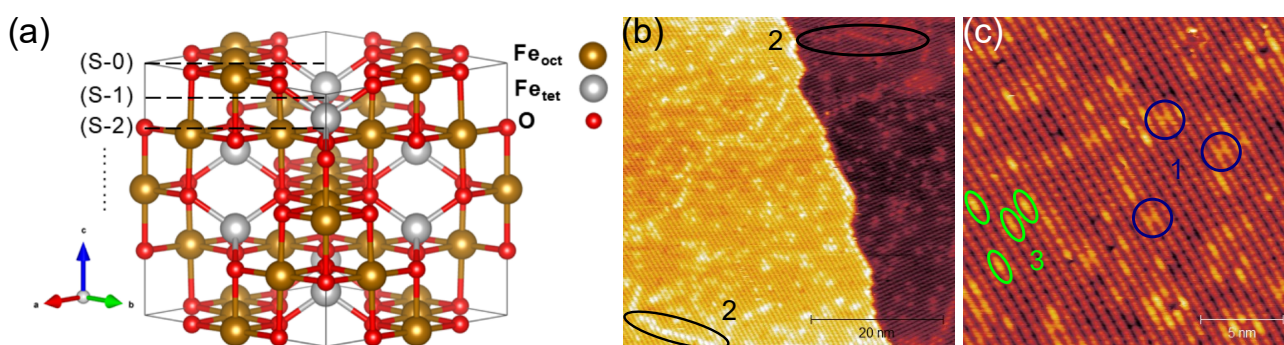
Figure 1.1: (a) Fe$_3$O$_4$ bulk crystal structure unit cell: O^{2-} ions (red) form an fcc lattice, half of the octahedral sites are occupied by Fe^{3+} and Fe^{2+} cations in a 1:1 ratio, one eighth of the tetrahedral sites are occupied by Fe^{3+}. One (Fe$_{oct}$)$_4$O$_8$ is indicated with (S-0), the (Fe$_{tet}$)$_2$ layer directly bellow is indicated with (S-1), and the third layer (again (Fe$_{oct}$)$_4$O$_8$) is indicated with (S-2). It becomes clear how the Fe rows change direction by 90° between the first (S-0) and the third (S-2) layer. Reprinted from Taskin, M. et al. *Phys. Rev. Materials* 2023, 7, 055801 under Creative Commons Attribution 4.0 License.[169] (b) Representative STM image of the Fe$_3$O$_4$(001) surface at room temperature, showing two adjacent terraces. In agreement with (a), the direction of the imaged Fe rows are rotated by 90° between the terraces. Antiphase domain boundaries are marked with 2. (c) Zoomed in image, with nicely resolved Fe rows. Unreconstructed unit cells are indicated with 1, surface OH groups with 3. *Imaging parameters: 1.5 V, 300 pA*

Due to the easy electron exchange between Fe^{2+} and Fe^{3+} ions in equivalent octahedral sites, magnetite exhibits a moderate electric conductivity,[170] which drops significantly when cooling below the Verwey transition at 120 K, where the crystal structure changes to a monoclinic one.[171–173] Within the temperature range investigated in this thesis (200 K to about 1000 K), the conductivity was always sufficiently high to perform STM, XPS and LEED measurements. As its name already suggests, magnetite has magnetic properties; it is a ferrimagnetic oxide: While Fe^{3+} spins are antiferromagnetically aligned, whereby their magnetic moment cancels out, the overall observed magnetism results from the ferromagnetic alignment of the spins in the Fe^{2+} sublattice.[174,175] Magnetite is characterized by a comparably high mobility of lattice and interstitial iron cations, resulting in a fast exchange between

surface and bulk already at low temperatures, e.g. shown in a study by Tober at al., where mass transport over several nm within a 15 min time scale could be observed already at 470 K.[176] Therefore, the surface and bulk chemistry are dominated by cation vacancies and interstitial iron cations.

In the <001> direction, the bulk magnetite unit cell consists of alternating layers of $(Fe_{tet}^{3+})_2$ (tetrahedrally coordinated Fe) and $(Fe_{oct}^{2.5+})_4O_8$ (octahedrally coordinated Fe).[121] Each of these planes has a net charge of +6 $((Fe_{tet})_2)$ or -6 $((Fe_{oct})_4O_8)$, therefore the surface region must have a charge of $\pm$ 3 electrons for compensation of the internal field. Under UHV conditions, the (001) surface is always terminated by the $(Fe_{oct})_4O_8$ layer which is imaged in the STM as parallel, undulating rows of iron (Fe_{oct}) atoms, which are rotated by 90°between adjacent terraces as a consequence of the spinel structure. Figure 1.1 (b) shows a representative STM image. The oxygen atoms are typically not imaged, as they have no electronic states in vicinity of the Fermi level.[177] For a long time, the exact structure of the surface, responsible for the observed reconstruction, was a subject of discussion, however nowadays the generally accepted model is the subsurface cation vacancy (SCV) structure, which was introduced by Bliem et al. in 2014, based on a systematic STM, LEED and DFT study in combination with the observation of specific adsorption sites.[177] It is shown in figure 1.2.
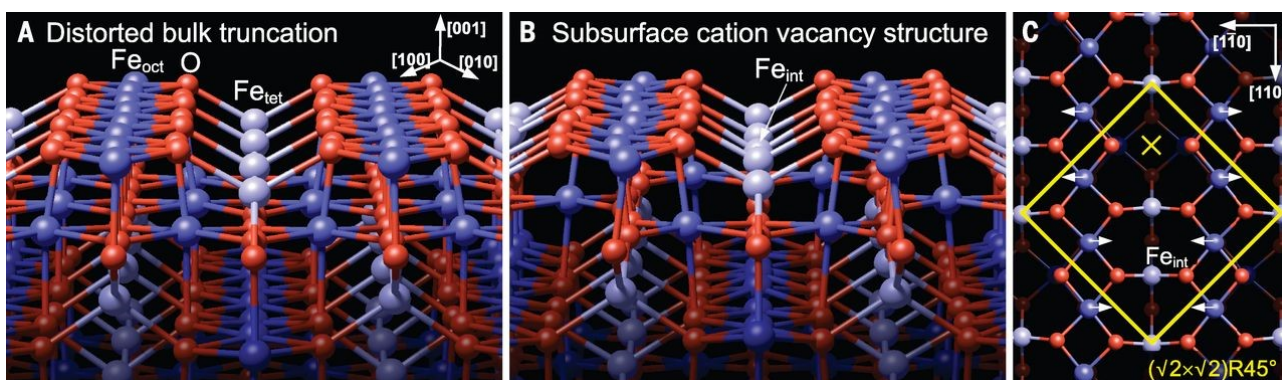

Figure 1.2: Subsurface cation vacancy structure of the Fe_3O_4(001) surface. Oxygen atoms are displayed in red, octahedral Fe in dark blue and tetrahedral Fe in light blue. (A) Outdated distorted bulk truncation model used prior to the introduction of the SCV model. (B) SCV structure with the additional interstitial tetrahedral Fe_{int} in the second layer and two octahedral vacancies in the third layer. (C) Top view of the SCV structure; the unit cell is indicated in yellow. From Bliem et al. *Science* **2014**, 346, 1215–1218.[177] Reprinted with permission from AAAS.

In comparison to a simple bulk truncation termination, in the SCV model two Fe_{oct} are removed in the third layer; one is added to the second layer as an interstitial, tetrahedral Fe_{int}, the second one is removed from the surface by diffusion into the bulk, resulting in an outermost unit cell stoichiometry of $Fe_{11}O_{16}$. As a consequence, the surface layer distorts leading to undulations in the Fe_{oct} rows, as is observed in the STM, yielding the characteristic ($\sqrt{2}$ x $\sqrt{2}$)$R45°$ reconstruction with a unit cell of 8.4 Å. Within each unit cell, one site without a second layer Fe_{tet} atom remains between the iron rows of the first layer (marked by an X in figure 1.2 (c)). The first layer oxygen atoms adjacent to this site exhibit a formal oxidation state of -1, necessary to obtain an overall charge of +3 in the outermost

unit cell, which is required by the crystal orientation for charge compensation. As discussed below, these act as preferential adsorption sites for a variety of adatoms, leading to a twofold coordination to the neighbouring oxygen atoms. The $Fe_3O_4(001)$ surface is enriched in Fe^{3+} when compared to the bulk, with all Fe cations in the first four layers being in a +3 oxidation state.[121, 177] Due to the intrinsic, high cation mobility of magnetite discussed earlier, the magnetite (001) surface tends to always maintain its stoichiometry under UHV conditions, as soon as the temperature is high enough for Fe diffusion: In an oxidizing atmosphere, Fe diffuses from the bulk to the surface, resulting in the growth of new Fe_3O_4 layers, and under reducing conditions, reduced, undercoordinated cations become mobile and diffuse into the bulk. Thus, the Fe_3O_4 bulk acts as an Fe atom reservoir, responding to the chemical potential at the surface. Upon annealing, the (001) surface undergoes an order-disorder phase transition around 720 K, whereby the reconstruction is seemingly lifted and a (1x1) surface is observed.[178, 179] During this phase transition the long range order is successively lost, due to highly fluctuating occupation of lattice sites; above 750 K no reconstruction is observed anymore. Upon cooling down, the phase transition is reversed, no hysteresis is observed.

The $Fe_3O_4(001)$ surface is rich in intrinsic surface defects, which can be detected in STM measurements: (i) Unreconstructed unit cells (marked 1 in figure 1.1 (c)) are point defects, where the surface reconstruction is lifted within one unit cell by occupying both Fe_{oct} vacancies in the third layer and removing the Fe_{int} in the second layer, resulting in an $Fe_{12}O_{16}$ stoichiometry.[121, 122] (ii) Antiphase domain boundaries (APDB) (marked 2 in figure 1.1 (b)) can be observed wherever two growth domains of the reconstruction meet, and are formed e.g. after the annealing step required for surface preparation, when the surface reconstructs during cooling down.[122, 180] They appear as line defects running along the surface with a 45° rotation with respect to the iron rows. Both, APDB and unreconstructed unit cells, lead to a local enrichment of Fe^{2+} in the subsurface and can be preferred adsorption sites for molecules.[122, 181–183] (iii) Another surface defect commonly observed are surface hydroxyls (marked 3 in figure 1.1 (c)), whereby an H atom binds to a surface O without Fe_{tet} in the second layer.[123, 184, 185] Already at room temperature, these H atoms show a characteristic hopping movement between two neighbouring rows, which either increases or decreases close to unreconstructed unit cells. Upon annealing to about 550 K, the surface hydroxyls desorb as water, containing one surface O atom.[181, 186] (iv) Finally, Fe adatoms are occasionally observed on the surface after preparation,[187] which can be a sign for excessive reduction.

The adsorption of single metal adatoms has been excessively studied on $Fe_3O_4(001)$ mostly by Parkinson et al.: At room temperature, low coverages of Fe, Au, Pd, Ag, Ni, Pt, Ir and Rh atoms have been shown to preferentially adsorb at the twofold coordinating surface site without Fe_{tet} in the second layer (marked with an X in figure 1.2 (c)).[188–195] The stability of the adsorbed atoms, however, depends on the specific element: Au and Ag atoms are stabilized in this adsorption geometry against thermally induced sintering up to 700 K, where larger particles are formed.[189, 191] Pt and Pd readily adsorb CO molecules (e.g. from the UHV chamber background), resulting in a weakening of the bond to the surface, and thus, leading to the formation of highly mobile carbonyls that are stabilized if they are located at surface hydroxyls.[190, 193] Thus, sintering occurs already at room temperature when diffusing

carbonyls meet. Similar observations were made by Marcinkowski et al. for Pd atoms in methanol atmosphere, where a methoxy species weakens the Pd-surface bond, resulting in sintering already at room temperature.[196] Ni, Ir and Rh get incorporated into the surface upon annealing, occupying either a third layer, octahedral vacancy or even replacing an Fe$_{oct}$ in the first layer; typically lifting the reconstruction.[192, 194, 195, 197, 198] Further, ferrite-forming metals such as Ti, Zr, Mn and Co have been shown to preferentially occupy the subsurface (third layer) octahedral vacancy immediately upon deposition at room temperature, without annealing.[192, 199] The fate of an adatom on the Fe$_3$O$_4$(001) surface upon annealing can be estimated by considering the preferred, element specific coordination environment, as well as the oxygen affinity, as summarized recently by Hulva et al.:[200] Group 11 metals, such as Au, prefer a twofold coordination, and therefore remain at the surface to avoid oversaturation. Pd and Pt, both group 10 metals, would prefer a fourfold coordination, however sintering wins against incorporation. Group 9 metals, as well as Ni, prefer a higher coordination environment and are therefore easily incorporated into the surface.

There are several studies focusing on metal nanoparticles on the Fe$_3$O$_4$ surface that are relevant for the scope of this thesis. Magnetite generally seems to be a suitable candidate to investigate encapsulation of Pt clusters, as SMSI-induced encapsulation has been observed on different facets: Zhang et al. have shown that thermally grown Pt nanoparticles on the (001) surface exhibit a cuboid shape, reflecting the cubic symmetry of the magnetite support.[139] Furthermore, the authors examined the SMSI-induced encapsulation of Pt nanoparticles and found a gradual loss of CO adsorption capacity in TPD experiments upon annealing to 1000 K, which they attribute to the formation of an FeO(111) layer on top of the particles, as confirmed by complementary LEED experiments. In an earlier work focusing on Pt nanoparticles on the magnetite (111) surface, Qin et al. reported a similar SMSI-induced encapsulation of the particles by an FeO(111) layer, as confirmed by the observation of a Moiré structure on top of the particles.[201] They attribute the diffusion of Fe atoms in or on the Pt particles to be the initial step for encapsulation.[202] Surprisingly, in a subsequent study by the same group, this encapsulating layer was shown to actually enhance the CO oxidation activity at ambient pressures, via the oxidation of the layer, which leads to the formation of an OFeO trilayer catalyst.[203] When it comes to clusters on Fe$_3$O$_4$(001), especially size-selected ones, the scientific literature is rather scarce. As discussed above, Bliem et al. showed that Pt atoms become mobile in CO atmosphere leading to agglomeration and cluster formation, whereby Pt$_2$ can only be stabilized as carbonyl.[193] As this growth process can be observed in situ in the STM, the size of each thereby forming cluster could be estimated by counting the contributing Pt carbonyls. These small clusters were then shown to catalyse oxidation reactions following a metal-assisted MvK mechanism: In CO or H$_2$ atmosphere, lattice oxygen atoms are hereby extracted from the cluster perimeter at 550 K, forming CO$_2$ or H$_2$O.[13] As discussed above, the resulting undercoordinated Fe atoms can diffuse into the bulk at these temperatures, maintaining the Fe$_3$O$_4$(001) surface stoichiometry, which leads to the formation of large holes around the clusters. A possible reaction pathway for a Pt cluster-catalyzed CO oxidation has been calculated recently by Meier et al. for (PtCO)$_2$, requiring a complicated mechanism that involves the replacement of a surface Fe$_{oct}$ by one Pt atom of the cluster in the catalytic

cycle.[204] In oxygen atmosphere at 550 K, Pt clusters catalyze the cleavage of O_2, resulting in the growth of new, pristine $Fe_3O_4(001)$ islands around the clusters, by pulling out Fe interstitials from the bulk. Furthermore, Rh atoms have also been shown to become mobile in an O_2 atmosphere at room temperature. Due to the higher oxygen affinity of Rh, they form small Rh_xO_y clusters, which changes the CO oxidation mechanism:[195] While Rh atoms catalyze CO oxidation via a MvK mechanism, the oxide clusters prefer a Langmuir-Hinshelwood pathway.

1.3 Outline of this Thesis

This thesis, investigates model catalytic systems of size-selected, sub-nanometer Pt clusters deposited on a magnetite (001) surface by means of STM, XPS, TPD and pulsed reactivity measurements under UHV conditions. The work aims at understanding on a fundamental level, how the clusters interact with the support material as a function of temperature. In a systematic approach, the investigation disentangles phenomena from lattice oxygen reverse spillover, to encapsulation and ripening, and elucidates how these affect the catalytic properties.

The second chapter introduces the experimental UHV system, followed by a description of the employed techniques and the corresponding data analysis methodology. The focus lies especially on the developments and improvements around the sniffer, a highly sensitive, pulsed reactivity setup.

Chapter three, is devoted to lattice oxygen reverse spillover. To this purpose, the reactivity of Pt_n clusters on $Fe_3O_4(001)$ is investigated via CO oxidation. We show how at elevated temperatures oxygen atoms from the surrounding of the clusters migrate on top of the clusters, resulting in a highly reactive oxygen species, readily oxidizing adsorbed CO. From highly sensitive, pulsed reactivity measurements we can thus conclude that in the MvK reaction pathway, the lattice oxygen actually reacts on top of the cluster.

Chapter four focusses on cluster encapsulation following the lattice oxygen reverse spillover and its effect on cluster ripening. Here, we deposit constant coverages of different cluster sizes and investigate their stability and morphology evolution as a function of annealing temperature. Similar to nanoparticles, the clusters get encapsulated by a thin iron oxide layer, as a consequence of SMSI. We provide evidence that the layer has a defective, FeO-like stoichiometry, and is actually covering the clusters. This encapsulating layer is found to stabilize larger clusters against Ostwald ripening up to about 800 K, however, smaller clusters sinter via Smoluchowski ripening already at much lower temperatures, indicating the diffusion of entire, encapsulated clusters to be possible on oxides.

This thesis ends with a conclusion, including an outlook for further research. The appendix includes a further published paper, investigating the bottom-up synthesis of carbon nitride networks on Au and highly oriented pyrolytic graphite (HOPG), by polymerization of 2,5,8-Triazido-s-heptazine. These networks are promising candidates for support materials in more applied cluster catalysis, as they are cheap, stable in liquid environments, and exhibit a defined porous structure that can be used to stabilize atoms or clusters on a surface. On Au, amorphous carbon nitride networks could be formed thermally, photochemically or via secondary electrons, on HOPG only the latter one resulted in highly

porous, amorphous, weakly interacting networks.

2 Experimental Methods

This chapter gives a brief overview over the UHV apparatus used in this thesis, including the cluster source, and introduces the UHV transfer suitcase built during this thesis. Furthermore, the experimental methodology, measurement protocols and data evaluation procedures are described, starting with the STM, followed by an in depth description of the sniffer setup, and finally XPS. This chapter concludes by explaining the sample preparation procedures.

2.1 Experimental System

This section aims at describing the UHV apparatus used to obtain the experimental data shown in this thesis. A much more detailed, in depth description can be found in.[205] Figure 2.1 gives a schematic overview of the entire experimental setup, as well as the pumping system.

Microscopy chamber

The microscopy chamber has a base pressure of $< 3 \times 10^{-11}$ mbar, measured using a Bayard-Alpert gauge (AML, AIG). The vacuum is maintained by an ion getter pump (Varian, VacIon 150) and a titanium sublimation pump (TSP) (VACGEN, ST22). This chamber houses the scanning probe microscope (Omicron, VT-AFM), capable of performing STM as well as atomic force microscopy (AFM) measurements within a large temperature range of about 150-800 K. The microscope is upgraded with an electronic add-on module (FAST) for video rate scanning and atom tracking experiments.[206] A homebuilt hydrogen doser with optional cracking filament for in-situ dosing of atomic hydrogen during STM measurements is installed. This chamber also hosts nine slots for storing samples, STM tips or cantilevers; the sample transfer is carried out using a wobble stick.

Preparation chamber

The preparation chamber exhibits a base pressure of $< 1 \times 10^{-10}$ mbar, measured by a Bayard-Alpert gauge (AML, AIG). The vacuum is generated using a turbomolecular pump (Pfeiffer vacuum, HiPace 300 M) with magnetic bearings to minimize mechanical vibrations of the system, as well as an ion getter pump with integrated TSP (Varian, VacIon plus 300). A QMS residual gas analyzer (SRS, RGA200) monitors the quality and composition of the vacuum. The preparation chamber is equipped with an x, y, z, θ manipulator, with sample heating stage, and cooling by liquid nitrogen flow (VAb, Dodecon). For sample cleaning via sputtering, an ion source (Specs, IQE 11/35), with attached Ar valve is installed, and a gas dosing system can provide up to four further gases for preparation or ex-
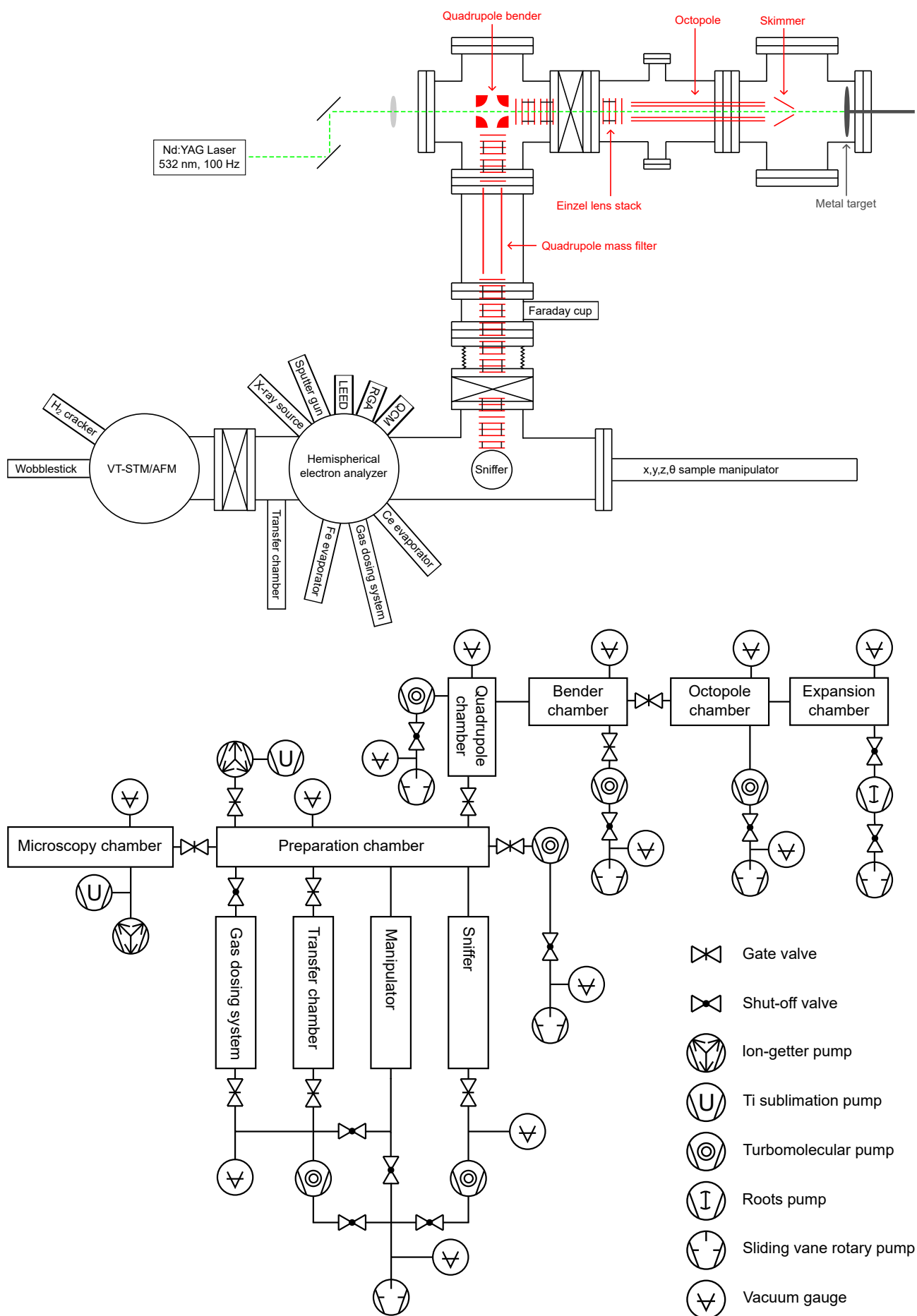
Figure 2.1: Top: Schematic overview of the UHV apparatus used in this thesis, including the cluster
source with the ion optics in red, as well as the laser beam path in green. Bottom: Pumping
scheme of the entire experimental setup.

periments. For thin film synthesis, a homebuilt Ce evaporator with integrated quartz crystal microbalance (QCM) and an Fe evaporator (Omicron, EFM3) with external QCM (INFICON, SL-A1E40) are available.

The preparation chamber is further equipped with a hemispherical electron analyzer (Omicron, EA125) and an X-ray source (Specs, XR50) in an almost magic angle geometry of 54.7° for XPS measurements. For surface structural analysis a low energy electron diffractometer (Specs, ErLEED) is installed. Reactivity measurements are carried out by a QMS (Pfeiffer vacuum, Prisma Plus) based Sniffer setup (compare section 2.3 for details), which is differentially pumped by a further turbomolecular pump (Pfeiffer vacuum, TMU 071 Y P). Sample transfer into the UHV system is carried out via an additional fast entry transfer chamber. It is equipped with a magnetic transfer rod, two additional sample storage positions and a separate electron beam heating stage, mostly used for degassing. Here, a further home-built molecule evaporator can be installed. The transfer chamber has a base pressure of $< 1 \times 10^{-8}$ mbar, maintained by another turbomolecular pump (Pfeiffer vacuum, TMU 071 P).

Cluster source

Size-selected metal clusters are generated using a homebuilt laser ablation cluster source, developed by Heiz et al,[207] based on an earlier design by Smalley.[208] As shown in figure 2.1, the source consists of four differentially pumped chambers and is separated from the preparation chamber by a UHV gate valve. In this way, UHV conditions can be maintained in the preparation chamber while the cluster source is operated. For the laser ablation, the 2nd harmonic (532 nm) of a pulsed (100 Hz) Nd:YAG laser (Innolas, Spitlight DPSS 250) is focused onto the metal target of choice. In this thesis, a Pt target (99.95%, ESG) was used. The target is rotating in a hypocycloidal way, ensuring a highly homogeneous ablation of the complete target disk, thus maximizing its lifetime. The thereby formed metal plasma is subsequently cooled via collisional cooling and the adiabatic expansion of a He (Westfalen, He 6.0) pulse, delivered by a pulsed piezo valve. This leads to the formation of a super cool, supersonic beam of neutral, as well as charged atoms and clusters. To prevent immediate cluster fragmentation in the first agglomeration and growth steps, any excess energy released by bond formation has to be dissipated quickly. This happens mainly via the collisional cooling with He atoms. The better this cooling, the larger cluster sizes can be formed. As a consequence, the initial cluster distribution depends on the He pulse pressure: A higher He pressure generally shifts the cluster distribution towards larger sizes. For generating the cluster sizes used in this thesis, He pulses of 5-12 bars have been applied. After the expansion, the supersonic cluster beam is separated from the residual gas using a skimmer and subsequently focused by a radio frequency octopole ion guide, which is followed by three electrostatic einzel lenses. These guide the cluster beam into a 90° quadrupole bender, which is necessary for removing neutral particles from the beam. Further einzel lenses focus the clusters into a quadrupole mass filter (Extrel, 150 QC) for m/z and thus size-selection (mass range: 1-16000 amu). Finally the clusters are guided by another set of electrostatic lenses towards the preparation chamber, where they are deposited onto the substrate of choice under soft-landing conditions (kinetic energy

< 1 eV/atom) to ensure the deposition of intact clusters on an intact surface. Depending on the cluster size, it can therefore be necessary to apply a retarding voltage onto the sample. Cluster coverages can be set during deposition by measuring the neutralization current of the charged clusters on the sample using a picoampmeter (SRS, SR570). Note that only either positively or negatively charged clusters can be generated; in this work exclusively positive ones have been used. For the clusters used in this thesis, a cluster current of 100-200 pA could be generated with this specific source.

UHV sample transfer suitcase

One major achievement during the course of this thesis was the construction and successful implementation of a sample transfer suitcase, which can be used for transporting samples between different experimental systems, while maintaining controlled UHV conditions. Sample preparation for single crystals used in surface science studies is complex, time consuming and sometimes rather expensive. Additionally, particular substrates might be unstable when exposed to air, which is especially true when it comes to highly reactive cluster materials. But even stable samples easily become covered by several monolayers of molecules (typically water and hydrocarbons) when being removed from the UHV system. Therefore transferring these highly complex samples between different experimental facilities is not trivial and usually avoided. However, when necessary equipment is not available at the own setup, or shared facilities like synchrotrons have to be used, sample transport becomes inevitable, especially when highly sophisticated sample preparation techniques like the size-selected cluster source are used. Such a transfer becomes possible when using a UHV suitcase, which maintains UHV conditions during the entire transport and thus rules out any contamination or degradation of the samples due to air exposure.

When building such a UHV suitcase, several key requirements have to be fulfilled: It has to keep UHV conditions over at least several days without external power supply, it should be compatible to most experimental systems and must be as lightweight and compact as possible, while being able to securely store several samples. The UHV suitcase built in this thesis is shown in figure 2.2 (a) and has already been successfully used for transfers to different UHV chambers and facilities, including the HIPPIE beamline of the MAX IV synchrotron in Lund, Sweden, and the Institute of Functional Interfaces at KIT, Karlsruhe.

The central part is a CF40 6-way T-piece, to which all other components are attached. A viewport (quartz glas) is used to observe transfer processes in the suitcase. The sample storage unit (shown in figure 2.2 (b)) is attached to a short transfer arm (Ferrovac) and allows to accommodate up to four different samples, whereby two storage positions offer additional vertical space for higher sample types. To ensure maximum compatibility, the UHV suitcase is based on the common flag-style sample holder design, which is (with some modifications) used in a variety of commercially available, as well as in custom-built systems, while most other, larger sample holder designs offer specific adapters. The flags point in a direction orthogonal to the arm axis. Figure 2.2 (c) shows a selection of different sample holders, which all can be transported with the UHV suitcase. A UHV gate valve in front of the sample storage arm permits transfers in a passive way, where samples are extracted from the UHV
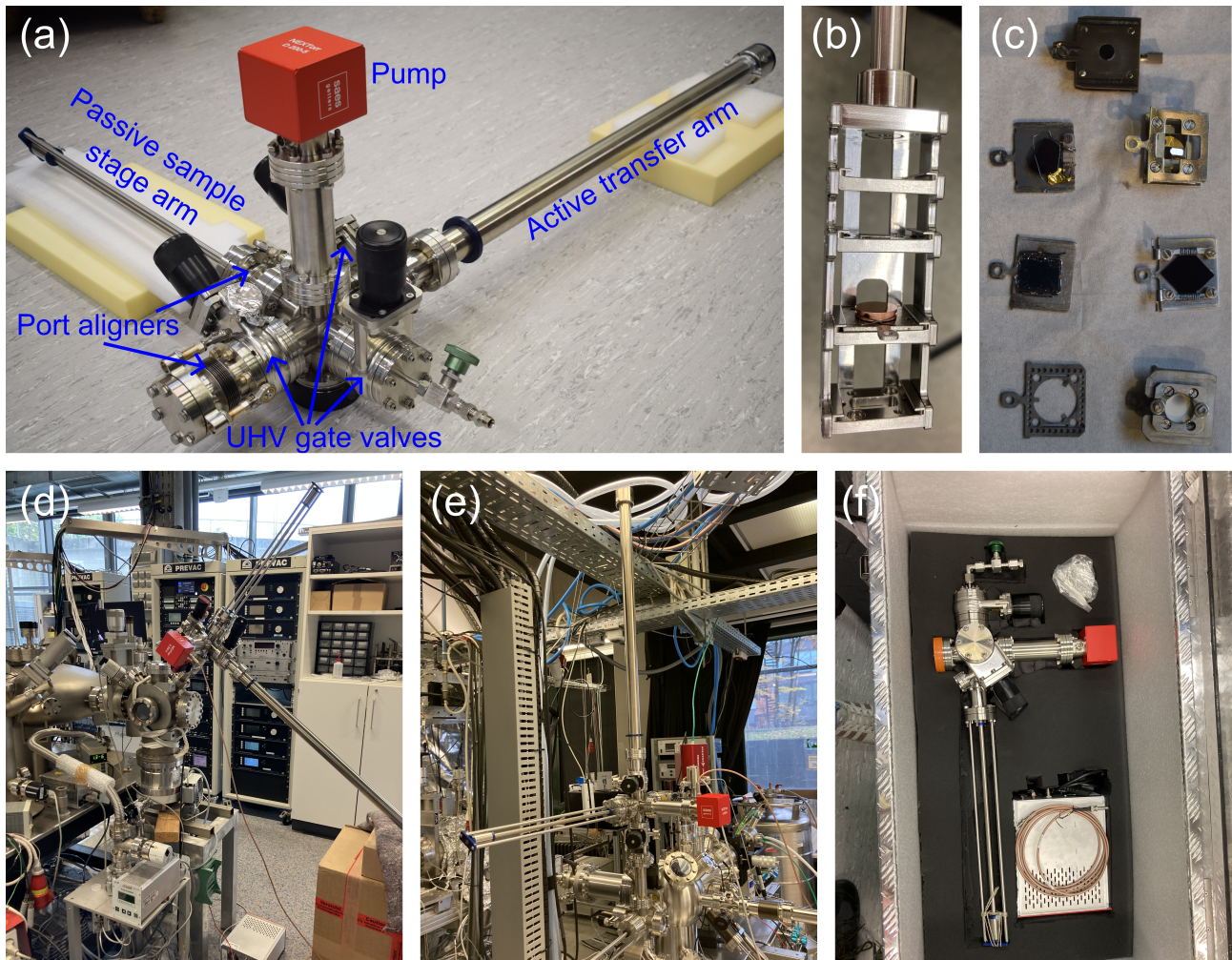
Figure 2.2: (a) Overview of the UHV transfer suitcase showing all relevant parts. (b) Sample storage unit with four sample positions mounted onto the passive transfer arm. The lower two positions are designed for thicker double decker samples. (c) Selection of different sample and tip holders based on the flag-style sample plate design, that can all be transported in the UHV suitcase. (d) UHV suitcase attached to transfer chamber in passive transfer mode. (e) UHV suitcase attached in active transfer mode. (f) Transport box with the suitcase already inside. The active transfer arm has to be unmounted for shipping.

suitcase sample storage by an active transfer arm attached to the target chamber. A port-aligner is directly attached to the storage arm for precise alignment during these transfers. Figure 2.2 (d) gives an example for such a passive transfer mounting. The sample storage arm can extend up to 26.5 cm inside the accommodating UHV system, with the uppermost sample at about 20.5 cm and the lowest at 26 cm. The sample storage requires accommodating UHV systems with an inner tube diameter of ≥ 36 mm. This has to be taken into account when considering transfer possibilities to other systems. A further, long transfer arm (Ferrovac) attached to the suitcase is equipped with a sample grabber for active sample transfer. With this arm it is not only possible to change sample positions within the storage unit in the suitcase, but also to transfer samples directly to suited receiver stages (e.g. on a manipulator) of the attached UHV system. This becomes possible by another gate valve mounted on the opposite side of the long transfer arm. An example for such a transfer situation is given in

figure 2.2 (e). An additional pumping port included in that gate valve enables direct attachment of the vacuum suitcase to the target system without need for intermediate pumping chambers. The long transfer arm can extend up to 48 cm into the accommodating UHV system. The minimal inner tube diameter on this side is limited by the desired sample holder size, which is 19 mm for standard plates. For shipping, the long transfer arm has to be removed. This is possible due to a third UHV gate valve, directly mounted in front of the active arm. This valve includes a pumping port, to permit reassembly at the target destination without venting the sample compartment. For compact and secure shipping of all necessary components, the transport box shown in figure 2.2 (f) has been designed.

To maintain UHV conditions also for prolonged times, the UHV suitcase is pumped by an ion pump (SAES Getters, NEXTorr D 200-5), that combines an ion getter pump (5 L/s) and a passive non-evaporable getter (NEG) sorption pump (200 L/s). While the former needs an external power supply, is mainly necessary to pump traces of non reactive gases, such as Argon, and additionally acts as a pressure gauge, the NEG pump only requires power upon initial activation or regeneration, and is able to maintain UHV conditions for more than a week without power. With this pumping system a UHV suitcase base pressure of $< 1x10^{-10}$ mbar can be maintained easily; when switching on the active ion pump again after a week without electricity, the pressure typically increases in the low 10^{-9} mbar range due to degassing, but the base pressure of $< 1x10^{-10}$ mbar is recovered within minutes. Note, that the UHV gate valves tend to leak in the 10^{-9} mbar range over time. Therefore, it is beneficial to blind flange and pump all gate valves on the air side when not in use.

Before initial pump activation or after venting, a system bake-out has to be carried out to achieve the desired vacuum base pressure. Typically this is done at around 140°C for 36-48 h, with a limiting temperature of 150°C given by the magnets of both transfer arms. The required time can be shortened to about 24 h by increasing the temperature only at the pump to about 160-170°C. In general, but especially for baking temperatures above 150°C, the magnets of the pump have to be removed to maintain their magnetization. After bake-out, the ion-getter pump is degassed first, by switching it on and off several times. Subsequently, the NEG pump is activated by a 1 h heating ramp that should be performed in the still warm (typically < 100°C) chamber. Note, that for bake-out as well as for activation, the suitcase must be attached to an UHV system with an additional pump (e.g. a pumping station), as the integrated pump cannot be used during these processes.

2.2 Scanning Tunneling Microscopy

Fundamental principle

Since its initial development in 1982 by Binnig and Rohrer,[209] STM has become a versatile, wide spread technique for investigating the structural and electronic properties of flat surfaces with up to atomic resolution. An atomically sharp tip is brought in close proximity of the investigated surface, while applying a bias voltage in between tip and sample. In vacuum, at distances below roughly 1 nm, electrons start to tunnel through the gap, which results in a measurable tunnelling current if both, the tip and the sample are electrically conductive.[210] In a simplified, one-dimensional picture, assuming

a rectangular potential barrier, the tunnelling current I close to the Fermi level is given by equation 2.1.[211]

$$I \propto e^{-2\kappa d} \quad \text{with} \quad \kappa = \frac{1}{\hbar}\sqrt{2m_e(V_B - E)} \tag{2.1}$$

Here, d is the distance between tip and sample, $\hbar$ is the reduced Planck's constant, m_e is the mass of the electron with an energy E (with repect to the Fermi level) and V_B is the tunnelling barrier height. The exponential dependency of the tunnelling current on the tip-sample distance, resulting from equation 2.1, is the key to STM measurements. For example, distance changes of only 0.1 Å already lead to a 20% change in current.[212] Thus the topography of the investigated sample can be imaged by scanning the tip across the surface while recording the tunnelling current. Figure 2.3 (a) schematically depicts a corresponding experimental setup.
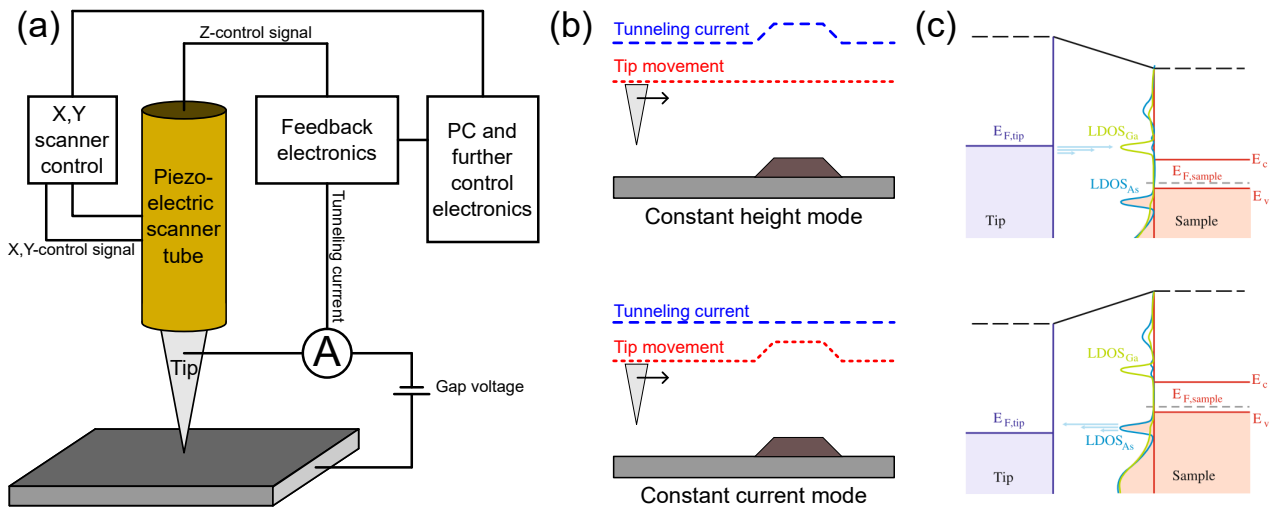
Figure 2.3: (a) Schematic overview of an STM setup. (b) Illustration of both basic STM measurement modes: Top: Constant height, bottom: Constant current. (c) Schematic of gap voltage dependent tunnelling on a semiconductor sample (GaAs). Top: Positive sample bias voltage; tunnelling occurs from tip to sample. Bottom: Negative sample voltage results in a tunnelling current from occupied sample states to unoccupied tip states. Reproduced with permission from Springer Nature.[212]

STM measurements can either be performed in constant height or constant current mode. In the former, the tip is kept at a constant vertical position, while the tunnelling current is recorded as a function of the lateral position of the tip. This allows rather high scanning speeds, but comes at the risk of crashing the tip on rougher surfaces. In constant current mode on the other hand, the tunnelling current is fed into a feedback loop that tries to keep the tunnelling current, and thus the tip-sample distance, constant by changing the absolute vertical position of the tip. Therefore, imaging is done by recording this vertical position of the tip as a function of the lateral one. Due to the feedback loop (kHz timescale), accidentally crashing the tip into the surface can be avoided, but the scanning speed is generally lower than in constant height mode. A comparison of both measurement modes is shown in figure 2.3 (b). Additionally, they can be used in combination, for example in the FAST STM tech-

nique.[206, 213] Here, images are recorded in constant height mode, while a slow feedback loop corrects for the overall slope of the sample, allowing high frame rates, while reducing the risk of tip crashes. In STM measurements, the tunnelling current not only depends on the tip-sample distance, but also on the electronic structure of surface and tip, and generally a convolution of both is measured.[212] As shown in figure 2.3 (c), the applied gap voltage determines what states are accessible for tunnelling and can contribute to the total tunneling current, resulting in the observed topographic contrast to often be bias voltage dependent. This has to be taken into account, when comparing heights extracted from the STM with real atomic distances. Furthermore, the sign of the gap voltage can also have a huge impact on the observed contrast, as tunneling occurs between completely different states: A positive sample voltage results in tunneling into unoccupied sample states, whereas with a negative sample voltage occupied sample states are measured. Especially for semiconductor surfaces, the contrast observed in STM is rather dominated by electronic than topographic effects: One perfect example is the r-TiO_2(110) surface, where typically the Ti atoms are observed, while bridging oxygen atoms, although even protruding from the surface, are imaged as depressions.[119] Another example is the magnetite (001) surface, where only the iron rows are measured in STM, as the surface oxygen atoms have no density of states in close to the Fermi level.[177] Furthermore, the Fe_3O_4(001) surface exhibits a prominent bias dependent contrast, whereby the undulations of the iron rows reverse in phase when the bias is increased.

Standard measurement settings

During this thesis STM measurements where exclusively performed in constant current mode, as cluster samples are intrinsically corrugated. A PI feedback loop with a P value of 0-1% and an I value of 1-2% were typically used in the Matrix program. Generally, the larger the investigated cluster size, the higher the feedback values have to be set, while vibrations induced in the system as a result of too high feedback parameters have to be avoided. The ideal tunnelling current and bias voltage have to be found for each substrate. The standard measurement parameters for the system Pt_x/Fe_3O_4(001) were a tunnelling current set point of 300 pA at a gap voltage of +1.5 V (tunneling into unoccupied sample states). The scanning speed was varied depending on the spacing between the points of the image; a larger spacing requires a lower measurement speed. On a standard 100 x 100 nm^2 image with 400 x 400 points, a measurement speed of 700 µs per point was used.

Tip preparation procedure

In STM measurements, the lateral shape of any observed feature is always a convolution of the actual shape (including electronic and physical structure) and the shape of the tip. Thus, the quality and obtainable resolution in STM measurements strongly depends on the shape of the tip. An atomically sharp tip provides an ideal prerequisites for obtaining atomic resolution. On the other hand, a blunt tip can critically reduce resolution, and a multiple tip may give rise to measurement artefacts, by imaging the same feature several times. Clusters are typically several layers in height and sharper than the STM tip, therefore a highly symmetric tip without any multiple tips is required. Thus a preparation

procedure to reliably obtain suited tips is necessary.

All measurements in this thesis where performed using commercially available Pt/Ir tips (UNISOKU) or etched W tips, whereby the Pt/Ir tips performed more reliably on reducible oxide supports at elevated temperatures. Whenever a new tip was introduced into the system, it was sputtered to remove adsorbates and oxide overlayers. For both types of tips, an Ar pressure of 5×10^{-6} mbar at an energy of 1.5 keV was used, yielding an ion current of around 200 nA at the tip. The Pt/Ir tips were commonly sputtered for 120 s, the W tips for 300 s. The same cleaning procedure was used for recovering blunt tips between measurements. The quality of freshly sputtered tips was improved further on a Au(111) single crystal, by intentionally driving them up to 15 nm into the gold while applying a constant potential. Thereby the immersion depth was first increased in 1 nm steps between consecutive attempts, until a sharp edge in the I-Z spectrocopy was observed, and then decreased again in 1 nm steps, down to a minimal depth of 2 nm. This procedure was repeated until stable imaging with the desired resolution was obtained. Any further tip preparation was typically done in situ on the investigated surface, by applying voltage pulses of 3.0-10.0 V for a duration of 50 ms, as well as by briefly inverting the gap voltage for a few seconds. Contrary to the Au(111) sample, intentionally crushing the tip into oxide crystals did typically not lead to any improvement.

STM data evaluation: Image correction and cluster height determination

Correction of STM images was performed by Gwyddion.[214] The overall background was subtracted for each image using the mean plane level correction, followed by the row-by-row alignment tool (median or median of differences). On top of that, the three point levelling tool, which allows to define a levelling plane by manually setting three points, was used for background correction of images exhibiting a considerable amount of atomic steps.

Statistical cluster height distribution analysis was performed using a home-written Igor routine. First, the STM images are background corrected, again by mean plane subtraction followed by row-by-row alignment (as above). Prior to cluster analysis, the pixel density is doubled for better cluster detection. The particles on the surface are identified using an apparent height threshold which has to be chosen individually depending on the investigated substrate and cluster size. Clusters the algorithm failed to detect were added manually. After detection, particle analysis was performed by drawing a profile thorough the cluster maximum and calculating their height with respect to either the median of the entire image excluding all particles, or the median around each individual particle. For the systems investigated in this thesis, no significant differences between both methods were observed. Cluster analysis was performed separately for each atomic terrace; clusters located at step edges, holes or the edge of the image were excluded from the height analysis, but considered for the coverage. This method of height determination includes a small error that arises from the fact that the median of the image may depend on the surface corrugation and especially the defect density.

2.3 Sniffer

This section gives an overview of the sniffer setup, starting with a technical description, followed
by introducing the measurement modes and the data evaluation. The sniffer, which has already been
implemented into the system during my Master's thesis,[215] was commissioned and continuously im-
proved during this work, measurement routines were established and a data evaluation software pro-
grammed.

2.3.1 Setup

The sniffer setup is a compact, homebuilt, QMS based TPD and reactivity measurement device, and
has been developed adapting a design by Harbich and co-workers.[216] It is specifically optimized for
high sensitivity investigations as on low coverages of supported metal clusters. The particular sniffer
used in this thesis is shown in figure 2.4 (a), a detailed technical description can be found in.[217]
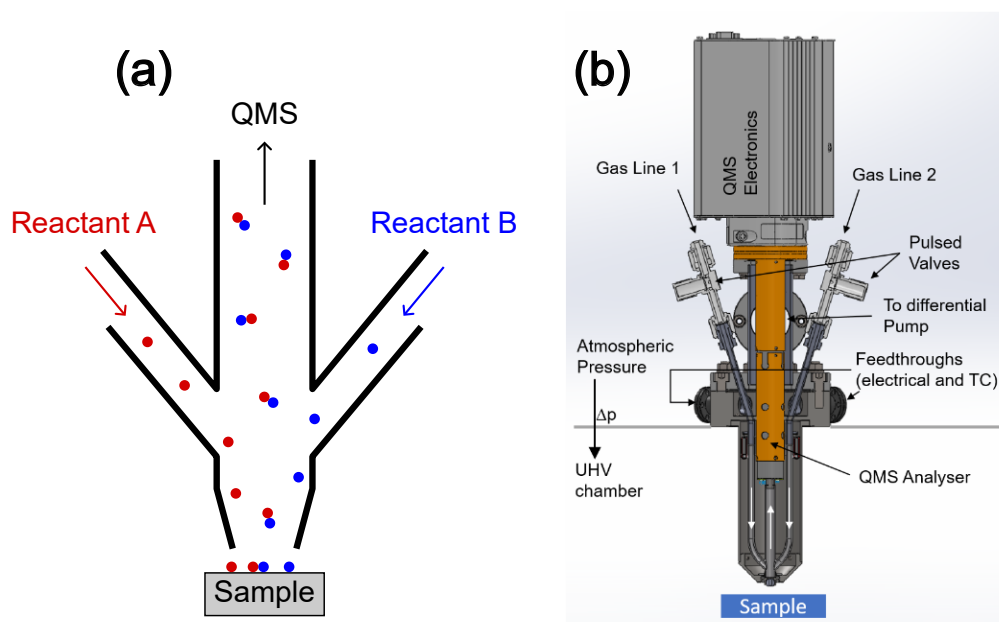
Figure 2.4: (a) Schematic illustration of the fundamental working principle of the sniffer. Reactants
can be dosed on the sample independently via the two side arms. Reaction products are
collected by the central tube, which guides them towards the QMS. (b) Drawing of the
sniffer setup, including all relevant parts. The gas flow directions are indicated by arrows.
Adapted from.[217]

The fundamental idea of this device is to combine a pulsed reactant doser with a differentially pumped
QMS for reaction product analysis. Up to two different gases can be pulsed simultaneously or alter-
nately using pulsed magnetic valves (Parker, Series 99). The dosage within each pulse can easily
be defined by the voltages applied to the valves (exponential scaling) or the set pre-pressures (linear
scaling). Typical dosages may range from about 100 Langmuir down to below 1 % of a Langmuir per
pulse (1 Langmuir is defined as a dosage of 1.33 x10^{-6} mbar for 1 s). After passing the valves, the
reactants are guided towards the sample by a quartz tube assembly consisting of two smaller tubes

for dosing which are connected to one larger central tube facing the sample. Note, that only about 50% of each reactant pulse can actually arrive at the sample surface, while the other half is directly pumped out of the system by the differential pumping of the sniffer itself, as can be determined by varying the distance to the sample. Any reaction products or desorbing species coming from the sample are collected in the central tube and guided towards the QMS, where they can be analyzed, and then removed by differential pumping. This fundamental working principle is displayed in figure 2.4 (b). At the side facing the sample, a quartz skimmer cone is attached directly to the central tube, with a hole of 3.6 mm diameter, which is smaller than the standard sample size of 4.4 mm. This ensures that almost exclusively molecules originating from the sample surface are collected, while species desorbing for example from the sample heater are avoided. Furthermore, the reactants are directly dosed onto the sample and not in the chamber background (comparable to a molecular beam doser), minimizing adsorption on the chamber walls or on cold spots on the manipulator and thus, further reducing background signals in the QMS. These advantages rely on the sample being as close as possible to the entrance of the cone, which additionally enhances the reaction product collection efficiency and therefore the sensitivity.
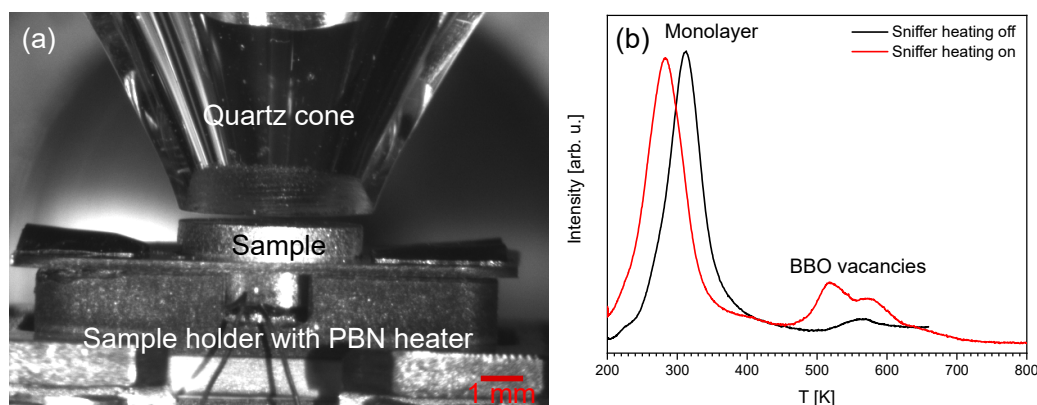
Figure 2.5: (a) Typical position of the sniffer quartz cone in front of the sample. The image was recorded with a 10 x magnification camera that is used for sample positioning. In this case, the sniffer-sample distance was about 250 μm. (b) H_2O TPD from r-TiO_2(110) clearly showing the effect of the sniffer heating. When the quartz tube assembly is hot, the desorption temperatures are comparable to the literature;[218] without heating, the entire spectrum is shifted to higher temperatures. The heating rate was 1 K/s

As shown in figure 2.5 (a), typically a cone-sample distance of 100-300μm is used. Under these conditions, the quartz glass wall thickness of ≈ 1 mm also contributes to the isolation from the rest of the chamber. To further improve the sensitivity, the entire quartz tube assembly can be heated, usually to a temperature between 100 and 200°C, preventing the adsorption of reactants or products. The heating is especially crucial when working with rather "sticky" gases like water. A very nice illustration is the TPD of H_2O from r-TiO_2(110), shown in figure 2.5 (b). Here, the entire spectrum shifts by about 30 K to higher temperatures, if the internal heating is not running.

Originally, the sniffer was designed to work at comparably high pressures up to the 1.0 x10^{-3} mbar

range. A tantalum cylinder, inserted in the ionization region of the QMS with small slits facing the filaments, was used for filament protection at such elevated pressures. This allows electrons to enter the ionization region, while keeping the gas load on the filaments reasonably low. However, during the course of this thesis, the Ta cylinder was replaced by a stainless steel one, with large gaps instead of slits, exposing the filaments to the entire ionization region. This was done for several reasons: Firstly, without thin slits, more electrons can enter the ionization chamber of the QMS, thus increasing the ionization probability. This led to an increase in signal of about a factor ten. Secondly, the original Ta cylinder was continuously heated, as well as bombarded by electrons, due to its close proximity to the filaments. As a consequence, some decomposition or reaction processes, involving the chamber background gases, were happening at this cylinder. Over the years, this resulted in an increase in C, CO_2 and O_2 background signals in the QMS, which strongly interfered with most measurements. After replacing the Ta cylinder however, these impurities vanished. This modification comes at the cost, that high pressure measurements are no longer possible, with the system now being limited to standard maximum pressure of the QMS, i.e. < 1.0 x10^{-4} mbar using the Faraday cup detector, and < 1.0 x10^{-5} mbar using the channeltron; both of these values are defined as being in the QMS, the actual pressure at the sample may still be higher.

2.3.2 Desorption and reactivity measurement

This section describes in detail the quadrupole mass spectrometry based methods for investigating desorption and reactivity used in this thesis. All of them can be easily performed using the sniffer setup. Each single method is only capable of delivering a certain specific information about the model catalytic system, a more complete picture about the chemical activity can only be achieved by combining all the techniques listed below.

Temperature programmed desorption

Temperature programmed desorption (TPD) is a comparably simple technique for investigating the adsorption of molecules on almost any substrate.[219,220] First, the sample is exposed to a well-defined quantity of the investigated adsorbate at a temperature sufficiently low to enable adsorption, which typically means room temperature or below. The sample is subsequently heated with a constant linear heating ramp of usually 1-2 K/s, while monitoring the desorption of the adsorbate as a function of the temperature in a QMS. High heating rates yield higher signal intensities and are thus better suited, if only a small desorption feature is expected. However, the faster the desorption, the more pumping becomes an issue, and the individual desorption features can get smeared out. Thus, the selected heating rate is always a trade-off between signal intensity and resolution. The quality of TPD spectra is generally improved by using a shielded, differentially pumped QMS with a skimmer cone, which reduces signal contributions from the chamber background.[220,221] This fundamental measurement procedure is schematically shown in figure 2.6 (a).
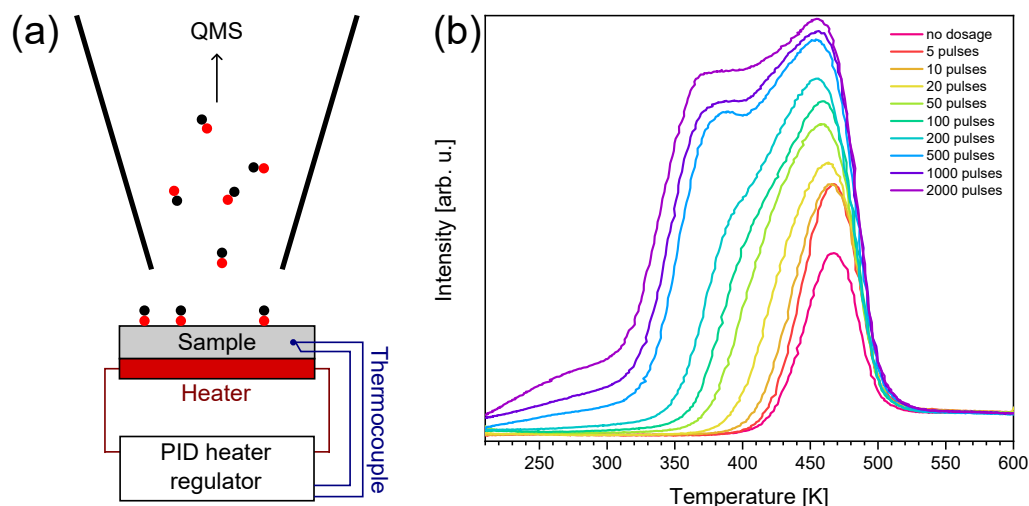
Figure 2.6: (a) Schematic illustration of the desorption of CO molecules from a sample, in a simplified version of the experimental setup used in this thesis. The skimmer cone in front of the sample avoids signal contribution from anywhere but the sample. (b) Example first order TPD of CO (m/z = 28) desorption from Rh(111) as a function of dosage typically used for sniffer calibration. Dosing has been performed in a pulsed way using the sniffer. The two observed desorption peaks correspond to on-top sites (high temperature peak) and bridge sites (low temperature peak).[222]

TPD measurements result in an individual desorption curve and temperature for every type of molecule on any substrate and can be used to gain both, qualitative and quantitative information on the nature of adsorption sites, type and strength of bonds, as well as desorption energies and kinetics. The desorption rate is generally described by the Polanyi-Wigner equation (equation 2.2):[223]

$$-\frac{d\theta}{dt} = \nu(\theta, T) \cdot \theta^n \cdot exp\left(-\frac{E_{des}(\theta, T)}{k_B T}\right) \tag{2.2}$$

θ is the adsorbate coverage, ν the frequency factor, n is the desorption order and E_{des} is the desorption energy. Both the frequency factor as well as the desorption energy may depend on temperature and coverage. The desorption order gives insights into the desorption mechanism, and can be determined by how the desorption maxima develop as a function of coverage.[219] A zero-order desorption kinetic results in a desorption peak which is shifted to higher temperatures for increasing adsorbate coverages and a common leading edge. It is typically observed when there is an unlimited reservoir of molecules with the same desorption energy, as for example for multilayer desorption. A first-order kinetic results in the desorption peak temperature being independent of the coverage. It is commonly observed for a unimolecular desorption process. An example is given in figure 2.6 (b), which is the CO desorption from Rh(111). Second-order desorption processes have peaks which shift to lower temperatures with increasing coverage and a common trailing edge, and are characteristic for recombinative desorption of molecules which dissociate on the surface upon adsorption.

Temperature programmed reaction

Temperature programmed reaction (TPR) measurements are closely related to TPD measurements and follow essentially the same experimental procedure: One or several reactants are adsorbed at low temperatures and subsequently the sample is heated with a linear heating ramp, while all potential reaction products are measured in a QMS.[219] This experimental technique allows to explore thermal reaction pathways, gives insights in activation energy barriers and can be used to determine reaction kinetics and thus reaction mechanisms. Due to the similarities to TPD experiments, TPD and TPR measurements are commonly conducted simultaneously. At higher temperatures, the TPR procedure is often problematic, as reactivity above the reactants' desorption temperatures cannot be detected. This temperature range can be accessed by pulsed reactivity measurements, providing additional chemical information.

Pulsed reactivity measurements

With the sniffer setup, reactivity measurements can be conducted also in a pulsed manner.[216,224,225] Therefore, one or two reactants are pulsed on a sample, either simultaneously or alternately, while the resulting product pulses are detected in a QMS. Several types of experiments are possible: Titration experiments are typically conducted isothermally, whereby a pulse series of a reactant A is used to react off a quantity of a reactant B on a surface. With this type of experiment the amount of B on the sample can be precisely quantified for that given temperature. One common example, which is shown in figure 2.7 (a), is the quantification of carbon impurities by oxidation with O_2.
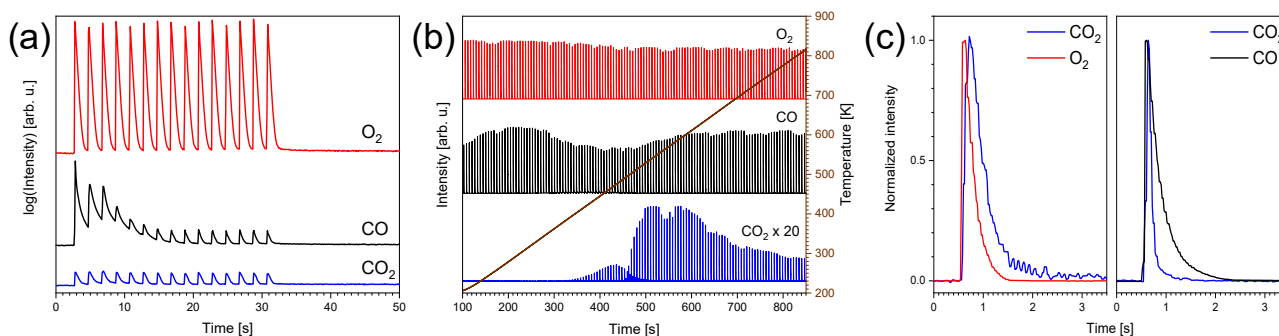
Figure 2.7: Types of experiments commonly performed using the sniffer setup. (a) Titration experiment: Removal and quantification of carbon impurities on a Rh(111) crystal by pulsing O_2 and monitoring CO and CO_2 formation. The product pulses do not entirely decay to zero, due to CO and CO_2 formation at the QMS filament, as well as impurities in the O_2. (b) Temperature programmed pulsed reactivity experiment: Pulsed CO_2 formation on a Pt(111) crystal, observed when alternately pulsing CO and O_2 as a function of temperature. The reactant and product traces are shown. (c) Reactant dependent product decay times, observed at 500 K during the CO oxidation shown in (b). We observe longer CO_2 pulse decay times synchronized with O_2 reactant pulses than with CO pulses.

The second, and more commonly used measurement mode of the sniffer is continuously pulsing reactants while ramping up the temperature, again with a constant linear rate of usually 1-2 K/s. With this

mode, temperature dependent thermal reactivity can be investigated, similar to TPR measurements. The advantage is that reactivity can also be explored in a temperature regime above the desorption temperature of one reactant. Furthermore, such a pulsed experiment can also be used to understand the reaction mechanism itself and explore various limitation regimes, as each pulse is a snapshot of the state of the system at a given temperature. This can be done by evaluating with which reactant pulse the recorded product pulses are synchronized. If for example two reactants A and B are pulsed alternately and the product pulse only appears synchronized with reactant A, than A is the limiting component. If product formation appears for both reactants, then some sort of equilibrium situation exists on the sample and both reactants are available beyond the pulse length, which usually induces an increased product background signal, due to continuous product formation. An example for this measurement mode is given in figure 2.7 (b) showing the CO oxidation on a Pt(111) single crystal.

If the pumping of the system is fast enough, additional information is available in a third measurement mode, by extracting the decay times of each product pulse, which is a convolution of pumping speed and product formation. Such a difference in decay times is typically observed around the onset temperature of the reaction, where the reaction kinetics and the reactant diffusion are still slow. At higher temperatures, the reaction becomes much faster and the pumping speed dominates. An example for different pulse decay times is given in figure 2.7 (c).

Pulsed experiments are specifically suited to investigate low density surface catalysts, where only very small quantities react and thus only tiny product signals are expected. Reactant pulses result in sharp product pulses, that can easily be distinguished from background noise, which might be more problematic for slow TPR-like measurements, where only slight increases of the background signal are expected. Furthermore, when comparing them to alternative experiments via background dosing, pulsed measurements only expose the chamber for a small amount of time to the reactant gases. This minimizes the additional product formation at hot filaments, resulting in a low signal background. This turned out to be especially crucial when performing highly sensitive, low background experiments using isotopically labelled gases, where pulsed dosing allowed for keeping the background signal of isotopes not naturally occuring in significant quantities low during the entire measurement.

Measurement parameters and procedure

For all the QMS based measurements performed during the course of this thesis, and independent of the investigated temperature range, the manipulator had to be fully cooled with liquid nitrogen, to a temperature which was typically < 100 K. This improves the vacuum and reduces the background signal in the QMS, leads to adequate cooling rates necessary to perform linear heating ramps over the entire required temperature range, and keeps the manipulator thermally stabilized to avoid crashing into the sniffer cone due to thermal expansion. When cooling the manipulator however, care must be taken that it is not already in close proximity of the sniffer cone, as the manipulator slightly shrinks and especially bends towards the sniffer when cooling.

For TPD and TPR measurements, reactant adsorption was typically either performed at room temperature or at 200 K, lower adsorption temperatures were only chosen if required for molecule adsorption,

as the low temperature cooling of the sample is rather time consuming. Reactant dosing at low temperatures was either done directly using the sniffer, where a standard dose of 0.1 L per pulse was used, or by filling the chamber background. The dosage per pule was determined by calibrating the pulse signal integral with the integral of the saturation coverage of CO on Pt(111), taking into account that only a fraction of the pulse actually reaches the sample. Note that for the first method, the sample has to be already in measurement position close to the sniffer, while for the second method the sample has to be significantly retracted (a few mm) to achieve the desired dosage. In measurement position the effective dosage from the surrounding chamber background is reduced. As a heating rate for all possible measurement types, 1 K/s turned out to be well-suited and was generally used.

The used QMS settings depend on the desired measurement. Generally, for all experiments, the Y_2O_3/Ir filament was operated at an emission current of 1 mA and all the electrostatic lens settings were optimized for maximum intensities, which always slightly reduces the peak quality, meaning the QMS peak of a singe mass in a mass scan is split in several maxima. This effect is very small and can be neglected, when performing calibration and experiment with exactly the same mass settings, and lens calibrations. Table 2.1 gives an overview over the different general measurement settings, set in the Quader control program, which are discussed below.

Table 2.1: QMS settings typically used for TPD/TPR and pulsed measurements.

	Masses	Pre-amplifier range	Dwell time	Pause	Resolution
TPD/TPR	1 - 4	10^{-7} - 10^{-12}	50 - 500 ms	1.0	50
Pulsed measurements	1	$\geq 10^{-10}$	$\leq$ 20 ms	1.0	50

The desired masses were selected for each measurement type, for detailed pulsed measurements typically only a single mass was selected to improve time resolution: The standard setting of a pause time parameter of 1.0 between consecutive masses yields an effective pause of 8 ms, except for the 10^{-11} and 10^{-12} amplifier range, where a pause of 215 ms results. To increase time resolution, the pause between the measured masses should be as small as possible, however when going below a value of 1.0 a signal contribution from the previous mass is detected in the trace of the following mass. Therefore, the pause time can only be decreased when measuring a single mass, which might slightly broaden a signal if sharp changes (e.g. pulses) occur. The amplifier range has to be selected according to the expected signal intensity, the 10^{-11} and 10^{-12} ranges however are limited the by considerably long pause times, and thus unsuited for fast pulsed reactivity measurements. The set dwell time should be sufficiently high to minimize noise, but have to meet the desired time resolution. For TPD and TPR measurements, typical values between 50 ms and 500 ms were used, while pulsed experiments were faster, with settings of 20 ms or less. Finally, the resolution parameter should stay at the standard setting of 50 for all measurement types. At higher values, neighbouring masses cannot be separated anymore, and at lower settings a significant amount of signal is lost. The applied channeltron voltage was set to get a signal amplification of a factor of 1000. The amplification factor is determined by introducing a defined quantity of gas (usually Ar, 1x10^{-7} mbar) and comparing the corresponding QMS signal intensity from the Faraday cup detector with that using the channeltron detector. The

amplification is the same for each measurement mode and should be checked regularly to compensate the ageing of the channeltron.

When measuring the sample temperature directly with the Sniffer QMS, the temperature is just added to the measurement channels, resulting in a decreased time resolution, as no masses are measured while the temperature is recorded. Thus, typically the QMS only measures the mass signals, while an external, LabVIEW based measurement program reads out up to four mass channels of the QMS and simultaneously records the sample temperature.

2.3.3 Pulsed reactivity data evaluation program

Depending on the set measurement parameters, a pulsed experiment may contain several hundreds of pulses, which require a suitable evaluation program. A Matlab code was developed during the course of this thesis, based on a simpler algorithm already included in my Master's thesis.[215] It features a graphical and intuitive user interface (GUI), offering several pulse evaluation alternatives. All measurements during this thesis were evaluated using this program, whereby individual evaluation parameters had to be found for each single data set. Thus, rather than giving all different evaluation parameter sets, this chapter intends to be a short, but detailed manual for pulse evaluation using said program. Each process step will be illustrated using an example measurement of CO_2 formation, observed when pulsing CO and O_2 alternately on a sample of Pt_{19} clusters supported on $Fe_3O_4(001)$, while ramping up the temperature.

First, the measurement file of interest has to be imported. The software either uses the native files generated by the QMS software (quadera) or the .lvm files generated by the LabVIEW based readout program mainly used for this particular sniffer. The time, temperature (if measured), and data column as well as the unit of the temperature (K or °C) have to be specified. In a next step, the data of interest can be cut out from the more extensive measurement files, allowing e.g. to remove the start and end parts of the data, where no pulses were recorded. One can specify, whether the cut data should keep the original time values, or be shifted to start at 0. It is also possible to subtract a constant offset, either manually or automatically (mean of the ten lowest values). Usually however, this preceeding offset subtraction is not necessary, as it can be performed successively in a more precise way. Figure 2.8 (a) shows the example data after this initial step.

In the second section, the parameters for pulse identification and integration have to be specified. The pulses are detected using the integrated Matlab peak identification function, where local maxima are found. It is absolutely crucial that every single peak (and thus pulse) is detected in this step, as only here the total number of pulses in the file is determined. Furthermore, one has to make sure, that no additional noise features are added to the peaks, which would almost certainly result in an error during further evaluation. This can be achieved by adjusting the parameters of the peak finding algorithm accordingly: A minimal peak distance (in data points), height, "prominence", and a minimal peak threshold can be defined. As the pulses typically dominate the measurement, usually the peak distance parameter is sufficient for detection; the set values depend on the time resolution of
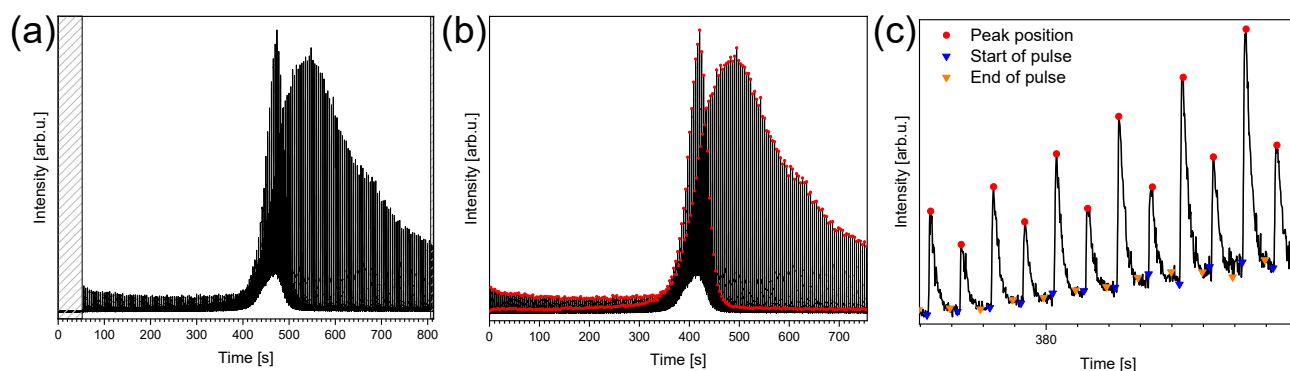
Figure 2.8: Pulsed data evaluation for CO_2 trace observed when alternately pulsing CO and O_2 on $Pt_{19}/Fe_3O_4(001)$ while ramping up the temperature. (a) Raw CO_2 data. The data of interest is selected by cutting out the marked areas. (b) Data set after pulse peak detection. It is absolutely crucial that every single peak is detected in this step, as this step determines the total number of pulses in the file. The peak positions are marked with red dots. (c) Zoomed-in region illustrating the definition of the pulse length. The start position is given by blue, the end position by orange triangles. Both have to be specified individually for each system and reactant gas, and are calculated with respect to the pulse maximum. Here, the set pulse length was 1.45 s, with the peak maximum after 0.25 s.

the analyzed data set and the pulse frequency. For very noisy data it can be beneficial to smooth the data prior to peak detection, even if this method introduces some error in the correct peak position. This smoothing is, however, only applied during pulse detection, further evaluation is again carried out based on the original data. Furthermore it is possible to define every other peak with respect to the first one, by setting an adequate delay. This method might not exactly return the exact peak positions and is therefore only suitable if the normal pulse detection fails. It is commonly used when pulsing two gases alternately, with one gas giving a much clearer product pulse than the other. The example data set after pulse detection is shown in figure 2.8 (b), where a minimal peak distance of 80 data points is sufficient to detect all peaks. There are no further possibilites to manually add, alter or remove pulse positions, thus this step has to be performed carefully.

In the next step, the actual pulse evaluation is performed. First, the pulse length has to be specified by setting start and end times with respect to the pulse maximum. When pulsing two gases alternately, it can happen that every second product pulse has a different length than the first one, for example when one of the gases is rather "sticky", such as H_2O or NH_3. In this case it is possible to set individual pulse lengths for each reactant gas. The pulse length definition on the example data set is shown in figure 2.8 (c) with an overall pulse length of 1.45 s and the peak after 0.25 s. In this step it is additionally possible to remove the dynamic background signal generated by continuous, not directly pulse-related, desorption and/or reaction processes underlying the pulsed data. This is performed by cutting out the pulses from the data set and using the background in between as a basis for a smoothing spline interpolation, which typically approximates well the underlying background. The smoothing parameter can be specified, however 0.002 works for almost all cases. Although not necessary for the pulse evaluation, using this dynamic background subtraction tool is generally highly advisable, as it extracts that part of the data that is excusively pulse-related. The data set shown in figure 2.8

is a great example for the presence of a high dynamic background. Figure 2.9 (a) shows the cut raw data from above, indicating the underlying background generated by a surface reaction with a purple line. Figure 2.9 (b) shows the same data set after background subtraction: only the pulse-related CO_2 formation remains. Finally, the pulse evaluation tool numerically integrates each individual pulse from start to end using the trapezoidal integration method. Using the integrated signal for each pulse instead of the signal maximum is usually preferred for data interpretation, as the true pulse maximum is not always exactly detected due to the dwell time in the QMS being longer than the actual pulse length of typically 5 ms. Figure 2.9 (c) shows the integrated signals pulse-by-pulse.
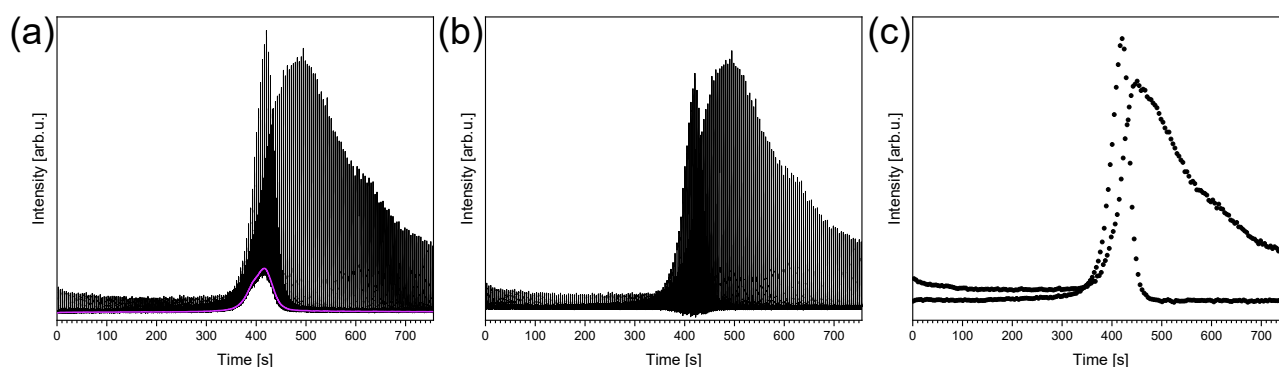
Figure 2.9: Continued evaluation on the data described in figure 2.8. (a) Data with marked underlying dynamic background (purple), which is generated by continuous CO oxidation on the clusters and is not directly related to the reactant pulses. (b) Same data set and intensity scale as in (a) after background subtraction. Only the pulse-related data remains. (c) Pulse integrals.

In a final step, the results of the evaluation process are displayed as a function of time and, if available, temperature. It is possible to separate the pulses into two sets (odd and even), intended for measurements where reactants are pulsed alternately. Furthermore, the final results, as well as those of each intermediate evaluation step, can be selected and exported as a .txt file into a folder of choice. When exporting multiple measurements into the same folder, files must be renamed, as the software would overwrite them otherwise. In most cases, the integrated pulse signals, as well as the underlying background as a function of temperature are the desired information, because they can be compared with complementary TPD measurements. Figure 2.10 shows these results for the example data set.

After this basic evaluation, which is performed for every measurement, the software gives further analysis options for specific problems: (i) In an additional step, the underlying dynamic background can be integrated, which might be useful for full quantification of the product formation for turn-over frequency determination. Again, there is an option to select the data of interest (e.g. a single desorption or reaction feature) and subtract either a constant offset (same as above) or an offset with a linear slope, whereby start and end vales are defined automatically (first and last value of the data set) or can be given manually. The data is then integrated numerically, using the trapezoidal method. This method gives the overall, cumulative integral, as well as the part of the integral corresponding to each
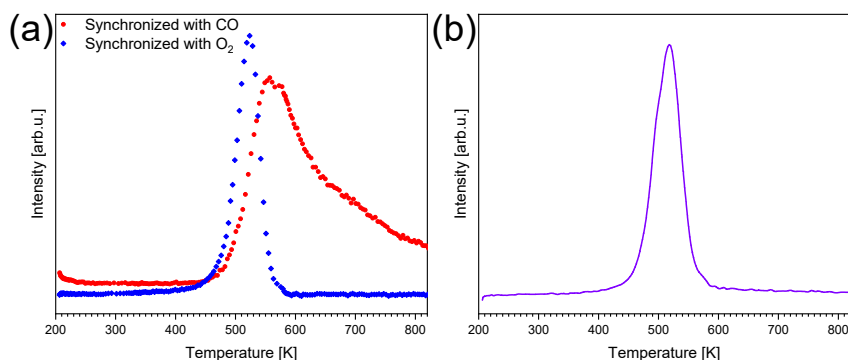
Figure 2.10: Evaluation results of the data described in figure 2.8. (a) Integrated pulses as a function of temperature, separated according to corresponding reactant gas. (b) Dynamic background as a function of temperature.

pulse, whereby the limits of integration are defined from the start position of the pulse to the start position of the next one. The integral values are given as a function of time and temperature and can be exported as a .txt file into a destination of choice. Figure 2.11 (a) shows the dynamic background of the example data set, with the main feature selected for integration and automatic linear background; the results of the integration are depicted in (b).
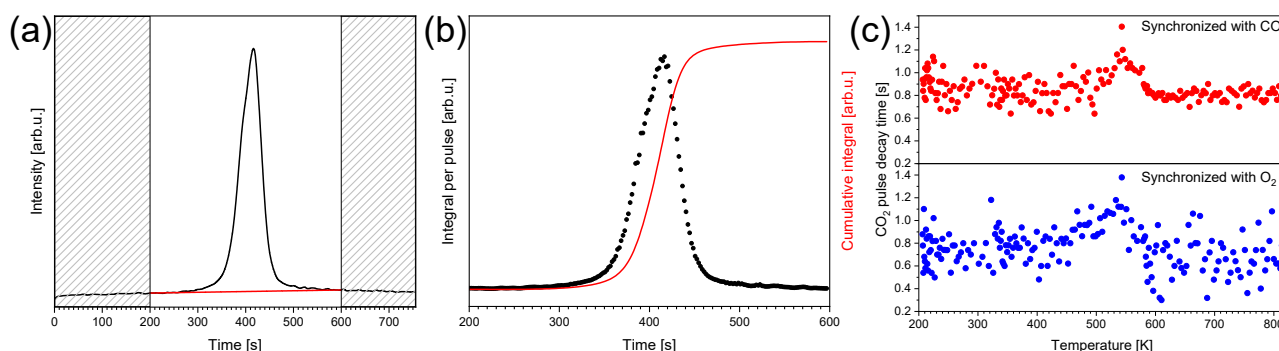
Figure 2.11: Additional evaluation methods performed on the data set described in figure 2.8 and following. (a) Dynamic background selection prior to integration. The red line indicates the automatically generated linear offset, that is subtracted. (b) Background integration results: Cumulative integral (red curve) and integral corresponding to each reactant pulse (black dots). (c) Pulse decay times (time until signal < 5% of corresponding peak maximum) for CO_2 pulses synchronized with CO (top) and O_2 (bottom).

(ii) A further data evaluation option is the analysis of the pulse signal decay times, which can give insights into the reaction kinetics (as described in section 2.3.2). First the pulse height is determined with respect to the average background between the pulse of interest and the previous one. As fitting of the sometimes extremely noisy cluster data is almost impossible, the decay times are determined as the time between the peak of each pulse and when the intensity drops either below an absolute threshold or one relative to the peak maximum with respect to the mean data between the end of the investigated peak and the start of the next one. Which method is used can be chosen by the user, however the second one gives the scientifically more relevant data, especially when the measured

pulse height varies a lot during the measurement. Pulses with decay lengths longer than the pulse length set above are automatically excluded from the evaluation. Additionally it is possible to apply a running average smooth, and/or interpolate the data prior to decay time analysis. If both options are selected, the data is first smoothed and then interpolated. Although smoothing broadens the pulse, it might be necessary for treating noisy data. Interpolation can be useful to determine half width half maxima (HWHM) when the overall pulse decay is fast and there are not enough data points in the top half of the pulse. Both, the smoothing window as well as the interpolation point multiplication factor can be chosen by the user. As some pulses tend to be on the same intensity levels as the background noise, leading to a wide dispersion of decay times, it is possible to exclude pulses below an intensity threshold. This can be set by either a constant value and/or by a fraction of the average peak height. The results are plotted as a function of time and, if available, temperature. Finally, it is again possible to separate the results according to the corresponding reactant, when two gases were used alternately. The results can be exported as .txt file into the folder of choice. This final evaluation is shown in figure 2.11 (c) for the example CO oxidation data set also used in the three previous figures, whereby the decay time was defined as signal < 5% of the corresponding peak height.

Overall, the sniffer setup is now thoroughly characterized, and measurement protocols and data evaluation routines have been established. A publication illustrating all these developments at the fundamental example of CO oxidation on Pt(111) is currently in preparation. The sniffer is now fully operational and will be used to investigate a variety of different systems in the near future, starting with a comparison of the catalytic CO oxidation activities of UHV-based cluster and single crystal model systems, with samples of more applied, nanoparticle-based powder catalysts.

2.4 X-ray Photoelectron Spectroscopy

Fundamental principle

X-ray photoelectron spectroscopy is a surface sensitive, non-destructive technique, that employs the photoelectric effect for qualitative and quantitative investigation of the elemental composition, chemical oxidation state and sometimes phase dispersion of any given conductive sample.[226] The basic measurement principle is rather simple: A surface is irradiated with X-rays of a specific energy, leading to the emission of core, valence and secondary electrons which are detected based on their kinetic energy, whereby XPS mainly focuses on the core electrons. This fundamental process is described in equation 2.3.[227]

$$h\nu = E_{\text{kin}} + E_{\text{b}} + \Phi_{\text{A}} \tag{2.3}$$

Here, $h\nu$ is the energy of the incident X-rays, E_{kin} is the kinetic energy of the emitted photoelectrons, E_{b} is the original binding energy of the electron, and Φ_{A} is the work function of the electron analyzer. Since Φ_{A} and $h\nu$ are typically known and constant and E_{kin} is measured, E_{b} can be determined due to

energy conservation. This is shown in figure 2.12 (a), which illustrates the photoelectric process in an energy diagram.
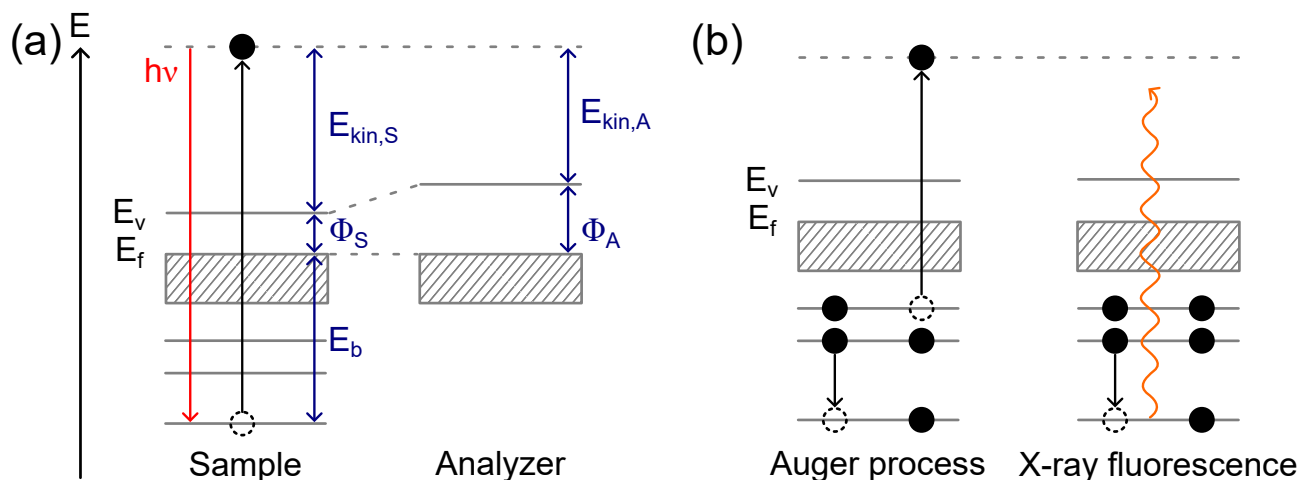

Figure 2.12: (a) Energy diagram of the photoelectric process where a core electron with binding energy E_b interacts with an incident photon with energy $h\nu$ and is removed from its shell. After overcoming the sample work function Φ_S, the resulting photoelectron has a kinetic energy of $E_{kin,S}$, which is measured by the analyzer reduced by the difference of Φ_A and Φ_S. (b) Both decay pathways for photo-holes. Left: Auger electron emission, right: X-ray fluorescence. Note that the positions of the energy levels in (a) and (b) are purely schematic and do not resemble any real system.

Reflecting the energy of the initial electron shell level, the binding energy of emitted core electrons is element specific, and each XPS peak can thus be assigned to a certain chemical element. Additionally, the chemical surroundings, oxidation state and charge can influence the energetic position of the electron shell levels, and thus the electron binding energies, leading to small shifts of the corresponding XPS peaks. Therefore, with the exception of hydrogen and helium, all elements can be identified and characterized with regard to their oxidation state.[228] The emitted photoelectrons typically have an energy of 40-2500 eV,[227] and therefore an inelastic mean free path of only a few nm in solids.[229] Thus XPS is highly surface sensitive, as it is only probing the uppermost atomic layers of the sample. The photoelectron emission is usually followed by the decay of the formed core shell electron vacancy,[230,231] depicted in figure 2.12 (b). An electron from an outer shell fills the vacancy, releasing the energy difference between the two shells. There are two different pathways for consecutive energy dissipation: X-ray fluorescence and Auger electron emission. In the former case, the excess energy is released in form of an element specific X-ray photon, whereas in the latter the energy is transferred to another electron which is then emitted and can be detected. Thus, XP spectra typically not only contain photoelectron peaks, but also Auger peaks. They can be easily differentiated due to the fact that the kinetic energy of photoelectrons depends on the incident X-ray wavelength, whilst the kinetic energy of Auger electrons does not. As XP spectra are normally referenced to the X-ray energy, a change in the excitation energy leads to a shift of the Auger peaks, while the photoelectron peaks stay at the same energy.[232] Similar to photoelectrons, Auger electrons deliver chemical information with

high surface sensitivity.

From equation 2.3 it becomes clear that monochromatic X-rays are required to obtain well resolved XP spectra. Simple lab sources use the characteristic X-rays of certain elements with sufficiently small line width. Most commonly either Al-$K_{\alpha1,2}$ (1486.6 eV) or Mg-$K_{\alpha1,2}$ (1253.6 eV) are used.[231] Apart from the main X-ray lines, other, weaker characteristic X-ray lines of different energy are emitted by these sources, which give rise to satellite peaks in the XP spectra, the positions of those can be found in ref..[232] To avoid these and further improve resolution, an X-ray monochromator can be used for selecting only the desired photon energy, coming at the expense of signal intensity. When even better resolution, or a higher flexibility in the photon energy is required, synchrotron radiation sources are the method of choice, which come with extremely high photon flux and an (almost) freely adjustable wide energy range.

Film thickness determination in XPS

XPS is a method well suited for determining the thickness of thin films covering a surface, and by using synchrotron-based XPS even the encapsulating layer thickness on top of clusters can be estimated. This works by measuring the XPS signal attenuation of the underlying material, due to inelastic electron scattering, as a function of the thin film thickness, assuming a homogeneous and stoichiometric film. Although this assumption may be over-simplified in the case of sub-nanometer clusters, it can still give a good indication whether clusters are actually covered by an oxide film, buried in the surface or whether their geometry changes. The signal attenuation as a consequence of inelastic scattering of a material A covered by a homogeneous film B is given in equation 2.4.[227]

$$\frac{I_A}{I_{A,0}} = exp\left(-\frac{d}{\lambda \cdot cos\theta}\right) \tag{2.4}$$

Here, I_A is the signal intensity of A with B on top, $I_{A,0}$ is the signal of the bare material A under the same measurement conditions, d is the film thickness of B, λ is the electron inelastic mean free path (IMFP) of the photoelectrons originating from A in material B, and θ is the electron detection angle with respect to the surface normal. In this thesis, all film thickness measurements were performed under normal emission conditions, elastic scattering was neglected, the IMFP was calculated using the TPP-2M equation (Tanuma, Powell and Penn algorithm), an empirical predictive formula used to estimate IMFPs in solids.[233]

Standard measurement settings

The X-ray source installed in the apparatus used in this thesis is equipped with a Mg/Al dual anode. Both are operated at 15 kV with a power of 400 W for Al and 300 W for Mg. Due to its higher power and thus photon flux, mainly the Al anode was used in this thesis. XPS measurements are either performed under normal or grazing emission conditions. For the latter one, the sample is rotated by 60° with respect to the analyzer. When measuring in grazing emission geometry, the detected electrons had to travel further within the bulk, compared to electrons from the same depth that are

exiting the sample in parallel to its surface normal, thus cutting the effective sampling depth in half. This increases the surface sensitivity. It however comes at the cost that with the current experimental setup it is almost impossible to eliminate all background signal contribution from the surrounding sample holder assembly, as the probed area increases beyond the (relatively small) sample area. The XP spectra are typically measured with the hemispherical analyzer in constant analyzer energy mode. There are three parameters for setting the desired analyzer resolution: The pass energy as well as entrance and exit slits. Their influence on the intensity and resolution was investigated in a systematic measurement of the Pt 4f level of a freshly prepared Pt(111) single crystal, shown in figure 2.13.

Entrance slit	Size	Exit slit	Size
1	6 mm x 12 mm	1	1 mm x 10 mm
2	6 mm diameter	2	3 mm x 10 mm
3	2 mm diameter	3	5 mm x 10 mm
4	1 mm diameter		
5	1 mm x 12 mm		
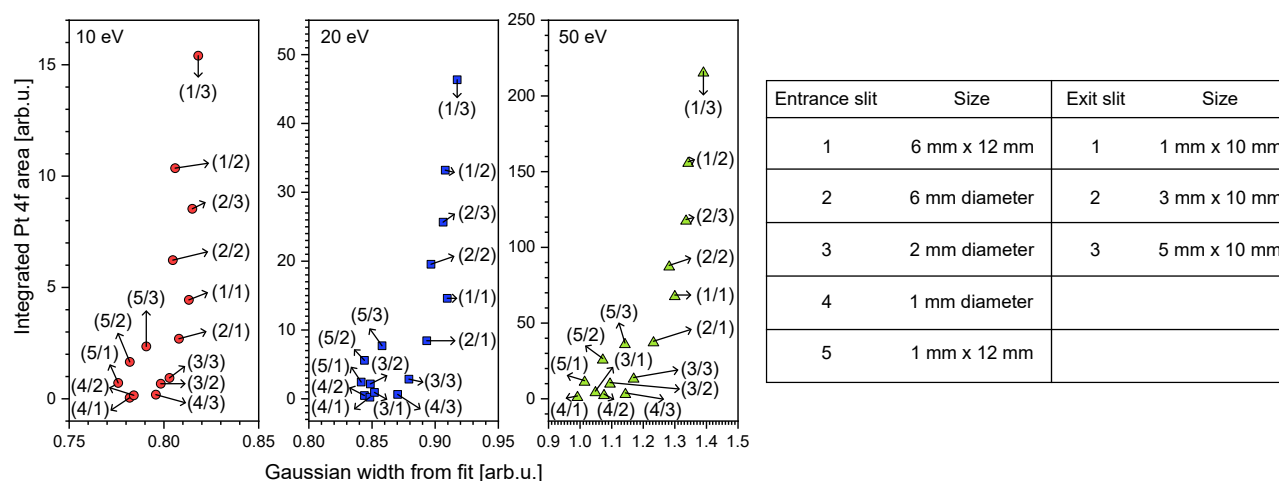
Figure 2.13: XPS peak area of a Pt 4f peak, measured on a Pt(111) single crystal, as a function of the peak resolution for different pass energies and different entrance and exit slit combinations given in parentheses. All spectra were fitted with a Doniach-Sunjic doublet function convoluted with a Gaussian function, and a linear background. Thereby, the Lorentzian width, the peak splitting, the peak ratio and the asymmetry factor have been fixed to the same values. Thus, the Gaussian width can be used to describe the analyzer resolution. All points are assigned to their corresponding entrance and exit slit values, respectively. The table on the right gives the sizes of the slits, as described in the analyzer manual.

When optimizing intensity, as well as resolution, it becomes clear, that the ideal measurement settings use the largest entrance and exit slits, while the resolution is determined by the specific pass energy. Based on these results, several standard measurement sets were defined, as shown in table 2.2.

Table 2.2: Standard measurement sets for overview and high resolutions spectra, assuming the largest entrance and exit slits being used.

	Pass energy	Step size	Dwell time	Number of sweeps
Overview scan	50 eV	0.5 eV	0.2 s	1
High resolution	20 eV	0.05 eV	0.5 s	1 - 10
Ultra high resolution	10 eV	0.05 eV	0.5 s	typically > 10

If the XPS setup is used for quantitative measurements, the non-linearity of the detection system has

to be taken into account. The used hemispherical analyzer is equipped with seven channeltron detectors, each with a dead time of 70 ns per count, yielding an overall deadtime of 10 ns for the entire detection system. This means that already at 1 Mcps about 10% of the signal is lost. In quantitative measurements, these losses can lead to an error and should be as small as reasonably possible. If for example an error below 3% is desired, the maximum count rate must not exceed 400000 cps. Therefore, it might sometimes be necessary to reduce the count rate. This can easily be done by changing the pass energy, as well as entrance and exit slits, as shown in figure 2.13.

So far, this section only describes the lab XPS setup, but the same procedures can essentially be applied to synchrotron XPS measurements. However, here depth sensitivity is typically changed by varying the photon energy, and thus the IMFP, rather than the sample-analyser geometry. The equilibrium of desired resolution, signal intensity and measurement time has to still be defined by setting pass energies, and entrance and exit slit sizes. Due to the high photon flux and brilliance, a much higher resolution is possible at similar measurement times, when compared to the lab XPS setup. When it comes to quantitative measurements, detector saturation can even be more of an issue than in the lab setup, since the high photon flux results in a much higher number of photo- and secondary electrons. Typically, saturation is avoided by adjusting the photon flux accordingly.

Data evaluation

XPS data treatment was performed using KolXPD.[234] All synchrotron based spectra were initially normalized to the corresponding photon flux and the number of individual scans included in one measurement. Spectra used for direct quantitative comparison were furthermore normalized to the low binding energy side. Spectra originating from the lab XPS system were typically highly reproducible, normalization was only rarely necessary. If XP-spectra were fitted, generally a Voigt function in combination with a Shirley background was used for non metallic components, metals were fitted using a Doniach-Sunjic function convoluted with a Gaussian and a linear background. Clusters are somehow in between, thus arguments for both fitting procedures can be found. However, usually the metal fitting procedure resulted in a better agreement of the fit for the clusters investigated in this thesis.

2.5 Sample Preparation

Atomically resolving microscopy experiments on size-selected clusters require particularly reproducible and reliable sample preparation protocols in order to exclude the presence even of single atoms of the cluster material from preceeding experiments. It is thus crucial to develop a cleaning procedure for each material which guarantees a highly reproducible surface morphology and stoichiometry, while reliably removing contaminants as well as clusters from previous experiments. In this section, the preparation procedures of all substrates, used for either testing, calibration or scientific measurements in this thesis, are described. All sputtering currents correspond to a sample size of 4.4 mm diameter in normal sputtering geometry. The success of these methods was checked regu-

larly by STM (cleanliness, surface structure, very low coverage impurities) and XPS (stoichiometry, impurities).

$Fe_3O_4(001)$

In this thesis, natural as well as synthetic magnetite $Fe_3O_4(001)$ crystals (SurfaceNet) have been used, which both were cleaned following the same procedure: Surface contaminants were removed by Ar^+ ion sputtering ($4x10^{-5}$ mbar, 1.0 keV, 20 min, 6 µA) at room temperature. To regain a flat and stoichiometric surface, the samples were subsequently annealed to 983 K for 20 min in an atmosphere of $5x10^{-7}$ mbar oxygen. At this temperature, the surface becomes mobile, while new layers of pristine magnetite grow on top of the crystal by reaction of interstitial iron atoms with oxygen. To avoid the persistence of small Fe_3O_4 islands, the oxygen was removed from the chamber before cooling down. Typically, several of these preparation cycles were necessary to obtain a clean surface. When introducing a new crystal to the system, about 20 cylces were sufficient to remove impurities, like Ca, K and C, diffusing out of the bulk. Clusters up to Pt_{20} could be reliably removed using 10 preparation cycles, larger, sintered nanoparticles typically required 15-20 cycles. Following this cleaning procedure it was possible to obtain clean surfaces, with the only remaining measurable impurity being Ar, which is intercalated into the subsurface region during sputtering. The Ar amount could be reduced by softer sputtering parameters during the last cycle ($5x10^{-6}$ mbar, 1.0 keV, 5 min).

r-$TiO_2(110)$

New rutile $TiO_2(110)$ single crystals (SurfaceNet) were initially reduced by seven cycles of Ar^+ ion sputtering at room temperature ($4x10^{-5}$ mbar, 1.0 keV, 20 min, 6 µA), followed by 20 min of UHV annealing at 800 K. During this procedure, the crystals' color changed from colorless or pale yellow to a light blue and the crystals became conductive. For further cleaning, the same sputtering parameters were applied. However, once the desired oxidation state was achieved, the annealing was still carried out for 20 min, but in $1x10^{-6}$ mbar of O_2, which was sufficient to maintain the oxidation state. Light blue crystals with a very rough surface were obtained by annealing to 800 K, while flat, dark blue/black crystals with a higher degree of reduction were obtained when annealing to 1000 K. In general, the last step of the last cleaning cycle prior to measurement was always annealing in UHV for 10 min. New crystals arrived heavily contaminated with K, and slight traces of Si, C, and Ca. To remove all of these contaminations a total of about 30 cleaning cycles was necessary. Note that when increasing the annealing temperature, further contaminants diffused to the surface, making several further cleaning cycles necessary for their removal. On $TiO_2(110)$, Pt_{10} clusters could be successfully removed by seven cleaning cycles, while sintered and strongly encapsulated Pt nanoparticles required more than 20 cycles. Similar to the $Fe_3O_4(001)$ surface, sub-surface Ar intercalation was detected by XPS and STM, and could not be removed.

Au(111)

The Au(111) single crystal (SPL) used in this thesis was cleaned by Ar^+ ion sputtering at room tem-

perature with an Ar pressure of 4×10^{-5} mbar and an ion energy of 800 eV, respectively 1.5-2.0 keV for highly carbon contaminated surfaces, for a duration of 5-20 min. Consecutive annealing to between 800 and 900 K for 10 min results in a flat and clean surface. New crystals can be used rather quickly, the crystal used in this thesis was clean after three preparation cycles. Since the clusters and carbon nitride films grown on this support were single layer high and not encapsulated, a maximum of five cleaning cycles were sufficient for their removal, usually less.

Pt(111)

The Pt(111) single crystal (SPL) was cleaned by repeated cycles of Ar^+ ion sputtering at room temperature (4×10^{-5} mbar, 1.0 keV, 5 min, 6 µA), followed by annealing at 1220 K for 5 min. This procedure results in a flat and mostly clean surface. However, the crystal used in this thesis was bulk-contaminated with C that diffuses from the bulk to the surface upon annealing. Therefore, an additional oxidation preparation step consisting of annealing in O_2 (5×10^{-7} mbar, 720 K, 5 min), followed by UHV annealing (1000 K, 3 min) to remove residual oxygen, was added to the procedure. This leads to a reproducibly clean surface.

Rh(111)

The Rh(111) single crystal (SPL) was cleaned by Ar^+ ion sputtering at room temperature (4×10^{-5} mbar, 1.5 keV, 10 min), followed by annealing. As this crystal is heavily carbon contaminated from previous graphene growth experiments, the first segment of the annealing process aims at diminishing the carbon concentration close to the surface. This is done by three consecutive annealing ramps, each going up to 1250 K, then back to 770 K with a ramp of $\pm$ 2 K/s in 1×10^{-7} mbar O_2. This procedure leads to the diffusion of carbon to the surface at lower temperatures, which then gets oxidized at higher temperatures. Finally, the crystal was annealed in UHV at 1250 K for 10 min, whereby the surface flattens and residual oxygen desorbs, yielding a reproducibly clean and flat surface.

HOPG

The highly oriented pyrolytic graphite (HOPG) crystals (TipsNano) used in this work, were prepared outside of the UHV chamber, directly before transferring the samples into the vacuum, by exfoliation of the uppermost layers using the 'Scotch Tape' method, followed by flattening of residual flakes by gently pressing onto the surface with a Kimwipe. After annealing the crystals in vacuum for about 5 min at 800-900 K to desorb adsorbates, they were clean and ready for use.

3 Results: Publication Summaries

This chapter provides summaries for the articles published in peer-reviewed journals over the course of this thesis, focusing on the cluster-support interactions of the investigated $Pt_n/Fe_3O_4(001)$ model catalytic system, and their relevance for catalytic reactions.

3.1 Cluster Catalysis with Lattice Oxygen: Tracing Oxygen Transport from a Magnetite (001) Support onto Small Pt Clusters

Contributions

Sebastian Kaiser	Planing and conduction of experiments, data analysis and visualization, writing
Farahnaz Maleki	DFT calculations
Ke Zhang	Participation in experiments, discussions
Wolfgang Harbich	Discussions
Ueli Heiz	Funding acquisition, discussions
Sergio Tosoni	DFT calculations, discussions
Barbara A. J. Lechner	Supervision, funding acquisition, discussions
Gianfranco Pacchioni	DFT calculations, discussions
Friedrich Esch	Supervision, funding acquisition, discussions

Size-selected Pt clusters are well known for their excellent CO oxidation activities.[11, 12, 50] On non-reducible supports, this reaction typically follows a Langmuir-Hinshelwood reaction mechanism, whereby the clusters adsorb CO, adsorb and dissociate O_2 and subsequently catalyze the CO_2 formation. On reducible oxides however, lattice oxygen can get involved in the reaction as well, leading to a Mars-van Krevelen mechanism. Here, CO adsorbs on the clusters and gets oxidized by an oxygen atom from the surrounding support, resulting in oxygen vacancies that are subsequently filled by re-

duction of O_2. Thus, the MvK mechanism allows to separate the CO oxidation and O_2 reduction step of this redox process. As shown in the introduction, the presence of metal clusters can activate lattice oxygen atoms, especially those at the cluster perimeter, but also those, nearby on the terrace, which are not in direct contact to the cluster.[71,93] Depending on the specific support, these activated lattice oxygen atoms may migrate on top of the cluster, in a lattice oxygen reverse spillover mechanism, as observed on CeO_2.[104,108] A full understanding of the underlying pathway of a MvK-catalyzed CO oxidation with clusters, requires thus to reveal the nature of the involved lattice oxygen species. To investigate whether the reaction takes place at the perimeter or on top of the cluster can be rather challenging in a mixed $CO+O_2$ reaction environment, as the oxygen can still adsorb dissociatively on the Pt clusters, and switching between the reduction and oxidation step can also be problematic, as these single crystal model systems tend to heavily restructure in an O_2 atmosphere at elevated temperatures, due to the growth of new surface layers.[13,235] Magnetite (001), our support of choice, offers the unique possibility to completely separate the CO oxidation step from the surface re-oxidation step, and thus to elucidate the role of the lattice oxygen atoms. This is due to the fact that $Fe_3O_4(001)$ maintains its original surface stoichiometry even under reducing conditions, since reduced, undercoordinated Fe cations tend to diffuse into the bulk, making available surface lattice oxygen throughout the entire reaction.[121]

This paper investigates the precise CO oxidation mechanism on Pt_5 and Pt_{19} clusters deposited on $Fe_3O_4(001)$. The reaction occurs via a MvK mechanism, leading to the formation of extended holes around the clusters, as a consequence of surface lattice oxygen removal and consecutive diffusion of the reduced Fe cations into the bulk.[13] STM measurements demonstrated that both cluster sizes stay randomly distributed and monodisperse, i.e. they maintain their size-selection, over the entire investigated temperature range. This was confirmed by CO TPD measurements, in which a clear size effect was observed: The desorption maximum from Pt_{19} appeared at 475 K, the one for Pt_5 was shifted to 550 K. Concomitant CO_2 evolution indicates a MvK oxidation mechanism with lattice oxygen, as no oxygen was dosed and measurements with isotopically pure CO exclude a Boudouard reaction. Pulsed reactivity measurements revealed that the lattice oxygen actually migrates on top of the Pt clusters, resulting in a highly reactive oxygen species. Pulsing CO during a temperature ramp while monitoring the resulting CO_2 product pulses allowed us to explore the reaction beyond the normal CO desorption temperature. The hereby observed pulsed CO_2 formation saturates at the temperature where the CO desorption from the clusters just ends, i.e. at the temperature where the maximum of adsorption sites on the clusters are available. Such a dependence on the availability of adsorption sites points straight forward to a reaction on the clusters (i.e. lattice oxygen reverse spillover), in contrast to a reaction at the cluster perimeter. Furthermore, quantifying the product pulses for both cluster sizes reveals that the CO_2 formation scales with the number of cluster surface atoms rather than perimeter atoms, proving the proposed lattice oxygen reverse spillover mechanism. This dependence on available adsorption sites was also shown in complementary pulsed oxygen experiments, in which O_2 was pulsed on CO pre-saturated clusters during a temperature ramp, while again monitoring the CO_2

product pulses: As soon as the poisoning CO starts to desorb, oxygen can adsorb dissociatively on the Pt clusters, where it immediately reacts with the remaining adsorbed CO in a classic Langmuir-Hinshelwood reaction. The CO_2 formation observed in this experiment closely resembles the course of the CO_2 formation observed in the initial CO TPD. This shows that the limiting factor for the lattice oxygen reverse spillover situation is indeed the availability of adsorption sites on the cluster, as this pulsed oxygen experiment essentially mimics an adsorption limited lattice oxygen reverse spillover situation. Furthermore, it was possible to accumulate small quantities of highly reactive spillover lattice oxygen on top of the clusters, forming CO_2 with co-adsorbed CO already at low temperature, i.e. just above room temperature. Subsequent CO TPD runs resulted in a loss of CO adsorption capacity upon annealing, due to SMSI-related cluster encapsulation.

DFT calculations on Pt_5 clusters on $Fe_3O_4(001)$, performed by our collaborators from the group of Gianfranco Pacchioni, revealed further details about the system and the lattice oxygen reverse spillover mechanism. The most stable Pt_5 adsorption geometry is a capped rhombus, 1.5 eV more favourable than the second best, pyramidal structure, limiting structural fluxionality. Upon adsorption, the clusters become positively charged and the magnetic moment of magnetite is partially quenched. As expected for a metal-assisted MvK mechanism, the oxygen vacancy formation energy at the cluster perimeter is reduced by up to 0.9 eV compared to the bare surface; for nearby oxygen atoms that are not in direct contact with clusters, the formation energy is still reduced by 0.5 eV. The calculations showed that the lattice oxygen reverse spillover is actually exothermic for one (-0.40 eV) and two (-0.64 eV), and only slightly endothermic for three spillover (0.17 eV) oxygen atoms, with an activation energy barrier of only 0.9 eV for the first oxygen atom, assuming the oxygen atom displacement from the crystal lattice to be the rate determining step. Thus, the spillover of multiple O atoms on the clusters is energetically accessible under the investigated reaction conditions. The calculations further indicate a restructuring of the clusters to a quasi two-dimensional geometry, that could be observed, for all investigated cluster sizes, as a decrease in apparent height in STM, whereby additional electronic effects (e.g. due to SMSI) could not be excluded.

In summary, this publication reveals the nature of the active oxygen species in a metal-assisted MvK reaction catalyzed by size-selected Pt clusters on $Fe_3O_4(001)$: An oxygen atom in close proximity to the Pt cluster is activated, migrates on top of the cluster, and forms a highly reactive oxygen species, which reacts with a co-adsorbed CO molecule. This lattice oxygen reverse spillover mechanism is thermodynamically favoured and, at elevated temperatures, mainly limited by the availability of free adsorption sites on the clusters, due to the comparably low activation energy barrier.

Research Article

Cluster Catalysis with Lattice Oxygen: Tracing Oxygen Transport from a Magnetite (001) Support onto Small Pt Clusters

Sebastian Kaiser, Farahnaz Maleki, Ke Zhang, Wolfgang Harbich, Ueli Heiz, Sergio Tosoni, Barbara A. J. Lechner,* Gianfranco Pacchioni, and Friedrich Esch

Cite This: *ACS Catal.* 2021, 11, 9519–9529

Read Online

ACCESS | Metrics & More | Article Recommendations | Supporting Information

ABSTRACT: Oxidation catalysis on reducible oxide-supported small metal clusters often involves lattice oxygen. The present work aims at differentiating whether the reaction takes place at the cluster/support interface or on the cluster. To that purpose, we trace the path of lattice oxygen from $Fe_3O_4(001)$ onto small Pt clusters during the CO oxidation. While oxygen vacancies form on many other supports, magnetite maintains its surface stoichiometry upon reduction thanks to high cation mobility. To investigate whether size-dependent oxygen affinities play a role, we study two specific cluster sizes, Pt_5 and Pt_{19}. By separating different reaction steps in our experiment, migrating lattice oxygen can be accumulated on the clusters. Temperature-programmed desorption (TPD) and sophisticated pulsed valve experiments indicate that CO oxidation occurs with this highly reactive oxygen on the Pt clusters. Scanning tunneling microscopy (STM) shows a decrease in the apparent height of the clusters, which density functional theory (DFT) explains as a restructuring following lattice oxygen reverse spillover.

KEYWORDS: *size-selected clusters, lattice oxygen reverse spillover, Mars van Krevelen mechanism, magnetite, platinum, pulsed reactivity, STM, DFT*
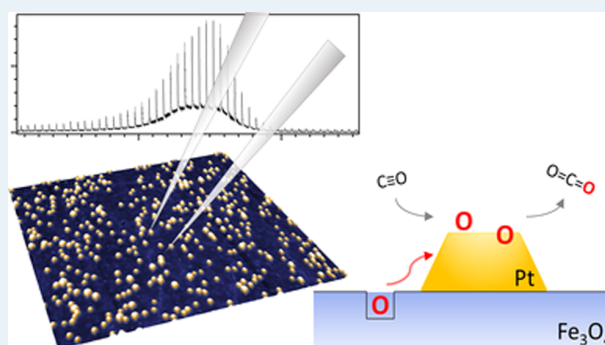
1. INTRODUCTION

From fine chemical synthesis over combustion control to electrode design, about 80% of industrial chemical processes rely on catalysts to improve energy and material efficiency,[1] of which about 90% are catalyzed heterogeneously.[2] Such a heterogeneous catalyst typically consists of small metal nanoparticles (several hundreds to thousands of atoms) or clusters (often defined as ≤100 atoms) dispersed on oxidic support materials.[3,4] In contrast to the bulk and large nanoparticles, small clusters exhibit discrete electronic states comparable to molecules, and therefore develop unique, strongly size-dependent chemical and physical properties. Small Pt clusters, for example, exhibit a nonmetallic behavior.[5] These properties can even change the catalytic behavior: Au, which is inert in the bulk state, becomes highly active and selective for redox catalysis.[6−8] In small particles, a large proportion of atoms is in direct contact with the underlying support, which can strongly influence their catalytic performance and stability. It can alter the catalytic activity of the particles indirectly,[9,10] itself being an integral part of the catalytic cycle,[11] and even encapsulate the particle in the strong metal−support interaction (SMSI),[12−14] thereby reducing[15] or enhancing[16] the catalytic activity.

In the case of CO oxidation on supported metal clusters, several reaction mechanisms have been distinguished based on the oxygen supply. When clusters are supported on non-reducible oxides, the CO oxidation typically takes place in a Langmuir−Hinshelwood mechanism, where CO and O_2 coadsorb from the gas phase and react.[17,18] On reducible oxide-supported clusters, on the other hand, the support can contribute lattice oxygen in a Mars van Krevelen (MvK) mechanism, thus not only providing a large oxygen reservoir but potentially also causing the entire catalyst system to restructure continuously.[19,20] The removal of lattice oxygen typically requires thermal activation, which can be facilitated in proximity to the clusters in a so-called metal-assisted MvK mechanism.[21] The resulting oxygen vacancies subsequently have to be refilled by gas-phase O_2 to complete the catalytic cycle. A central question remains whether the oxidation step takes place at the cluster/support interface or on the cluster.
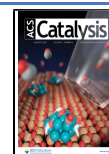
For larger nanoparticles, on supports such as ceria[22,23] and $Co_3O_4(111)$,[24] it was demonstrated that the reaction takes place on the particles via an oxygen reverse spillover, i.e., lattice oxygen transport onto the particles, which we will thus refer to as "lattice oxygen reverse spillover". In contrast to this oxygen originating from the lattice, classical reverse spillover typically involves species originating from the gas phase that first adsorb on the support and subsequently migrate to the catalytic sites.[25]

Here, we study a similar CO oxidation catalyst with two important differences. We use small monodisperse clusters at the extreme low end of the size scale (namely, Pt_5 and Pt_{19}) and deposit them on a magnetite, $Fe_3O_4(001)$, support, where we expect the oxygen exchange to be influenced by high cation mobility. While oxygen vacancies created on the above-mentioned supports need to be refilled from the gas phase, magnetite can maintain its surface stoichiometry by facile iron diffusion into the bulk,[26] thus providing a flexible oxygen reservoir. Magnetite is a magnetic, abundant, and reducible metal oxide, which crystallizes in an inverse spinel structure with Fe^{2+} occupying octahedral sites and Fe^{3+} occupying tetrahedral and octahedral sites in a 1:1 ratio, within an fcc-O^{2-} anion lattice.[27−29] Its (001) surface reconstructs into the subsurface cation vacancy (SCV) structure, whereby only Fe^{3+} occurs in the uppermost layers, yielding a $(\sqrt{2} \times \sqrt{2})R45°$ reconstruction.[30] In a scanning tunneling microscope (STM), this structure is observed in the form of parallel, undulating rows of iron atoms in octahedral sites, rotated 90° between adjacent terraces. The $Fe_3O_4(001)$ surface is rich in surface defects such as surface hydroxyls, antiphase domain boundaries (APDB) between the two reconstruction domains, or Fe-rich point defects such as unreconstructed unit cells and Fe adatoms.[31−34] These defects also act as adsorption and dissociation sites, thus participating in the surface chemistry.[35−37]

In the present work, we combine a multimodal experimental approach comprising scanning tunneling microscopy (STM), temperature-programmed desorption (TPD), and highly sensitive pulsed-reactivity experiments with state-of-the-art density functional theory (DFT) calculations to investigate a $Pt_n/Fe_3O_4(001)$ model catalyst during exposure to a CO oxidation reaction environment. We demonstrate lattice oxygen reverse spillover onto the small Pt clusters, observe a size dependence of CO poisoning, and identify an oxygen-induced restructuring of the clusters.

2. METHODS

2.1. Experimental Methods.
Naturally grown $Fe_3O_4(001)$ samples (SurfaceNet GmbH) were prepared by several preparation cycles, each consisting of 20 min Ar^+ ion sputtering at room temperature (4×10^{-5} mbar Ar, 1 keV, 3.6 μA sputter current), followed by annealing in 5×10^{-7} mbar O_2 at 983 K. This procedure yields a reproducible and clean surface, which was checked for stoichiometry as well as carbon impurities using X-ray photoelectron spectroscopy (XPS) and STM on a regular basis. For heating, a boron nitride heater located directly in the sample holder in contact with the sample was used; the temperature was measured by a type K thermocouple directly attached to the crystal.

Size-selected Pt clusters were generated by a laser ablation source.[38] Pt is evaporated from a rotating target using the second harmonic of a pulsed Nd:YAG laser; the resulting plasma is subsequently cooled in the adiabatic expansion of a He pulse (Westfalen AG, grade 6.0). This yields a supersonic beam of clusters, which is focused by several electrostatic lenses and guided toward a 90° quadrupole bender for positive charge selection. The resulting beam is mass-selected by a quadrupole mass filter and subsequently soft-landed on the substrate (i.e., with a kinetic energy <1 eV/atom). The clusters were deposited at room temperature. For TPD and reactivity measurements, a cluster density of 0.05 clusters/nm^2 was used, and for STM, a lower cluster coverage of 0.01 clusters/nm^2 allowed optimal evaluation of the terrace background around each cluster.

All experiments were carried out under ultrahigh vacuum (UHV) conditions, with a system base pressure of $<1 \times 10^{-10}$ mbar. All STM measurements were performed in constant current mode with a commercial Omicron VT-SPM instrument using electropolished Pt/Ir tips (Unisoku). STM image processing was performed with Gwyddion[39] using plane subtraction and row by row alignment tools for background correction. The height distribution of the particles was determined using a home-written Igor routine by the detection of the particles via an intensity threshold, drawing a profile through the cluster maximum and determining the height of the cluster with respect to its surrounding background.

The experimental setup was recently equipped with a device for high sensitivity TPD and reactivity measurements, the so-called sniffer, which was built adapting a design by Bonanni et al.[40] In short, this device combines a pulsed reactant doser with a differentially pumped quadrupole mass spectrometer (QMS, Pfeiffer Vacuum GmbH, QMA 200 Prisma Plus). Up to two different reactants can be pulsed independently. The reactants as well as the desorption and reaction products are guided using a heated quartz tube assembly. As the distance between the sniffer entrance and the sample is typically in the range of only ~100−200 μm, the investigated surface is sufficiently decoupled from the rest of the chamber; thus, a high amount of reactant can be dosed while keeping UHV conditions in the surrounding chamber. In the present study, each pulse corresponded to a dosage of approximately 0.1 L. This decoupling in combination with the guiding tubes results in the vast majority of the desorption and reaction products reaching the QMS, yielding a very high sensitivity, as well as the spectra being free of any additional peaks caused by desorption from, e.g., the sample holder or the manipulator. The TPD and pulsed-reactivity experiments were carried out using O_2 (Westfalen AG, grade 5.0) and $C^{18}O$ (Eurisotop, 96.1%). All reactivity and TPD-related samples have been saturated with $C^{18}O$ during cluster deposition to gain control over the CO species adsorbed on the clusters despite CO being codeposited as a molecular beam during deposition with our cluster source. The delay between the pulses during the reactivity measurements was 4 s for O_2, 2.5 s for $C^{18}O$, and 2.5 s when pulsing O_2 and $C^{18}O$ alternately. The evaluation of the pulsed-reactivity data was carried out using a Matlab-based evaluation tool that differentiates between pulse-related gas signals and background by detecting single peaks and evaluating in a pre-set time window. The thus-determined background comprises offsets, desorption signals, initial pulse valve transients, and reactivity linked to long residence times and is subtracted; afterward, each pulse is integrated numerically. For details, see Figure S1 in the Supporting Information (SI).

2.2. Computational Models and Methods.
DFT calculations have been performed to model the lattice oxygen reverse spillover process. To this end, we considered a Pt_5

cluster supported on the $Fe_3O_4(001)$ surface, Pt_5/Fe_3O_4, where a single cluster size is considered. In a real heterogeneous catalyst consisting of supported metal nanoparticles, the overall performance results from the convolution of the individual clusters activities; results obtained for a single cluster size may differ, at least quantitatively, from those of the real catalyst.[41] However, in this study, we are considering mass-selected, monodispersed Pt clusters, in particular Pt_5 and Pt_{19}, to be able to specifically compare experimental results with DFT models on exactly the same cluster size.

For the calculations, we used the code VASP 5.[42] The core electrons are described with the projector-augmented wave method.[43,44] O(2s, 2p), Fe(3s, 3p, 3d, 4s), and Pt(5d, 6s) electrons are treated explicitly. Spin-polarized calculations are carried out at the level of the generalized gradient approximation (GGA) adopting the Perdew, Burke, and Ernzerhof (PBE) exchange−correlation functional;[45] the exact values might vary slightly with the use of different functionals.[46] The strongly correlated character of Fe(3d) electrons is accounted for as in the GGA + U approach[47,48] by applying a Hubbard U parameter of 3.8 eV to the Fe 3d states.[30] The magnetic structure of Fe_3O_4 is correctly reproduced. Long-range dispersion is included according to the D3 method introduced by Grimme.[49] The relaxation of the magnetite bulk lattice parameters and internal coordinates has been performed with a $3 \times 3 \times 3$ K-point grid and a kinetic energy cutoff of 600 eV. All subsequent calculations on the (001) surface have then been carried out with a $2 \times 2 \times 1$ K-point grid and a kinetic energy cutoff of 400 eV. The calculations on the gas phase Pt clusters are carried out in Γ point only in a cubic 25 Å box. The truncation criteria for the electronic and ionic loops are 10^{-5} eV and 10^{-2} eV/Å, respectively. Kinetic barriers are calculated according to the climbing image-nudged elastic band approach,[50] considering four images along the reaction path.

The (001) surface of the magnetite is modeled by a ($\sqrt{2} \times \sqrt{2}$)R45° $Fe_{35}O_{48}$ slab, according to the subsurface-vacancy model formerly proposed by Parkinson and co-workers.[30] Further details on the model structures are reported in Section S2 of the SI.

To model the formation of an O vacancy, we distinguish three nonequivalent oxygen lattice positions on the $Fe_3O_4(001)$ surface. O1 and O2 lie on threefold-coordinated surface sites connecting Fe atoms in tetrahedral positions. O3 lies on top of an Fe ion in an octahedral site (see Figure S4). The thermodynamic stability of the O vacancy (estimated with respect to the pristine surface and $1/2$ O_2) depends on the site where the oxygen atom is removed. In particular, O3 located on top of Fe ions in octahedral sites can be removed at a cost of 2.91 eV; removal of O2 (3.10 eV) and O3 (3.55 eV) requires more energy (see also Section S3, SI).

3. RESULTS AND DISCUSSION

To identify how CO binds to $Pt_n/Fe_3O_4(001)$ and whether it reacts with lattice oxygen, we start with a discussion of the TPD spectra of CO-saturated surfaces without an external oxygen supply. Subsequently, the reactivity linked with either the CO or O_2 reactant is monitored by pulsed-reactivity measurements. A low-temperature reaction peak demonstrates that the lattice oxygen reverse spillover leads to a highly reactive oxygen species on the cluster. Finally, we will show that the lattice oxygen reverse spillover leads to structural changes of the clusters. We should note at this point that over

the entire temperature range discussed below, STM indicates that the cluster coverage remains constant and the distribution monodisperse. In the following, ripening can thus be excluded from the discussion. To define the terminology concerning the coordination of oxygen used in the following, we discriminate between oxygen adsorbed (a) on top of the cluster (i.e., only coordinated to Pt), (b) on the cluster (i.e., coordinated to Pt, but not necessarily exclusively so), (c) at the rim or the interface (i.e., coordinated to both Pt and Fe), and (d) in the periphery (i.e., somewhere around the cluster).

3.1. Setting the Stage: CO Oxidation in TPD Measurements. Figure 1a shows CO desorption curves from Pt_5 (orange) and Pt_{19} clusters (gray) deposited onto the $Fe_3O_4(001)$ surface. First, Pt_{19} clusters exhibit a broad desorption feature with an onset temperature of around 350
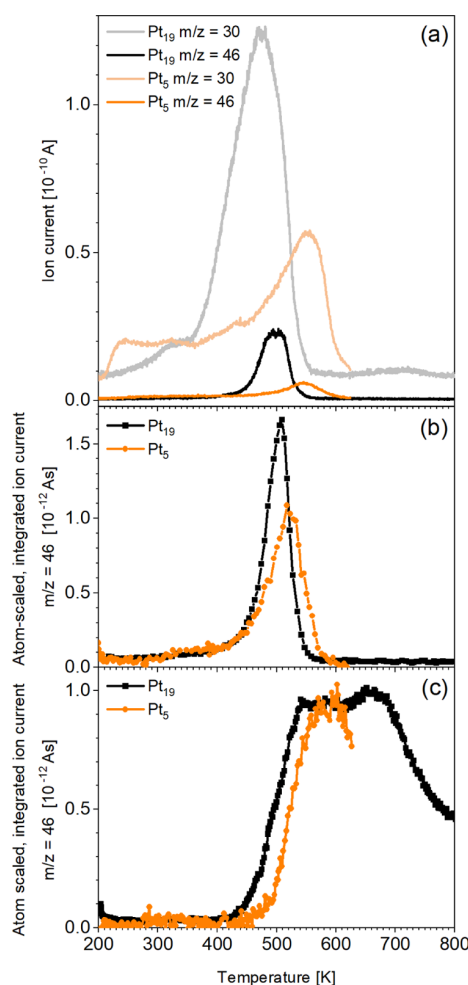
Figure 1. TPD and pulsed-reactivity spectra of Pt_{19} (black, gray) and Pt_5 (orange) supported on $Fe_3O_4(001)$. Using the same cluster density of 0.05 clusters/nm², the resulting atom density is ∼4 times higher for the Pt_{19} sample. (a) Saturation TPD curves of $C^{18}O$ adsorbed at 200 K. The $C^{18}O$ ($m/z = 30$) and $C^{18}O^{16}O$ ($m/z = 46$) traces are shown. (b) $C^{18}O^{16}O$ ($m/z = 46$) production as a function of temperature, synchronized with O_2 reactant pulses on $C^{18}O$-saturated samples. (c) $C^{18}O^{16}O$ ($m/z = 46$) formation synchronized with $C^{18}O$ reactant pulses on $C^{18}O$-saturated samples. The heating rate was 1 K/s. All pulsed data were integrated and normalized to the number of Pt atoms per cluster.

K and a peak temperature of 475 K. This feature is not observed on the bare magnetite surface (see Figure S5 in the SI), agrees with the temperature range reported for CO desorption from Pt nanoparticles on $Fe_3O_4(001)$,[51] and can therefore be assigned to the clusters. Second, the weak and broad feature with a maximum at 710 K is similar to the CO recombinative desorption from Fe(111).[52] We thus conclude that it results from CO, which has been adsorbed dissociatively on the small number of highly reduced iron sites, most likely Fe adatoms, which are common defects on the $Fe_3O_4(001)$ surface.[31] Finally, there is another small feature around 330 K. Such features have been tentatively assigned in the literature to reduced iron sites that surround Pt nanoparticles on $Fe_3O_4(111)$ when the strong metal–support interaction sets in.[53] While this interaction requires higher temperatures not yet reached here, there could already be clusters present in close proximity to reduced iron defects.

The CO desorption features of Pt_5 are comparable to those of Pt_{19}, with the difference that the desorption maxima are shifted to higher temperatures, indicating stronger binding. Note that all Pt_5 measurements end at 625 K, as cluster ripening was observed in STM when heating to higher temperatures (see Figure S6). The main CO desorption feature from Pt_5 with an onset at around 420 K and a peak at 550 K is assigned to the clusters. A lower temperature feature at around 430 K is observed, comparable to the one observed at 330 K for Pt_{19}. For both cluster sizes, this feature is located around the onset temperature of the main desorption peak, i.e., both features are shifted similarly. This might indicate a similar origin of the lower temperature feature, namely, due to clusters in the vicinity of reduced surface defect sites.

In both samples, we observe weak desorption signals in the temperature range <300 K, which we assign to desorption from defects in the magnetite support (see TPD for bare magnetite in Figure S5).[35] Since their intensity decreases upon cluster deposition, we conclude that a significant part of the clusters is most likely located on surface defect sites such as unreconstructed unit cells or antiphase domain boundaries.[31,54] Note that the background at these low temperatures varies with the state of the single crystal, which we suspect is due to slight changes in sample cleanliness, oxidation state, and/or defect density. The measurements comparing bare and cluster-covered magnetite were therefore recorded in a close temporal sequence.

Having understood the CO features, we can now interpret the $C^{18}O^{16}O$ production signals recorded simultaneously with the CO desorption (also shown in Figure 1a). Since no oxygen is dosed, this CO_2 production, observed for both cluster sizes, must be strictly related to the availability of lattice oxygen for reaction with CO. During the TPD measurements, only $C^{18}O^{16}O$ and no $C^{18}O_2$ is observed, excluding a Boudouard-type reaction ($2CO \rightarrow C + CO_2$). We are thus observing a MvK reaction. For Pt_{19}, the CO_2 feature has an onset temperature located at around 400 K and a broad peak at 500 K. Pt_5 exhibits a similar feature, starting below 420 K with the peak at 545 K. Note that we observe a change in the apparent cluster height in the same temperature range in STM measurements, as will be discussed later. As no CO_2 desorption could be detected for the bare $Fe_3O_4(001)$ surface (see Figure S5), we attribute the CO_2 signals to the presence of the clusters. For both cluster sizes, they exhibit about the same onset temperature and peak position with respect to the

corresponding CO desorption peaks, indicating that the CO_2 formation is closely related to the CO desorption.

3.2. Exploring the Reaction Mechanism by Overcoming Reactant Limitations: Pulsed-Reactivity Measurements.

Complementary to the TPD experiments, we performed pulsed valve experiments that give access to the reaction rate synchronized with a given reactant pulse. In these background-corrected measurements (see Section S1), each data point is the integral over a product pulse and correlates with the reaction rate at a given temperature. These reactant-synchronized pulsed measurements allow us to investigate adsorption limitations, (i) of oxygen adsorption by CO poisoning (in pulsed O_2 experiments) and (ii) of CO adsorption at high temperatures (in pulsed CO experiments).

We start with pulsing O_2 onto the CO precovered sample and observe the CO_2 production shown in Figure 1b for Pt_5 (orange) and Pt_{19} clusters (black). The CO_2 formation starts around 400 K for both cluster sizes and peaks at 505 K for Pt_{19} and 520 K for Pt_5, respectively. This difference reflects the slightly higher binding energy of CO on Pt_5. While the cluster surface is poisoned with CO at low temperatures, binding sites for dissociative O_2 adsorption become available above the onset temperature of CO desorption, leading to the coadsorption of oxygen and CO on the same cluster.[18] At this temperature, the CO oxidation in a classical Langmuir–Hinshelwood manner is already facile on clusters,[55] and hence a high reaction rate is observed as soon as the adsorption limitations are overcome. The similarity to the CO_2 production in the TPD indicates that it is adsorption-limited as well. As we will discuss in detail in Section 3.5, DFT confirms that the activation barrier for the initial lattice oxygen reverse spillover is below 1 eV, hence far less than the CO binding energy calculated, e.g., for Pt_2 clusters on $Fe_3O_4(001)$.[56]

We note that the CO_2 production peak on Pt_5 in the pulsed experiments is at a somewhat lower temperature than the peak observed in TPD, contrary to Pt_{19}. This observation can be explained by a reaction limitation due to a lack of CO, which is not replenished during the measurement. When supplying CO by alternating CO and O_2 pulses (see Figure S7), the CO_2 formation synchronized with the O_2 pulses follows the shape of the corresponding CO_2 TPD trace, with the same onset and peak temperatures, thus confirming the hypothesis above.

We now describe the opposite experiment, pulsing CO without providing any oxygen. Figure 1c shows the CO_2 production observed for both investigated cluster sizes as a function of temperature. For Pt_{19}, CO_2 formation starts at around 425 K, reaching a plateau between 550 and 670 K with an approximately constant CO_2 formation rate. On Pt_5, an onset temperature of 450 K is observed, with a maximum at 590 K. This experiment allows probing the behavior of the CO_2 formation over a wider temperature range since the reactant is refreshed continuously by pulses and thus also available beyond the CO desorption temperature. As expected, the CO_2 production starts at the onset temperature of CO_2 formation in the TPD experiment, for both cluster sizes, although at a slightly higher temperature, where oxygen migration onto the cluster is no longer hindered by CO. The signal saturates once all available cluster sites can accommodate reactive oxygen atoms. This temperature coincides with the temperature where CO desorption is complete. Interestingly, the normalized peak intensity is the same for both cluster sizes. The number of active sites hence scales with the surface and not the rim of the cluster.[57] The upper limit of

the plateau could be due to encapsulation effects or due to limited oxygen coverage: chemisorption on stepped Pt(112) leads to O_2 desorption just below 700 K.[58] All of the plateau characteristics point to a reaction that is limited by free adsorption sites on the cluster surface and that also proceeds on the cluster, via lattice oxygen reverse spillover. In contrast, an interface reaction would not saturate as long as CO (and lattice oxygen) are available since the two reactants do not compete for adsorption sites.

3.3. Lattice Oxygen Reverse Spillover in Sequential CO TPDs.

Having shown the ease of lattice oxygen reverse spillover once adsorption sites are available, we now use this highly reactive oxygen species in a low-temperature reaction. We know from the literature that the CO oxidation on Pt clusters after sequential adsorption of oxygen and CO already takes place below 400 K.[18,55]

In the experiment in Figure 2, we show that it is indeed possible to observe an additional CO_2 production feature when
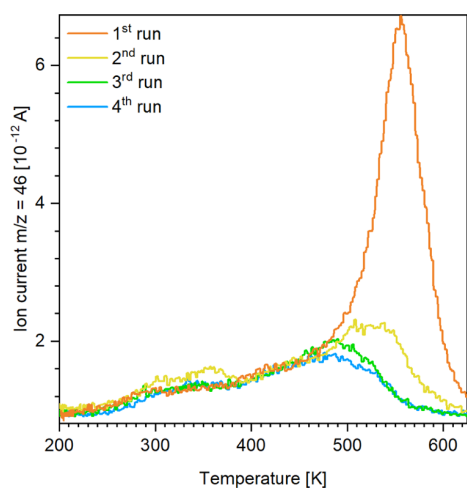
Figure 2. $C^{18}O^{16}O$ ($m/z = 46$) formation in subsequent CO-TPD spectra of Pt_5 supported on $Fe_3O_4(001)$. In each run, the surface is saturated with $C^{18}O$ at 200 K; the heating rate was 1 K/s. Only in the second run (yellow), a CO_2 production feature around 300−370 K is observed. The main feature above 500 K decreases during the first two runs. Figure S8 shows the corresponding $C^{18}O$ desorption signals.

populating the clusters with oxygen by reverse spillover prior to CO adsorption. Figure 2 shows a sequence of CO_2 production TPD curves on a Pt_5 sample, each taken after saturating the surface with CO at 200 K. Remarkably, the anticipated low-temperature CO_2 feature around 300−370 K is observed only for one out of four runs, the second one. In the first run, CO poisoning and an activation barrier initially hinder oxygen migration onto the cluster and subsequently lead to high-temperature CO_2 formation. In contrast, the second run already starts with a certain coverage of reactive oxygen on the clusters, accumulated from lattice oxygen reverse spillover during the first temperature ramp after complete CO removal, which requires heating to beyond 550 K. At this high-temperature end of the TPD, however, cluster encapsulation due to SMSI starts as well, an effect that strongly affects the cluster reactivity, as studied for nanoparticles,[51] while requiring further investigation for clusters. Here, it leads to the well-known loss of CO adsorption capability that we see in the corresponding series of CO TPDs (see Figure S8). It is,

therefore, experimentally impossible to fully disentangle lattice oxygen reverse spillover from the onset of encapsulation. As a consequence, the low-temperature CO_2 production is not repeated in the third and fourth run. Only in the second run, we reach a starting situation where the cluster is CO-free, while the encapsulation is still incomplete. Note that the low intensity of the resulting low-temperature CO_2 production feature is likely caused by this partial encapsulation. Summing up, this experiment provides direct proof for reverse spillover of lattice oxygen.

3.4. Effects of the Lattice Oxygen Reverse Spillover on the Cluster Structure: STM Measurements.

In the following, we focus on the effects of this lattice oxygen reverse spillover on the cluster structure concerning the geometry and electronic state. Figure 3a−e shows a series of STM images displaying Pt_{19} clusters on a defect-rich $Fe_3O_4(001)$ surface, recorded at the temperatures indicated in the figure. The clusters appear as bright protrusions on the surface and seem to be largely randomly distributed while maintaining their size upon deposition. At all temperatures investigated here, the clusters are still monodisperse; ripening or disintegration is not observed. At 473 K and even more pronounced at 573 K, tiny holes form around some of the clusters, but not all (details see Figure S9). Such holes are typically observed on this surface when oxygen atoms are removed, leaving behind under-coordinated iron atoms that diffuse into the bulk.[20] This is a direct consequence of the lattice oxygen reverse spillover occurring in the periphery of the clusters. The hole formation is more or less pronounced depending on the amount of CO in the chamber background that reacts off oxygen from the clusters, creating free adsorption sites for renewed oxygen migration.

Upon annealing, the cluster brightness seems to decrease, indicating a decline in their apparent height, while the coverage remains constant (confirmed by statistical analysis of several images of the same sample at different temperatures). This finding is quantified in Figure 3f for Pt_{19}, where the cluster height distributions at different temperatures are presented in histograms. Dashed red lines are used to indicate the approximate correspondence to atomic layers. While the Pt_{19} clusters are about three atomic layers high at room temperature, they flatten to between one and two layers at 573 K. The transition takes place between 423 and 523 K, which is the temperature range where CO_2 formation is observed in Figure 1a. This strong correlation in temperature suggests that the change in apparent height is caused by lattice oxygen reverse spillover.

When comparing several cluster sizes in Figure 3g, we find that this is a common phenomenon. The decrease in apparent height holds for all investigated cluster sizes, suggesting the lattice oxygen reverse spillover to be a universal effect for the $Pt_n/Fe_3O_4(001)$ system. Such a behavior could either be explained by a real geometry change of the clusters or by a change in the density of states due to oxygen adsorption.

3.5. DFT Calculations Reveal Further Mechanistic Details.

The experimental results point to some mechanistic aspects that require theoretical investigation. In particular, we consider the following questions: (i) How easy is it to remove lattice oxygen from bare magnetite vs in the periphery of a cluster? (ii) Is lattice oxygen reverse spillover endo- or exothermic, and can we confirm that the clusters can be covered by considerable amounts of oxygen? (iii) What is the
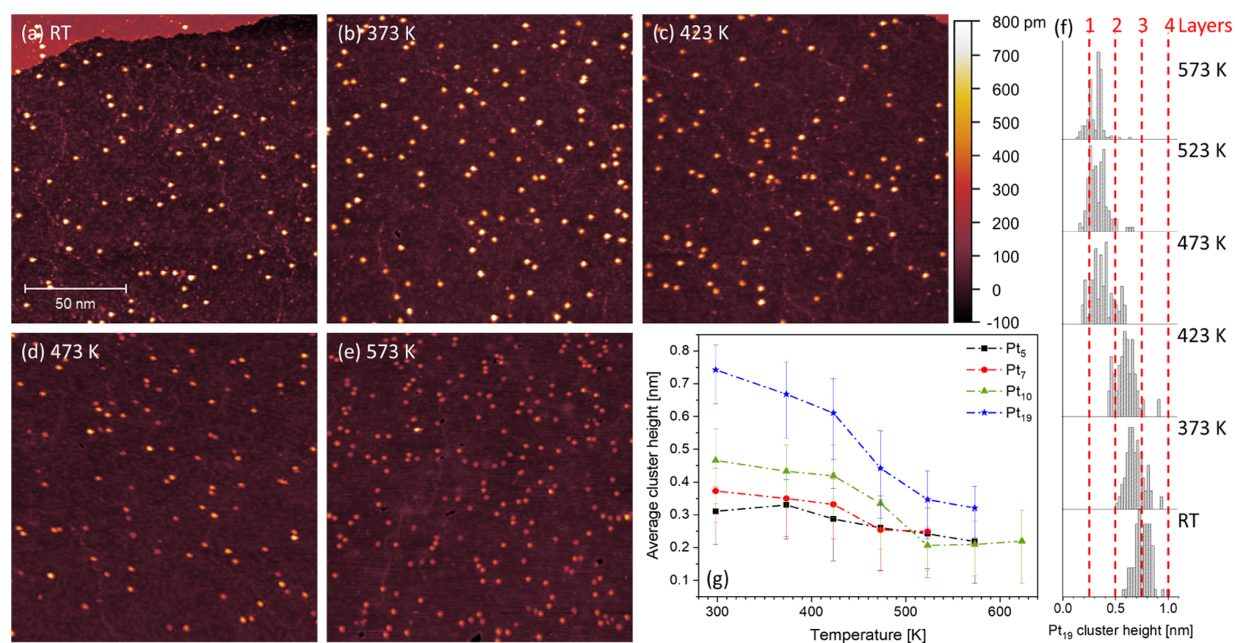
Figure 3. Height evolution of Pt_n/Fe$_3$O$_4$(001) as a function of temperature. (a−e) STM images (150 × 150 nm^2) of Pt_{19} clusters (0.01 clusters/nm^2) measured at the temperatures indicated. All images have been scaled to the same false color scale for height comparison. Note that (e) is from a second set of experiments with a slightly higher cluster coverage than (a)−(d). The coverage in (e) is consistent with the coverage of the same sample after RT deposition. (f) Height profiles comparing the size distribution of Pt_{19} in (a)−(e) as a function of temperature. (g) Evolution of the average cluster height as a function of temperature for Pt_5, Pt_7, Pt_{10}, and Pt_{19}. Imaging parameters: V_b = 1.50 V; (a, e) I_t = 300 pA, (b−d) I_t = 400 pA.
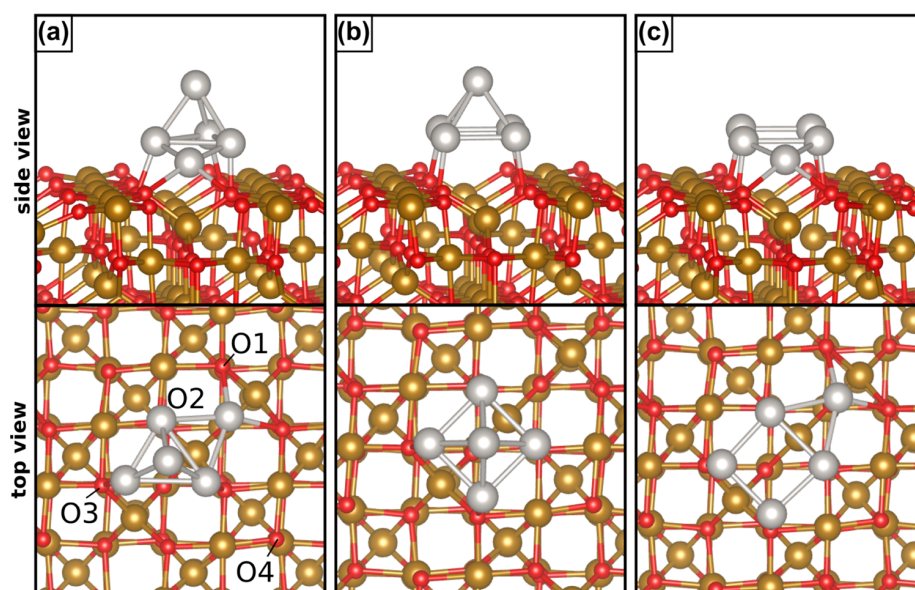
Figure 4. Pt_5 clusters on the Fe$_3$O$_4$(001) surface. (a)−(c) are the three most stable isomers, with isomer (a) being 1.5 and 1.78 eV lower in energy than the isomers in (b) and (c), respectively. Red, brown, and gray spheres correspond to O, Fe, and Pt atoms, respectively.

activation barrier? (iv) Can the apparent height change in STM be explained by a restructuring?

First, we studied the structure of a gas phase Pt_5 cluster, starting from the most stable isomers reported in the literature.[59−65] This led to six isomers with very similar stability; the energy difference between the ground state and the least stable of the six isomers considered here is 0.35 eV, and sometimes different structures are separated by a few

millielectronvolts, suggesting a fluxional behavior of the gas phase clusters (see Section S9, SI). Upon deposition on Fe$_3$O$_4$, some of the structures retain the topology of the gas phase, while others undergo a strong rearrangement. The Pt_5 adsorption energies (Table S4), computed with respect to Fe$_3$O$_4$(001) and the most stable Pt_5 isomer (Pt_5 in Figure S10i), show that the ground state corresponds to a capped rhombus, with an adsorption energy of −4.51 eV, shown in
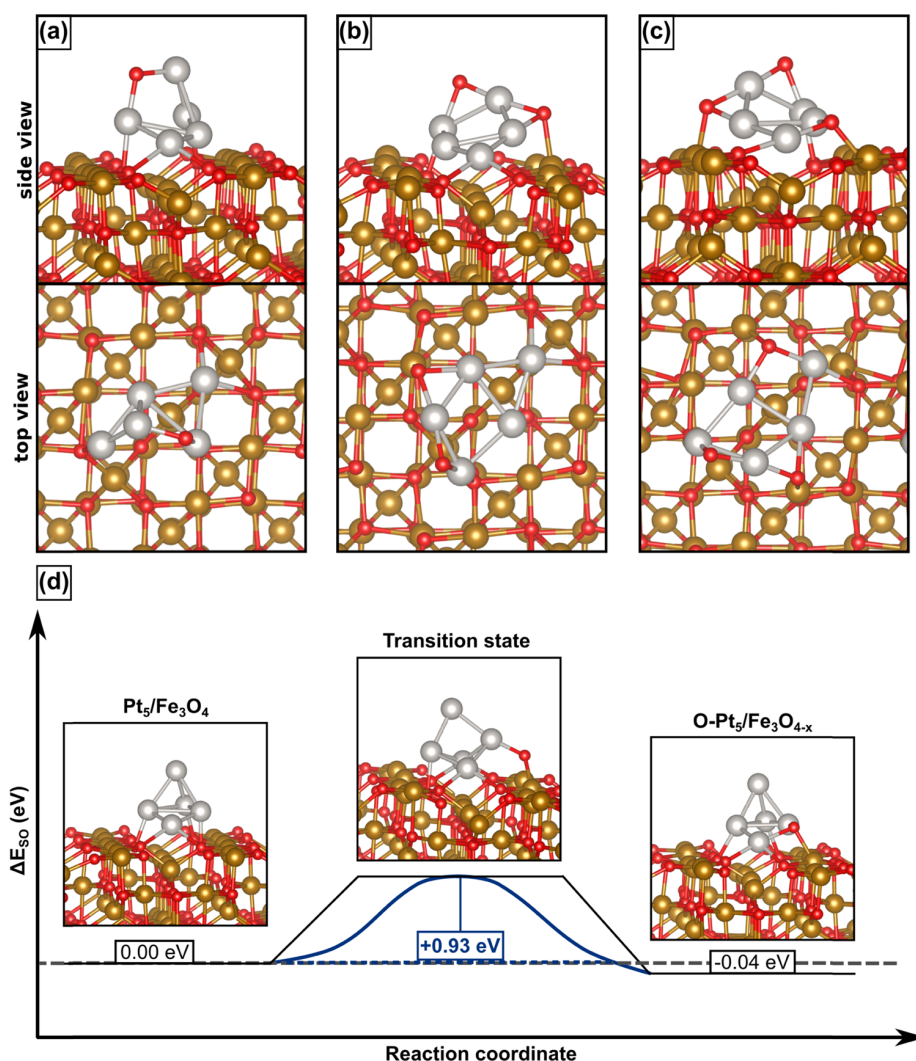
Figure 5. Side and top views of the most stable structures obtained for reverse spillover of (a) one, (b) two, and (c) three lattice oxygen atoms. In (d), the energy profile to displace an O atom from a lattice position to Pt_5 is shown.

Figure 4a, followed by a square pyramidal Pt_5 cluster (Figure 4b) and a planar structure (Figure 4c). Note that the most stable isomer, Figure 4a, is 1.5 eV more favorable than the next one, which shows that the surface has a strong stabilizing effect on this structure. This also suggests that the conversion of one isomer into another is much more difficult than in the gas phase.

Upon deposition, the Pt cluster becomes slightly positively charged (by 0.3 e) and a partial quenching of the magnetic moment of the support occurs, with a reduction from 3.3 μ_B per Fe_3O_4 formula unit in the clean surface to 2.59 μ_B when Pt_5 is adsorbed, as shown in Table S4.

We now start addressing question (i). The formation energy of an O vacancy on the clean $Fe_3O_4(001)$ surface is about 3 eV (see Table S2 and Section S3). The addition of a metal/oxide interface may facilitate the removal of the O atoms in contact with the metal adduct.[21] We have explored this possibility by removing O atoms from four possible sites in the cluster periphery, indicated in Figure 4a, involving O either in direct contact with Pt_5 or at some distance. The formation energy of an O vacancy on Pt_5/Fe_3O_4 is reduced with respect to the clean surface. In particular, the formation of V_{O2} has a cost of

1.98 eV, about 0.9 eV smaller than the most favorable case on the clean surface, which costs 2.91 eV. Also, the removal of an O atom not in direct contact with Pt_5 (such as V_{O4}) is slightly easier by almost 0.5 eV (see also Section S10, SI). These results point to a metal-assisted MvK mechanism.

In a second step, we address question (ii) regarding the endo-/exothermicity of the reverse spillover. The mechanism of lattice oxygen reverse spillover involves the displacement of O atoms from the lattice positions and their adsorption on the supported metal cluster. To model this process, we have started from the most favorable case of O removal (V_{O2} in Figure 4a) and have readsorbed an O atom on various sites of Pt_5. A preliminary exploration of O adsorption on gas-phase Pt_5 provides information about the most stable adsorption sites (see Table S3). O adsorbs preferentially in a bridge mode or as a terminal Pt−O group, followed by threefold hollow sites. When the cluster is adsorbed on Fe_3O_4, additional adsorption sites are present at the Pt_5/Fe_3O_4 interface. In some cases, the lattice oxygen reverse spillover process is endothermic, but there are also structures where the product is more stable than the initial configuration. The most favorable case is shown in Figure 5a, where an O from the interface is inserted into a Pt−

Pt bond, which is preferred by -0.40 eV (see Table S6 and Figure S11 for further details). Thus, lattice oxygen reverse spillover involving a single O atom is thermodynamically favorable.

This leads us to question (iii) where we want to connect the lattice oxygen vacancy formation with the oxygen adsorption on the cluster by a viable path. This process is activated, and the kinetic barrier has been estimated for the initial step of the reaction, i.e., the displacement of an O atom from an O2 lattice site (see Figure 4a) to a nearby interfacial site where it binds at the cluster rim, shown in Figure 5. For this specific path, the whole process is almost thermoneutral, and the barrier of 0.93 eV can be overcome by thermal effects at the temperatures involved in the experiments described above. It is reasonable to assume that the displacement of the O atom from the lattice is the rate-determining step of the whole process: further diffusion of O-species on Pt_5 should occur with low barriers due to similar bond strengths of various adsorption sites.

Next, we have considered the case of the removal of a second O atom from various lattice sites and its readsorption on Pt_5O. Also, in this case, we found a few structures where the process is exothermic. The formation of the most stable isomer, shown in Figure 5b, where two O atoms are adsorbed on a bridge site, is exothermic by -0.64 eV (see also Table S7 and Figure S12). Finally, the process has also been considered for a third O atom, which is removed from the cluster/oxide interface and readsorbed on Pt_5, forming an oxidized Pt_5O_3-supported cluster, as shown in Figure 5c. This generates a large number of possible initial combinations, and we could explore only a few of them. In the most favorable case (Figure 5c), the transfer of three O atoms is slightly endothermic, by 0.17 eV only. We cannot exclude the existence of even more favorable isomers, and entropic effects are expected to further favor the process. This supports the evidence that multiple lattice oxygen reverse spillover from magnetite onto a Pt cluster is energetically accessible (for further details, see Figure S13 and Table S8).

This opens the question of the best channel for CO oxidation via CO reaction with an O atom of Fe_3O_4 at the interface of Pt_5 with the support or with the O atoms adsorbed on the Pt cluster. The experiments show a complex behavior as a function of CO poisoning, reaction temperature, cluster size, etc. and suggest that the number of active sites scales with the number of surface and not the rim atoms of the clusters. With our simplified models, we cannot determine active sites directly but instead compare the energy required to remove the three kinds of oxygen atoms present in the catalyst: lattice oxygen, Pt_5 rim oxygen, or oxygen present on top of the cluster. Oxygen removal from the lattice costs about 3 eV (Table S2 and Section S3). The removal of a lattice O atom from the periphery of the Pt_5/Fe_3O_4 cluster costs 2.0, 2.5, 2.7, and 3.1 eV (Table S5), depending on the site (on average 2.6 eV). These numbers can be compared to the cost of desorbing an O atom from Pt_5O supported on Fe_3O_{4-x}, where an O vacancy has been created. In the most stable configuration, the cost is 2.38 eV (see Figure S14), indicating that the Pt−O bond is strong and that at low O coverage, removing the O adatoms from a Pt cluster has a comparable cost to removing O atoms from the cluster/oxide interface. Next, we considered O removal from Pt_5O_2 (here, two O vacancies have been created on Fe_3O_4); removing the O atom bound only to the Pt_5 cluster costs 2.36 eV, while the removal of the O atom at the boundary with the oxide costs 2.22 eV (Figure S14). Things

change for even higher O coverages though. We have removed each of the three O atoms bound to Pt_5 in Pt_5O_3/Fe_3O_{4-3x} and the cost is 1.72, 2.20, and 2.24 eV, respectively, Figure S14 (on average 2.05 eV). This suggests that for more pronounced lattice oxygen reverse spillover or higher O coverages on Pt clusters, the reaction of CO with adsorbed oxygen becomes preferred.

Finally, in question (iv), we want to rationalize the structural changes observed in the STM images. Lattice oxygen reverse spillover indeed induces a structural change in the supported cluster, as apparent in Figures 4 and 5. In particular, there is a tendency to rearrange the structure of Pt_5 from three-dimensional (3D) to a quasi-two-dimensional (quasi-2D) as the O loading increases. To quantify this effect, we have computed the average cluster height with respect to the Fe_3O_4 surface for all of the cases discussed here, and indeed there is an overall reduction of the cluster height (see Section S12, SI). This could indicate that the height evolution observed in STM, as shown in Figure 3, is due to geometry changes and not purely an electronic effect. At this point, we cannot fully rule out a thermal restructuring, leading to a change of the cluster structure.

Furthermore, Fe spillover from Fe_3O_4 onto Pt_5 and Pt_5O_3 has been considered, following a similar strategy as described above for lattice oxygen reverse spillover. In all cases considered, however, Fe reverse spillover is highly unfavorable (see Section S13, SI). Thus, if Fe diffusion occurs, this will be toward the bulk of magnetite, not toward the supported Pt clusters. These results suggest that the encapsulation of Pt clusters due to SMSI effects follows more complex paths than the diffusion of isolated Fe atoms.

4. CONCLUSIONS

A central question concerning cluster catalysis with lattice oxygen, in a Mars van Krevelen mechanism, is whether the reaction occurs at the cluster−support interface or whether the oxygen first migrates onto the cluster to react there. We studied this distinction on the example of metal-assisted MvK in the CO oxidation on small, size-selected Pt_n clusters supported on magnetite $Fe_3O_4(001)$ in a multimodal experiment, supported by DFT calculations. The detailed TPD and pulsed-reactivity experiments revealed a reaction on the cluster that involves reverse spillover of lattice oxygen, a phenomenon hitherto not reported on this support. Via annealing-induced migration, highly reactive lattice oxygen can be accumulated on the clusters and react in a low-temperature window of 300−370 K.

As our calculations for Pt_5 clusters showed, this reverse spillover process is exothermic for the first two oxygen atoms, with an initial migration activation barrier below 1 eV, much lower than the CO desorption barrier. Thus, the lattice oxygen reverse spillover is driven by overcoming CO poisoning and scales with the availability of free adsorption sites. The maximum obtainable turnover rates observed in the pulsed-reactivity experiments scale with the number of cluster surface atoms.

STM investigations showed that the clusters remain monodisperse throughout all experiments but with a distinct decrease in apparent height, concomitant to the formation of holes due to lattice oxygen removal. The calculations suggest that this change could be due to a true geometrical adaptation upon lattice oxygen reverse spillover, resulting in a transition from 3D to 2D clusters.

Larger Pt nanoparticles on the same support have been shown to become encapsulated by a thin, reduced iron oxide film due to SMSI.[51] In first experiments, we found this effect to also occur on small clusters, at temperatures where lattice oxygen reverse spillover already occurred. Calculations suggest that the growth of thin oxide films occurs through more complex paths than the mere diffusion of isolated Fe atoms, warranting more extensive future investigations.

■ ASSOCIATED CONTENT

ⓢ Supporting Information

The Supporting Information is available free of charge at https://pubs.acs.org/doi/10.1021/acscatal.1c01451.

Pulsed-reactivity data evaluation (Section S1); characterization of the magnetite bulk and (001) surface by DFT calculations (Section S2); formation of a surface oxygen vacancy on various sites (Section S3); CO desorption from bare magnetite and magnetite-supported clusters in TPD (Section S4); ripening of Pt_5 in STM (Section S5); alternating CO and O_2 pulses on $Pt_5/Fe_3O_4(001)$ (Section S6); loss of CO adsorption capability upon cluster encapsulation (Section S7); hole formation in cluster periphery (Section S8); platinum clusters in the gas phase: structure relaxation and oxygen adsorption (Section S9); adsorption of Pt_5 on $Fe_3O_4(001)$ and formation of oxygen vacancies (Section S10); lattice oxygen reverse spillover (Section S11); impact of lattice oxygen reverse spillover on cluster height (Section S12); and iron spillover (Section S13) (PDF)

■ AUTHOR INFORMATION

Corresponding Author

Barbara A. J. Lechner − *Chair of Physical Chemistry, Department of Chemistry, Technical University of Munich, 85748 Garching, Germany;* ⓞ orcid.org/0000-0001-9974-1738; Email: bajlechner@tum.de

Authors

Sebastian Kaiser − *Chair of Physical Chemistry, Department of Chemistry, Technical University of Munich, 85748 Garching, Germany; Catalysis Research Center, Technical University of Munich, 85748 Garching, Germany*

Farahnaz Maleki − *Dipartimento di Scienza dei Materiali, University of Milano-Bicocca, 20125 Milano, Italy;* ⓞ orcid.org/0000-0002-5747-1319

Ke Zhang − *Chair of Physical Chemistry, Department of Chemistry, Technical University of Munich, 85748 Garching, Germany; Catalysis Research Center, Technical University of Munich, 85748 Garching, Germany*

Wolfgang Harbich − *Institute of Physics, Ecole Polytechnique Fédérale de Lausanne, CH-1015 Lausanne, Switzerland;* ⓞ orcid.org/0000-0002-1515-151X

Ueli Heiz − *Chair of Physical Chemistry, Department of Chemistry, Technical University of Munich, 85748 Garching, Germany; Catalysis Research Center, Technical University of Munich, 85748 Garching, Germany;* ⓞ orcid.org/0000-0002-9403-1486

Sergio Tosoni − *Dipartimento di Scienza dei Materiali, University of Milano-Bicocca, 20125 Milano, Italy;* ⓞ orcid.org/0000-0001-5700-4086

Gianfranco Pacchioni − *Dipartimento di Scienza dei Materiali, University of Milano-Bicocca, 20125 Milano, Italy;* ⓞ orcid.org/0000-0002-4749-0751

Friedrich Esch − *Chair of Physical Chemistry, Department of Chemistry, Technical University of Munich, 85748 Garching, Germany; Catalysis Research Center, Technical University of Munich, 85748 Garching, Germany;* ⓞ orcid.org/0000-0001-7793-3341

Complete contact information is available at:
https://pubs.acs.org/10.1021/acscatal.1c01451

Notes

The authors declare no competing financial interest.
The structures of the calculations reported in this paper are available upon reasonable request to the authors.

■ ACKNOWLEDGMENTS

■ REFERENCES

(1) Ma, Z.; Zaera, F. Heterogeneous Catalysis by Metals. In *Encyclopedia of Inorganic Chemistry*, 2nd ed.; King, R. B., Ed.; John Wiley & Sons: Chichester, 2005; pp 1768−1784.

(2) Rothenberg, G. *Catalysis: Concepts and Green Applications*; Wiley-VCH: Weinheim, 2008; pp 129−131.

(3) Bell, A. T. The Impact of Nanoscience in Heterogeneous Catalysis. *Science* 2003, 299, 1688−1691.

(4) Schauermann, S.; Nilius, N.; Shaikhutdinov, S.; Freund, H. J. Nanoparticles for Heterogeneous Catalysis: New Mechanistic Insights. *Acc. Chem. Res.* 2013, 46, 1673−1681.

(5) Eberhardt, W.; Fayet, P.; Cox, D. M.; Fu, Z.; Kaldor, A.; Sherwood, R.; Sondericker, D. Photoemission from Mass-Selected Monodispersed Pt Clusters. *Phys. Rev. Lett.* 1990, 64, 780−783.

(6) Valden, M.; Lai, X.; Goodman, D. W. Onset of Catalytic Activity of Gold Clusters on Titania with the Appearance of Nonmetallic Properties. *Science* 1998, 281, 1647−1650.

(7) Sanchez, A.; Abbet, S.; Heiz, U.; Schneider, W.-D.; Häkkinen, H.; Barnett, R. N.; Landman, U. When Gold Is Not Noble: Nanoscale Gold Catalysts. *J. Phys. Chem. A* 1999, 103, 9573−9578.

(8) Bus, E.; Prins, R.; van Bokhoven, J. A. Origin of the Cluster-Size Effect in the Hydrogenation of Cinnamaldehyde over Supported Au Catalysts. *Catal. Commun.* 2007, 8, 1397−1402.

(9) Crampton, A. S.; Rotzer, M. D.; Landman, U.; Heiz, U. Can Support Acidity Predict Sub-Nanometer Catalyst Activity Trends? *ACS Catal.* 2017, 7, 6738−6744.

(10) Lee, S.; Lee, B.; Seifert, S.; Winans, R. E.; Vajda, S. Fischer-Tropsch Synthesis at a Low Pressure on Subnanometer Cobalt Oxide Clusters: The Effect of Cluster Size and Support on Activity and Selectivity. *J. Phys. Chem. C* 2015, 119, 11210−11216.

(11) Walenta, C. A.; Kollmannsberger, S. L.; Courtois, C.; Pereira, R. N.; Stutzmann, M.; Tschurl, M.; Heiz, U. Why Co-Catalyst-Loaded

Rutile Facilitates Photocatalytic Hydrogen Evolution. *Phys. Chem. Chem. Phys.* **2019**, *21*, 1491−1496.

(12) Tauster, S. J. Strong Metal-Support Interactions. *Acc. Chem. Res.* **1987**, *20*, 389−394.

(13) Dulub, O.; Hebenstreit, W.; Diebold, U. Imaging Cluster Surfaces with Atomic Resolution: The Strong Metal-Support Interaction State of Pt Supported on TiO2(110). *Phys. Rev. Lett.* **2000**, *84*, 3646−3649.

(14) Qin, Z. H.; Lewandowski, M.; Sun, Y. N.; Shaikhutdinov, S.; Freund, H. J. Encapsulation of Pt Nanoparticles as a Result of Strong Metal-Support Interaction with Fe3O4(111). *J. Phys. Chem. C* **2008**, *112*, 10209−10213.

(15) Polo-Garzon, F.; Blum, T. F.; Bao, Z.; Wang, K.; Fung, V.; Huang, Z.; Bickel, E. E.; Jiang, D.; Chi, M.; Wu, Z. In Situ Strong Metal−Support Interaction (SMSI) Affects Catalytic Alcohol Conversion. *ACS Catal.* **2021**, *11*, 1938−1945.

(16) Lewandowski, M.; Sun, Y. N.; Qin, Z. H.; Shaikhutdinov, S.; Freund, H. J. Promotional Effect of Metal Encapsulation on Reactivity of Iron Oxide Supported Pt Catalysts. *Appl. Catal., A* **2011**, *391*, 407−410.

(17) Kunz, S.; Schweinberger, F. F.; Habibpour, V.; Röttgen, M.; Harding, C.; Arenz, M.; Heiz, U. Temperature Dependent CO Oxidation Mechanisms on Size-Selected Clusters. *J. Phys. Chem. C* **2010**, *114*, 1651−1654.

(18) Heiz, U.; Sanchez, A.; Abbet, S.; Schneider, W. D. Catalytic Oxidation of Carbon Monoxide on Monodispersed Platinum Clusters: Each Atom Counts. *J. Am. Chem. Soc.* **1999**, *121*, 3214−3217.

(19) Widmann, D.; Behm, R. J. Activation of Molecular Oxygen and the Nature of the Active Oxygen Species for Co Oxidation on Oxide Supported Au Catalysts. *Acc. Chem. Res.* **2014**, *47*, 740−749.

(20) Bliem, R.; van der Hoeven, J.; Zavodny, A.; Gamba, O.; Pavelec, J.; de Jongh, P. E.; Schmid, M.; Parkinson, G. S. An Atomic-Scale View of CO and H2 Oxidation on a Pt/Fe3O4 Model Catalyst Angewandte. *Angew. Chem., Int. Ed.* **2015**, *127*, 13999−14002.

(21) Ruiz Puigdollers, A.; Schlexer, P.; Tosoni, S.; Pacchioni, G. Increasing Oxide Reducibility: The Role of Metal/Oxide Interfaces in the Formation of Oxygen Vacancies. *ACS Catal.* **2017**, *7*, 6493−6513.

(22) Zafiris, G. S.; Gorte, R. J. Evidence for Low-Temperature Oxygen Migration from Ceria to Rh. *J. Catal.* **1993**, *139*, 561−567.

(23) Happel, M.; Mysliveček, J.; Johánek, V.; Dvořák, F.; Stetsovych, O.; Lykhach, Y.; Matolín, V.; Libuda, J. Adsorption Sites, Metal-Support Interactions, and Oxygen Spillover Identified by Vibrational Spectroscopy of Adsorbed CO: A Model Study on Pt/Ceria Catalysts. *J. Catal.* **2012**, *289*, 118−126.

(24) Lykhach, Y.; Faisal, F.; Skála, T.; Neitzel, A.; Tsud, N.; Vorokhta, M.; Dvořák, F.; Beranová, K.; Kosto, Y.; Prince, K. C.; Matolín, V.; Libuda, J. Interplay between the Metal-Support Interaction and Stability in Pt/Co3O4(111) Model Catalysts. *J. Mater. Chem. A* **2018**, *6*, 23078−23086.

(25) Röttgen, M. A.; Abbet, S.; Judai, K.; Antonietti, J. M.; Wörz, A. S.; Arenz, M.; Henry, C. R.; Heiz, U. Cluster Chemistry: Size-Dependent Reactivity Induced by Reverse Spill-Over. *J. Am. Chem. Soc.* **2007**, *129*, 9635−9639.

(26) Arndt, B.; Lechner, B. A. J.; Bourgund, A.; Grånäs, E.; Creutzburg, M.; Krausert, K.; Hulva, J.; Parkinson, G. S.; Schmid, M.; Vonk, V.; Esch, F.; Stierle, A. Order-Disorder Phase Transition of the Subsurface Cation Vacancy Reconstruction on Fe3O4(001). *Phys. Chem. Chem. Phys.* **2020**, *22*, 8336−8343.

(27) Fleet, M. E. The Structure of Magnetite. *Acta Crystallogr., Sect. B: Struct. Crystallogr. Cryst. Chem.* **1981**, *37*, 917−920.

(28) Verwey, E. J. W.; Heilmann, E. L. Physical Properties and Cation Arrangement of Oxides with Spinel Structures I. Cation Arrangement in Spinels. *J. Chem. Phys.* **1947**, *15*, 174−180.

(29) Verwey, E. J.; Haayman, P. W.; Romeijn, F. C. Physical Properties and Cation Arrangement of Oxides with Spinel Structures II. Electronic Conductivity. *J. Chem. Phys.* **1947**, *15*, 181−187.

(30) Bliem, R.; McDermott, E.; Ferstl, P.; Setvin, M.; Gamba, O.; Pavelec, J.; Schneider, M. A.; Schmid, M.; Diebold, U.; Blaha, P.; Hammer, L.; Parkinson, G. S. Subsurface Cation Vacancy Stabilization of the Magnetite (001) Surface. *Science* **2014**, *346*, 1215−1218.

(31) Parkinson, G. S. Iron Oxide Surfaces. *Surf. Sci. Rep.* **2016**, *71*, 272−365.

(32) Parkinson, G. S.; Novotny, Z.; Argentero, G.; Schmid, M.; Pavelec, J.; Kosak, R.; Blaha, P.; Diebold, U. Carbon Monoxide-Induced Adatom Sintering in a Pd-Fe3O4 Model Catalyst. *Nat. Mater.* **2013**, *12*, 724−728.

(33) Novotny, Z.; Mulakaluri, N.; Edes, Z.; Schmid, M.; Pentcheva, R.; Diebold, U.; Parkinson, G. S. Probing the Surface Phase Diagram of Fe3O4(001) towards the Fe-Rich Limit: Evidence for Progressive Reduction of the Surface. *Phys. Rev. B* **2013**, *87*, No. 195410.

(34) Parkinson, G. S.; Novotný, Z.; Jacobson, P.; Schmid, M.; Diebold, U. A Metastable Fe(A) Termination at the Fe3O4(001) Surface. *Surf. Sci.* **2011**, *605*, L42−L45.

(35) Hulva, J.; Jakub, Z.; Novotny, Z.; Johansson, N.; Knudsen, J.; Schnadt, J.; Schmid, M.; Diebold, U.; Parkinson, G. S. Adsorption of CO on the Fe3O4(001) Surface. *J. Phys. Chem. B* **2018**, *122*, 721−729.

(36) Meier, M.; Hulva, J.; Jakub, Z.; Pavelec, J.; Setvin, M.; Bliem, R.; Schmid, M.; Diebold, U.; Franchini, C.; Parkinson, G. S. Water Agglomerates on Fe3O4(001). *Proc. Natl. Acad. Sci. U.S.A.* **2018**, *115*, E5642−E5650.

(37) Pavelec, J.; Hulva, J.; Halwidl, D.; Bliem, R.; Gamba, O.; Jakub, Z.; Brunbauer, F.; Schmid, M.; Diebold, U.; Parkinson, G. S. A Multi-Technique Study of CO2 Adsorption on Fe3O4 Magnetite. *J. Chem. Phys.* **2017**, *146*, No. 014701.

(38) Heiz, U.; Vanolli, F.; Trento, L.; Schneider, W. D. Chemical Reactivity of Size-Selected Supported Clusters: An Experimental Setup. *Rev. Sci. Instrum.* **1997**, *68*, 1986−1994.

(39) Nečas, D.; Klapetek, P. Gwyddion: An Open-Source Software for SPM Data Analysis. *Cent. Eur. J. Phys.* **2012**, *10*, 181−188.

(40) Bonanni, S.; Aït-Mansour, K.; Hugentobler, M.; Brune, H.; Harbich, W. An Experimental Setup Combining a Highly Sensitive Detector for Reaction Products with a Mass-Selected Cluster Source and a Low-Temperature STM for Advanced Nanocatalysis. *Eur. Phys. J. D* **2011**, *63*, 241−249.

(41) Zhang, Z.; Zandkarimi, B.; Alexandrova, A. N. Ensembles of Metastable States Govern Heterogeneous Catalysis on Dynamic Interfaces. *Acc. Chem. Res.* **2020**, *53*, 447−458.

(42) Kresse, G.; Furthmüller, J. Efficiency of Ab-Initio Total Energy Calculations for Metals and Semiconductors Using a Plane-Wave Basis Set. *Comput. Mater. Sci.* **1996**, *6*, 15−50.

(43) Blöchl, P. E. Projector Augmented-Wave Method. *Phys. Rev. B* **1994**, *50*, 17953−17979.

(44) Kresse, G.; Joubert, D. From Ultrasoft Pseudopotentials to the Projector Augmented-Wave Method. *Phys. Rev. B: Condens. Matter Mater. Phys.* **1999**, *59*, 1758−1775.

(45) Perdew, J. P.; Burke, K.; Ernzerhof, M. Generalized Gradient Approximation Made Simple. *Phys. Rev. Lett.* **1996**, *77*, 3865−3868.

(46) Pacchioni, G. Modeling Doped and Defective Oxides in Catalysis with Density Functional Theory Methods: Room for Improvements. *J. Chem. Phys.* **2008**, *128*, No. 182505.

(47) Anisimov, V. I.; Zaanen, J.; Andersen, O. K. Band Theory and Mott Insulators: Hubbard U Instead of Stoner I. *Phys. Rev. B* **1991**, *44*, 943−954.

(48) Dudarev, S.; Botton, G.; Savrasov, S. Y.; Humphreys, C. J.; Sutton, A. P. Electron-Energy-Loss Spectra and the Structural Stability of Nickel Oxide: An LSDA+U Study. *Phys. Rev. B: Condens. Matter Mater. Phys.* **1998**, *57*, 1505−1509.

(49) Grimme, S.; Antony, J.; Ehrlich, S.; Krieg, H. A Consistent and Accurate Ab Initio Parametrization of Density Functional Dispersion Correction (DFT-D) for the 94 Elements H-Pu. *J. Chem. Phys.* **2010**, *132*, No. 154104.

(50) Henkelman, G.; Uberuaga, B. P.; Jónsson, H. Climbing Image Nudged Elastic Band Method for Finding Saddle Points and Minimum Energy Paths. *J. Chem. Phys.* **2000**, *113*, 9901−9904.

(51) Zhang, K.; Shaikhutdinov, S.; Freund, H.-J. Does the Surface Structure of Oxide Affect the Strong Metal-Support Interaction with Platinum? Platinum on Fe3O4(001) versus Fe3O4(111). *ChemCatChem* **2015**, *7*, 3725−3730.

(52) Whitman, L. J.; Richter, L. J.; Gurney, B. A.; Villarrubia, J. S.; Ho, W. Co Adsorption Site Occupations on Fe(111) vs Coverage and Temperature: The Kinetics of Adsorption and Reaction. *J. Chem. Phys.* **1989**, *90*, 2050−2062.

(53) Sun, Y. N.; Qin, Z. H.; Lewandowski, M.; Shaikhutdinov, S.; Freund, H. J. CO Adsorption and Dissociation on Iron Oxide Supported Pt Particles. *Surf. Sci.* **2009**, *603*, 3099−3103.

(54) Parkinson, G. S.; Manz, T. A.; Novotný, Z.; Sprunger, P. T.; Kurtz, R. L.; Schmid, M.; Sholl, D. S.; Diebold, U. Antiphase Domain Boundaries at the $Fe_3O_4(001)$ Surface. *Phys. Rev. B: Condens. Matter Mater. Phys.* **2012**, *85*, No. 195450.

(55) Beniya, A.; Higashi, S.; Ohba, N.; Jinnouchi, R.; Hirata, H.; Watanabe, Y. CO Oxidation Activity of Non-Reducible Oxide-Supported Mass-Selected Few-Atom Pt Single-Clusters. *Nat. Commun.* **2020**, *11*, No. 1888.

(56) Hulva, J.; Meier, M.; Bliem, R.; Jakub, Z.; Kraushofer, F.; Schmid, M.; Diebold, U.; Franchini, C.; Parkinson, G. S. Unraveling CO Adsorption on Model Single-Atom Catalysts. *Science* **2021**, *371*, 375−379.

(57) The intensity shown in Figure 1c is normalized to the number of Pt atoms per cluster. Taking the average cluster heights at ≥450 K from our STM measurements (see Section 3.4) into account for a conservative geometrical estimate, we can estimate the number of atoms at the rim and on the surface of the clusters and normalize them to the number of cluster atoms: Pt_5 is a single layer cluster with 5 (normalized 1) rim atoms and 5 (normalized 1) surface atoms (see Figure 4c) and Pt_{19} a bilayer cluster with ∼9 (normalized 0.5) rim and ∼16 (normalized 0.8) surface atoms, respectively. The number of active sites hence scales with the surface and not the rim of the cluster as we see similar activities per cluster atom.

(58) Szabó, A.; Henderson, M. A.; Yates, J. T. Oxidation of CO by Oxygen on a Stepped Platinum Surface: Identification of the Reaction Site. *J. Chem. Phys.* **1992**, *96*, 6191−6202.

(59) Sebetci, A. A Density Functional Study of Bare and Hydrogenated Platinum Clusters. *Chem. Phys.* **2006**, *331*, 9−18.

(60) Xiao, L.; Wang, L. Structures of Platinum Clusters: Planar or Spherical. *J. Phys. Chem. A* **2004**, *108*, 8605−8614.

(61) Yang, S. H.; Drabold, D. A.; Adams, J. B.; Ordejón, P.; Glassford, K. Density Functional Studies of Small Platinum Clusters. *J. Phys.: Condens. Matter* **1997**, *9*, L39−L45.

(62) Heredia, C. L.; Ferraresi-Curotto, V.; López, M. B. Characterization of PtN (N=2−12) Clusters through Global Reactivity Descriptors and Vibrational Spectroscopy, a Theoretical Study. *Comput. Mater. Sci.* **2012**, *53*, 18−24.

(63) Bhattacharyya, K.; Majumder, C. Growth Pattern and Bonding Trends in Ptn (n=2−13) Clusters: Theoretical Investigation Based on First Principle Calculations. *Chem. Phys. Lett.* **2007**, *446*, 374−379.

(64) Grönbeck, H.; Andreoni, W. Gold and Platinum Microclusters and Their Anions: Comparison of Structural and Electronic Properties. *Chem. Phys.* **2000**, *262*, 1−14.

(65) Sebetci, A.; Güvenç, Z. B. Energetics and Structures of Small Clusters: PtN, N = 2-21. *Surf. Sci.* **2003**, *525*, 66−84.

Supporting Information for

Cluster Catalysis with Lattice Oxygen:

Tracing Oxygen Transport from a Magnetite(001)

Support onto Small Pt Clusters

Sebastian Kaiser,[1,2] Farahnaz Maleki,[3] Ke Zhang,[1,2] Wolfgang Harbich,[4] Ueli Heiz,[1,2] Sergio Tosoni,[3] Barbara A. J. Lechner,[1,] Gianfranco Pacchioni,[3] Friedrich Esch[1,2]*

[1] Chair of Physical Chemistry, Department of Chemistry, Technical University of Munich, Lichtenbergstr. 4, 85748 Garching, Germany

[2] Catalysis Research Center, Technical University of Munich, Lichtenbergstr. 4, 85748 Garching, Germany

[3] Dipartimento di Scienza dei Materiali, University of Milano-Bicocca, via Roberto Cozzi 55, 20125 Milano, Italy

[4] Institute of Physics, Ecole Polytechnique Fédérale de Lausanne, CH-1015 Lausanne, Switzerland

* bajlechner@tum.de

S1. Pulsed reactivity data evaluation
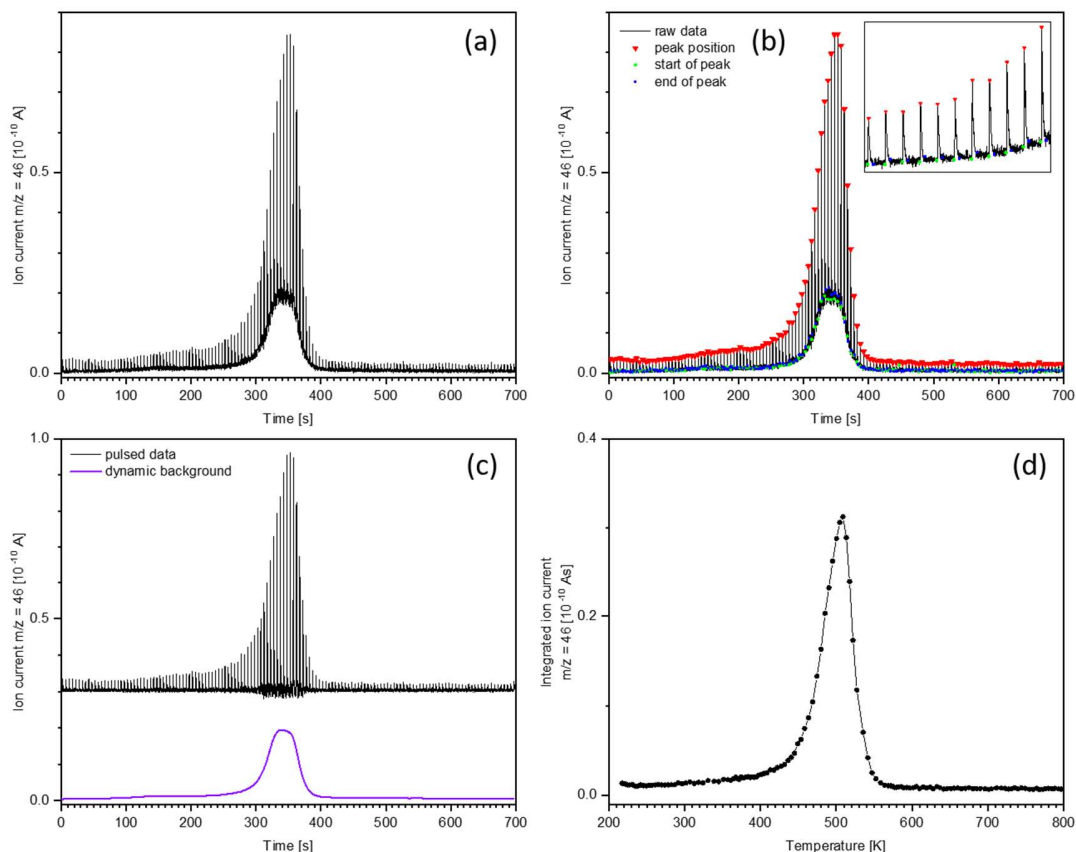
Figure S1. Evaluation procedure for pulsed valve sniffer measurements. (a) displays the measured raw data, consisting of a series of pulses convoluted with a continuous dynamic background (usually caused by desorption or reaction products). As both components contain information about the investigated system, it is necessary to separate them. First, the peak position (red), as well as the start (green) and end (blue) of each peak are detected, as shown in (b). The inset shows a zoomed-in section to better illustrate the method. The data in between the pulses (determined by the start and end points of the pulses) is smoothed and interpolated to determine the dynamic background, which is then subtracted. (c) shows the pulsed data after background subtraction (black, with an offset of 3×10^{-11} A), as well as the subtracted background (purple). Finally, each individual pulse is integrated numerically and the resulting values are plotted vs. temperature, as shown in (d).

S2. Characterization of magnetite bulk and (001) surface by DFT calculations

We started from the experimental crystal structure of Fe_3O_4 using a supercell with a $Fe_{24}O_{32}$ ($(Fe_3O_4)_8$) formula. Fe_3O_4 (magnetite) has the structure of a cubic inverse spinel with Fe^{3+} in the tetrahedral sites and a 50:50 mixture of Fe^{2+} and Fe^{3+} in the octahedral sites.[1] Tetrahedral and octahedral sublattices are anti-ferrimagnetically aligned in Fe_3O_4, such that the magnetic moments of the Fe^{3+} cations on each sublattice cancel each other, and a nominal net magnetization of 4 μ_B per Fe_3O_4 formula unit derives from the Fe^{2+} cations. We first optimized the lattice and internal coordinates with PBE+U+D3. The calculated lattice parameters (Table S1) show a slight distortion from the cubic symmetry. The lattice volume is overestimated by 2%, indicating a reasonable agreement of the hereby adopted computational method with the experiment.

Table S1. Calculated and experimental lattice parameters (a, b and c, Å) and cell volume ($Å^3$) of cubic Fe_3O_4.

	Calc.	Exp.[a]
a	8.451	8.397
b	8.458	8.397
c	8.458	8.397
Cell Volume	604.59	592.1

[a] Data from ref [2]

The calculated electronic structure displays 4 unpaired electrons per formula unit, as reported in experiments (32 unpaired electrons in the unit cell). Figure S2 shows the spin density iso-surface of magnetite. Fe atoms in tetrahedral positions (Fe^{3+}) are spin down while the Fe atoms in octahedral sites are spin up (half Fe^{3+} and half Fe^{2+}), consistent with an anti-ferrimagnetic ordering. In agreement with previous reports adopting a similar level of theory, magnetite is a semimetal, displaying conducting character on one spin channel and a small band gap (≈ 0.5 eV) on the other.
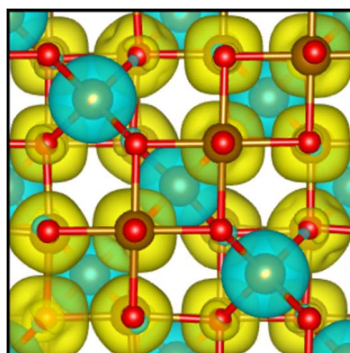
Figure S2. Spin-density iso-surface (0.01 $|e|/Å^3$) of bulk Fe_3O_4, with α (spin-up) electrons density in yellow and β (spin-down) in cyan.

The magnetite(001) surface is modelled following the sub-surface cation vacancy structure proposed by Parkinson.[3] The 1×1 cell's content is $Fe_{35}O_{48}$, where one Fe ion in an octahedral site of the subsurface layer has been removed. The hereby adopted slab model contains 12 atomic layers; the ions from the bottom 4 layers are kept frozen in their bulk lattice position, and all others are relaxed. As previously observed,[1] one Fe atom in the second atomic layer moves during the relaxation from an octahedral to a tetrahedral site, Figure S3. There are thus 13 Fe atoms in tetrahedral and 22 Fe atoms in octahedral positions. The total number of unpaired electrons in the supercell is 40 (3.3 per formula unit, showing a remarkable quenching of the magnetic moment with respect to the bulk).
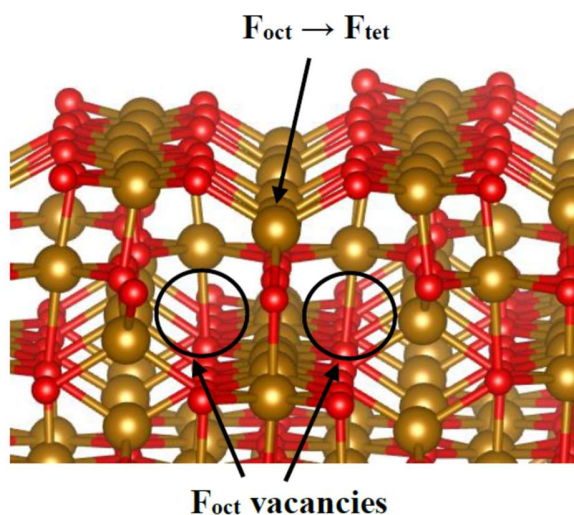
Figure S3. Optimized structure of the subsurface cation vacancy model of Fe_3O_4(001).

S3. Formation of a surface oxygen vacancy on various sites

In this section, we describe the effect of generating an oxygen vacancy on the surface of magnetite. Given the focus of the present paper on the surface properties of magnetite, we did not consider the vacancy formation in the subsurface and bulk regions. As shown in Figure S4, there are three non-equivalent O atoms on the first atomic layer of the $Fe_3O_4(001)$ slab: O1 and O2 are next to an iron atom in a tetrahedral site and O3 is above an iron atom in an octahedral site (Figure S4). The formation energy of an oxygen vacancy (E_f), Table S2, is calculated as follows:

$$E_f = E[Fe_3O_{4-x}] + E[\tfrac{1}{2} O_2] - E[Fe_3O_4] \tag{1}$$

$$E'_f = E[Fe_3O_{4-x}] + E[O] - E[Fe_3O_4] \tag{2}$$

The O3 vacancy has the lowest formation energy of 2.91 eV; the other oxygens are removed at a somewhat higher cost, as shown in Table S2. Notably, the formation of a vacancy in O3 increases the net magnetization per formula unit from 3.4 μ_B (pristine surface) to 3.8 μ_B, while the removal of O1 or O2 species has little effect on the magnetization.

Table S2. Formation energy of an oxygen vacancy (E_f computed with respect to $\tfrac{1}{2} O_2$ and E'_f computed with respect to atomic O, in eV) and magnetic moment per unit cell (M_{total}, μ_B) on the (001) surface of Fe_3O_4, illustrated in Figure S4.

	E_f	E'_f	M_{total}
V_{O1}	3.55	6.93	3.34
V_{O2}	3.10	6.48	3.32
V_{O3}	2.91	6.30	3.79
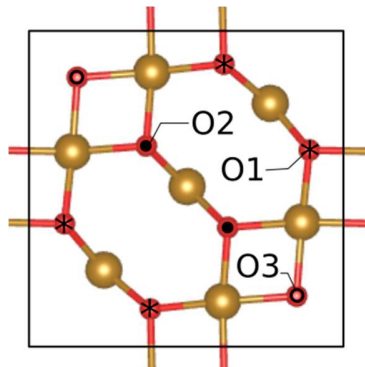
Figure S4. Top view of the first and second atomic layers of the $Fe_3O_4(001)$ unit cell. O1, O2 and O3 indicate the non-equivalent O atoms on the surface of the $Fe_3O_4(001)$ slab.

S4. CO desorption from bare magnetite and magnetite-supported clusters in TPD
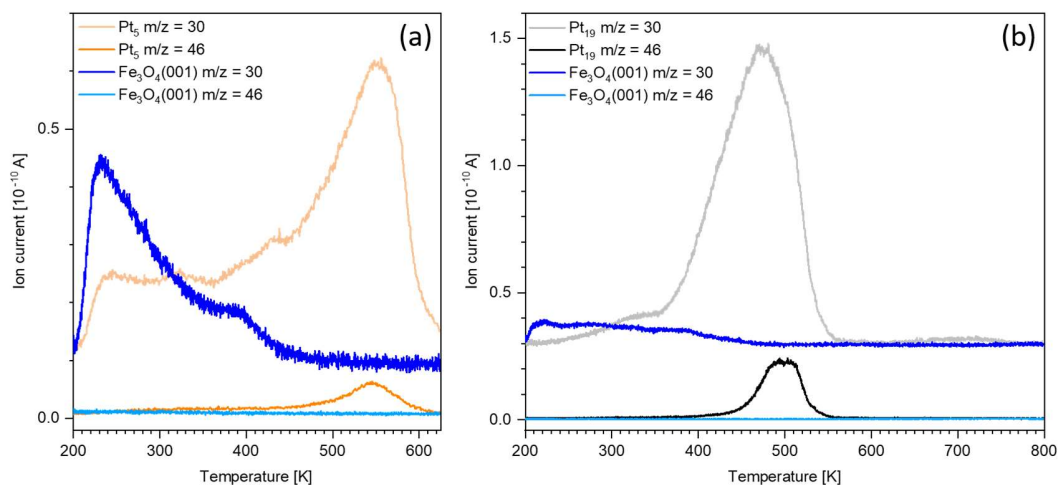
Figure S5. Saturation $C^{18}O$ TPD curves of (a) Pt_5 (orange) and (b) Pt_{19} (gray) supported on $Fe_3O_4(001)$ compared to the corresponding desorption curves from the clean support (blue). The heating rate was 1 K/s. The $C^{18}O$ (m/z = 30) and $C^{18}O^{16}O$ (m/z = 46) signals are shown. The clean magnetite surface exhibits several overlapping, not very distinct CO desorption features in the temperature region investigated here. The desorption starts immediately upon heating and is finished below 450 K. These background desorption features are the high temperature shoulder of a much larger desorption peak located around 180 K, which is attributed to an unidentified magnetite surface defect.[4] It can be observed that especially the beginning of the background CO desorption around 230 K is much less pronounced with clusters deposited on the $Fe_3O_4(001)$ surface, indicating that a part of the defects are no longer accessible CO adsorption sites. This effect can be explained by at least some of the clusters occupying surface defect sites. Furthermore, it is shown that no CO_2 desorption or production from the bare $Fe_3O_4(001)$ surface is detectable in the measured temperature region (cyan).

S5. Ripening of Pt$_5$ in STM
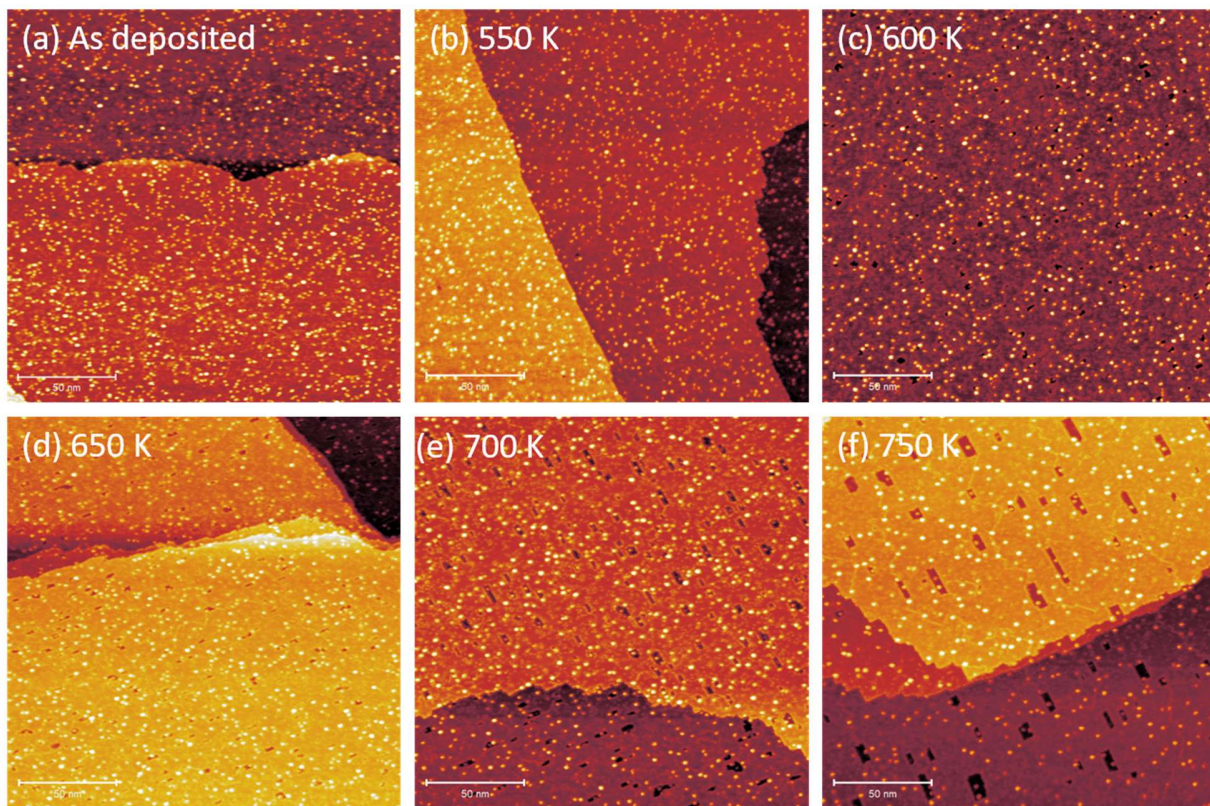
Figure S6. STM image series of Pt$_5$ clusters (0.05 clusters/nm^2) on Fe$_3$O$_4$(001), (a) as deposited at RT, (b-f) measured at RT after annealing to the temperatures indicated, respectively. Up to an annealing temperature of 600 K, the number of clusters stays constant. Above 650 K, gradual cluster ripening is observed, yielding fewer clusters with an average size of about Pt$_{15-20}$ at 750 K. The approximate size is calculated by comparing the apparent height and number of clusters at 750 K with the as-deposited sample. Upon annealing, hole formation in the periphery of some clusters is observed, due to lattice oxygen migrating onto the clusters and reaction with background CO, while the residual, reduced iron atoms diffuse into the bulk. *Imaging parameters: V_b = 1.50 V; I_t = 300 pA.*

S6. Alternating CO and O_2 pulses on $Pt_5/Fe_3O_4(001)$
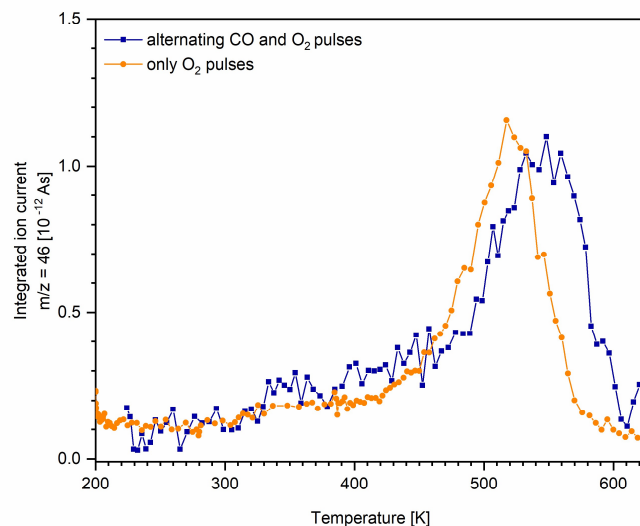
Figure S7. CO_2 production synchronized with O_2 pulses as a function of temperature, obtained by pulsing only O_2 (orange) and alternatingly pulsing CO and O_2 (blue) on CO pre-covered Pt_5 clusters on $Fe_3O_4(001)$. Both curves have been normalized to the number of Pt atoms per cluster. When additionally pulsing CO, the onset of the CO_2 production peak synchronized with O_2 pulses is shifted to higher temperatures, indicating a stronger initial poisoning of the cluster surface by CO since the CO pulses shift the desorption equilibrium. The peak position is similarly shifted from 520 K to 550 K. This indicates a reaction limitation due to a lack of CO when only pulsing O_2.

S7. Loss of CO adsorption capability upon cluster encapsulation
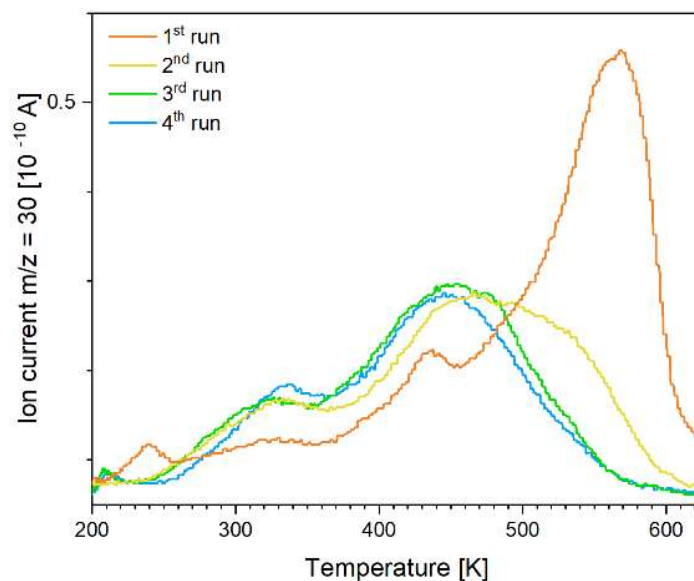
Figure S8. Subsequent saturation $C^{18}O$ TPD curves (m/z = 30) of Pt_5 clusters (0.05 clusters/nm^2) on Fe_3O_4(001), corresponding to the TPD experiments shown in Figure 2. For every run, the surface was saturated with $C^{18}O$ at 200 K, the heating rate was 1 K/s. The main peak in the first run (orange) at 550 K is attributed to the clusters. Several lower temperature features are observed as well, which most certainly are related to surface defects (as described in section 3.1 in the main text). In the second run (yellow) the cluster-related desorption feature decreases significantly, while two broad lower temperature peaks arise at 325 K and 450 K. In the third TPD run (green), the CO desorption from the cluster vanishes almost completely, while the lower temperature peaks become slightly more pronounced. In the fourth run (blue), only the lower temperature peaks occur. This subsequent decrease in CO adsorption capability of the clusters is attributed to encapsulation as a result of SMSI, comparable to Pt nanoparticles supported on Fe_3O_4(001) that become encapsulated by an FeO layer upon annealing.[5] The TPD series indicates that after the first run, the clusters are partially encapsulated, with still a fraction of their surface accessible for CO adsorption. In the following runs, the clusters become completely encapsulated, thus no cluster-related CO desorption is observed anymore. The lower temperature features appear simultaneously with the encapsulation of the clusters and may therefore originate from CO desorption from the encapsulating layer, which is expected to be non-stoichiometric reduced iron oxide, since the lower temperature peaks are well within the temperature range of CO desorption from FeO surfaces.[6] However, more experiments have to be done for further clarification.

S8. Hole formation in cluster periphery
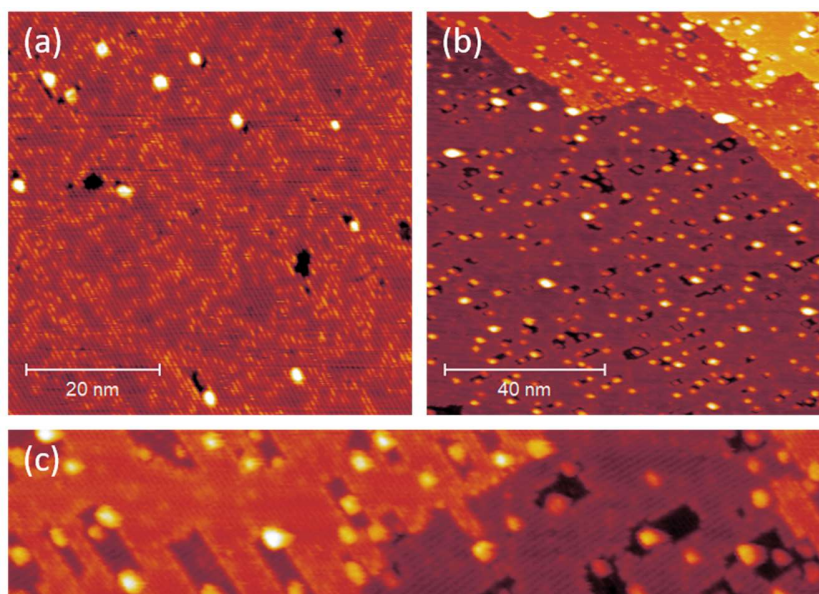
Figure S9. Hole formation around Pt clusters on Fe_3O_4(001). (a) shows Pt_{10} clusters (0.01 clusters/nm^2) measured at 573 K. Clear hole formation in the cluster periphery can be observed caused by the removal of lattice oxygen around the clusters by reverse spillover and reaction with CO from the chamber background, followed by Fe migration into the bulk. (b) and (c) display Pt_{19} (0.05 clusters/nm^2) measured at RT after annealing to 590 K in 1 x 10^{-7} mbar CO for 2 minutes. Again, hole formation around the clusters can be observed, but much more pronounced compared to samples annealed in UHV as a consequence of the higher CO partial pressure. The holes exhibit a rectangular shape which changes direction between two neighboring terraces, following the direction of the atomic rows of the support. This becomes very obvious in the zoomed-in area in (c). The holes are fairly large compared to the clusters, indicating a facile oxygen diffusion towards the clusters at elevated temperatures. The edges of the holes are straight and terminated by an iron row of the magnetite lattice, but more rough perpendicular to them. This indicates that the oxygen diffusion is more favorable along an atomic row, suggesting the initial removal of an oxygen atom from a pristine atomic row to be most difficult. *Imaging parameters: V_b = 1.50 V; (a) I_t = 500 pA, (b, c) I_t = 300 pA.*

S9. Platinum clusters in the gas phase: structure relaxation and oxygen adsorption

The minimum energy structures of gas phase Pt clusters have been studied in previous DFT investigations.[7–13] For instance, the calculations with a B3PW91 hybrid functional show that a Pt_5 cluster with distorted squared pyramid geometry, Figure S10(iii), is the lowest energy isomer.[7] Here, we have considered six of the most stable isomers, and recomputed their stabilities and structures at the PBE+U+D3 level, Figure S10. Four isomers are within an energy of 200 meV, and all six isomers are within 0.35 eV, with energy differences of 70-80 meV, respectively. This suggests a high fluxionality in the gas phase. Of course, once deposited on an oxide support, the structural flexibility of the Pt clusters could be reduced.

(i)	(ii)	(iii)
E = 0.00 eV	E = 0.07 eV	E = 0.15 eV
(iv)	(v)	(vi)
E = 0.20 eV	E = 0.30 eV	E = 0.35 eV
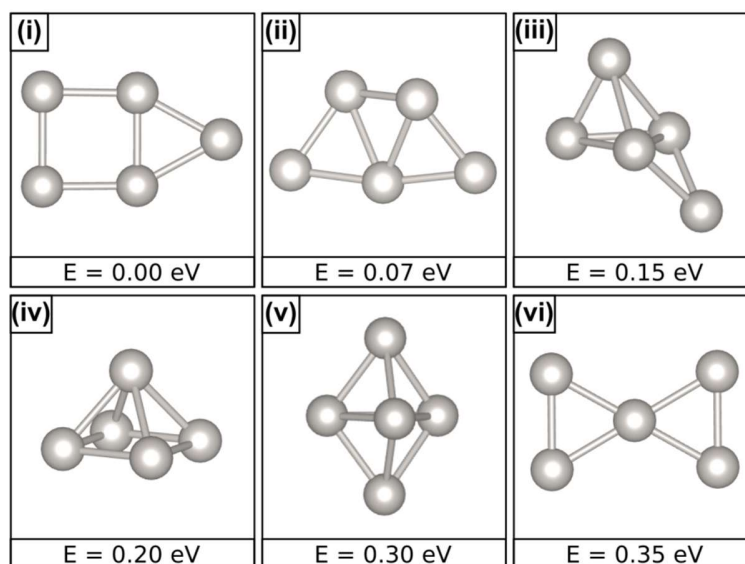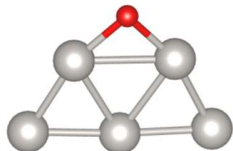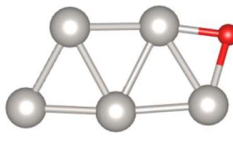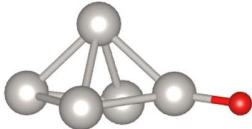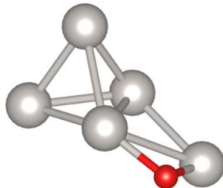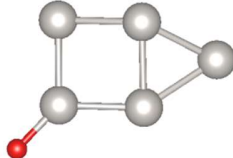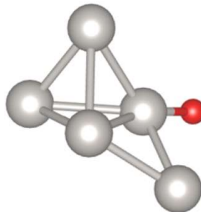
Figure S10. Optimized structures and relative energies of isomers of the Pt_5 gas phase cluster.
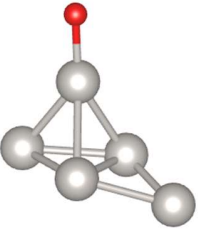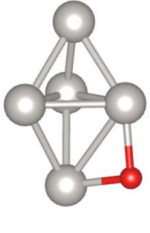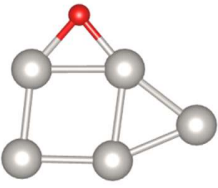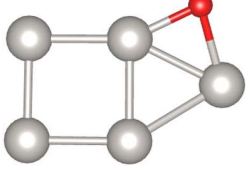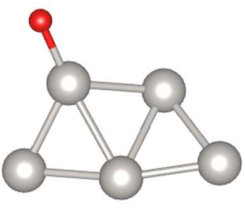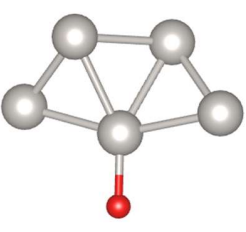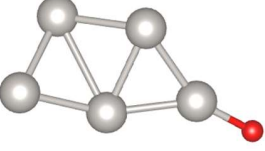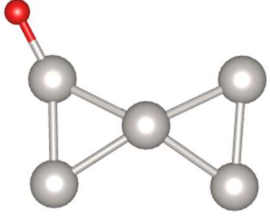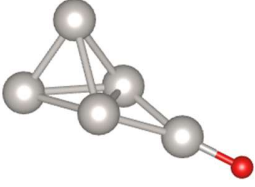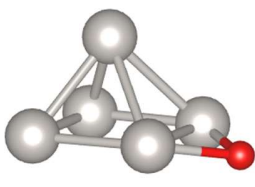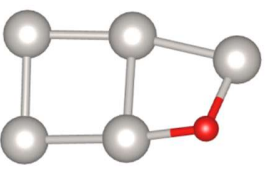
We consider the preferred adsorption sites for a single O atom on the various isomers of gas phase Pt_5. Altogether, we have considered 25 possible structures, and this is not necessarily an exhaustive sample. The adsorption of an O atom on the (i) to (vi) Pt_5 clusters, summarized in Table S3, occurs in three positions: terminal, bridge and hollow. In many cases, the position of the adsorbed O atom and/or the shape of cluster change during optimization. Table S3 reports the optimized structures, their relative energy (E_R), and the adsorption energy (E_{ADS}) of an O atom with respect to the most stable Pt_5 (i) cluster and ½ O_2 molecule, calculated as follows:
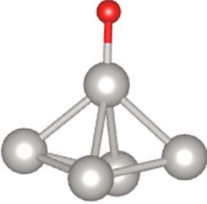
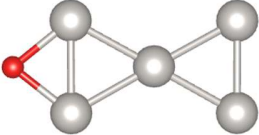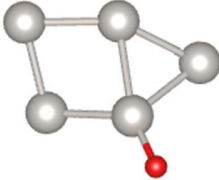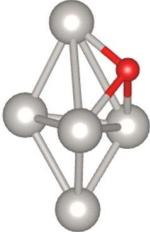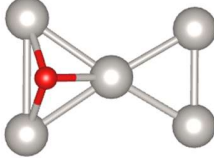$$Pt_5(i) + ½ O_2 \rightarrow O\text{-}Pt_5(n) \qquad \Delta E = E_{ADS} \qquad (3)$$
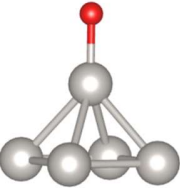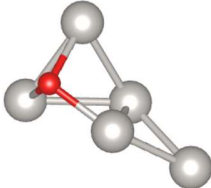
The most stable gas phase Pt_5O cluster is planar, with the Pt atoms forming three fused triangles and the O atom adsorbed in a Pt-Pt bridge position. The next most stable isomer has a completely different structure: it is three-dimensional with the adsorbed O in a terminal position, bound to an apical Pt atom. It is 0.42 eV higher in energy than the ground state structure. Also the next two stable isomers 3 and 4, Table S3, show the presence of O in a terminal position. In general, an O atom binds preferentially in a Pt-Pt bridge site only if the Pt-Pt distance is such to favour its coordination. Cases where the O atom is in a hollow site are clearly higher in energy.

Table S3. Relative energy (E_R, eV) and adsorption energy (E_{ADS}, eV) of an adsorbed O atom on Pt_5 clusters.

Structure		E_R	E_{ADS}	Structure		E_R	E_{ADS}
1		0.00	-2.42	13		0.95	-1.47
2		0.42	-2.00	14		0.98	-1.44
3		0.53	-1.89	15		1.09	-1.33

4		0.63	-1.80	16		1.11	-1.31
5		0.65	-1.78	17		1.16	-1.27
6		0.67	-1.75	18		1.18	-1.24
7		0.67	-1.75	19		1.21	-1.21
8		0.77	-1.65	20		1.26	-1.17
9		0.83	-1.60	21		1.30	-1.12

10		0.83	-1.59	22		2.11	-0.31
11		0.86	-1.56	23		2.12	-0.30
12		0.91	-1.52	24		2.18	-0.24
				25		2.22	-0.20

S10. Adsorption of Pt$_5$ on Fe$_3$O$_4$(001) and formation of oxygen vacancies

Table S4. Adsorption energy (E_{ADS}, eV), Bader charge (q, |e|), and spin polarization of adsorbed Pt$_5$ clusters on Fe$_3$O$_4$ and total spin magnetic moment per unit cell (M_{total}, μ_B).

Figure	E_{ADS}[a]	q(Pt$_5$)	M (Pt$_5$)	M_{total}
4(a)	-4.51	0.33	0.08	2.59
4(b)	-3.01	0.25	1.12	3.17
4(c)	-2.73	0.33	0.19	3.22
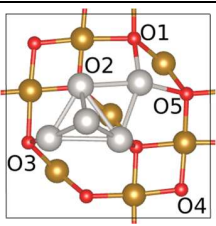
[a] Energy change related to the reaction Pt$_5$(i) + Fe$_3$O$_4 \rightarrow$ Pt$_5$(n)/Fe$_3$O$_4$

The Pt$_5$ adsorption energies, reported in Table S4, are calculated with respect to the clean support and the gas phase cluster in its most stable configuration (capped square, Figure S10(i)).

The formation energy of the oxygen vacancy (E_f), Table S5, has been calculated according to the following equation:

$$E_f = E[(Pt_5/Fe_3O_{4-x})] + E[½\, O_2] - E[(Pt_5/Fe_3O_4)] \qquad (4)$$

Table S5. O vacancy energy (E_f, eV), Bader charge (q, |e|), spin polarization of an adsorbed Pt$_5$ cluster (Figure 4(a)) and total spin magnetic moment per unit cell (M, μ_B). The position of the O atom removed is shown in the Figure.

	E_f	q(Pt$_5$)	M (Pt$_5$)	M_{total}
V_{O1}	3.14	-0.27	0.20	2.61
V_{O2}	1.98	-0.37	0.27	3.24
V_{O3}	2.66	-0.50	0.28	2.49
V_{O4}	2.46	0.24	0.35	3.40

As discussed in the main text, we observe a general decrease in the formation energy in the presence of the platinum clusters with respect to the clean support. The reduction of the substrate upon oxygen removal, however, does not imply a remarkable charge transfer to the cluster, as shown by the Bader charges. In some cases, in particular V_{O1} and V_{O3}, a significant decrease of the net magnetization is reported.

15

S11. Lattice oxygen reverse spillover

(i)   Displacement of one oxygen atom

The study of the formation of an O vacancy on the clean support has shown that O2 is the easiest O to remove, as shown in Table S5. In this section, we consider the energetic cost of displacing the O2 atom from the support and adsorbing it on a Pt_5 cluster. The process corresponds to the final state of a lattice oxygen reverse spillover effect. The O atom has been re-adsorbed on various sites of the supported Pt_5 cluster, always starting from the most stable structure, Figure 4(a) in the main text, corresponding to the Pt_5(iii) gas phase isomer. Other structures have also been considered, some of them being unstable. For instance, O adsorption on one of the triangular facets of Pt_5 always resulted in an O atom bound to a bridge site. The most stable isomers found are shown in Figure S11 in order of stability (see also Table S6).
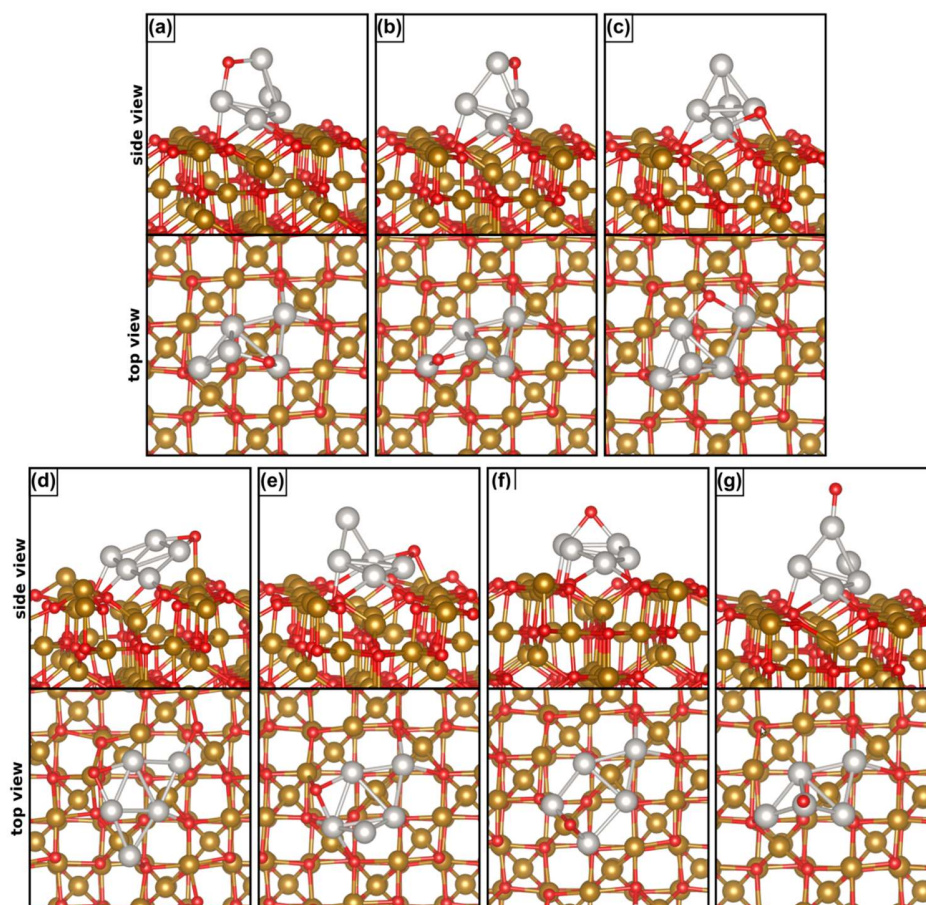
Figure S11. Various isomers of Pt_5O supported on Fe_3O_4. The structures have been obtained starting the geometry optimization from Pt_5/Fe_3O_4, Figure 4(a).

16

The most stable structure is that of a capped rhombus Pt_5 with an O atom adsorbed on one bridge site, shown in Figure S11(a). The corresponding energy is -0.40 eV lower than that of Pt_5/Fe_3O_5 (see Table S6).

Table S6. O reverse spillover energy (E_{SO}, eV), Bader charge (q, |e|), spin polarization of $Pt_5/Fe_3O_4(001)$ and the total spin magnetic moment per unit cell (M_{total}, μ_B).

Figure	E_{SO}[a]	$q(Pt_5)$	$q(O_{spill})$	$M(Pt_5)$	M_{total}
S11 (a)	-0.40	0.25	-0.68	0.03	3.26
S11 (b)	-0.15	0.29	-0.68	0.70	3.32
S11 (c)	-0.04	0.67	-0.86	0.48	3.27
S11 (d)	0.40	0.14	-0.82	0.98	3.80
S11 (e)	0.74	0.27	-0.81	0.08	4.51
S11 (f)	0.86	0.40	-0.72	0.07	3.92
S11 (g)	1.68	0.22	-0.57	0.13	3.46

[a] E_{SO} refers to the energy of this reaction: $Pt_5/Fe_3O_4 \rightarrow O\text{-}Pt_5/Fe_3O_{4\text{-}x}$

This shows that the lattice oxygen reverse spillover in this specific case is an exothermic process. A second isomer, Figure S11(b), is only 0.25 eV higher in energy and differs from the isomer of Figure S11(a) only for the Pt-Pt bond that is bridge-bonded by O. A third interesting structure is shown in Figure S11(c). Here, the O atom is bridging a Pt-Pt bond at the cluster/oxide interface. It can be considered the first step in the migration of an O atom from the support onto the cluster. The isomer shown in Figure S11(c) is -0.04 eV lower in energy than the starting structure, i.e. is thermoneutral with respect to the case where no O vacancy has been formed on the support, and no oxygen has been transferred to Pt_5. Other Pt_5O isomers are shown in Figure S11(d)-(g); they are all higher in energy than the three best structures shown in Figure S11(a)-(c).

(ii)   Displacement of two oxygen atoms
Next, we have considered the spillover of two oxygen atoms from the magnetite surface onto Pt_5. Different O atoms have been removed from the support, and different adsorption positions have been considered on Pt_5O, starting from the most stable structures obtained for the case of a single O reverse spillover, as shown Figure S11. The results are reported in Figure S12 and Table S7.
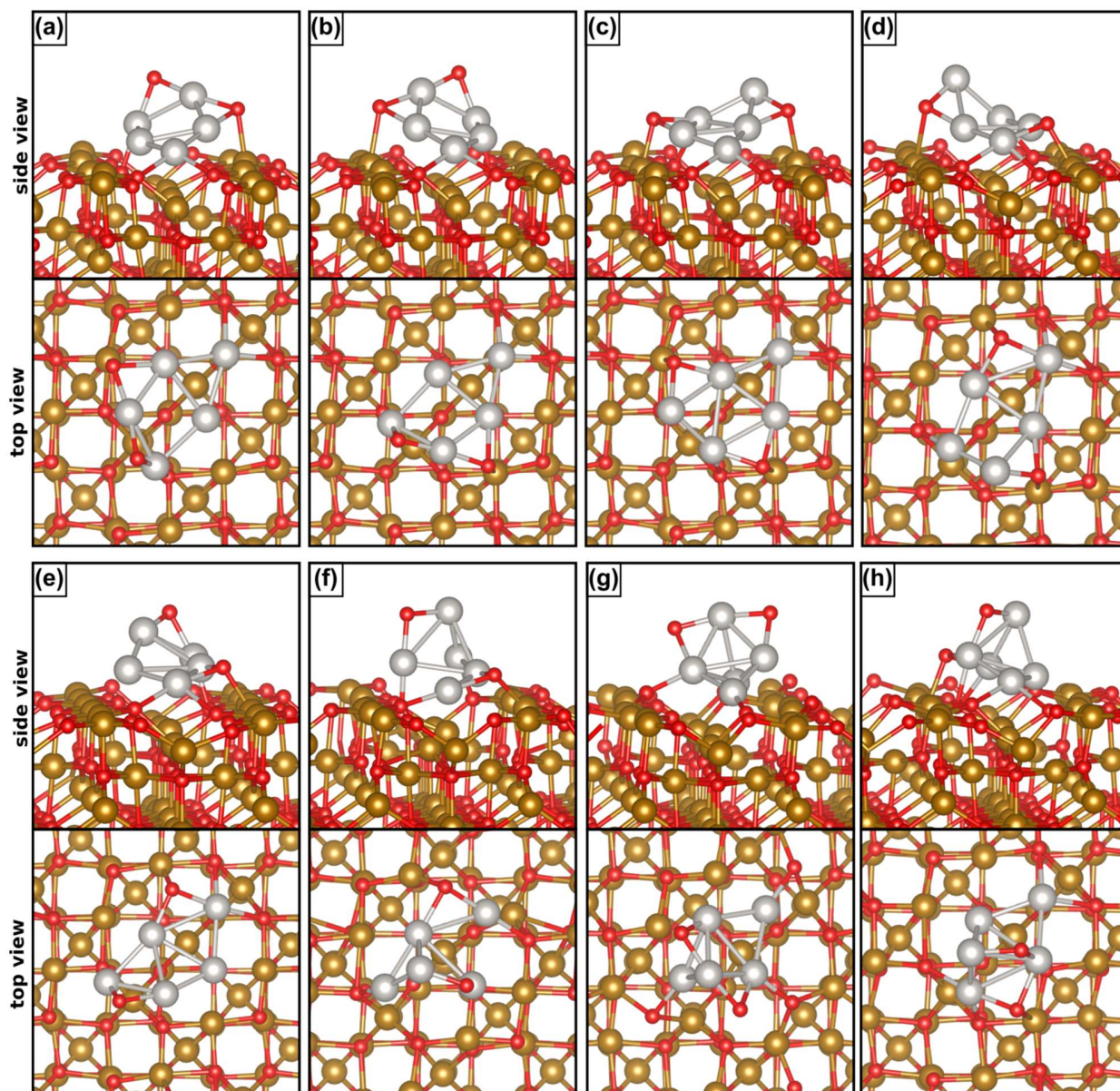
Figure S12. Various isomers of Pt_5O_2 supported on Fe_3O_{4-x}. The structures have been obtained starting the geometry optimization from Pt_5O/Fe_3O_{4-x}, Figure 5(a). (a) to (d) O2 and O4 spillover; (e) O1 and O2 spillover; (g) and (h) O2 and O4 spillover (see Table S5).

We found two isomers, shown in Figure S12(a) and (b) whose structures are *lower* in energy, by -0.64 and by -0.56 eV, Table S7, than the regular, non-defective surface with adsorbed Pt_5. This is an important result which shows that multiple oxygen transfer from the support to a small Pt cluster is thermodynamically favorable, and by a considerable amount. These two structures have been obtained by removing the O2 and O4 atoms of the surface, in the periphery of the Pt_5 cluster, as

shown in Figure 5(b) in the main text. An important observation is that after geometry optimization, the Pt_5O_2 cluster changes its structure and from 3D (Figure S11(a)) it becomes nearly flat, as shown in Figure S12(a) and (b).

Pt_5 structures that maintain the original 3D shape, a capped rhombus (Figures S11(f) and (g)), are slightly below or slightly above the Pt_5/Fe_3O_4 reference, but clearly higher in energy than the nearly 2D ground state structures.

These results show two important trends: (1) multiple lattice oxygen reverse spillover is an energetically favorable process; and (2) the adsorption of two oxygen atoms on Pt_5 leads to a restructuring that tends to flattens the cluster structure. In order to confirm these trends, in the next Section we considered the spillover of three oxygen atoms.

Table S7. Oxygen spillover energy (E_{SO}, eV), Bader charge (q, |e|), spin polarization of $Pt_5/Fe_3O_4(001)$ and the total spin magnetic moment per unit cell (M, μ_B).

	Figure	E_{SO}[a]	q(Pt₅)	q (2O_spill)	M (Pt₅)	M_total
O2, O4	S12 (a)	-0.64	0.37	-1.52	0.21	2.54
	S12 (b)	-0.56	0.48	-1.50	0.15	3.92
	S12 (c)	0.59	0.41	-1.62	0.19	3.96
	S12 (d)	0.83	0.46	-1.61	0.19	3.93
	S12 (e)	0.86	0.49	-1.52	0.56	2.54
O1, O2	S12 (f)	0.30	0.53	-1.58	0.65	3.34
O2, O4	S12 (g)	-0.04	0.73	-1.40	0.35	3.18
	S12 (h)	1.66	1.07	-1.46	0.40	3.99

[a] E_{SO} refers to the process: $Pt_5/Fe_3O_4 \rightarrow 2O\text{-}Pt_5/Fe_3O_{4\text{-}x}$

(iii)   Displacement of three oxygen atoms

We finally considered the case where three oxygen atoms are displaced from the magnetite surface onto the Pt_5 cluster, with formation of a Pt_5O_3 unit and three oxygen vacancies. The number of potential isomers is huge, and we restricted the analysis to the sites where oxygen is easier to remove, O1, O2, and O4 or O1, O2 and O5, and to a few structures derived from the best isomers of Pt_5O_2, as shown in Figure S13 and Table S8. The two most stable structures are shown in Figure S13 (a) and (b) and correspond to a flat or nearly flat Pt_5 with three oxygen atoms in bridge sites; some of them remain at the cluster/support interface and thus coordinated to Fe atoms of the support, providing anchoring points for the nanocluster. These two structures are only 0.17 and 0.23 eV higher in energy, respectively, than the pristine Pt_5/Fe_3O_4, showing that even the transfer

of three oxygen atoms is energetically possible (the reaction is only slightly endothermic). We cannot exclude that some more favorable isomers exist, but this already provides sufficient evidence that multiple oxygen transfer from magnetite to supported Pt clusters is possible.
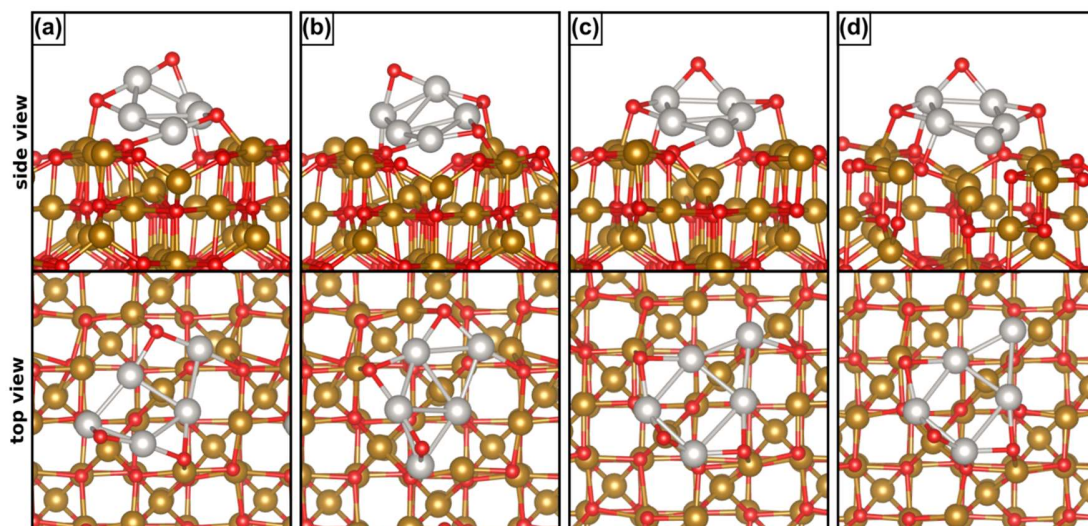

Figure S13. Various isomers of Pt_5O_3 supported on Fe_3O_{4-x}. The structures have been obtained starting the geometry optimization from Pt_5O_2/Fe_3O_{4-x}, (a) to (c) O1, O2 and O4 spillover; (d) O1, O2 and O5 spillover (see Table S5).

Table S8. Three O spillover energy (E_{SO}, eV), Bader charge (q, $|e|$), spin polarization of $Pt_5/Fe_3O_4(001)$ and the total spin magnetic moment per unit cell (M, μ_B).

Figure	E_{SO}[a]	$q(Pt_5)$	$q (3O_{spill})$	$M (Pt_5)$	M_{total}
S13 (a)	0.17	0.85	-2.43	0.31	3.16
S13 (b)	0.23	1.00	-2.48	0.10	4.58
S13 (c)	0.95	0.71	-2.35	0.79	2.57
S13 (d)	3.85	0.93	-2.68	0.11	3.33

[a] E_{SO} refers to the process: $Pt_5/Fe_3O_4 \rightarrow 3O\text{-}Pt_5/Fe_3O_{4-x}$
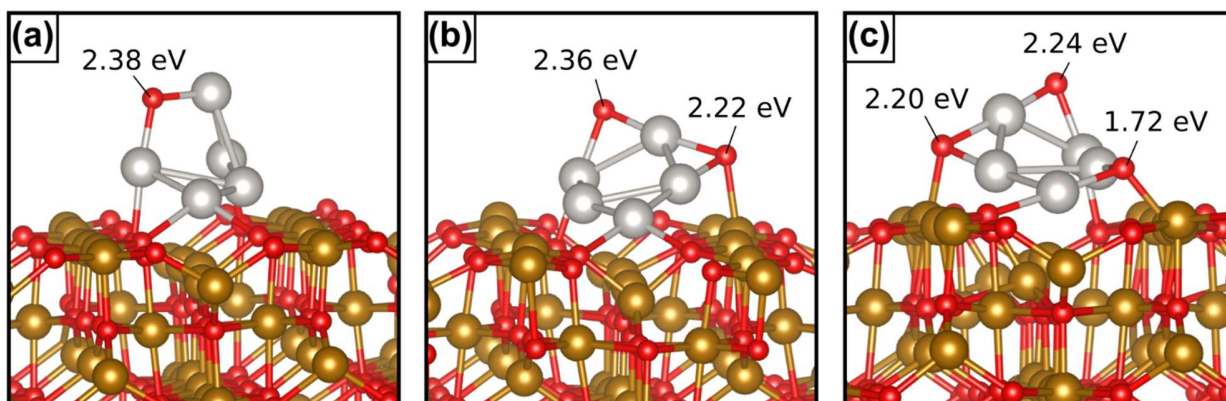
Figure S14. Energy (in eV) required to remove O atoms bound on top of Pt_5 or at the rim, i.e. at the interface between Pt_5 and Fe_3O_{4-x}.

S12. Impact of lattice oxygen reverse spillover on cluster height

In Table S9 we provide some evidence that the lattice oxygen reverse spillover mechanism, with formation of Pt_xO_y clusters, can contribute to a structural change and in particular to a transition from 3D to 2D. For all the structures considered, we have computed the average vertical distance of the Pt atoms from the surface of magnetite. Since the atoms of the surface may be involved in structural changes, we have taken the vertical distance of the Pt atoms from the bottom layer of our slab, whose coordinates are fixed. The most stable Pt_5 cluster, shown in Figure 4 (a) in the main text, is taken as a reference. We define ΔZ as the difference of the average distance of the Pt atoms in the various oxidized clusters (see Figures S11-S13).

The most stable Pt_5O cluster (see Figure S11 (a)), exhibits $\Delta Z = -0.102$ Å; the most stable Pt_5O_2 cluster (see Figure S12 (a)) has $\Delta Z = -0.386$ Å; and the most stable Pt_5O_3 cluster (see Figure S13 (a)) has $\Delta Z = -0.426$ Å. This trend is not fortuitous and is found also for the other most stable Pt_xO_y clusters, as shown in Table S9. The physical reason for this is that some of the O atoms bind at the cluster rim, and interact also with Fe ions on the surface. In order to increase this bonding, the cluster flattens its structure, resulting in a transition from 3D to 2D.

Table S9. Different distances of Pt_5O_x clusters to the magnetite support with respect to Pt_5/Fe_3O_4.

	Figures	Z_{avg}(Å)	ΔZ(Å)
Pt_5/Fe_3O_4	**4 (a)**	**13.734**	**0.000**
	4 (b)	13.908	0.174
	4 (c)	13.424	-0.310
One O spillover	S11 (a)	13.632	-0.102
	S11 (b)	13.662	-0.072
	S11 (c)	13.735	0.001
	S11 (d)	13.478	-0.256
	S11 (e)	13.419	-0.315
	S11 (f)	13.245	-0.489
	S11 (g)	13.631	-0.103
Two O spillover	S12 (a)	13.348	-0.386
	S12 (b)	13.344	-0.390
	S12 (c)	13.408	-0.326

	S12 (d)	13.414	-0.320
	S12 (e)	13.284	-0.450
	S12 (f)	13.547	-0.187
	S12 (g)	13.512	-0.222
	S12 (h)	13.478	-0.256
Three O spillover	S13 (a)	13.308	-0.426
	S13 (b)	13.435	-0.299
	S13 (c)	13.172	-0.562
	S13 (d)	13.312	-0.062

$Z_{avg} = \Sigma \ z(Fe,O) \ bottom \ layer/m - \Sigma \ z(Pt) \ cluster/n$

$\Delta Z = Z_{avg}(Pt_xO_y) - Z_{avg}(Pt_5)$

S13. Iron spillover

There are two kinds of non-equivalent Fe atoms on the first and second atomic layers of the $Fe_3O_4(001)$ slab: Fe atoms in the octahedral and tetrahedral positions, respectively, as shown in Figure S15. The formation energy of a Fe vacancy (E_f), listed in Table S10, is calculated according to the following equations:

$$E_f = E[Fe_{3-x}O_4] + E[Fe\ (s)] - E[Fe_3O_4] \qquad (5)$$

$$E'_f = E[Fe_{3-x}O_4] + E[Fe\ (g)] - E[Fe_3O_4] \qquad (6)$$
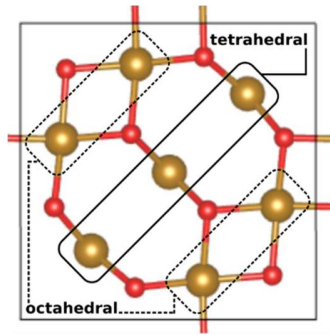
Figure S15. Top view of the first and second atomic layers of the $Fe_3O_4(001)$ unit cell. Fe atoms in octahedral and tetrahedral sites on the surface of an $Fe_3O_4(001)$ slab are marked by dashed and full lines, respectively.

Table S10. Formation energy of an iron vacancy (E_f computed with respect to solid Fe and E'_f, computed with respect to atomic Fe, in eV) and magnetic moment per unit cell (M_{total}, μ_B) on the (001) surface of Fe_3O_4.

	E_f	E'_f	M_{total}
$Fe_{3-x}O_4$ ($V_{Fe\_tetrahedral}$)	6.60	9.35	3.69
$Fe_{3-x}O_4$ ($V_{Fe\_octahedral}$)	6.64	9.39	2.08

Here, we discuss the Fe vacancy formation for the case of the most stable Pt_5/Fe_3O_4 structure (Figure 4(a)). As shown in Figure S16, there are 7 non-equivalent Fe atoms in the first and second atomic layers of the $Fe_3O_4(001)$ slab. We have considered two vacancies in tetrahedral (Fe1 and Fe2 shown in Figure S16) and two vacancies in octahedral (Fe3 and Fe4 shown in Figure S16) positions on the surface of the Pt_5/Fe_3O_4 structure. The optimized structures are shown in Figure S17.

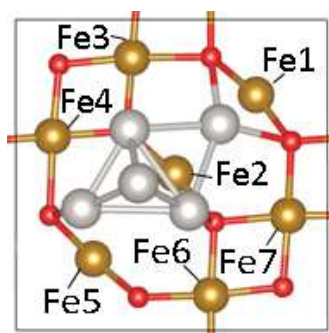**Figure S16.** The non-equivalent Fe atoms in the first and second atomic layers of the Pt_5/Fe_3O_4 structure shown in Figure 4(a).
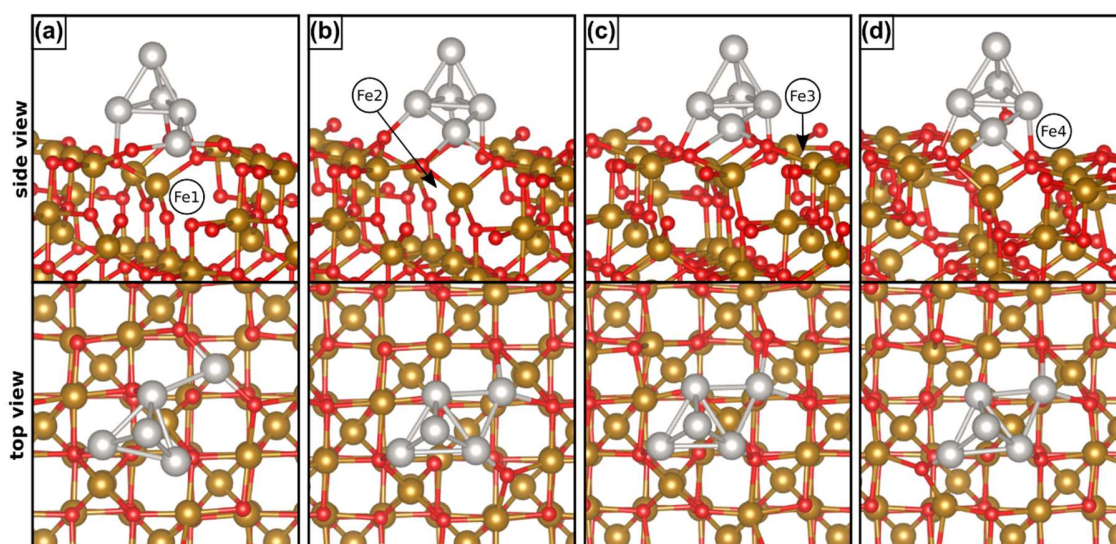

Figure S17. The optimized structures of Fe vacancies in the first layer of the Pt_5/Fe_3O_4 structure shown in Figure 4 (a).

The formation energy of the iron vacancy (E_f), given in Table S11, has been calculated according to the following equation:
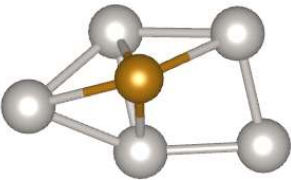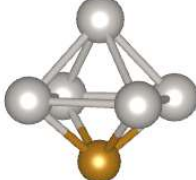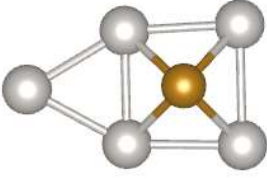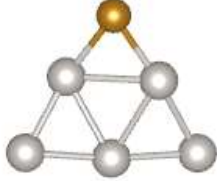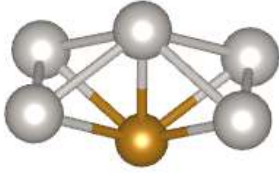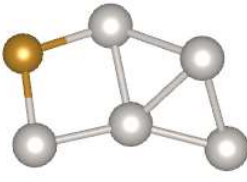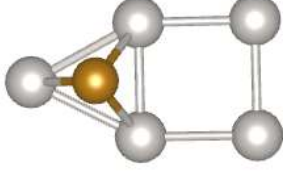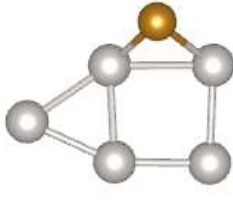
$$E'_f = E[(Pt_5/Fe_{3-x}O)] + E[Fe\ (g)] - E[(Pt_5/Fe_3O_4)] \qquad (7)$$
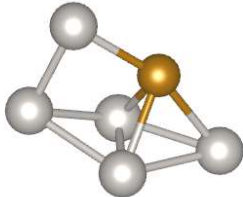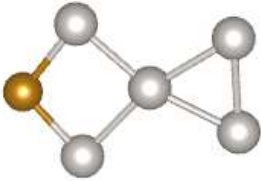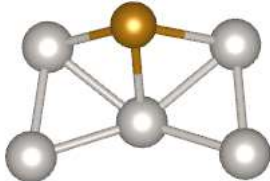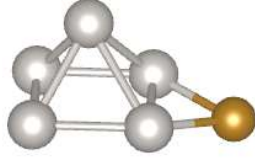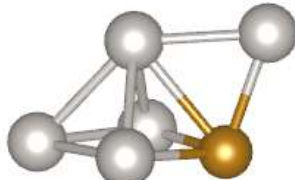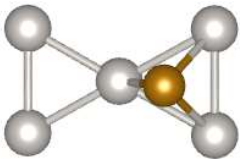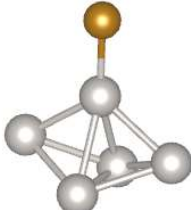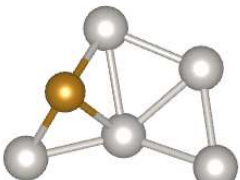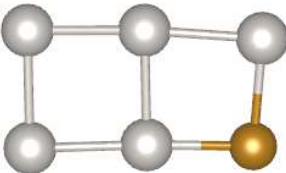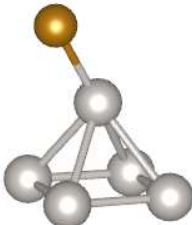
Table S11. Fe vacancy energy (E_f, eV) and total spin magnetic moment per unit cell (M, μ_B).

	Figure	E'_f	M_{total}
V_{Fe1}	S17(a)	6.70	4.84
V_{Fe2}	S17 (b)	6.90	3.64
V_{Fe3}	S17 (c)	7.69	2.52
V_{Fe4}	S17 (d)	6.37	2.87

We then consider the preferred adsorption sites for a single Fe atom on the various isomers of Pt_5 in the gas phase. Altogether, we have considered 20 possible isomers. Table S12 reports the optimized structures and their relative energy (E_R). The binding energy of Fe to Pt_5 in the most stable isomer is -0.99 eV.

Table S12. Relative energy (E_R, eV) of an adsorbed Fe atom on Pt_5 clusters.

Structure		E_R	Structure		E_R
1		0.00	11		0.82
2		0.06	12		0.95
3		0.16	13		1.04
4		0.23	14		1.10

5		0.28		15		1.49
6		0.39		16		1.76
7		0.49		17		2.39
8		0.56		18		2.71
9		0.69		19		2.74
10		0.73		20		2.76

We now consider the energetic cost of displacing the Fe1 (tetrahedral) and Fe4 (octahedral) atoms, indicated in Figure S16, from the support and adsorbing it on the Pt_5 cluster. The Fe atom has been re-adsorbed on various sites of the supported Pt_5 cluster, starting from the most stable structure (Figure 4 (a) in the main text). Figure S18 (a)-(c) and (e)-(f) shows the optimized structures. Based on our results for the Pt_5Fe gas phase isomers (Table S12), the re-adsorption of the Fe atom on the triangular facet of a supported Pt_5(i) cluster, Figure 4 (c), has also been studied. Figure S18 (d) shows the optimized structure.

Figure S18. Various isomers of Pt_5Fe supported on Fe_3O_4.

Table S13. Fe spillover energy (E_{SO}, eV) and its site shown in Figure S16 and total spin magnetic moment per unit cell (M, μ_B).

Figure	Fe site	$E_{SO}^{(a)}$	M_{total}
S18 (a)	Fe1	2.38	4.83
S18 (b)	Fe1	2.53	4.07
S18 (c)	Fe4	2.61	3.23
S18 (d)	Fe4	3.18	1.75
S18 (e)	Fe4	3.38	4.17
S18 (f)	Fe1	4.17	3.57
S18 (g) [b]	Fe4	0.14	3.24

[a] $Pt_5/Fe_3O_4 \rightarrow Fe-Pt_5/Fe_{3-x}O_4$ $\qquad \Delta E = E_{SO}$
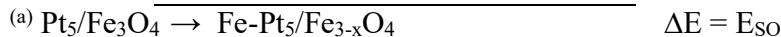
[b] In this case, during the optimization, the Fe atom adsorbed on a triangular facet of Pt_5 moved back to the Fe_3O_4 surface.

In all cases, the Fe spillover implies a remarkable cost (between 2.38 eV and 4.17 eV, depending on the initial and final sites). Case (g) looks like an outlier displaying an almost thermoneutral formation energy, but is in fact a failed attempt, where the Fe ion spontaneously left the Pt_5 cluster and moved back to its lattice site during the relaxation.

Next, we consider the energetic cost of displacing the Fe1 (tetrahedral) or Fe4 (octahedral) atoms (see Figure S16) from the support and adsorbing them on the Pt_5O_3 cluster. The Fe atom has been re-adsorbed on the triangular facet of the supported Pt_5O_3 cluster starting from the most stable structure shown in Figure S13 (a). The results are summarized in Figure S19 and Table S14, indicating a non-favorable process.
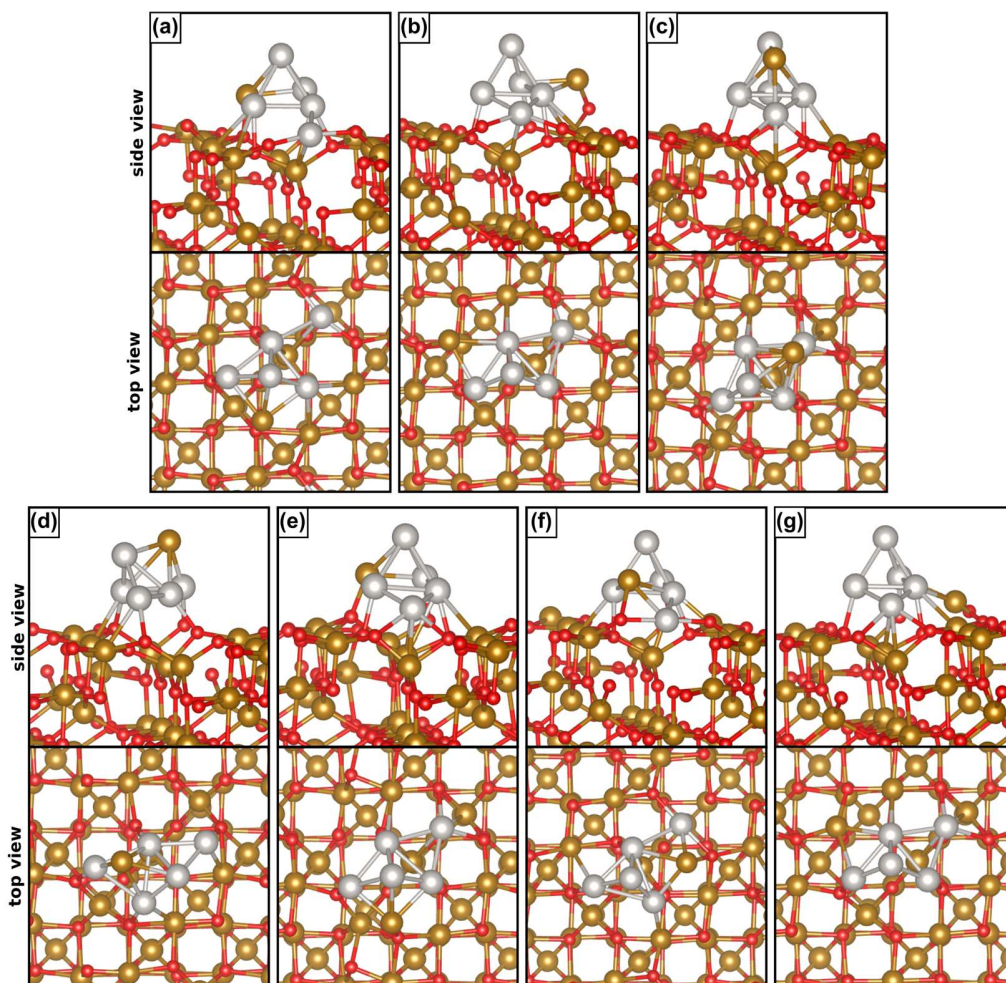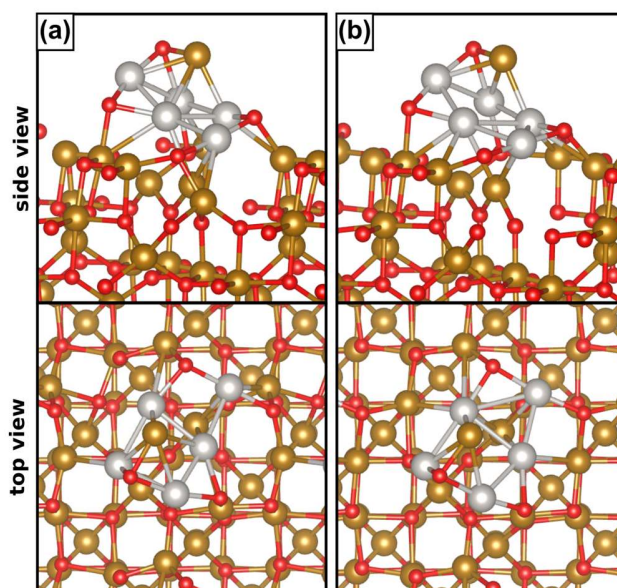
Figure S19. Various isomers of Pt_5O_3Fe supported on Fe_3O_4.

Table S14. Fe spillover energy (E_{SO}, eV) and its site shown in Figure S16 and total spin magnetic moment per unit cell (M, μ_B).

Figure	Fe site	$E_{SO}^{(a)}$	M_{total}
S19 (a)	Fe4	2.18	2.59
S19 (b)	Fe1	3.70	4.12

[a] E_{SO} refers to the process: $Pt_5/Fe_3O_4 \rightarrow Pt_5O_3Fe/Fe_{3-x}O_{4-y}$

References

(1)   Parkinson, G. S. Iron Oxide Surfaces. *Surf. Sci. Rep.* **2016**, *71* (1), 272–365.

(2)   O'Neill, H. S. C.; Dollase, W. A. Crystal Structures and Cation Distributions in Simple Spinels from Powder XRD Structural Refinements: $MgCr_2O_4$, $ZnCr_2O_4$, Fe_3O_4 and the Temperature Dependence of the Cation Distribution in ZnAl2O4. *Phys. Chem. Miner.* **1994**, *20* (8), 541–555.

(3)   Bliem, R.; McDermott, E.; Ferstl, P.; Setvin, M.; Gamba, O.; Pavelec, J.; Schneider, M. A.; Schmid, M.; Diebold, U.; Blaha, P.; Hammer, L.; Parkinson, G. S. Subsurface Cation Vacancy Stabilization of the Magnetite (001) Surface. *Science* **2014**, *346* (6214), 1215–1218.

(4)   Hulva, J.; Jakub, Z.; Novotny, Z.; Johansson, N.; Knudsen, J.; Schnadt, J.; Schmid, M.; Diebold, U.; Parkinson, G. S. Adsorption of CO on the $Fe_3O_4(001)$ Surface. *J. Phys. Chem. B* **2018**, *122* (2), 721–729.

(5)   Zhang, K.; Shaikhutdinov, S.; Freund, H.-J. Does the Surface Structure of Oxide Affect the Strong Metal-Support Interaction with Platinum? Platinum on $Fe_3O_4(001)$ versus $Fe_3O_4(111)$. *ChemCatChem* **2015**, *7* (22), 3725–3730.

(6)   Kelemen, S. R.; Kaldor, A.; Dwyer, D. J. The Adsorption of CO on Clean and Potassium Promoted FeO Surfaces. *Surf. Sci.* **1982**, *121* (1), 45–60.

(7)   Sebetci, A. A Density Functional Study of Bare and Hydrogenated Platinum Clusters. *Chem. Phys.* **2006**, *331* (1), 9–18.

(8)   Xiao, L.; Wang, L. Structures of Platinum Clusters: Planar or Spherical. *J. Phys. Chem. A* **2004**, *108* (41), 8605–8614.

(9)   Yang, S. H.; Drabold, D. A.; Adams, J. B.; Ordejón, P.; Glassford, K. Density Functional Studies of Small Platinum Clusters. *J. Phys. Condens. Matter* **1997**, *9* (5), L39–L45.

(10)   Heredia, C. L.; Ferraresi-Curotto, V.; López, M. B. Characterization of Pt_N (N=2–12) Clusters through Global Reactivity Descriptors and Vibrational Spectroscopy, a Theoretical Study. *Comput. Mater. Sci.* **2012**, *53* (1), 18–24.

(11)   Bhattacharyya, K.; Majumder, C. Growth Pattern and Bonding Trends in Pt_n (n = 2-13) Clusters: Theoretical Investigation Based on First Principle Calculations. *Chem. Phys. Lett.* **2007**, *446* (4–6), 374–379.

(12)   Grönbeck, H.; Andreoni, W. Gold and Platinum Microclusters and Their Anions: Comparison of Structural and Electronic Properties. *Chem. Phys.* **2000**, *262* (1), 1–14.

(13)   Sebetci, A.; Güvenç, Z. B. Energetics and Structures of Small Clusters: Pt_N, N = 2-21. *Surf. Sci.* **2003**, *525* (1–3), 66–84.

3.2 Does Cluster Encapsulation Inhibit Sintering? Stabilization of Size-Selected Pt Clusters on Fe$_3$O$_4$(001) by SMSI

Contributions

Sebastian Kaiser	Planing and conduction of experiments, data analysis and visualization, writing
Johanna Plansky	Participation in experiments, data analysis and visualization
Matthias Krinninger	Participation in experiments, discussions
Andrey Shavorskiy	Experimental support at synchrotron
Suyun Zhu	Experimental support at synchrotron
Ueli Heiz	Funding acquisition, discussions
Friedrich Esch	Supervision, funding acquisition, discussions
Barbara A. J. Lechner	Supervision, funding acquisition, discussions

Size-selected sub-nanometer metal clusters are not only highly material efficient, due to their high percentage of surface atoms, but can also exhibit exceptional, strongly size-dependent catalytic activities, due to other reasons, i.e. electronic or structural effects.[12,51,53] Thus, maintaining a stable dispersion during the course of a chemical reaction is crucial for the sustainable application of cluster-based catalysts under industrial conditions. This prerequisite, however, limits their potential use, since clusters are intrinsically metastable, i.e. they have a strong tendency to sinter,[23,62] especially in reactive atmospheres. Cluster stabilization and size control is therefore the key to industrial cluster catalysis.

One promising approach is based on encapsulation of the clusters due to SMSI, a strategy, which has already been shown to improve the stability of nanoparticles on reducible oxide supports.[132] Although being an established concept for nanoparticles, as discussed in detail in the introduction, it has not been shown conclusively if also highly fluxional clusters without defined crystalline facets can exhibit an encapsulated SMSI state, and whether it can suppress sintering.

This paper investigates Pt_5, Pt_{10} and Pt_{19} clusters on $Fe_3O_4(001)$ at different annealing temperatures and provides evidence for an SMSI related encapsulation that indeed suppresses Ostwald ripening. As shown by STM, all three cluster sizes can be deposited randomly and size-selected at room temperature. For all three sizes, CO TPDs showed a clear, cluster-related desorption feature in the first run, concomitantly with CO_2 formation, due to a reaction of the adsorbed CO with spillover lattice oxygen on the clusters (compare section 3.1). In a subsequent TPD run, this CO_2 production vanished, while the cluster-related CO desorption peak was strongly decreased. This behaviour clearly indicates a loss of CO adsorption capability on the clusters due to encapsulation, especially as new, low temperature desorption features, appearing in the second TPD run, hint towards a defective FeO-like layer forming on the clusters. Complementary high resolution synchrotron XPS measurements of Pt_{19} revealed that indeed an encapsulating layer is formed on the clusters around 523 K, resulting in a Pt 4f signal attenuation, observed in surface sensitive measurements, whereas a lack of attenuation in more bulk sensitive measurements excludes Pt dissolution in the magnetite crystal. Fe 3p measurements showed an enrichment of Fe^{2+} at the surface from 523 K on, confirming the encapsulating layer to have an FeO-like stoichiometry, as already indicated by CO desorption traces. It is difficult to fully elucidate the morphology of this encapsulating layer, and while for larger clusters (Pt_{19}) the results hint towards an actual developed layer, this is hardly imaginable for the smallest clusters, where we instead imagine a conglomerate of Pt, Fe and O to be formed.

To investigate cluster sintering, a sample for each cluster size was annealed stepwise. Between the annealing steps, extensive STM measurements at room temperature give access to a statistical evaluation of several thousand clusters, which reveals details about the size-dependent ripening process. Initially, between 473 and 623 K, a decrease in apparent height was observed for all sizes, in line with clusters restructuring due to lattice oxygen reverse spillover, whereby a further, SMSI-related electronic effect could not be excluded. The two smallest cluster sizes exhibit Smoluchowski ripening, with onset temperatures that depend on the respective size: Sintering sets in at 523 K for Pt_5 and at 623 K for Pt_{10}, as evident from an immediate loss in coverage and increase in apparent cluster height. This shows that cluster diffusion is still possible for small clusters, although being at the verge of encapsulation. Smoluchowski ripening is about to be complete at 773 K, yielding larger, immobile particles that are still in the cluster size regime. The Pt_{19} clusters, however, remain size-selected up to this temperature. From 823 K on, all cluster sizes showed a significant coarsening of the size distribution as a consequence of Ostwald ripening, finally resulting in large, square nanoparticles above 1000 K. Remarkably, Ostwald ripening sets in more than 200 K above the Hüttig temperature of Pt

(608 K),[236] which is considered the maximum onset temperature for Ostwald ripening, indicating a significant stabilization of the clusters by SMSI.

In summary, we have shown that sub-nanometer clusters can indeed become encapsulated as a consequence of SMSI. The encapsulating layer exhibits a defective FeO-like stoichiometry, comparably to Pt nanoparticles on the same surface.[139] The details of the film morphology remain unknown. Small clusters sinter via Smoluchowski ripening, indicating that cluster diffusion on an oxide support is possible even when these clusters are encapsulated. Ostwald ripening only sets in around 800 K, 200 K above the Hüttig temperature, providing evidence that encapsulation is in fact a valid strategy to stabilize clusters against sintering.

Does Cluster Encapsulation Inhibit Sintering? Stabilization of Size-Selected Pt Clusters on Fe₃O₄(001) by SMSI

Sebastian Kaiser,[#] Johanna Plansky,[#] Matthias Krinninger, Andrey Shavorskiy, Suyun Zhu, Ueli Heiz, Friedrich Esch,* and Barbara A. J. Lechner*
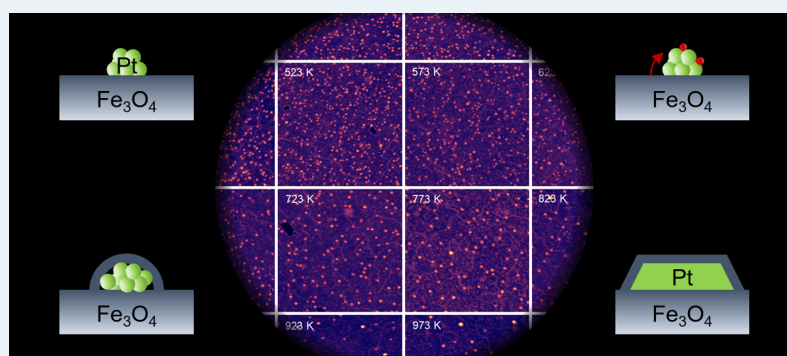
Read Online

ACCESS | 📊 Metrics & More | 📖 Article Recommendations | 🗐 Supporting Information

ABSTRACT: The metastability of supported metal nanoparticles limits their application in heterogeneous catalysis at elevated temperatures due to their tendency to sinter. One strategy to overcome these thermodynamic limits on reducible oxide supports is encapsulation via strong metal−support interaction (SMSI). While annealing-induced encapsulation is a well-explored phenomenon for extended nanoparticles, it is as yet unknown whether the same mechanisms hold for subnanometer clusters, where concomitant sintering and alloying might play a significant role. In this article, we explore the encapsulation and stability of size-selected Pt₅, Pt₁₀, and Pt₁₉ clusters deposited on Fe₃O₄(001). In a multimodal approach using temperature-programmed desorption (TPD), X-ray photoelectron spectroscopy (XPS), and scanning tunneling microscopy (STM), we demonstrate that SMSI indeed leads to the formation of a defective, FeO-like conglomerate encapsulating the clusters. By stepwise annealing up to 1023 K, we observe the succession of encapsulation, cluster coalescence, and Ostwald ripening, resulting in square-shaped crystalline Pt particles, independent of the initial cluster size. The respective sintering onset temperatures scale with the cluster footprint and thus size. Remarkably, while small encapsulated clusters can still diffuse as a whole, atom detachment and thus Ostwald ripening are successfully suppressed up to 823 K, i.e., 200 K above the Hüttig temperature that indicates the thermodynamic stability limit.

KEYWORDS: *size-selected clusters, strong metal−support interaction, sintering, encapsulation, heterogeneous catalysis, scanning tunneling microscopy, temperature-programmed desorption, X-ray photoelectron spectroscopy*

1. INTRODUCTION

To maximize material efficiency and to fully exploit non-scalable electronic effects in very small, subnanometer particles (called clusters) as heterogeneous catalysts, one has to counteract the intrinsic tendency of these metastable particles to sinter. Reducible oxides are both successful in stabilizing clusters and offer the possibility to exploit synergistic particle−support effects to tune catalytic activity and selectivity.[1,2] In terms of stabilization, adequate cluster binding sites at defects prevent cluster diffusion, while dewetting prevents atom diffusion.[3] Additionally, stabilization of particles by overgrowth of thin reducible oxide layers through the strong metal−support interaction (SMSI) effect has recently come into the focus of interest again.[4] The concept, first discussed by Tauster et al.,[5] holds for group VIII metals on reducible oxides and is well-established in ultrahigh vacuum (UHV) where an encapsulation layer, formed by reductive annealing, has been described as a reduced film of self-limiting thickness and defined stoichiometry for large nanoparticles and extended metal islands.[6,7] The stabilization of nanoparticles by SMSI effects has numerous implications in catalysis, ranging from methanol steam reforming,[8,9] over the water−gas shift reaction,[10] to low-temperature CO oxidation,[11] and the

hydrogen oxidation reaction (HOR) under harsh oxidative conditions.[12,13] In terms of selectivity and activity tuning, SMSI has recently been invoked for its impact in CO_2 reduction, where the encapsulation suppresses methane in favor of CO formation in various catalytic systems.[14−16]

In real catalysts, the influence of SMSI can be observed as deactivation or change in selectivity,[1] but it is often challenging to differentiate it from sintering and to attribute it to a specific atomic-scale process, like particle encapsulation, or an electronic effect (for a recent example, see the article by Han et al.).[17] To disentangle the effects of SMSI and sintering, highly defined model systems—ideally with atomically defined particle sizes and controlled support stoichiometry—are required. For example, recent studies have shown that the growth of an encapsulation layer can be strongly dependent on pressure conditions[18] and on steady-state redox dynamics.[19] In this context, many questions still remain, particularly pertaining to the growth dynamics of the film, its permeability to diffusion of small reactants, and the stability of the encapsulated particles. To date, the encapsulation phenomenon by SMSI has only been investigated for nanoparticles, but its extension to the subnanometer scale is still a largely unexplored territory. Specifically, the small cluster footprint strongly facilitates cluster diffusion in the temperature regimes where encapsulation takes place. Atomically resolving microscopy combined with highly sensitive reactivity measurements provides unmatched insights into encapsulation and sintering processes on the atomic scale, allowing us to discern whether the clusters remain size-selected or might even be completely integrated into the substrate. Such dynamic effects are increasingly discussed in the literature in the context of single-atom versus cluster catalysis[20] and potential interchange between the two.[21−23] In our research, we study the cluster encapsulation and concomitant sintering behavior on the atomic scale with sound statistics and across a wide temperature range, with the aim to enable heterogeneous catalysis at stabilized subnanometer particles under harsh conditions.

Clusters have been shown to exhibit various exciting size effects that can be exploited for their catalytic activity, in the extreme case leading to drastic changes in turnover frequencies with the addition or removal of just a single atom to/from the cluster.[24,25] As a consequence, where sintering control is already a key issue in nanoparticle catalysts, it is even more crucial when it comes to stabilizing specific cluster sizes. Two distinct sintering mechanisms have been described, Ostwald and Smoluchowski ripening.[3,26−28] Ostwald ripening is particle coarsening by detachment of single atoms, which diffuse and reattach to other particles.[29] While the maximum onset temperature depends on the particle material and can be estimated by the so-called Hüttig temperature, where atoms start to detach from undercoordinated sites,[30,31] smaller particles (i.e., those with a high curvature) such as clusters exhibit a higher vapor pressure and thus start to sinter much earlier.[32] This curvature dependence generally leads to particles of larger diameter growing at the expense of smaller ones. Smoluchowski ripening, on the other hand, is sintering by migration of entire particles and coalescence with neighboring ones, yielding only multiples of the original cluster size.[33] While Ostwald ripening critically depends on the atom detachment energy, the onset temperature for Smoluchowski ripening is determined by the strength of the particle−support interaction influencing the diffusion energy

barrier, which scales approximately with the cluster footprint, typically resulting in an atom-by-atom size dependence.[34]

To date, various approaches to particle stabilization have been suggested. For subnanometer clusters, it has been shown that size selection alone can kinetically mitigate Ostwald ripening.[35] However, theoretical calculations suggest that sintering can indeed be accelerated in cluster sizes that exhibit a large number of isomers that fluxionally interconvert.[36] Other stabilization methods such as alloying with stabilizing metals[37,38] or increasing the particle distance by use of high-surface-area supports[39] have been shown to successfully prevent particle sintering. Last but not least, particle redispersion strategies have been presented as alternatives for reactivating catalysts.[23] Here, we follow the stabilization approach via SMSI as a pathway that maintains cluster size selection and hence the potential to fully control catalyst activity.

In the present work, we investigate the encapsulation and sintering of size-selected Pt_{5-19} clusters deposited on a magnetite, $Fe_3O_4(001)$, support. Iron oxides are abundant materials that exhibit a rich redox chemistry,[40] and magnetite in particular is magnetic, reducible, and conductive. It crystallizes in an inverse spinel structure, whereby the O^{2-} anions form an fcc lattice with Fe^{2+} occupying octahedral sites and Fe^{3+} tetrahedral and octahedral sites in a 1:1 ratio.[41−43] The $Fe_3O_4(001)$ surface reconstructs into the subsurface cation vacancy (SCV) reconstruction, yielding a ($\sqrt{2} \times \sqrt{2}$)R45° structure with only Fe^{3+} occupying the uppermost layers.[44] This reconstruction can be observed as parallel, undulating rows in scanning tunneling microscopy (STM), which are rotated by 90° between two adjacent atomic terraces. The (001) surface exhibits a variety of different defects,[45−48] which can participate in its surface chemistry as adsorption and dissociation sites for molecules.[49−52] Moreover, we have recently shown that lattice oxygen from the magnetite support can readily participate in catalytic reactions by migrating onto Pt clusters, which we termed lattice oxygen reverse spillover.[53] Here, we use temperature-programmed desorption (TPD), high-resolution synchrotron X-ray photoelectron spectroscopy (XPS), and STM measurements to show the formation of an encapsulating SMSI layer even on these small clusters, investigate its redox state and morphology, and clarify the sintering mechanism for Pt_5, Pt_{10}, and Pt_{19} clusters, where we pinpoint the cluster size-dependent onset of Smoluchowski ripening and subsequently that of Ostwald ripening.

2. EXPERIMENTAL METHODS

Natural $Fe_3O_4(001)$ crystals (SurfaceNet GmbH) were prepared by a series of cleaning cycles, each consisting of Ar^+-ion bombardment (20 min, 4×10^{-5} mbar Ar, 1 keV, 5.0 μA sputter current) and subsequent annealing in an oxygen atmosphere (20 min, 5×10^{-7} mbar O_2, 983 K). The reproducibility of the preparation procedure and the cleanliness and stoichiometry of the crystals were checked regularly by STM and XPS. Size-selected Pt clusters were generated using a laser ablation cluster source.[54] Here, the second harmonic of a Nd:YAG laser is used to evaporate Pt from a rotating target, yielding a plasma, which is subsequently cooled in the adiabatic expansion of a He pulse (Westfalen AG, grade 6.0), resulting in a broad distribution of clusters. A series of electrostatic lenses guides the clusters toward a 90° bender for charge selection, followed by a quadrupole mass filter for

size selection. Finally, the clusters are deposited onto the substrate under soft landing conditions (kinetic energy <1 eV/atom). For all experiments, cluster deposition was carried out at room temperature. A cluster coverage of 0.05 clusters/nm^2 was deposited.

The TPD and STM measurements were performed under UHV conditions, with a system base pressure of $<1 \times 10^{-10}$ mbar. Temperature control is performed with the same sample holder for all experiments, using a pyrolytic boron nitride heater located directly below the sample and a type K thermocouple in direct contact with the sample, with an absolute estimated accuracy of ± 5 K. All TPD experiments were carried out using the sniffer, a mass spectrometer-based (Pfeiffer Vacuum GmbH, QMA 200 Prisma Plus) reactivity measurement device, designed for high sensitivity measurements of low-coverage cluster samples.[55] To maximize the signal and ensure a low signal-to-noise ratio, all TPD-related samples have been saturated with $C^{18}O$ (Eurisotop, 96.1%) already during cluster deposition.

The STM measurements were performed in constant current mode with a commercial Scienta Omicron VT-AFM instrument, using homemade etched W tips. To disentangle time and temperature effects, we systematically annealed the sample for 10 min in 50 K steps before measuring the resulting cluster distribution at room temperature. The STM images were processed with Gwyddion using the plane subtraction and row-by-row alignment tools for background correction.[56] The height distribution of the particles was determined using a home-written Igor routine, by detecting the particles via an intensity threshold, drawing a profile through the cluster maximum, and determining the height of the cluster with respect to the median background of the image. For higher statistical significance, the cluster heights of ten 100×100 nm^2 STM images were used, recorded both in the center and at the edge of the sample for each annealing temperature. A minority of clusters which were located at step edges, at the edge of the image, or in small holes were excluded from the height analysis but included in the coverage determination. In images with more than one terrace, a separate evaluation was carried out for each terrace.

High-resolution XPS measurements were performed at the APXPS endstation of the HIPPIE beamline,[57] MAX IV laboratory in Lund, Sweden, which is equipped with a Scienta Omicron HiPP-3 electron energy analyzer. A homebuilt UHV suitcase with a base pressure of $\sim 1 \times 10^{-10}$ mbar was used for sample transfer after cluster deposition in our laboratories in Munich to the beamline in Lund, ensuring clean, intact and still size-selected cluster samples. To desorb any adsorbates accumulated during the several-day-long transport in the UHV suitcase (presumably mainly CO and traces of hydrocarbons), we started the experiment by heating the sample to 373 K to desorb the adsorbates. This resulted in a shift of 0.6 eV to lower binding energies, corresponding to CO desorption,[58,59] and a reduction of the peak width for the Pt 4f signal, and no clear shift in the Fe 3p (compare Figure S1). For heating, an infrared laser directly illuminating the back of the sample was used. The temperature was measured with a type K thermocouple mounted to the side of the crystal. Below, we indicate the temperatures as measured, which could be somewhat underestimated due to limited heat transfer. The XP spectra were acquired in UHV with photon energies of 307 and 921 eV and a constant pass energy and emission angle (normal emission). Initial checks showed no significant beam

damage, thus we recorded all spectra at the same spot on the sample (i.e., with the same cluster coverage) to allow quantitative comparison of the spectra. In data evaluation using KolXPD,[60] the binding energies were calibrated with respect to the Fermi edge and all spectra normalized to their low-binding-energy background. A Shirley background was subtracted from the spectra before quantitative analysis.

3. RESULTS AND DISCUSSION

3.1. Encapsulation of Subnanometer Clusters Induced by Strong Metal−Support Interaction.

To investigate whether and how SMSI influences cluster sintering dynamics, we first need to establish that encapsulation of clusters actually occurs. In our recent work on lattice oxygen reverse spillover on $Pt/Fe_3O_4(001)$, we have already found first indications for cluster encapsulation in our TPD experiments, namely, the loss of CO adsorption sites and thus CO_2 formation capability upon heating beyond a certain temperature threshold.[53] We now investigate this phenomenon in more detail on the example of Pt_{19}, by TPD and high-resolution XPS, focusing on the exact growth conditions, redox state, and morphology of the encapsulating layer, starting with the CO TPD from our previous work (compare Figure 1, first run).
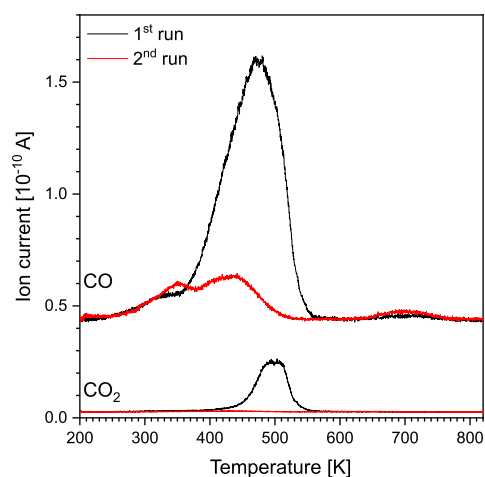

Figure 1. Two subsequent CO TPD spectra of Pt_{19} clusters supported on $Fe_3O_4(001)$ recorded after exposing the sample to a saturating amount of $C^{18}O$ at 200 K ($\sim$10 L) before each run. The $C^{18}O$ ($m/z = 30$, top, offset for clarity) and $C^{18}O^{16}O$ ($m/z = 46$, bottom) traces are shown. The heating rate was 1 K/s. A clear loss of the main desorption feature in the second run can be observed for both traces, with new, lower temperature features appearing in the CO trace, which hint at the presence of FeO defect sites. Furthermore, the CO_2 production is completely suppressed in the second run.

The main CO desorption feature in the first run (black), with a peak at 475 K, arises from desorption from the clusters, as it is not observed on the clean magnetite surface (see Figure S2).[50,53] The rather weak, broad feature around 700 K, in contrast, belongs to recombinative desorption of CO from reduced Fe sites such as Fe adatoms.[46,61] In the second TPD run (red), the main CO desorption peak has vanished completely and instead two new, overlapping and less intense desorption features with maxima at 350 and 430 K emerge. Indeed, the new CO desorption features appearing in the second TPD are comparable to literature spectra from oxygen
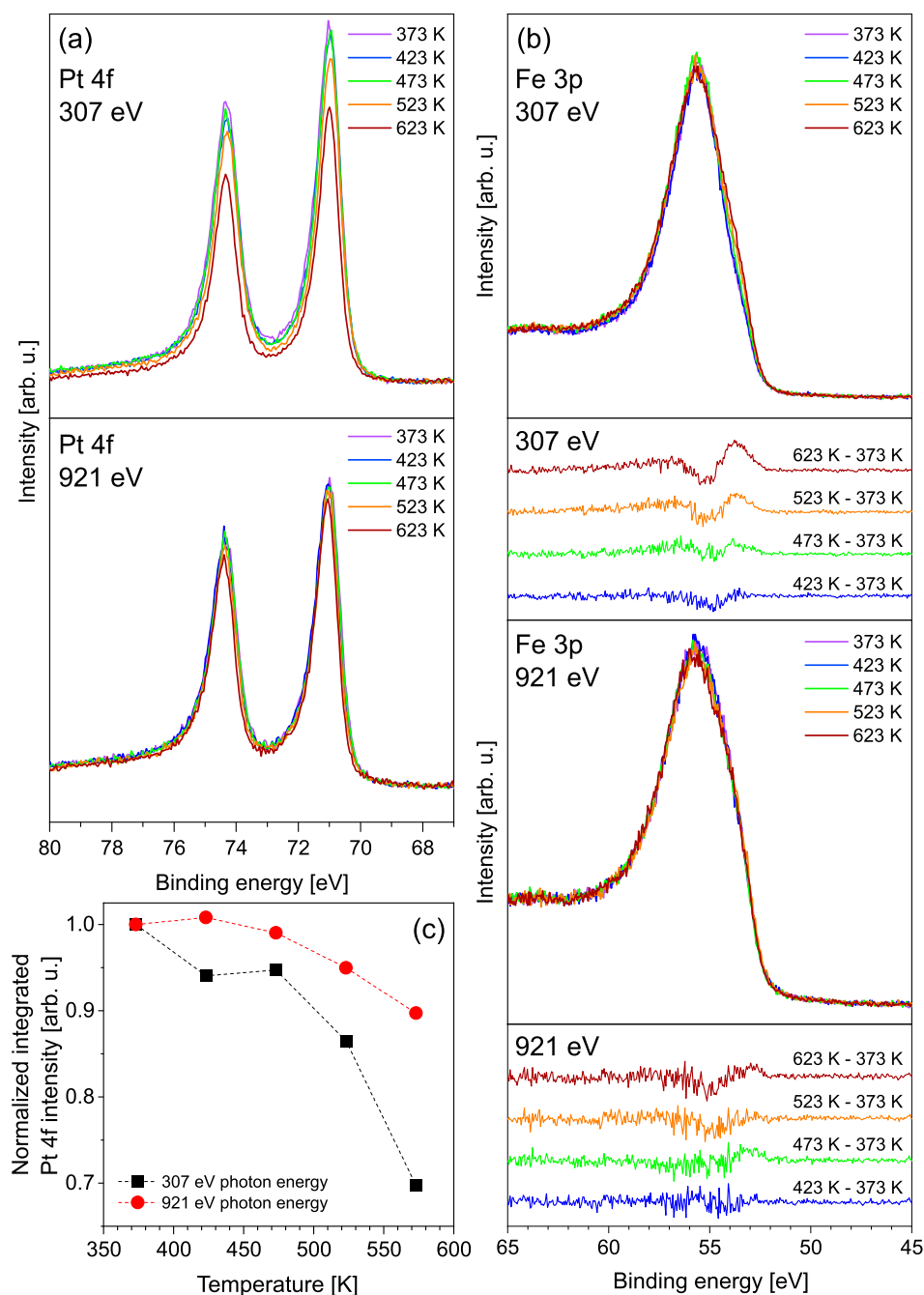
Figure 2. XP spectra of $Pt_{19}/Fe_3O_4(001)$ (0.05 clusters/nm^2) measured at 307 eV (highly surface-sensitive) and 921 eV photon energy (more bulk-sensitive), at the indicated temperatures in UHV. (a) Pt 4f spectra and (b) Fe 3p spectra with corresponding difference spectra for each photon energy below. (c) Evolution of the Pt 4f integrals for each photon energy, scaled to the first spectrum, respectively.

vacancy defect sites on FeO films.[62] Additionally, the desorption peak at 700 K has increased significantly in intensity compared to the first TPD run, again hinting at a more reduced surface which is in perfect agreement with an SMSI encapsulation state similar to that described for Pt nanoparticles on different magnetite facets.[7,63] Control measurements via STM showed that these TPD runs are ramped quickly enough that sintering is still avoided.[53]

Concurrently with the CO desorption, CO_2 formation is observed as a broad feature in the first TPD run, originating from catalytic CO oxidation with lattice oxygen,[53] which is completely lost in the second run. When dosing the same

quantity of clusters on top of the already heated sample, the same signal reappears in the first run after redeposition and disappears again in a second run (see Figure S2). Importantly, the resulting FeO defect-related peak intensity scales with Pt cluster coverage, indicating the formation of reduced iron oxide in the vicinity of the clusters. Since magnetite is known to maintain its surface stoichiometry upon surface reduction by cation diffusion into the bulk,[64−66] those reduced FeO species must be located *on* the clusters, rather than around them, which is direct evidence for an SMSI effect. Note that due to the small cluster size, a stoichiometric, crystalline encapsulating layer, as observed for nanoparticles, is unlikely. The adsorption

sites at the cluster surface are more likely blocked by a conglomerate of iron and oxygen atoms of unknown structure and stoichiometry that is hardly distinguishable from a Pt–FeO alloy.

To further confirm the encapsulation, we subsequently softly sputtered an encapsulated cluster sample, whereby indeed the encapsulating layer could be partially removed (restoring some of the original CO adsorption sites) and lost again during another TPD (see Figure S3). This particular encapsulation state is thus reproducibly obtained during a heating ramp to 820 K.

To sum up, the TPD experiments strongly indicate that the clusters get encapsulated by iron oxide upon annealing as a consequence of SMSI, whereby the desorption feature assignment indicates iron cations in a reduced state. We find that the loss in CO adsorption sites and hence cluster encapsulation also holds true for Pt_5 and Pt_{10} (see Figure S4).

To confirm the presence of reduced FeO and the encapsulation of Pt clusters, we performed high-resolution synchrotron XPS measurements on $Pt_{19}/Fe_3O_4(001)$, shown in Figure 2. We start by evaluating the attenuation of the Pt 4f signal induced by the encapsulating layer, comparing highly surface- and more bulk-sensitive measurements, recorded at 307 and 921 eV photon energy, respectively. Figure 2a displays the Pt 4f region measured at the indicated temperatures between 373 and 623 K. The binding energy remains unchanged, but upon increasing the temperature, a significant decrease in intensity is observed starting around 523 K in the surface-sensitive spectra (top panel), whereas the more bulk-sensitive spectra change much less significantly (bottom panel). This effect is quantified in Figure 2c, where the XP spectra from Figure 2a are integrated and for each photon energy normalized to the corresponding 373 K spectrum. Evidently, the Pt 4f signal decrease is more pronounced for the surface-sensitive measurement, as expected for an SMSI-induced encapsulation of clusters, thus confirming our interpretation of the TPD experiments and ruling out evaporation of Pt into the gas phase. A dissolution or diffusion of the clusters into the bulk, on the other hand, can be excluded by the only slightly decreasing Pt 4f signal in the more bulk-sensitive measurement at 921 eV photon energy, as well as by the STM measurements (discussed below), which is consistent with previous reports in the literature where neither Pt atoms nor clusters can be incorporated in bulk magnetite.[20,65,67] This experiment already gives insights into the morphology of the encapsulating layer. Although alloying cannot be excluded entirely, the reduction of the signal intensity indicates an additional layer on top of the clusters, which is also in line with the sputtering experiment described above. Modeling the attenuation by an FeO encapsulating layer, a nominal average thickness of about 2.2 Å can be calculated,[46,68–71] comparable to the 2.5 Å for a bilayer in bulk FeO.[72] These findings agree well with those reported for larger Pt nanoparticles on $Fe_3O_4(111)$, where the encapsulating layer has been identified as an FeO bilayer under UHV conditions.[73]

Figure 2b shows the Fe 3p XPS region measured at the indicated temperatures. In the main peak, no significant change is observed for either photon energy, suggesting that the support overall remains unchanged upon heating. Cluster-related changes in the Fe 3p signal are expected to be minimal due to the low coverage. Indeed, we observe the development of a small low-binding-energy shoulder in the Fe 3p region measured with 307 eV photon energy, in the same temperature

range in which the decrease of the Pt 4f signal occurs. Fitting these peaks is not trivial,[74,75] and minimal changes can be overlooked easily. We instead use the difference spectra to interpret the data, as shown in Figure 2b for both photon energies. Here, in the more surface-sensitive spectra the shoulder is apparent as a peak around 53.8 eV that increases in intensity when the temperature is increased beyond ∼500 K. We assign this peak to Fe^{2+}.[74] At the same time, the signal corresponding to Fe^{3+}, at around 55.2 eV, decreases in intensity.[74] For the more bulk-sensitive measurement at 921 eV photon energy, the observed changes are in principle the same, but the intensity differences are significantly lower. Note that these transformations occur well below the known phase transition temperature of magnetite (001) around 720 K.[64] Thus, a slight increase in the Fe^{2+} content on the surface can be deduced, which we assign to the encapsulating SMSI layer, since all major changes in the Fe 3p signal develop around the same temperature where the highest decrease in the Pt 4f signal is observed. In agreement with our interpretation of the TPD experiments, the encapsulating layer on subnanometer clusters thus consists of reduced iron oxides, presumably FeO-like, similar to that around larger nanoparticles. The appearance of the encapsulating Fe^{2+} species is not necessarily a direct transformation of surface-Fe^{3+} species, but rather an extraction of interstitials to form the encapsulation layer. Indeed, DFT calculations showed that surface-Fe^{3+} extraction and subsequent adsorption on a Pt cluster is rather energy intensive.[53]

Summarizing, our TPD and XPS experiments confirm for the first time that encapsulation induced by SMSI indeed occurs also for subnanometer clusters and not only for extended nanoparticles and islands. We could identify the encapsulating layer as reduced defect-rich iron oxide, which covers the clusters.

3.2. Cluster-Size-Dependent Sintering Mechanisms.
Having established encapsulation of Pt clusters, we now proceed to investigating how cluster sintering occurs under the SMSI conditions identified above. In particular, we investigate which ripening mechanisms occur, whether the cluster size plays a role, and what the sintered particles look like. Pt_5, Pt_{10}, and Pt_{19} clusters on $Fe_3O_4(001)$ were deposited with similar cluster coverages at room temperature and subsequently annealed to increasingly higher temperatures in 50 K steps. Figure 3 shows representative STM images at the temperatures where the most significant changes occur (for a complete set of images see Figures S5–S7), while a detailed height profile analysis of 10 images at each temperature and cluster size is given in Figure 4 (the complete set of height histograms is shown in Figures S8–S10). The clusters appear as bright protrusions in STM images, while the atomic-scale contrast and defects of the magnetite surface are also visible with a lower corrugation. Even though STM cannot distinguish individual atoms within the cluster, we can exclude the presence of single-atom species like those reported previously.[67] We investigate four main temperature ranges in turn below, which we will relate to as-deposited size-selected clusters, lattice oxygen reverse spillover and encapsulation, cluster diffusion (Smoluchowski ripening), and Ostwald ripening.

As evidenced by the STM images in Figure 3a–c and corresponding height profiles in Figure 4, the as-deposited clusters are indeed size-selected, intact, and randomly distributed on the surface. To give a reference for cluster
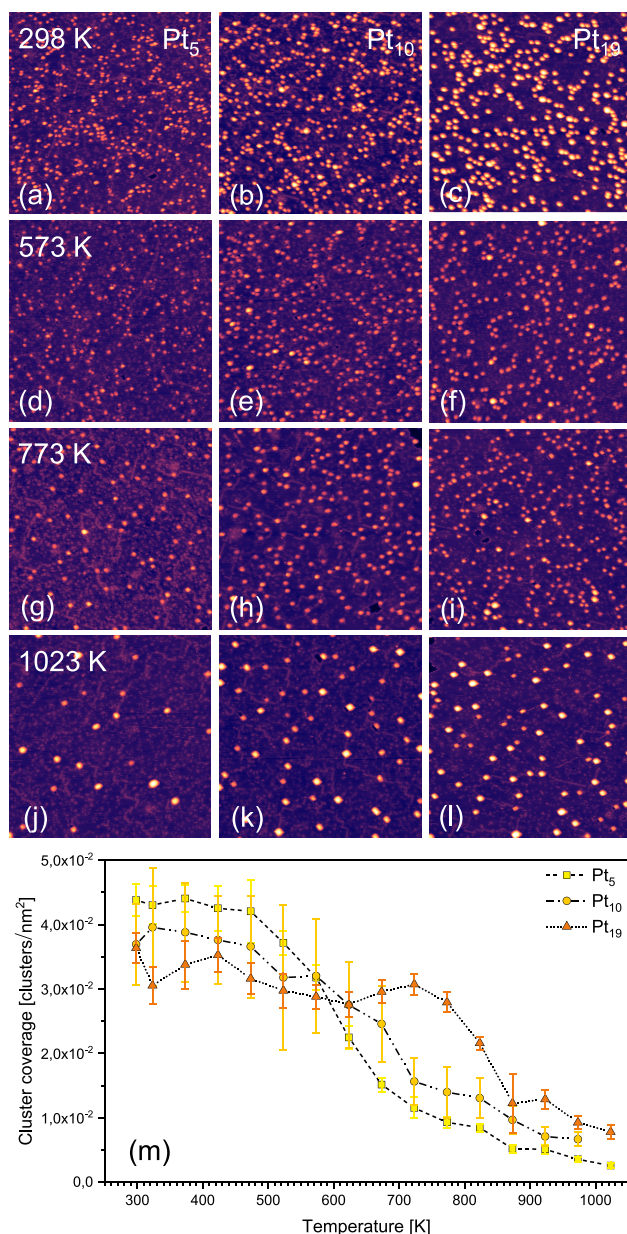
Figure 3. STM images of Pt_5 (left), Pt_{10} (center), and Pt_{19} (right column) clusters on $Fe_3O_4(001)$ (~0.05 clusters/nm²) are shown (a–c) as-deposited, after annealing for 10 min each to (d–f) 573 K, (g–i) 773 K, and (j–l) 1023 K. For height comparison, all images use the same color scale. Imaging conditions: 1.5 V, 300 pA, 100 × 100 nm², and RT. (m) Cluster coverage as a function of temperature, extracted from ten 100 × 100 nm² images for each condition and cluster size, leading to an initial number of ~5000 clusters contributing to the evaluation.

cluster heights within each cluster size distribution are due to structural isomers and various adsorption sites on the surface.

When annealing up to 423 K, no significant changes are observed in the coverage nor height profiles for all three cluster sizes. In the temperature window from 473 to 573 K (see the Supporting Information), a decrease in apparent height is observed for all cluster sizes, which reaches a minimum after annealing to 623 K, yielding approximately single-layer Pt_5 and Pt_{10} clusters and Pt_{19} between one and two layers. Note that the cluster coverage initially remains unchanged but begins to drop for Pt_5 and Pt_{10} due to cluster-diffusion-induced sintering at cluster-footprint-dependent onset temperatures, as seen in Figures 3m and S8–S10. As we described previously, the initial height decrease of the clusters results from lattice oxygen reverse spillover.[53] Furthermore, as shown above, the clusters become encapsulated by the reduced FeO layer in the same temperature range where a semiconductor-like conductivity has been described for encapsulated Pt nanoparticles on $TiO_2(110)$.[6] Such a change in the electronic nature of the particle can additionally affect the imaging and therefore also contribute to the observed decrease in apparent height.

For Pt_5 and Pt_{10} clusters, the apparent cluster height increases again upon further annealing to 773 K, coinciding with a pronounced decrease in coverage due to sintering. With each temperature step, the coverage decreases further, until 773 K, where the curve flattens again. At the same time, the coverage and height distribution for Pt_{19} clusters remains unchanged, i.e., the clusters are still size-selected. Notably, for all three initial cluster sizes, the height distributions now have a similar width predominantly between one and 2.5 layers. The sinter resistance of the larger Pt_{19} combined with the similar resulting height distributions for all three initial sizes is clear evidence for Smoluchowski ripening, i.e., sintering by cluster diffusion. The diffusion barrier for clusters scales with their footprint and thus their interaction with the support.[34] Our data indicates that all Pt_{19} isomers have a footprint large enough to be stabilized against diffusion in this temperature regime, which is why the sintering process of the smaller clusters naturally terminates when all clusters reach this size range. Therefore, already the coalescence of two Pt_{10} or four Pt_5 clusters is sufficient to immobilize the resulting particles which makes the formation of larger nanoparticles statistically unlikely. Consequently, a narrow size distribution without much larger particles at this point is expected even after sintering, which is exactly what is observed in Figures 3g–i and 4. As the coverage curve in Figure 3m demonstrates, the Pt_5 clusters begin to sinter at 523 K, i.e., 100 K before Pt_{10}, another strong indication for footprint dependence. Remarkably, we thus observe that even encapsulated clusters can still diffuse across the surface, substantiating our hypothesis that an Fe–O agglomerate covers the clusters rather than a stoichiometric, rigid film.

By further increasing the temperature to 823 K, the situation changes. For all three investigated cluster samples, of which only the Pt_{19} clusters were still size-selected up to 773 K, a peak at lower heights of about one atomic layer grows in Figure 4, indicating a relatively larger proportion of smaller clusters. When annealing further to 873 K, this peak dominates the spectrum. Additionally, weak peaks at three and four atomic layers start to appear, implying the formation of larger particles. This observation of diverging cluster sizes is typical for Ostwald ripening, where larger particles grow at the expense of smaller ones that exhibit a higher vapor pressure.[32]

layering, we can use the height distributions and compare them with the bulk Pt(111) step height of about 2.26 Å,[76] while keeping in mind that clusters typically have non-fcc structures and their apparent heights are influenced by electronic effects. The as-deposited Pt_5 clusters exhibit a height distribution with a single clear peak between one and two atomic layers. In contrast, the distribution for Pt_{10} clusters has a double peak around two and 2.5 layers and Pt_{19} clearly displays at least three separate heights, with a most common apparent height between three and four atomic layers. The different apparent

Figure 4. Histograms showing height distributions of Pt_5, Pt_{10}, and Pt_{19} clusters on $Fe_3O_4(001)$ for different selected annealing temperatures. Absolute cluster numbers are indicated on the *y*-scale. For each temperature and cluster size, an area of 100 000 nm^2 was analyzed (corresponding to the same data used in Figure 3m). To guide the eye, we added red dotted lines in bulk Pt(111) step increments.

Further increasing the temperature to 1023 K, the now strongly sintered particles are mainly two to four atomic layers in height, with a small number being one or five layers high. At the same time, the coverage has decreased yet again for each initial cluster size. The particles formed at this final temperature adopt a square shape aligned with the cubic symmetry of the underlying support (Figure 3 and details enlarged in Figure S11) and have sharp apparent heights which can be clearly assigned to atomic layers, comparable to the results observed for atomic Pt deposition and sintering on the same support.[63] We enter a size regime where we start to have a clear crystalline-like layering while the internal atom arrangement and thus the overall particle shape are still dominated by the support registry. From the resulting particle coverage and size distribution, and taking into account the initially deposited amount of Pt, we roughly estimate that most particles contain between 50 and 150 atoms.

We have thus shown that both Smoluchowski and Ostwald ripening occur for size-selected Pt clusters on $Fe_3O_4(001)$, whereby the mechanism strongly depends on the cluster size. Smaller clusters sinter via coalescence up to a size where the increasing diffusion barrier starts to be larger than that for atom detachment and Ostwald ripening dominates. Experimentally, it is impossible in this system to investigate sintering of the bare clusters since encapsulation occurs in a similar temperature window. Theoretical calculations for a comparable system, namely, Pd clusters on $CeO_2(111)$ indicate a similar effect.[34] There, Smoluchowski ripening is only possible for Pd_4 or smaller, whereas larger clusters sinter via Ostwald ripening.

As mentioned in Section 1, sintering of clusters via Ostwald ripening invariably begins at the empirical Hüttig temperature at the latest,[3,37] which is related to the melting point of the respective particle material and has been reported to be 608 K for Pt.[30] The actual onset temperature depends on the interaction with the support that influences the atom detachment energy. For unselected Pt clusters on Si_3N_4 films, for example, it has been shown that cluster sintering already sets in at 453 K.[35] In contrast, we observe Ostwald ripening of Pt on $Fe_3O_4(001)$ starting at a temperature of 823 K, which is roughly 200 K *above* the Hüttig temperature, indicating a strong stabilization against sintering beyond the thermodynamic limit. With the strong experimental evidence

for an encapsulating SMSI layer described above, we conclude that the clusters are stabilized by encapsulation. While the encapsulating layer clearly mitigates Ostwald ripening, the smallest clusters can still diffuse even when covered with an FeO-like conglomerate, leading to Smoluchowski ripening. The observation of moving encapsulated particles is in contrast to the recent literature, where an SMSI layer stabilizes Pt nanoparticles on titania against migration.[19]

4. CONCLUSIONS

In the present work, we have investigated the stability of small size-selected Pt clusters deposited on $Fe_3O_4(001)$ to elucidate the strong metal−support interaction (SMSI) for catalytically active particles in the nonscalable size regime. Combined XPS and TPD experiments give clear evidence for the occurrence of encapsulation of subnanometer clusters. While the cluster surface is no longer accessible for CO adsorption, increased desorption from reduced iron oxide species points toward the formation of a defective FeO-like species encapsulating the clusters. Indeed, we observe the formation of a cluster-related Fe^{2+} species, concomitant to an attenuation of the Pt 4f signal.

For a precise analysis of the cluster stability, we performed STM studies of Pt_5, Pt_{10}, and Pt_{19}, starting from comparable cluster coverages and annealing stepwise to 1023 K. The evolution of cluster coverage and apparent height indicates successive cluster coalescence (Smoluchowski) and Ostwald ripening regimes, with a transition temperature that strongly depends on the cluster footprint and thus on the initial cluster size. The final particle distribution appears to be independent from the initial cluster size and overall deposited Pt atom coverage, and shows square particle shapes with well-defined layer heights.

Remarkably, both sintering mechanisms are observed despite the encapsulation. That being said, Ostwald ripening sets in at an unexpectedly high temperature of 823 K, i.e.,200 K above the Hüttig temperature. We therefore conclude that the encapsulating layer strongly stabilizes the clusters against atom detachment while still initially allowing diffusion of the smallest clusters. As one might expect for particles close to the atomic limit of the size regime, all our observations point to an encapsulating layer that is rather a conglomerate of Fe and O atoms surrounding the clusters than a stoichiometric, rigid iron oxide layer. It remains to be shown how the encapsulating layer changes in composition and morphology while clusters diffuse and coalesce, decay, and grow. With our experimental approach, we provide a new route to investigating model catalysts on the atomic scale to pave the way toward controlled use of SMSI for highly selective and sinter-resistant cluster catalysts in real heterogeneous catalysis.

ASSOCIATED CONTENT

Ⓢ Supporting Information

The Supporting Information is available free of charge at https://pubs.acs.org/doi/10.1021/acscatal.3c00448.

> XP spectra including as-deposited measurements and desorption of adsorbates (S1); additional Pt_{19} deposition on already encapsulated $Pt_{19}/Fe_3O_4(001)$ (S2); partial removal of SMSI-induced layer by soft sputtering (S3); subsequent CO TPDs for Pt_5 and Pt_{10} clusters on $Fe_3O_4(001)$ (S4); representative STM images for all annealing temperatures for Pt_5, Pt_{10}, and Pt_{19} clusters on $Fe_3O_4(001)$ (S5); cluster height distributions for all

annealing temperatures for Pt_5, Pt_{10}, and Pt_{19} clusters on $Fe_3O_4(001)$ (S6); and sintered Pt nanoparticles on $Fe_3O_4(001)$ (S7) (PDF)

AUTHOR INFORMATION

Corresponding Authors

Friedrich Esch − *Chair of Physical Chemistry and Catalysis Research Center, Department of Chemistry, School of Natural Sciences, Technical University of Munich, 85748 Garching, Germany;* ⓞ orcid.org/0000-0001-7793-3341; Email: friedrich.esch@tum.de

Barbara A. J. Lechner − *Functional Nanomaterials Group and Catalysis Research Center, Department of Chemistry, School of Natural Sciences, Technical University of Munich, 85748 Garching, Germany; Institute for Advanced Study, Technical University of Munich, 85748 Garching, Germany;* ⓞ orcid.org/0000-0001-9974-1738; Email: bajlechner@tum.de

Authors

Sebastian Kaiser − *Chair of Physical Chemistry and Catalysis Research Center, Department of Chemistry, School of Natural Sciences, Technical University of Munich, 85748 Garching, Germany;* ⓞ orcid.org/0000-0001-8474-6261

Johanna Plansky − *Functional Nanomaterials Group and Catalysis Research Center, Department of Chemistry, School of Natural Sciences, Technical University of Munich, 85748 Garching, Germany;* ⓞ orcid.org/0000-0001-5065-5871

Matthias Krinninger − *Functional Nanomaterials Group and Catalysis Research Center, Department of Chemistry, School of Natural Sciences, Technical University of Munich, 85748 Garching, Germany*

Andrey Shavorskiy − *MAX IV Laboratory, Lund University, Lund 221 00, Sweden;* ⓞ orcid.org/0000-0002-7517-5089

Suyun Zhu − *MAX IV Laboratory, Lund University, Lund 221 00, Sweden*

Ueli Heiz − *Chair of Physical Chemistry and Catalysis Research Center, Department of Chemistry, School of Natural Sciences, Technical University of Munich, 85748 Garching, Germany;* ⓞ orcid.org/0000-0002-9403-1486

Complete contact information is available at:
https://pubs.acs.org/10.1021/acscatal.3c00448

Author Contributions

#S.K. and J.P. contributed equally.

Notes

The authors declare no competing financial interest.

■ REFERENCES

(1) Pu, T.; Zhang, W.; Zhu, M. Engineering Heterogeneous Catalysis with Strong Metal−Support Interactions: Characterization, Theory and Manipulation. *Angew. Chem., Int. Ed.* **2023**, *62*, No. e202212278.

(2) Shi, X. Y.; Zhang, W.; Zhang, C.; Zheng, W. T.; Chen, H.; Qi, J. G. Real-space observation of strong metal-support interaction: State-of-the-art and what's the next. *J. Microsc.* **2016**, *262*, 203−215.

(3) Fukamori, Y.; König, M.; Yoon, B.; Wang, B.; Esch, F.; Heiz, U.; Landman, U. Fundamental Insight into the Substrate-Dependent Ripening of Monodisperse Clusters. *ChemCatChem* **2013**, *5*, 3330−3341.

(4) Kim, J.; Choi, H.; Kim, D.; Park, J. Y. Operando Surface Studies on Metal-Oxide Interfaces of Bimetal and Mixed Catalysts. *ACS Catal.* **2021**, *11*, 8645−8677.

(5) Tauster, S. J. Strong Metal-Support Interactions. *Acc. Chem. Res.* **1987**, *20*, 389−394.

(6) Dulub, O.; Hebenstreit, W.; Diebold, U. Imaging Cluster Surfaces with Atomic Resolution: The Strong Metal-Support Interaction State of Pt Supported on $TiO_2(110)$. *Phys. Rev. Lett.* **2000**, *84*, 3646−3649.

(7) Qin, Z. H.; Lewandowski, M.; Sun, Y. N.; Shaikhutdinov, S.; Freund, H. J. Encapsulation of Pt Nanoparticles as a Result of Strong Metal-Support Interaction with $Fe_3O_4(111)$. *J. Phys. Chem. C* **2008**, *112*, 10209−10213.

(8) Lunkenbein, T.; Schumann, J.; Behrens, M.; Schlögl, R.; Willinger, M. G. Formation of a ZnO Overlayer in Industrial Cu/ZnO/Al_2O_3 Catalysts Induced by Strong Metal-Support Interactions. *Angew. Chem.* **2015**, *127*, 4627−4631.

(9) Luo, Z.; Zhao, G.; Pan, H.; Sun, W. Strong Metal−Support Interaction in Heterogeneous Catalysts. *Adv. Energy Mater.* **2022**, *12*, No. 2201395.

(10) Zhu, M.; Tian, P.; Kurtz, R.; Lunkenbein, T.; Xu, J.; Schlögl, R.; Wachs, I. E.; Han, Y. F. Strong Metal−Support Interactions between Copper and Iron Oxide during the High-Temperature Water-Gas Shift Reaction. *Angew. Chem., Int. Ed.* **2019**, *58*, 9083−9087.

(11) Sun, Y. N.; Qin, Z. H.; Lewandowski, M.; Carrasco, E.; Sterrer, M.; Shaikhutdinov, S.; Freund, H. J. Monolayer iron oxide film on platinum promotes low temperature CO oxidation. *J. Catal.* **2009**, *266*, 359−368.

(12) Stühmeier, B. M.; Selve, S.; Patel, M. U. M.; Geppert, T. N.; Gasteiger, H. A.; El-Sayed, H. A. Highly Selective Pt/TiO_x Catalysts for the Hydrogen Oxidation Reaction. *ACS Appl. Energy Mater.* **2019**, *2*, 5534−5539.

(13) Geppert, T. N.; Bosund, M.; Putkonen, M.; Stühmeier, B. M.; Pasanen, A. T.; Heikkilä, P.; Gasteiger, H. A.; El-Sayed, H. A. HOR Activity of Pt-TiO_{2-Y} at Unconventionally High Potentials Explained: The Influence of SMSI on the Electrochemical Behavior of Pt. *J. Electrochem. Soc.* **2020**, *167*, No. 084517.

(14) Xin, H.; Lin, L.; Li, R.; Li, D.; Song, T.; Mu, R.; Fu, Q.; Bao, X. Overturning CO_2 Hydrogenation Selectivity with High Activity via Reaction-Induced Strong Metal-Support Interactions. *J. Am. Chem. Soc.* **2022**, *144*, 4874−4882.

(15) Zhang, Y.; Zhang, Z.; Yang, X.; Wang, R.; Duan, H.; Shen, Z.; Li, L.; Su, Y.; Yang, R.; Zhang, Y.; Su, X.; Huang, Y.; Zhang, T. Tuning selectivity of CO_2 hydrogenation by modulating the strong metal-support interaction over Ir/TiO_2 catalysts. *Green Chem.* **2020**, *22*, 6855−6861.

(16) Li, S.; Xu, Y.; Chen, Y.; Li, W.; Lin, L.; Li, M.; Deng, Y.; Wang, X.; Ge, B.; Yang, C.; Yao, S.; Xie, J.; Li, Y.; Liu, X.; Ma, D. Tuning the Selectivity of Catalytic Carbon Dioxide Hydrogenation over Iridium/Cerium Oxide Catalysts with a Strong Metal−Support Interaction. *Angew. Chem., Int. Ed.* **2017**, *56*, 10761−10765.

(17) Han, G.; Song, H. C.; Kim, S. H.; Park, J. Y. Role of the Support Oxidation State on the Catalytic Activity of Two-Dimensional Pt/TiO_x Catalysts. *J. Phys. Chem. C* **2023**, *127*, 4096−4103.

(18) Petzoldt, P.; Eder, M.; Mackewicz, S.; Blum, M.; Kratky, T.; Günther, S.; Tschurl, M.; Heiz, U.; Lechner, B. A. J. Tuning Strong Metal-Support Interaction Kinetics on Pt-Loaded $TiO_2(110)$ by Choosing the Pressure: A Combined Ultrahigh Vacuum/Near-Ambient Pressure XPS Study. *J. Phys. Chem. C* **2022**, *126*, 16127−16139.

(19) Frey, H.; Beck, A.; Huang, X.; van Bokhoven, J. A.; Willinger, M. G. Dynamic interplay between metal nanoparticles and oxide support under redox conditions. *Science* **2022**, *376*, 982−987.

(20) Kraushofer, F.; Parkinson, G. S. Single-Atom Catalysis: Insights from Model Systems. *Chem. Rev.* **2022**, *122*, 14911−14939.

(21) Fu, Q.; Saltsburg, H.; Flytzani-Stephanopoulos, M. Active Nonmetallic Au and Pt Species on Ceria-Based Water-Gas Shift Catalysts. *Science* **2003**, *301*, 935−938.

(22) Xie, S.; Liu, L.; Lu, Y.; Wang, C.; Cao, S.; Diao, W.; Deng, J.; Tan, W.; Ma, L.; Ehrlich, S. N.; Li, Y.; Zhang, Y.; Ye, K.; Xin, H.; Flytzani-Stephanopoulos, M.; Liu, F. Pt Atomic Single-Layer Catalyst Embedded in Defect-Enriched Ceria for Efficient CO Oxidation. *J. Am. Chem. Soc.* **2022**, *144*, 21255−21266.

(23) Maurer, F.; Jelic, J.; Wang, J.; Gänzler, A.; Dolcet, P.; Wöll, C.; Wang, Y.; Studt, F.; Casapu, M.; Grunwaldt, J. D. Tracking the formation, fate and consequence for catalytic activity of Pt single sites on CeO_2. *Nat. Catal.* **2020**, *3*, 824−833.

(24) Crampton, A. S.; Rotzer, M. D.; Landman, U.; Heiz, U. Can Support Acidity Predict Sub-Nanometer Catalyst Activity Trends? *ACS Catal.* **2017**, *7*, 6738−6744.

(25) Beniya, A.; Higashi, S.; Ohba, N.; Jinnouchi, R.; Hirata, H.; Watanabe, Y. CO Oxidation Activity of Non-Reducible Oxide-Supported Mass-Selected Few-Atom Pt Single-Clusters. *Nat. Commun.* **2020**, *11*, No. 1888.

(26) Ostwald, W. Über die vermeintliche Isomerie des roten und gelben Quecksilberoxyds und die Oberflächenspannung fester Körper. *Z. Phys. Chem.* **1900**, *34U*, 495−503.

(27) Smoluchowski, M. Drei Vorträge über Diffusion, brownsche Bewegung und Koagulation von Kolloidteilchen. *Z. Phys. Chem.* **1916**, *17*, 557−585.

(28) Hu, K. J.; Plant, S. R.; Ellis, P. R.; Brown, C. M.; Bishop, P. T.; Palmer, R. E. Atomic Resolution Observation of a Size-Dependent Change in the Ripening Modes of Mass-Selected Au Nanoclusters Involved in CO Oxidation. *J. Am. Chem. Soc.* **2015**, *137*, 15161−15168.

(29) Hansen, T. W.; Delariva, A. T.; Challa, S. R.; Datye, A. K. Sintering of Catalytic Nanoparticles: Particle Migration or Ostwald Ripening? *Acc. Chem. Res.* **2013**, *46*, 1720−1730.

(30) Moulijn, J. A.; van Diepen, A. E.; Kapteijn, F. Catalyst deactivation: Is it predictable? What to do? *Appl. Catal., A* **2010**, *32*, 3−16.

(31) Argyle, M. D.; Bartholomew, C. H. Heterogeneous Catalyst Deactivation and Regeneration: A Review. *Catalysts* **2015**, *5*, 145−269.

(32) Wan, Q.; Hu, S.; Dai, J.; Chen, C.; Li, W. X. First-Principles Kinetic Study for Ostwald Ripening of Late Transition Metals on $TiO_2(110)$. *J. Phys. Chem. C* **2019**, *123*, 1160−1169.

(33) Li, Z.; Chen, H. Y. T.; Schouteden, K.; Picot, T.; Liao, T. W.; Seliverstov, A.; van Haesendonck, C.; Pacchioni, G.; Janssens, E.; Lievens, P. Unraveling the atomic structure, ripening behavior, and electronic structure of supported Au_{20} clusters. *Sci. Adv.* **2020**, *6*, No. eaay4289.

(34) Su, Y. Q.; Liu, J. X.; Filot, I. A. W.; Hensen, E. J. M. Theoretical Study of Ripening Mechanisms of Pd Clusters on Ceria. *Chem. Mater.* **2017**, *29*, 9456−9462.

(35) Wettergren, K.; Schweinberger, F. F.; Deiana, D.; Ridge, C. J.; Crampton, A. S.; Rötzer, M. D.; Hansen, T. W.; Zhdanov, V. P.; Heiz, U.; Langhammer, C. High Sintering Resistance of Size-Selected

Platinum Cluster Catalysts by Suppressed Ostwald Ripening. *Nano Lett.* **2014**, *14*, 5803–5809.

(36) Zandkarimi, B.; Poths, P.; Alexandrova, A. N. When Fluxionality Beats Size Selection: Acceleration of Ostwald Ripening of Sub-Nano Clusters. *Angew. Chem., Int. Ed.* **2021**, *60*, 11973–11982.

(37) Zandkarimi, B.; Gorey, T. J.; Li, G.; Munarriz, J.; Anderson, S. L.; Alexandrova, A. N. Alloying with Sn Suppresses Sintering of Size-Selected Subnano Pt Clusters on SiO_2 with and without Adsorbates. *Chem. Mater.* **2020**, *32*, 8595–8605.

(38) Niu, Y.; Schlexer, P.; Sebok, B.; Chorkendorff, I.; Pacchioni, G.; Palmer, R. E. Reduced Sintering of Mass-Selected Au Clusters on SiO_2 by Alloying with Ti: An Aberration-Corrected STEM and Computational Study. *Nanoscale* **2018**, *10*, 2363–2370.

(39) Yin, P.; Hu, S.; Qian, K.; Wei, Z.; Zhang, L.; Lin, Y.; Huang, W.; Xiong, H.; Li, W. X.; Liang, H. W. Quantification of critical particle distance for mitigating catalyst sintering. *Nat. Commun.* **2021**, *12*, No. 4865.

(40) Jiang, Y.; Zhu, Y.; Zhou, D.; Jiang, Z.; Si, N.; Stacchiola, D.; Niu, T. Reversible oxidation and reduction of gold-supported iron oxide islands at room temperature. *J. Chem. Phys.* **2020**, *152*, No. 074710.

(41) Fleet, M. E. The Structure of Magnetite. *Acta Crystallogr., Sect. B* **1981**, *37*, 917–920.

(42) Verwey, E. J. W.; Heilmann, E. L. Physical Properties and Cation Arrangement of Oxides with Spinel Structures I. Cation Arrangement in Spinels. *J. Chem. Phys.* **1947**, *15*, 174–180.

(43) Verwey, E. J.; Haayman, P. W.; Romeijn, F. C. Physical Properties and Cation Arrangement of Oxides with Spinel Structures II. Electronic Conductivity. *J. Chem. Phys.* **1947**, *15*, 181–187.

(44) Bliem, R.; Mcdermott, E.; Ferstl, P.; Setvin, M.; Gamba, O.; Pavelec, J.; Schneider, M. A.; Schmid, M.; Diebold, U.; Blaha, P.; Hammer, L.; Parkinson, G. S. Subsurface cation vacancy stabilization of the magnetite (001) surface. *Science* **2014**, *346*, 1215–1218.

(45) Parkinson, G. S.; Novotný, Z.; Jacobson, P.; Schmid, M.; Diebold, U. A Metastable Fe(A) Termination at the Fe3O4(001) Surface. *Surf. Sci.* **2011**, *605*, L42–L45.

(46) Parkinson, G. S. Iron Oxide Surfaces. *Surf. Sci. Rep.* **2016**, *71*, 272–365.

(47) Parkinson, G. S.; Manz, T. A.; Novotný, Z.; Sprunger, P. T.; Kurtz, R. L.; Schmid, M.; Sholl, D. S.; Diebold, U. Antiphase domain boundaries at the Fe₃O₄(001) surface. *Phys. Rev. B* **2012**, *85*, No. 195450.

(48) Bourgund, A.; Lechner, B. A. J.; Meier, M.; Franchini, C.; Parkinson, G. S.; Heiz, U.; Esch, F. Influence of Local Defects on the Dynamics of O–H Bond Breaking and Formation on a Magnetite Surface. *J. Phys. Chem. C* **2019**, *123*, 19742–19747.

(49) Gamba, O.; Hulva, J.; Pavelec, J.; Bliem, R.; Schmid, M.; Diebold, U.; Parkinson, G. S. The Role of Surface Defects in the Adsorption of Methanol on Fe₃O₄(001). *Top. Catal.* **2017**, *60*, 420–430.

(50) Hulva, J.; Jakub, Z.; Novotny, Z.; Johansson, N.; Knudsen, J.; Schnadt, J.; Schmid, M.; Diebold, U.; Parkinson, G. S. Adsorption of CO on the Fe₃O₄(001) Surface. *J. Phys. Chem. B* **2018**, *122*, 721–729.

(51) Meier, M.; Hulva, J.; Jakub, Z.; Pavelec, J.; Setvin, M.; Bliem, R.; Schmid, M.; Diebold, U.; Franchini, C.; Parkinson, G. S. Water Agglomerates on Fe₃O₄(001). *Proc. Natl. Acad. Sci. U.S.A.* **2018**, *115*, E5642–E5650.

(52) Marcinkowski, M. D.; Yuk, S. F.; Doudin, N.; Smith, R. S.; Nguyen, M. T.; Kay, B. D.; Glezakou, V. A.; Rousseau, R.; Dohnálek, Z. Low-Temperature Oxidation of Methanol to Formaldehyde on a Model Single-Atom Catalyst: Pd Atoms on Fe₃O₄(001). *ACS Catal.* **2019**, *9*, 10977–10982.

(53) Kaiser, S.; Maleki, F.; Zhang, K.; Harbich, W.; Heiz, U.; Tosoni, S.; Lechner, B. A. J.; Pacchioni, G.; Esch, F. Cluster Catalysis with Lattice Oxygen: Tracing Oxygen Transport from a Magnetite (001) Support onto Small Pt Clusters. *ACS Catal.* **2021**, *11*, 9519–9529.

(54) Heiz, U.; Vanolli, F.; Trento, L.; Schneider, W. D. Chemical reactivity of size-selected supported clusters: An experimental setup. *Rev. Sci. Instrum.* **1997**, *68*, 1986–1994.

(55) Bonanni, S.; Aït-Mansour, K.; Hugentobler, M.; Brune, H.; Harbich, W. An experimental setup combining a highly sensitive detector for reaction products with a mass-selected cluster source and a low-temperature STM for advanced nanocatalysis. *Eur. Phys. J. D* **2011**, *63*, 241–249.

(56) Nečas, D.; Klapetek, P. Gwyddion: An open-source software for SPM data analysis. *Cent. Eur. J. Phys.* **2012**, *10*, 181–188.

(57) Zhu, S.; Scardamaglia, M.; Kundsen, J.; Sankari, R.; Tarawneh, H.; Temperton, R.; Pickworth, L.; Cavalca, F.; Wang, C.; Tissot, H.; Weissenrieder, J.; Hagman, B.; Gustafson, J.; Kaya, S.; Lindgren, F.; Kallquist, I.; Maibach, J.; Hahlin, M.; Boix, V.; Gallo, T.; Rehman, F.; D'Acunto, G.; Schnadta, J.; Shavorskiy, A. HIPPIE: A New Platform for Ambient-Pressure X-Ray Photoelectron Spectroscopy at the MAX IV Laboratory. *J. Synchrotron Radiat.* **2021**, *28*, 624–636.

(58) Shimizu, S.; Noritake, H.; Koitaya, T.; Mukai, K.; Yoshimoto, S.; Yoshinobu, J. Site-specific chemical states of adsorbed CO on Pt(997): A high resolution XPS study. *Surf. Sci.* **2013**, *608*, 220–225.

(59) Toyoshima, R.; Yoshida, M.; Monya, Y.; Suzuki, K.; Amemiya, K.; Mase, K.; Mun, B. S.; Kondoh, H. A high-pressure-induced dense CO overlayer on a Pt(111) surface: A chemical analysis using in situ near ambient pressure XPS. *Phys. Chem. Chem. Phys.* **2014**, *16*, 23564–23567.

(60) Libra, J. *KolXPD: Spectroscopy Data Measurement and Processing*, 2015.

(61) Whitman, L. J.; Richter, L. J.; Gurney, B. A.; Villarrubia, J. S.; Ho, W. Co adsorption site occupations on Fe(111) vs coverage and temperature: The kinetics of adsorption and reaction. *J. Chem. Phys.* **1989**, *90*, 2050–2062.

(62) Kelemen, S. R.; Kaldor, A.; Dwyer, D. J. The Adsorption of CO on Clean and Potassium Promoted FeO Surfaces. *Surf. Sci.* **1982**, *121*, 45–60.

(63) Zhang, K.; Shaikhutdinov, S.; Freund, H.-J. Does the Surface Structure of Oxide Affect the Strong Metal-Support Interaction with Platinum? Platinum on Fe₃O₄(001) versus Fe₃O₄(111). *ChemCatChem* **2015**, *7*, 3725–3730.

(64) Arndt, B.; Lechner, B. A. J.; Bourgund, A.; Grånäs, E.; Creutzburg, M.; Krausert, K.; Hulva, J.; Parkinson, G. S.; Schmid, M.; Vonk, V.; Esch, F.; Stierle, A. Order-disorder phase transition of the subsurface cation vacancy reconstruction on Fe₃O₄(001). *Phys. Chem. Chem. Phys.* **2020**, *22*, 8336–8343.

(65) Bliem, R.; Van Der Hoeven, J.; Zavodny, A.; Gamba, O.; Pavelec, J.; De Jongh, P. E.; Schmid, M.; Diebold, U.; Parkinson, G. S. An Atomic-Scale View of CO and H₂ Oxidation on a Pt/Fe₃O₄ Model Catalyst Angewandte. *Angew. Chem.* **2015**, *127*, 13999–14002.

(66) Novotny, Z.; Mulakaluri, N.; Edes, Z.; Schmid, M.; Pentcheva, R.; Diebold, U.; Parkinson, G. S. Probing the surface phase diagram of Fe₃O₄(001) towards the Fe-rich limit: Evidence for progressive reduction of the Surface. *Phys. Rev. B* **2013**, *87*, No. 195410.

(67) Bliem, R.; van der Hoeven, J. E. S.; Hulva, J.; Pavelec, J.; Gamba, O.; de Jongh, P. E.; Schmid, M.; Blaha, P.; Diebold, U.; Parkinson, G. S. Dual Role of CO in the Stability of Subnano Pt Clusters at the Fe₃O₄ (001) Surface. *Proc. Natl. Acad. Sci. U.S.A.* **2016**, *113*, 8921–8926.

(68) The encapsulating layer thickness was calculated based on the Pt 4f signal attenuation.[69] Using a density of 5.9 g/cm³,[46] and a band gap of 2.1 eV,[70] the electron inelastic mean free path for a nominal FeO layer was calculated to be 7.22 Å for 307 eV and 16.78 Å for 921 eV photon energy.[71]

(69) Riviere, J. C.; Myhra, S. *Handbook of Surface and Interface Analysis: Methods for Problem-Solving.*; CRC Press, 2009; p 237.

(70) Di Sabatino, S.; Koskelo, J.; Berger, J. A.; Romaniello, P. Photoemission spectrum in paramagnetic FeO under pressure: Towards an ab initio description. *Phys. Rev. Res.* **2021**, *3*, No. 013172.

(71) Tanuma, S.; Penn, D. R. Calculations of Electron Inelastic Mean Free Paths. *Surf. Interface Anal.* **1993**, *20*, 77–89.

(72) Ritter, M.; Ranke, W.; Weiss, W. Growth and structure of ultrathin FeO films on Pt(111) studied by STM and LEED. *Phys. Rev. B* **1998**, *57*, 7240–7251.

(73) Lewandowski, M.; Sun, Y. N.; Qin, Z. H.; Shaikhutdinov, S.; Freund, H. J. Promotional effect of metal encapsulation on reactivity of iron oxide supported Pt catalysts. *Appl. Catal., A* **2011**, *391*, 407−410.

(74) Yamashita, T.; Hayes, P. Analysis of XPS spectra of Fe^{2+} and Fe^{3+} ions in oxide materials. *Appl. Surf. Sci.* **2008**, *254*, 2441−2449.

(75) Bagus, P. S.; Nelin, C. J.; Brundle, C. R.; Crist, B. V.; Lahiri, N.; Rosso, K. M. Combined multiplet theory and experiment for the Fe2p and 3p XPS of FeO and Fe_2O_3. *J. Chem. Phys.* **2021**, *154*, No. 094709.

(76) Krupski, K.; Moors, M.; Jóźwik, P.; Kobiela, T.; Krupski, A. Structure Determination of Au on Pt(111) Surface: LEED, STM and DFT Study. *Materials* **2015**, *8*, 2935−2952.

📖 Recommended by ACS

Size-Dependent Structures and Catalytic Properties of Supported Bimetallic PtSn Catalysts for Propane Dehydrogenation Reaction

Hongliu Wan, Lichen Liu, *et al.*

MAY 16, 2023
ACS CATALYSIS　　　　　　　　　　　　　　　READ 🔗

Unraveling Multiscale Kinetics over Subnanometer Cluster Catalysts: H_2 Desorption from $Pt_3(-H)_2/\gamma$-Al_2O_3(110)

George Yan and Dionisios G. Vlachos

JULY 31, 2023
ACS CATALYSIS　　　　　　　　　　　　　　　READ 🔗

Elucidating the Initial Oxidation of Pt(111) Using Large-Scale Atomistic Thermodynamics: A ReaxFF Study

Dajo Boden, Jörg Meyer, *et al.*

NOVEMBER 18, 2022
THE JOURNAL OF PHYSICAL CHEMISTRY C　　　READ 🔗

Breaking the Structure–Activity Relationship in Toluene Hydrogenation Catalysis by Designing Heteroatom Ensembles Based on a Single-Atom Alloying Approach

Akira Oda, Atsushi Satsuma, *et al.*

JULY 17, 2023
ACS CATALYSIS　　　　　　　　　　　　　　　READ 🔗

Get More Suggestions >

Supporting Information for

Does cluster encapsulation inhibit sintering? Stabilization of size-selected Pt clusters on Fe$_3$O$_4$(001) by SMSI

Sebastian Kaiser,[‡,1,2] Johanna Plansky,[‡,2,3] Matthias Krinninger,[2,3] Andrey Shavorskiy,[4] Suyun Zhu,[4] Ueli Heiz,[1,2] Friedrich Esch,[1,2,] and Barbara A. J. Lechner [2,3,5,*]*

[1] Chair of Physical Chemistry, Department of Chemistry, School of Natural Sciences, Technical University of Munich, Lichtenbergstr. 4, 85748 Garching, Germany

[2] Catalysis Research Center, Technical University of Munich, Lichtenbergstr. 4, 85748 Garching, Germany

[3] Functional Nanomaterials Group, Department of Chemistry, School of Natural Sciences, Technical University of Munich, Lichtenbergstr. 4, 85748 Garching, Germany

[4] MAX IV Laboratory, Lund University, Lund 221 00 Sweden

[5] Institute for Advanced Study, Technical University of Munich, Lichtenbergstr. 2a, 85748 Garching, Germany

* friedrich.esch@tum.de; bajlechner@tum.de

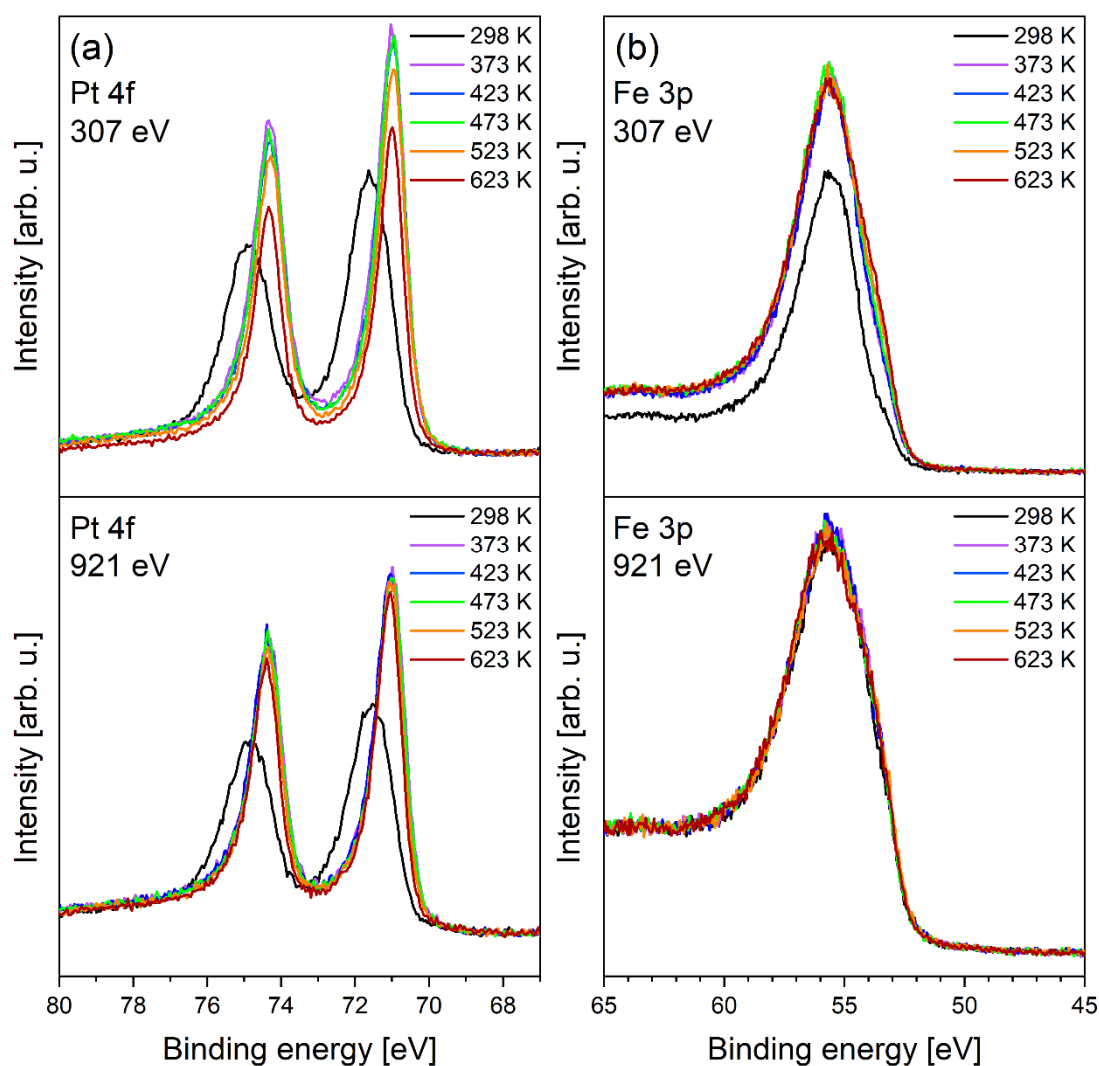**S1. XP spectra including as-deposited measurements and desorption of adsorbates**

Figure S1. XP spectra including the as-deposited room temperature measurements of $Pt_{19}/Fe_3O_4(001)$ (0.05 clusters/nm^2) measured at 307 eV (upper panels, more surface sensitive) and 921 eV photon energy (lower panels, more bulk sensitive) at the indicated temperatures, showing the Pt 4f region (a), and Fe 3p region (b). To desorb any adsorbates accumulated during the transport in UHV (e.g. CO, H_2O or hydrocarbons), the sample has been initially heated to 373 K. A shift of 0.6 eV to lower binding energy as well as a reduction of the peak width is observed in the Pt 4f signal for both photon energies. This shift corresponds to the desorption of CO from the Pt clusters.[1,2] Simultaneously, the Fe 3p signal shows no clear shift, but a strong increase in signal intensity for 307 eV photon energy upon this first annealing step, which is not observed for the 921 eV measurement. This points to an adsorbate overlayer on top of the magnetite crystal, which desorbs upon annealing to 373 K. From there on, no large intensity changes are observed in the Fe 3p signal, implying that this first annealing is sufficient to remove the adsorbates.

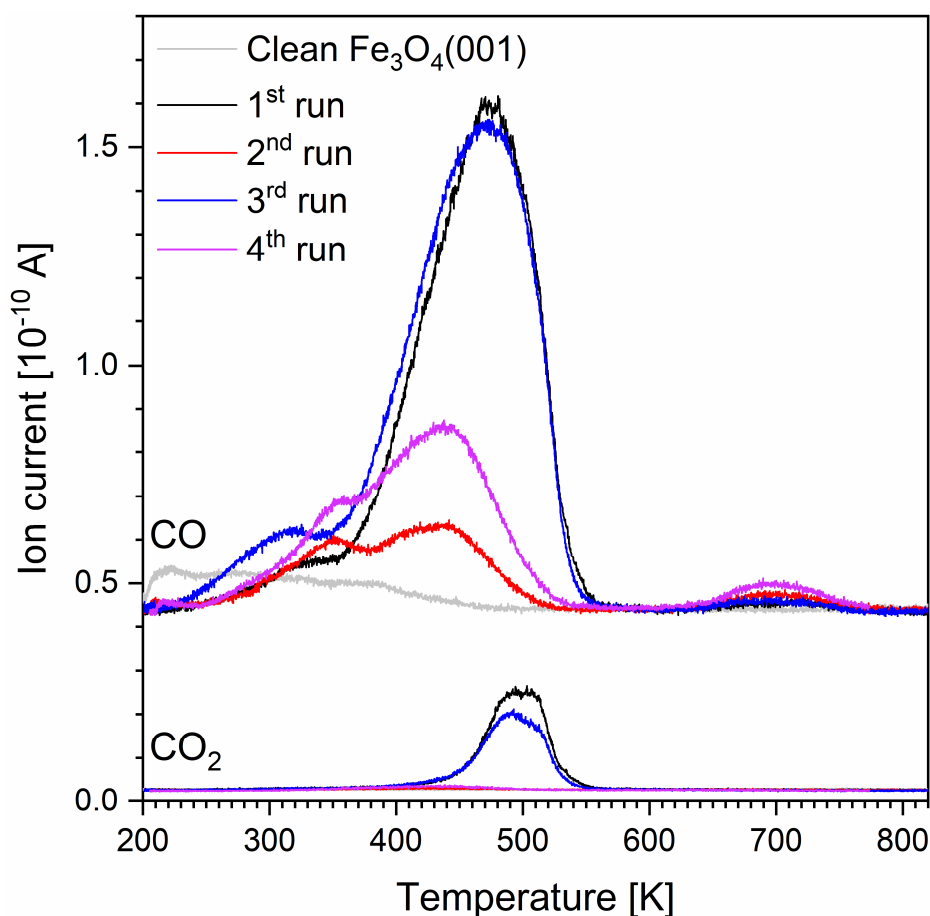## S2. Additional Pt$_{19}$ deposition on already encapsulated Pt$_{19}$/Fe$_3$O$_4$(001)

Figure S2. Subsequent TPD spectra (heating rate 1 K/s) of Pt$_{19}$ clusters on Fe$_3$O$_4$(001) (initial coverage 0.05 clusters/nm^2), measured after saturating the sample with C^{18}O (~10 L) at 200 K. The C^{18}O (m/z = 30, top) as well as the C^{18}O^{16}O (m/z = 46, bottom) traces are shown. The desorption spectra from the bare Fe$_3$O$_4$(001) substrate prior to cluster deposition are shown in gray. In the first run (black), a CO desorption feature corresponding to desorption from the clusters is observed at 475 K. CO$_2$ formation as a consequence of lattice oxygen reverse spillover is detected simultaneously.[3] In the second run (red), the cluster-related CO desorption as well as the CO$_2$ production have vanished completely. Two new features at 350 K and 430 K arise instead, corresponding to desorption from the encapsulating FeO-like conglomerate.[4] Upon deposition of another 0.05 clusters/nm^2 on the sample (blue), the initial peaks reappear in the CO and CO$_2$ traces, in addition to the second run features observed before. In a final, fourth run (magenta). the CO$_2$ formation has vanished once more, and again, only the encapsulating layer-related features are observed in the CO trace, with about twice the intensity of the second run. It becomes evident that the CO desorption from the FeO-like features directly scales with the cluster coverage and must therefore originate in the vicinity of the clusters. As the magnetite surface itself maintains its stoichiometry upon reduction by diffusion of undercoordinated iron into the bulk,[5,6] the desorption features appearing in the second and fourth runs confirm the formation of an encapsulating FeO-like layer on the clusters.

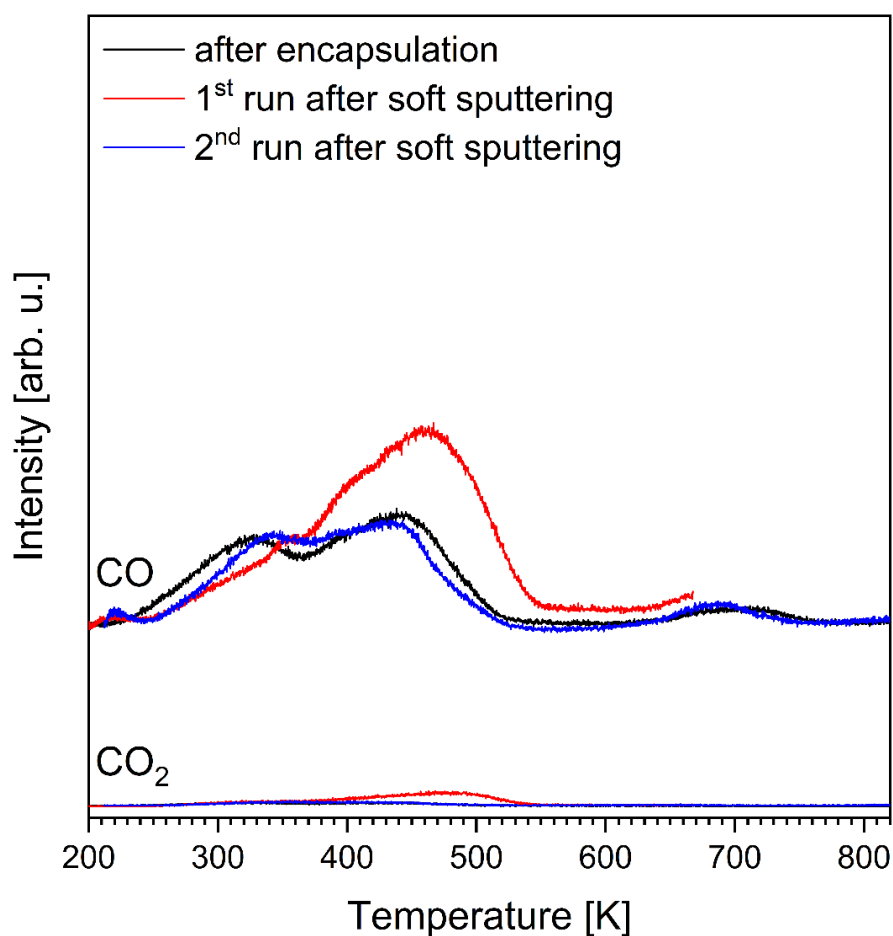## S3. Partial removal of SMSI induced layer by soft sputtering

Figure S3. Subsequent TPD spectra (heating rate 1 K/s) of Pt_{19} clusters on $Fe_3O_4(001)$ (initial coverage 0.05 clusters/nm^2), measured after saturating the sample with $C^{18}O$ (~10 L) at 200 K. Again, the $C^{18}O$ (m/z = 30, top) as well as the $C^{18}O^{16}O$ (m/z = 46, bottom) traces are shown. The clusters have been encapsualted as a consequence of SMSI by annealing to 820 K. The first run after encapsulation (black) shows the two characteristic CO desorption features from the FeO-like encapsulating conglomerate at 350 K and 430 K, while CO_2 formation is not observed. After softly sputtering the sample (40 s, 1 x 10^{-6} mbar Ar, 1 keV), the CO desorption has changed (red). Here, the intensity of the SMSI layer-related 350 K feature decreases and a new peak arises with a maximum at 475 K. CO_2 formation is observed concurrently. The new peaks correspond to those observed for as-deposited clusters, giving clear evidence that the encapsulating layer could be partially removed by sputtering, recovering the pristine Pt cluster surface. It can thus be concluded that, upon annealing, the clusters become indeed encapsulated rather than forming an alloy. Note, that although the measurement has been stopped earlier, the sample was still annealed to 820 K in this run. A last TPD experiment (blue) is highly similar to the first run after encapsulation (black), showing esentially the same desorption features and intensities, meaning that after this soft sputtering, the clusters are re-encapsulated reproducibly. We thus conclude that during sputtering the majority of the clusters have stayed intact and just the encapsulating layer has been removed.

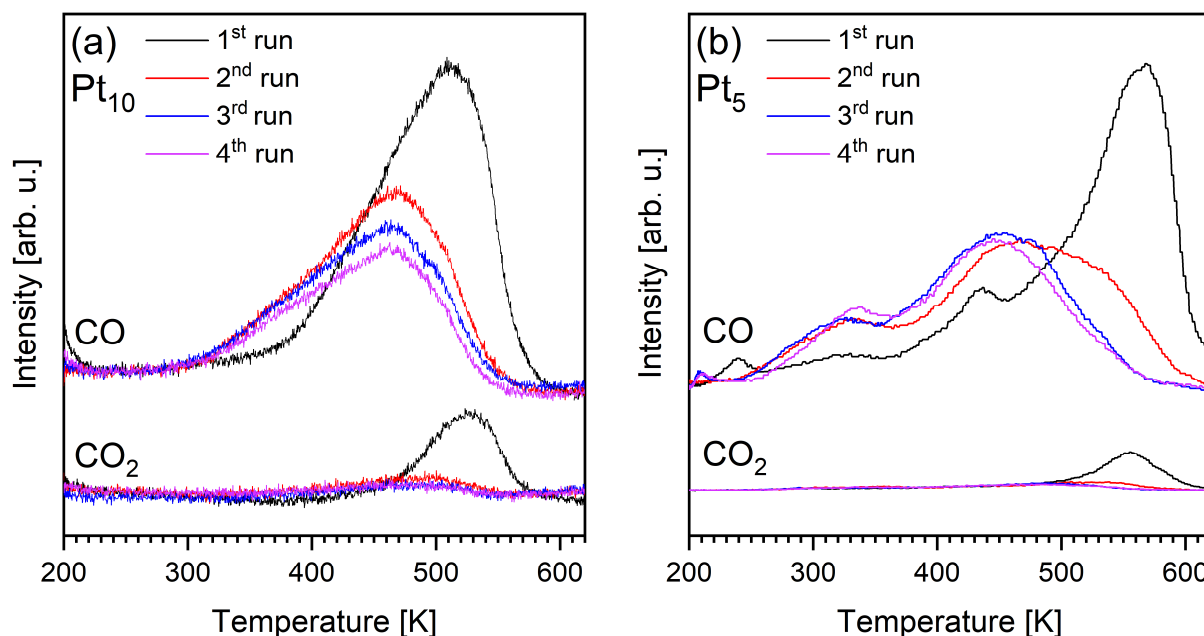**S4. Subsequent CO TPDs for Pt$_5$ and Pt$_{10}$ clusters on Fe$_3$O$_4$(001)**

Figure S4. C^{18}O TPD spectra of (a) Pt$_{10}$ and (b) Pt$_5$ clusters deposited on an Fe$_3$O$_4$(001) surface (0.05 clusters/nm^2), showing the C^{18}O (m/z = 30, top) and the C^{18}O^{16}O (m/z = 46, bottom) traces. The samples have been saturated with CO at 200 K (~10 L) before each run, the heating rate was 1 K/s. Both cluster sizes show a clear desorption peak in the first run (black), at 510 K for Pt$_{10}$ and 550 K for Pt$_5$, which is attributed to the clusters. Analogous to Pt$_{19}$ (see Figure 1), CO$_2$ formation is observed concurrently with the main CO desorption features for both cluster sizes. In the second run (red), the main CO desorption feature is strongly reduced in intensity, while new peaks arise at 360 K and 460 K for Pt$_{10}$ and 325 K and 450 K, which are assigned to desorption from an encapsulating FeO-like layer. As expected, also the CO$_2$ formation has decreased significantly. When completing the encapsulating layer growth in the third (blue) and fourth (magenta) runs, the CO$_2$ formation, as well as the original cluster-related CO desorption peaks vanish completely. These results are very similar to those observed for Pt$_{19}$ clusters. We thus conclude that Pt$_5$ and Pt$_{10}$ clusters are also encapsulated by a reduced iron oxide conglomerate upon annealing.

S5. Representative STM images for all annealing temperatures for Pt$_5$, Pt$_{10}$ and Pt$_{19}$ clusters on Fe$_3$O$_4$(001)

Figure S5. Representative set of STM images of Pt$_5$ clusters on Fe$_3$O$_4$(001) (initial coverage of 0.05 clusters/nm^2), measured at room temperature after annealing for 10 min to the temperatures indicated in the respective panels. For easier cluster height comparison, all Figures of Section S5 are set to the same color scale of 1.4 nm range. *Imaging conditions:* 1.5 V, 300 pA, 100 x 100 nm^2.
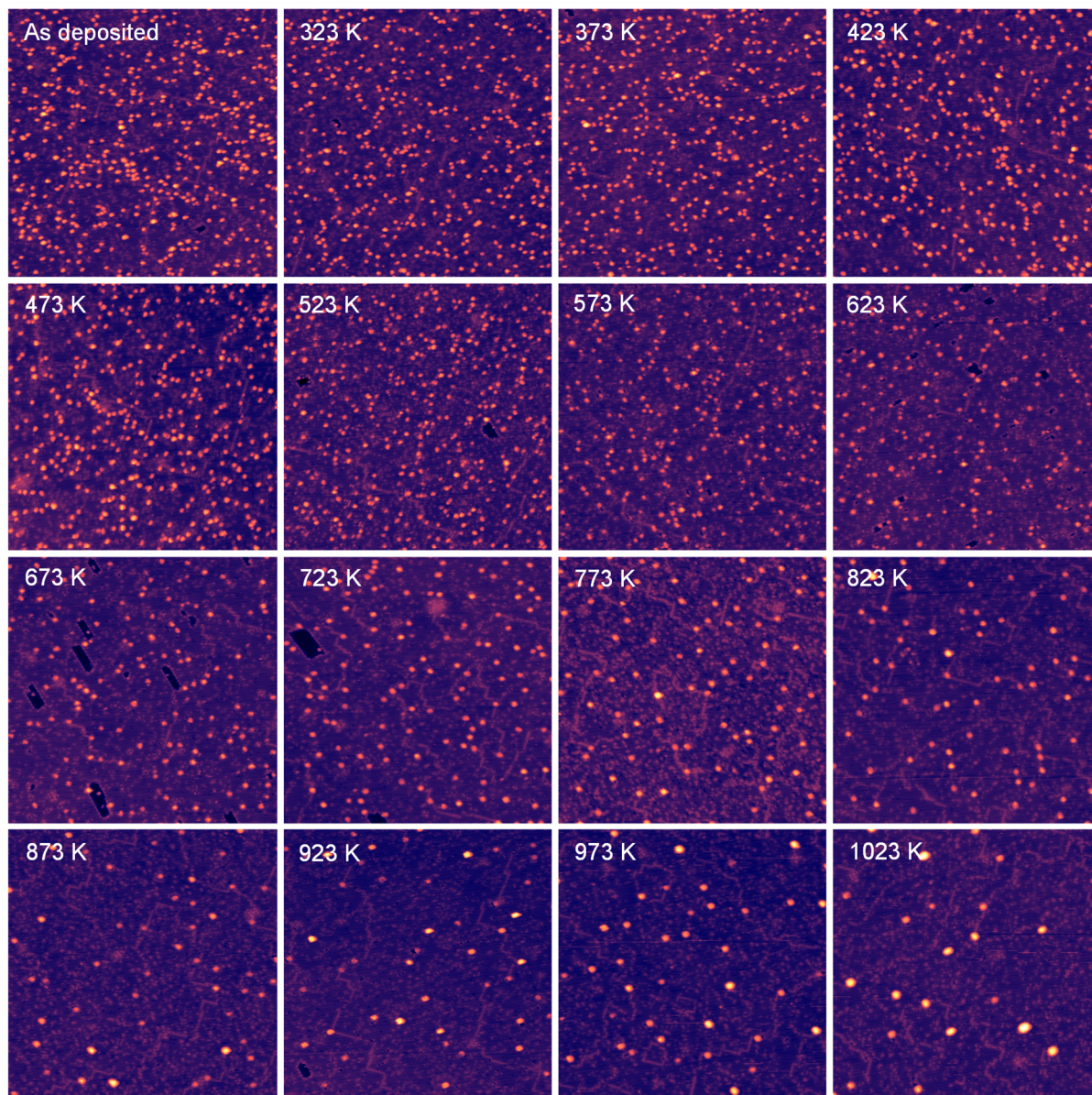
Figure S6. Representative set of STM images of Pt_{10} clusters on $Fe_3O_4(001)$ (initial coverage of 0.05 clusters/nm^2), measured at room temperature after annealing for 10 min to the temperatures indicated in the respective panels. For easier cluster height comparison, all Figures of Section S5 are set to the same color scale of 1.4 nm range. *Imaging conditions:* 1.5 V, 300 pA, 100 x 100 nm^2.
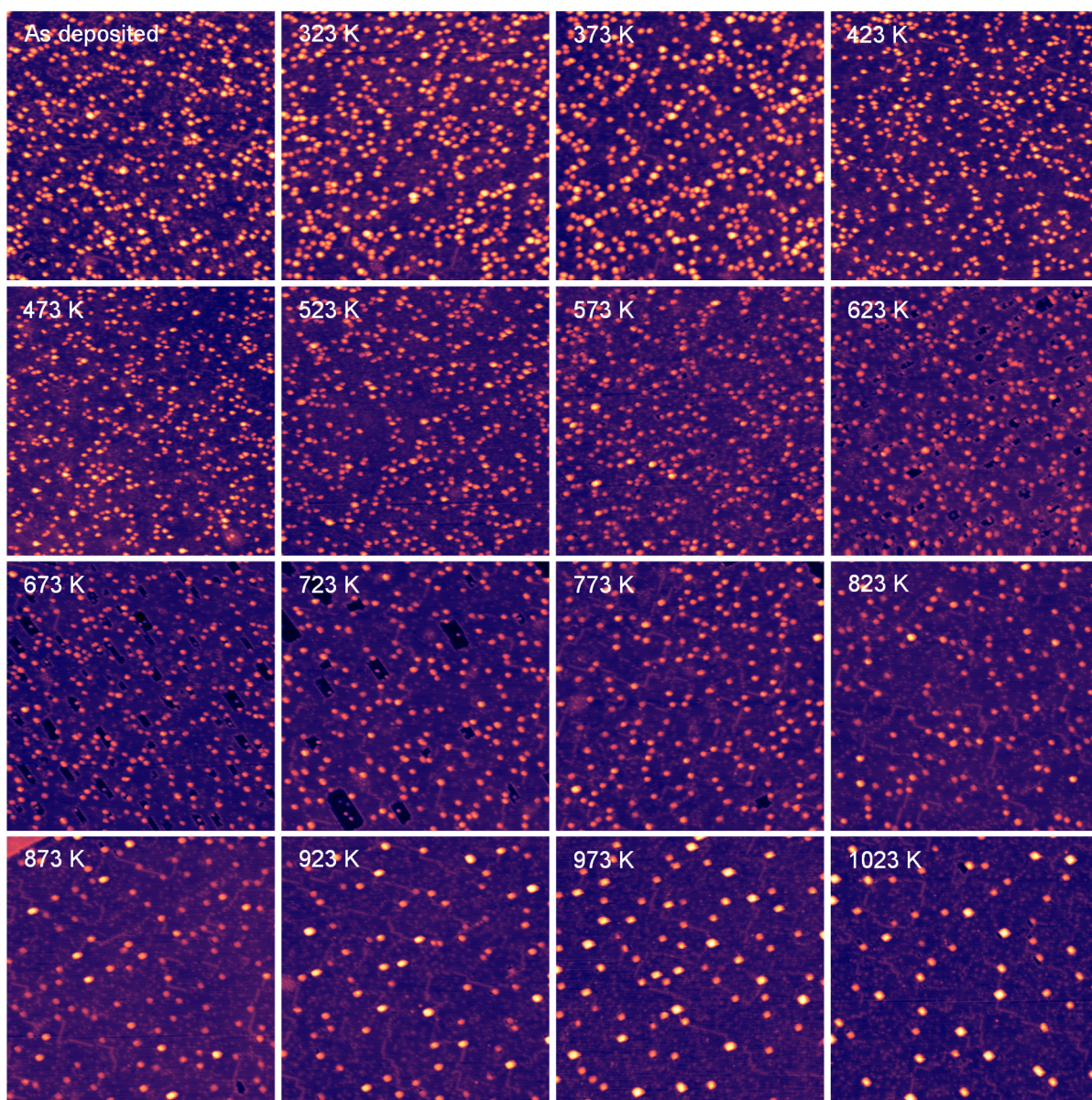
Figure S7. Representative set of STM images of Pt$_{19}$ clusters on Fe$_3$O$_4$(001) (initial coverage of 0.05 clusters/nm^2), measured at room temperature after annealing for 10 min to the temperatures indicated in the respective panels. For easier cluster height comparison all Figures of Section S5 are set to the same color scale of 1.4 nm range. *Imaging conditions:* 1.5 V, 300 pA, 100 x 100 nm^2.
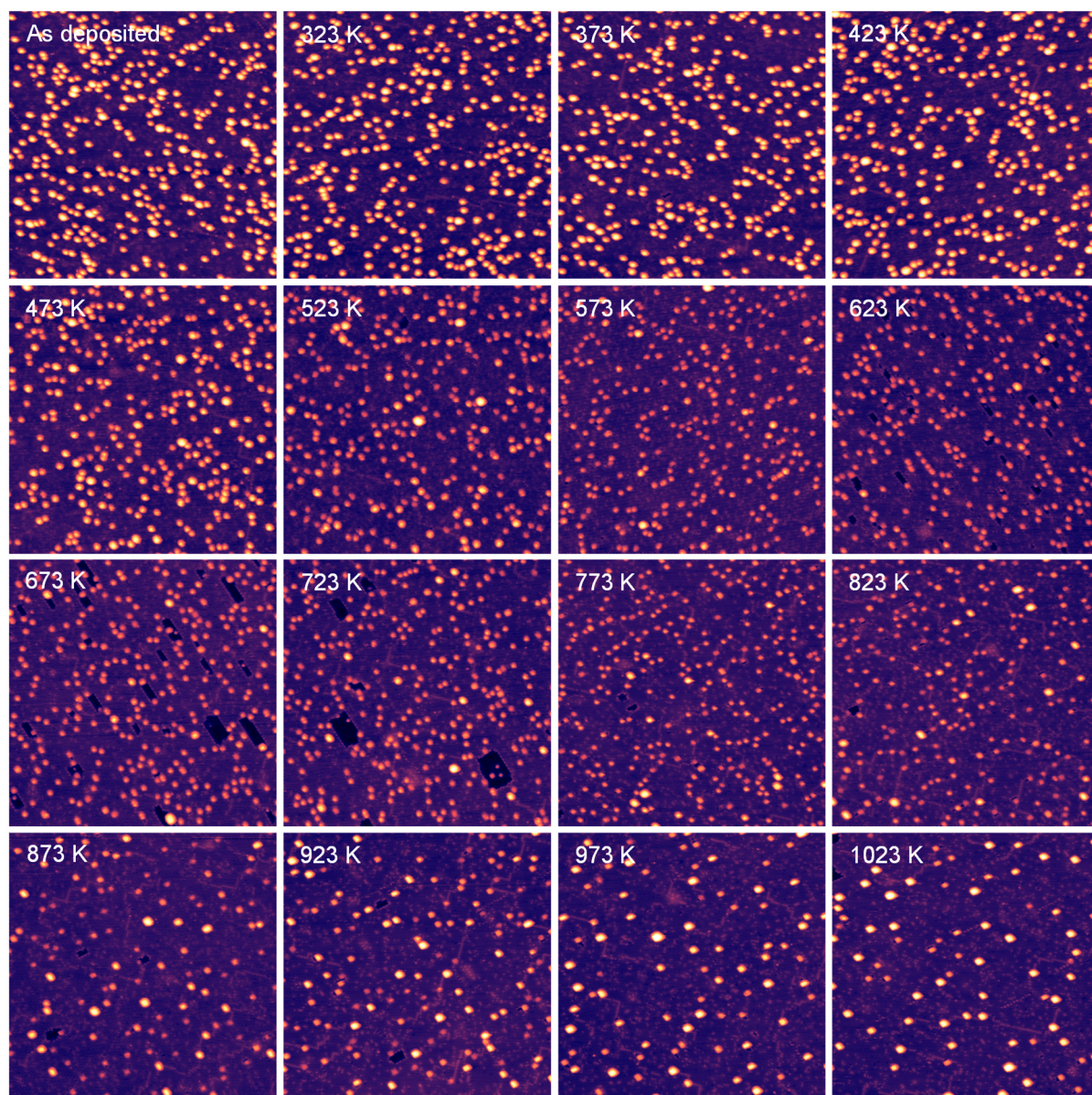
S6. Cluster height distributions for all annealing temperatures for Pt$_5$, Pt$_{10}$ and Pt$_{19}$ clusters on Fe$_3$O$_4$(001)

Figure S8. Apparent cluster height distributions of Pt$_5$/Fe$_3$O$_4$(001) (initial coverage of 0.05 clusters/nm^2), corresponding to the data in Figure S5 and nine further images at each condition. A total area of 100 000 nm^2 has been investigated. The annealing temperatures are indicated in the respective graphs. Red dotted lines indicating the atomic step height of a Pt(111) surface are added as a guide to the eye.
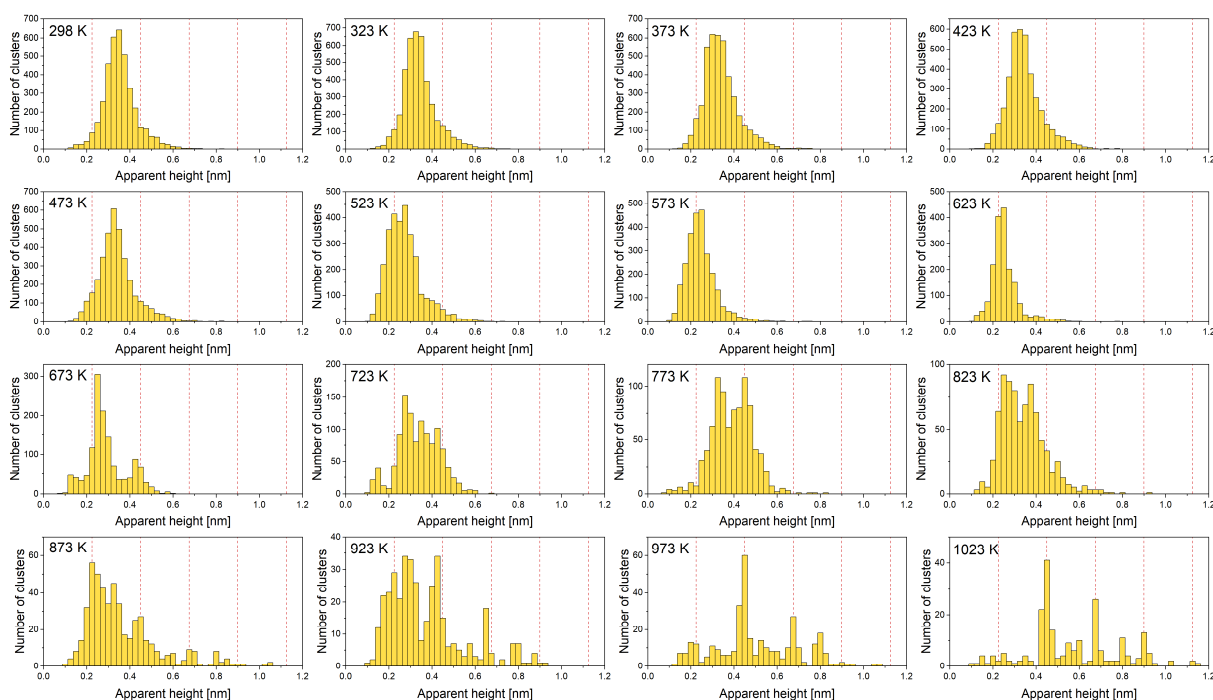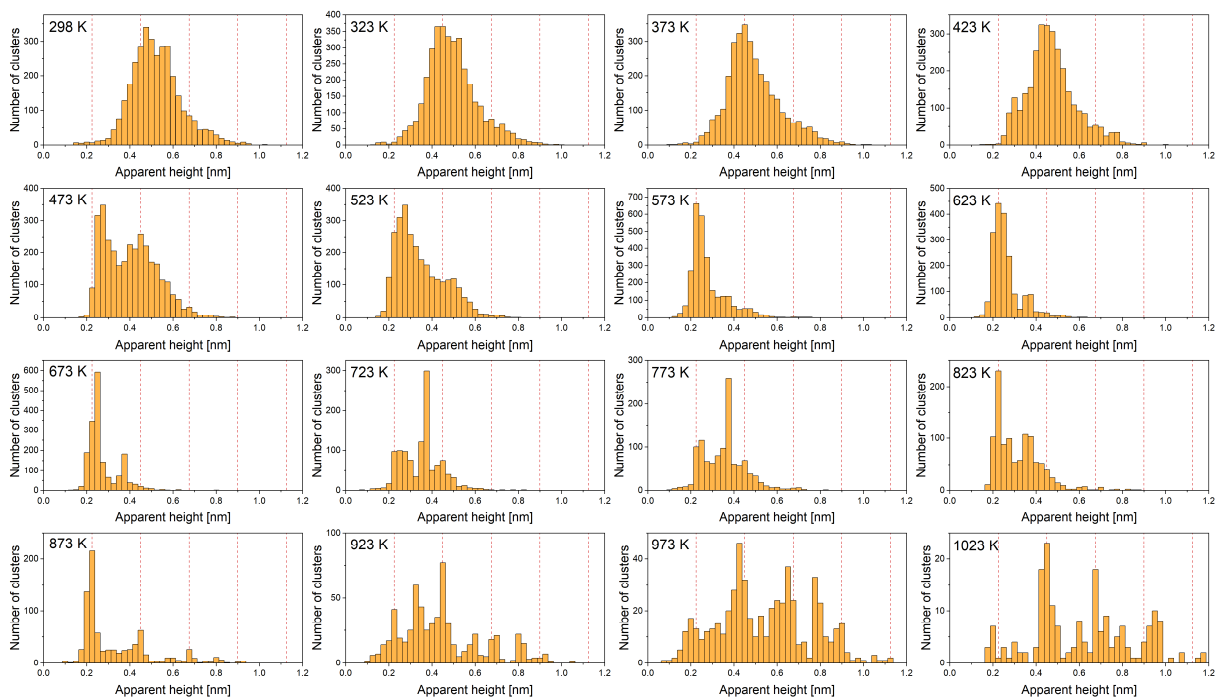
Figure S9. Apparent cluster height distributions of $Pt_{10}/Fe_3O_4(001)$ (initial coverage of 0.05 clusters/nm^2), corresponding to the data in Figure S6. and nine further images at each condition. A total area of 100 000 nm^2 has been investigated. The annealing temperatures are indicated in the respective graphs. Red dotted lines indicating the atomic step height of a Pt(111) surface are added as a guide to the eye. Note that the transition to single layer clusters between 423 K and 473 K sets in slightly earlier than for the Pt_5 sample. This is related to a lower CO desorption temperature on Pt_{10}, which is prerequisite for the lattice oxygen reverse spillover.[3]
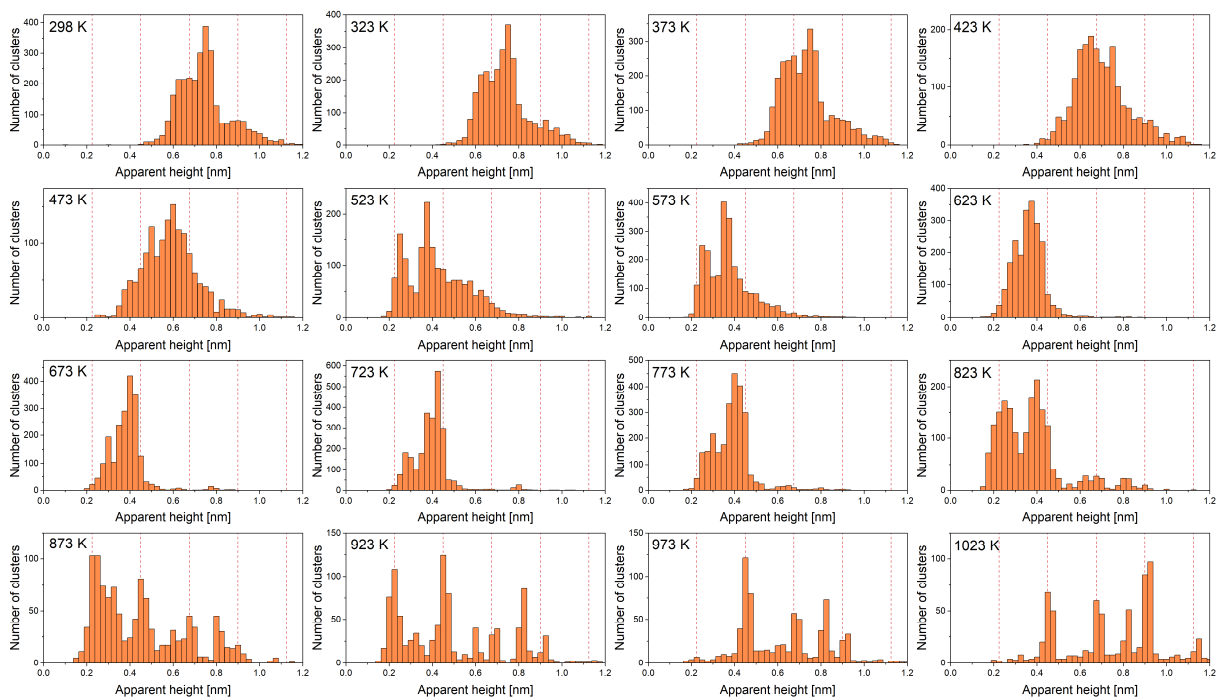
Figure S10. Apparent cluster height distributions of Pt_{19}/Fe_3O_4(001) (initial coverage of 0.05 clusters/nm^2), corresponding to the data in Figure S7. and nine further images at each condition. A total area of 100 000 nm^2 has been investigated. The annealing temperatures are indicated in the respective graphs. Red dotted lines indicating the atomic step height of a Pt(111) surface are added as a guide to the eye.

S7. Sintered Pt nanoparticles on Fe$_3$O$_4$(001)
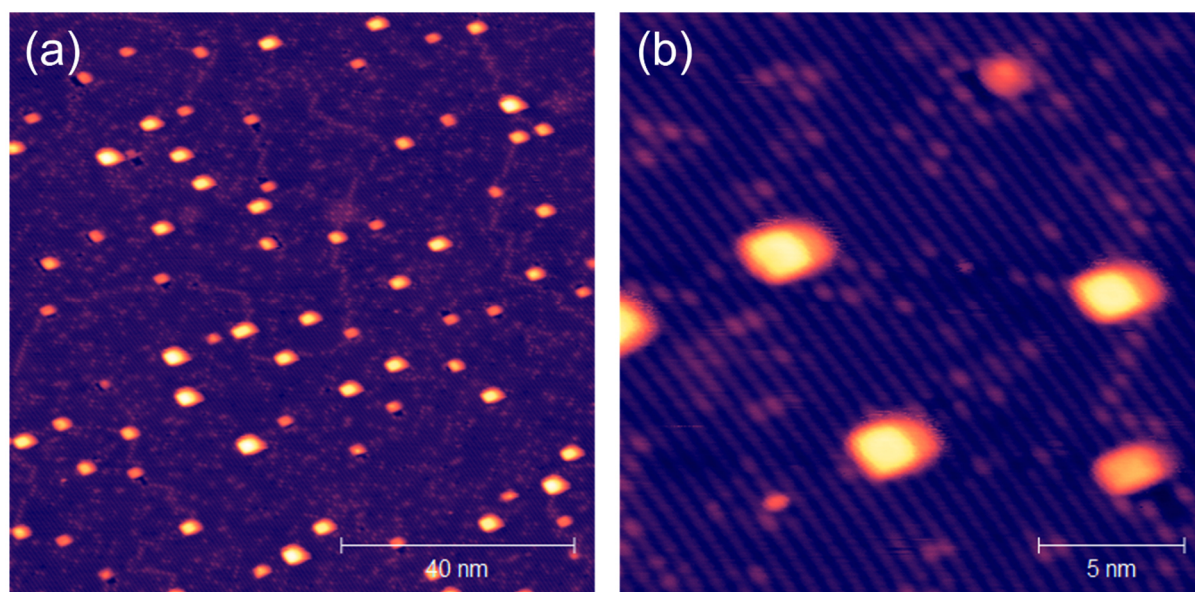
Figure S11. Pt nanoparticles on Fe$_3$O$_4$(001), grown by sintering of Pt$_{19}$ clusters at 1023 K for 10 min. (a) The overview image shows that all particles exhibit a rectangular, rather crystalline shape, adapting the cubic symmetry of the underlying magnetite substrate.[7] The particles are estimated to consist of roughly 50 – 150 atoms. (b) Zooming in reveals that all nanoparticles are aligned with the atomic rows of the substrate, confirming the particle growth being dominated by the cubic symmetry of the surface. *Imaging conditions:* 1.5 V, 300 pA, (a) 100 x 100 nm^2, (b) 20 x 20 nm^2.

References

(1)   Shimizu, S.; Noritake, H.; Koitaya, T.; Mukai, K.; Yoshimoto, S.; Yoshinobu, J. Site-specific chemical states of adsorbed CO on Pt(997): A high resolution XPS study. *Surf. Sci.* **2013**, *608*, 220–225.

(2)   Toyoshima, R.; Yoshida, M.; Monya, Y.; Suzuki, K.; Amemiya, K.; Mase, K.; Mun, B. S.; Kondoh, H. A high-pressure-induced dense CO overlayer on a Pt(111) surface: A chemical analysis using in situ near ambient pressure XPS. *Phys. Chem. Chem. Phys.* **2014**, *16*, 23564–23567.

(3)   Kaiser, S.; Maleki, F.; Zhang, K.; Harbich, W.; Heiz, U.; Tosoni, S.; Lechner, B. A. J.; Pacchioni, G.; Esch, F. Cluster Catalysis with Lattice Oxygen: Tracing Oxygen Transport from a Magnetite (001) Support onto Small Pt Clusters. *ACS Catal.* **2021**, *11*, 9519–9529.

(4)   Kelemen, S. R.; Kaldor, A.; Dwyer, D. J. The Adsorption of CO on Clean and Potassium Promoted FeO Surfaces. *Surf. Sci.* **1982**, *121*, 45–60.

(5)   Arndt, B.; Lechner, B. A. J.; Bourgund, A.; Grånäs, E.; Creutzburg, M.; Krausert, K.; Hulva, J.; Parkinson, G. S.; Schmid, M.; Vonk, V.; Esch, F.; Stierle, A. Order-disorder phase transition of the subsurface cation vacancy reconstruction on Fe_3O_4(001). *Phys. Chem. Chem. Phys.* **2020**, *22*, 8336–8343.

(6)   Bliem, R.; Hoeven, J. Van Der; Zavodny, A.; Gamba, O.; Pavelec, J.; Jongh, P. E. De; Schmid, M.; Diebold, U.; Parkinson, G. S. An Atomic-Scale View of CO and H_2 Oxidation on a Pt/Fe_3O_4 Model Catalyst Angewandte. *Angew. Chemie* **2015**, *127*, 13999–14002.

(7)   Zhang, K.; Shaikhutdinov, S.; Freund, H.-J. Does the Surface Structure of Oxide Affect the Strong Metal-Support Interaction with Platinum? Platinum on Fe_3O_4(001) versus Fe_3O_4(111). *ChemCatChem* **2015**, *7*, 3725–3730.

4 Conclusions and Outlook

This thesis, I have explored how the electron, oxygen and cation buffering properties of a reducible oxide can affect the morphology, stability and reactivity of supported sub-nanometer clusters, at the example of Pt_n on $Fe_3O_4(001)$. The controlled deposition of monodisperse, size-selected Pt clusters on the thoroughly characterized (001) facet of magnetite creates one of the most well-defined catalytic model systems as starting point for this thesis. The combination of atomically resolving STM, high resolution XPS, highly sensitive TPD and pulsed reactivity measurements, delivers structural, chemical and reactivity information that allows to disentangle the involved elementary processes, revealing new insights into catalysis beyond this model system.

It is the intricate interaction between clusters and reducible oxide supports that defines the catalytic activity and a variety of dynamic structure modifications under reaction environments and at elevated temperatures. In this thesis, the annealing temperature is used as the control parameter, its stepwise increase giving access to different cluster-support interaction regimes, which were investigated for Pt_5, Pt_{10} and Pt_{19} on magnetite (001). After cluster deposition at room temperature, the catalytic system appears to be stable within the time frame of the experiments (days). When annealing to temperatures of 473-623 K, one observes a first effect for all investigated cluster sizes: Lattice oxygen reverse spillover, i.e. the annealing-induced migration of lattice oxygen atoms onto the Pt clusters. The clusters facilitate the reverse spillover by activating lattice oxygen atoms in their immediate surrounding. The resulting oxygen atoms on top of the clusters are an activated, highly reactive oxygen species, at disposal for subsequent oxidation reactions. The mechanism is exothermic, with a considerably low activation barrier, thus only limited by the availability of adsorption sites (CO poisoning) in this temperature regime. From a temperature of about 523 K, strong metal-support interaction leads to an encapsulation of the Pt clusters via the formation of a reduced, defective FeO-like layer. The temperature overlap with the lattice oxygen reverse spillover regime suggests that the oxygen migration is the initial step of encapsulation. Although XPS and sputter experiments point towards an FeO-like layer covering the larger, Pt_{19} clusters, the encapsulating layer is assumed to instead be a conglomerate of FeO and Pt for smaller Pt_5 and Pt_{10} clusters. Furthermore, within this temperature range, a change in apparent cluster height is observed in the STM, caused by (i) a change in cluster morphology induced by spillover lattice oxygen, as calculated by DFT, and/or (ii) a hypothesized change in the electronic structure, due to SMSI.

Whereas both phenomena discussed so far do not show a clear particle size effect, cluster ripening exhibits a strong footprint and thus size dependence: Sintering already sets in within the encapsula-

tion temperature range, and while Pt_5 slowly starts to sinter at 523 K, and Pt_{10} only at 100 k higher temperatures, both via Smoluchowski ripening, no cluster coalescence is observed for larger Pt_{19} clusters. Pt cluster diffusion thus is possible on $Fe_3O_4(001)$, and one might speculate about the underlying mechanism, as the diffusion starts at the verge of encapsulation: It is not clear whether completely encapsulated clusters can still diffuse. Pt_{19} clusters sinter via Ostwald ripening at surprisingly high temperatures of 800 K, like all clusters in the investigated size range. This is 200 K above the Hüttig temperature, which indicates suppression of sintering due to encapsulation. Most probably, the atoms have to pass the encapsulating layer in both directions for detachment and reattachment at the cluster. Finally, above 1000 K and independently of the initial cluster size and atom coverage, Ostwald ripening results in similar size distributions of square-shaped nanoparticles that reproduce the square symmetry of the underlying support. Differences in the initial Pt loading manifest rather in the resulting coverage.

What do these findings imply for the discussion of catalytic activity? While Bliem et al. have previously reported that CO and H_2 oxidation on Pt clusters on $Fe_3O_4(001)$ takes place via a MvK mechanism,[13] we add evidence that the involved lattice oxygen reacts on top of the clusters. This phenomenon is not limited to Fe_3O_4, but has also been observed on CeO_2,[104] and can likely be extended to other reducible oxide supports, where a MvK mechanism occurs. On CeO_2, lattice oxygen reverse spillover has been hypothesized to play an even more important role on powder supports, where the nanoparticulate structure makes the oxygen migration exothermic, as calculated for $Pt_8/CeO_2(111)$.[108] Furthermore, this thesis provides strong evidence for the occurrence of a classic SMSI-induced encapsulation, even for clusters in the non-scalable size regime. Concerning catalysis, this leads to the following conclusions: (i) SMSI has to be considered a relevant phenomenon in catalysis, all the way down to the lower end of the size scale. (ii) Surprisingly, the encapsulating layer appears very similar in stoichiometry and reactivity to what is observed for nanoparticles.[139] (iii) SMSI-induced cluster encapsulation can be used to delay the onset of Ostwald ripening and represents hence an interesting development towards cluster stabilization for applied catalysis. The annealing series presented here is an excellent example of the typical treatment of applied catalysts by calcination and delineates a strategy how to steer the final size distribution depending on temperature and adequate initial loadings.

In a more general perspective, this thesis sheds light on the structural dynamics of the cluster-support system and how the particular cluster-support interactions on the reducible oxides lead to a complex entanglement of Fe, O and Pt diffusion processes. Even without a reactive atmosphere, only by annealing, the entire system appears highly dynamic and gives a glimpse of what might actually happen in an industrial catalyst. The challenge of cluster catalysis research is the development of catalysts that are dynamic but stable, in a way that the clusters can dynamically adapt to the reaction conditions, while avoiding deactivation via sintering. Understanding and controlling these dynamic processes while connecting them to the chemical reaction is the key to the design of cluster-based catalysts, whereby a purposeful encapsulation can help to mitigate their intrinsic metastability.

This work combined various experimental techniques and thus created new possibilities to study the system Pt_n/Fe_3O_4 along several aspects. However, especially regarding dynamic questions, the full potential of these methods has not been fully exploited yet: Video-rate FAST-STM (frames per second range) with integrated drift correction, as well as the atom tracking technique (100 μs range), which has been implemented into the experimental system during this thesis, allow to explore dynamics on the atomic scale with improved time-resolution.[206, 237] One ongoing project, with the publication already in preparation, is the in-situ investigation of cluster diffusion under full vertical and lateral feedback, using the atom tracking technique, combined with complementary STM images recorded before and afterwards. This investigation aims at elucidating the diffusion mechanism, path and rate as a function of temperature and encapsulation. Additionally, the impact of the intrinsic Fe_3O_4 surface defects (unreconstructed unit cells, antiphase domain boundaries, surface hydroxyls) is examined, by performing atom tracking measurements on samples with varying defect concentrations.

Concerning the MvK reaction, one follow-up project, already started during this thesis, investigates the dynamics of the holes formed on the surface after oxygen removal and iron diffusion into the bulk. In-situ normal and FAST-STM movies of the catalytic reaction in different atmospheres allow to address a fundamental question: How is the nucleation of the holes initiated and what is their consecutive growth mechanism? As the MvK reaction happens at the clusters, but the holes typically extend at least several nanometers away from them, (surface) diffusion of lattice oxygen atoms on the terraces or along step edges is required. This diffusion will be explored by combining FAST-STM and sniffer measurements for samples with controlled roughness, and is anticipated to provide insight into the hole growth mechanism and rate. Additionally, clusters are commonly found in the holes, meaning that they either have to move into the holes via diffusion or by removal of the terrace underneath them. By combining all the experiments suggested above, it may be possible to elucidate the precise underlying mechanism on the atomic scale.

As was demonstrated in this thesis, the sniffer setup is a powerful tool for characterizing model catalysts along several aspects. It can be used in future experiments to reveal how the cluster-support interactions discussed here affect the reactivity. Several model reactions are suggested to explore specifically the catalytic properties of the $Pt_n/Fe_3O_4(001)$ system: (i) CO oxidation, using a mixture of isotopically labeled CO and O_2, is a prototypical model reaction to further explore the MvK mechanism, comparing the activity and the reaction mechanism of pristine and encapsulated clusters. (ii) One central question in catalysis research is whether the SMSI-induced encapsulating layer is permeable for small molecules, such as hydrogen. This problem may be addressed by comparing the ethylene hydrogenation (molecular H_2) or the water-gas shift reaction (H_2O, H^+ ions) activity of as-deposited and encapsulated clusters, at low and elevated temperatures (lattice oxygen availability). (iii) CO_2 hydrogenation is an ideal reaction to compare the effect of the encapsulating layer on clusters and on nanoparticles, as for nanoparticles a significant change in product selectivity from CH_4 to CO was observed.[132]

Having established that the SMSI effect, which was previously only reported for nanoparticles, also holds for clusters in this particular system, I anticipate that it can be expanded to other cluster-

reducible oxide systems. By comparing the results obtained in this thesis to Pt clusters on other supports that classically show SMSI, e.g. TiO_2, this fundamental concept can be generalized in the non-scalable size regime, an important next step in cluster catalysis research.

Bibliography

[1] European Commission, Directorate General for Climate Action. *Going climate-neutral by 2050: a strategic long term vision for a prosperous, modern, competitive and climate neutral EU economy.*; Publications Office, **2019**.

[2] Federal Ministry for Economic Affairs and Energy; *The National Hydrogen Strategy*; **2020**.

[3] Ertl, G.; Knözinger, H.; Schüth, F.; Weitkamp, J. *Handbook of Heterogeneous Catalysis*, 2nd ed.; Wiley-VCH, **2008**.

[4] Prins, R.; Wang, A.; Li, X.; Sapountzi, F. *Introduction to Heterogeneous Catalysis*, 2nd ed.; World Scientific, **2022**.

[5] Hagen, J. *Industrial Catalysis*; Wiley-VCH, **2005**.

[6] Bell, A. T. *Science* **2003**, *299*, 1688–1691.

[7] Baerns, M.; Behr, A.; Brehm, A.; Gmehling, J.; Hinrichsen, K.-O.; Hofmann, H.; Onken, U.; Palkovits, R.; Renken, A. *Technische Chemie*, 2nd ed.; Wiley-VCH, **2013**.

[8] Bell, A. T. *Science* **2003**, *299*, 1688–1691.

[9] Schauermann, S.; Nilius, N.; Shaikhutdinov, S.; Freund, H.-J. *Acc. Chem. Res.* **2013**, *46*, 1673–1681.

[10] Perco, D.; Loi, F.; Bignardi, L.; Sbuelz, L.; Lacovig, P.; Tosi, E.; Lizzit, S.; Kartouzian, A.; Heiz, U.; Baraldi, A. *Commun. Chem.* **2023**, *6*, 61.

[11] Beniya, A.; Higashi, S.; Ohba, N.; Jinnouchi, R.; Hirata, H.; Watanabe, Y. *Nat. Commun.* **2020**, *11*, 1888.

[12] Heiz, U.; Sanchez, A.; Abbet, S.; Schneider, W.-D. *J. Am. Chem. Soc.* **1999**, *121*, 3214–3217.

[13] Bliem, R.; van der Hoeven, J.; Zavodny, A.; Gamba, O.; Pavelec, J.; de Jongh, P. E.; Schmid, M.; Diebold, U.; Parkinson, G. S. *Angew. Chem.* **2015**, *127*, 14205–14208.

[14] Hu, K.-J.; Plant, S. R.; Ellis, P. R.; Brown, C. M.; Bishop, P. T.; Palmer, R. E. *J. Am. Chem. Soc.* **2015**, *137*, 15161–15168.

[15] Niu, Y.; Schlexer, P.; Sebok, B.; Chorkendorff, I.; Pacchioni, G.; Palmer, R. E. *Nanoscale* **2018**, *10*, 2363–2370.

[16] Heiz, U.; Landman, U. *Nanocatalysis*; Springer Science & Business Media, **2007**.

[17] Sanchez, A.; Abbet, S.; Heiz, U.; Schneider, W.-D.; Häkkinen, H.; Barnett, R.; Landman, U. *J. Phys. Chem. A* **1999**, *103*, 9573–9578.

[18] Woodham, A. P.; Meijer, G.; Fielicke, A. *Angew. Chem. Int. Ed.* **2012**, *18*, 4444–4447.

[19] Hagen, J.; Socaciu, L. D.; Le Roux, J.; Popolan, D.; Bernhardt, T. M.; Wöste, L.; Mitrić, R.; Noack, H.; Bonačić-Kouteckỳ, V. *J. Am. Chem. Soc.* **2004**, *126*, 3442–3443.

[20] Fung, V.; Jiang, D.-e. *J. Phys. Chem. C* **2017**, *121*, 10796–10802.

[21] Yang, S. H.; Drabold, D. A.; Adams, J. B.; Ordejón, P.; Glassford, K. *J. Phys.: Condens. Matter* **1997**, *9*, L39.

[22] Bhattacharyya, K.; Majumder, C. *Chem. Phys. Lett.* **2007**, *446*, 374–379.

[23] Zandkarimi, B.; Poths, P.; Alexandrova, A. N. *Angew. Chem.* **2021**, *133*, 12080–12089.

[24] Häkkinen, H.; Abbet, S.; Sanchez, A.; Heiz, U.; Landman, U. *Angew. Chem. Int. Ed.* **2003**, *42*, 1297–1300.

[25] Lechner, B. A. J.; Knoller, F.; Bourgund, A.; Heiz, U.; Esch, F. *J. Phys. Chem. C* **2018**, *122*, 22569–22576.

[26] Sun, G.; Sautet, P. *J. Am. Chem. Soc.* **2018**, *140*, 2812–2820.

[27] Kaden, W. E.; Wu, T.; Kunkel, W. A.; Anderson, S. L. *Science* **2009**, *326*, 826–829.

[28] Rao, B.; Jena, P. *J. Chem. Phys.* **1999**, *111*, 1890–1904.

[29] Morton, S. M.; Silverstein, D. W.; Jensen, L. *Chem. Rev.* **2011**, *111*, 3962–3994.

[30] Cheng, H.-P.; Berry, R.; Whetten, R. *Phys. Rev. B* **1991**, *43*, 10647.

[31] Wang, L.-S.; Li, X.; Zhang, H.-F. *Chem. Phys.* **2000**, *262*, 53–63.

[32] Wang, L.-S.; Cheng, H.-S.; Fan, J. *J. Chem. Phys.* **1995**, *102*, 9480–9493.

[33] Zheng, L.-S.; Karner, C.; Brucat, P.; Yang, S.; Pettiette, C.; Craycraft, M.; Smalley, R. *J. Chem. Phys.* **1986**, *85*, 1681–1688.

[34] Bergmann, L.; Schaefer, C. *Gase, Nanosysteme, Flüssigkeiten*; Walter de Gruyter, **2005**.

[35] Seidl, M.; Meiwes-Broer, K.-H.; Brack, M. *J. Chem. Phys.* **1991**, *95*, 1295–1303.

[36] Harris, I.; Kidwell, R.; Northby, J. *Phys. Rev. Lett.* **1984**, *53*, 2390.

[37] Schmidt, M.; Kusche, R.; von Issendorff, B.; Haberland, H. *Nature* **1998**, *393*, 238–240.

[38] Knight, W.; Clemenger, K.; De Heer, W. A.; Saunders, W. A.; Chou, M.; Cohen, M. L. *Phys. Rev. Lett.* **1984**, *52*, 2141.

[39] Solov'yov, I. A.; Solov'yov, A. V.; Greiner, W.; Koshelev, A.; Shutovich, A. *Phys. Rev. Lett.* **2003**, *90*, 053401.

[40] Haberland, H.; Hippler, T.; Donges, J.; Kostko, O.; Schmidt, M.; Von Issendorff, B. *Phys. Rev. Lett.* **2005**, *94*, 035701.

[41] Wrigge, G.; Hoffmann, M. A.; Issendorff, B. v. *Phys. Rev. A* **2002**, *65*, 063201.

[42] Eberhardt, W.; Fayet, P.; Cox, D.; Fu, Z.; Kaldor, A.; Sherwood, R.; Sondericker, D. *Phys. Rev. Lett.* **1990**, *64*, 780.

[43] Billas, I. M.; Châtelain, A.; de Heer, W. A. *J. Magn. Magn. Mater.* **1997**, *168*, 64–84.

[44] Meyer, J.; Tombers, M.; van Wüllen, C.; Niedner-Schatteburg, G.; Peredkov, S.; Eberhardt, W.; Neeb, M.; Palutke, S.; Martins, M.; Wurth, W. *J. Chem. Phys.* **2015**, *143*, 104302.

[45] Apsel, S.; Emmert, J.; Deng, J.; Bloomfield, L. *Phys. Rev. Lett.* **1996**, *76*, 1441.

[46] Cox, A.; Louderback, J.; Apsel, S.; Bloomfield, L. *Phys. Rev. B* **1994**, *49*, 12295.

[47] Cox, A.; Louderback, J.; Bloomfield, L. *Phys. Rev. Lett.* **1993**, *71*, 923.

[48] Heiz, U.; Sherwood, R.; Cox, D.; Kaldor, A.; Yates Jr, J. *J. Phys. Chem.* **1995**, *99*, 8730–8735.

[49] Kaden, W. E.; Kunkel, W. A.; Roberts, F. S.; Kane, M.; Anderson, S. L. *J. Chem. Phys.* **2012**, *136*, 204705.

[50] Watanabe, Y.; Wu, X.; Hirata, H.; Isomura, N. *Catal. Sci. Technol.* **2011**, *1*, 1490–1495.

[51] Crampton, A. S.; Rötzer, M. D.; Landman, U.; Heiz, U. *ACS Catal.* **2017**, *7*, 6738–6744.

[52] Valden, M.; Lai, X.; Goodman, D. W. *Science* **1998**, *281*, 1647–1650.

[53] Yamazoe, S.; Koyasu, K.; Tsukuda, T. *Acc. Chem. Res.* **2014**, *47*, 816–824.

[54] Johnson, G. E.; Mitrić, R.; Bonačić-Kouteckỳ, V.; Castleman Jr, A. *Chem. Phys. Lett.* **2009**, *475*, 1–9.

[55] Bus, E.; Prins, R.; van Bokhoven, J. A. *Catal. Commun.* **2007**, *8*, 1397–1402.

[56] Arenz, M.; Landman, U.; Heiz, U. *ChemPhysChem* **2006**, *7*, 1871–1879.

[57] Levin, N.; Lengyel, J.; Eckhard, J. F.; Tschurl, M.; Heiz, U. *J. Am. Chem. Soc.* **2020**, *142*, 5862–5869.

[58] Levin, N.; Margraf, J. T.; Lengyel, J.; Reuter, K.; Tschurl, M.; Heiz, U. *Phys. Chem. Chem. Phys.* **2022**, *24*, 2623–2629.

[59] Lengyel, J.; Levin, N.; Ončák, M.; Jakob, K.; Tschurl, M.; Heiz, U. *Chem.–Eur. J.* **2023**, *29*, e202203259.

[60] Popescu, R.; Schneider, R.; Gerthsen, D.; Böttcher, A.; Löffler, D.; Weis, P.; Kappes, M. *Surf. Sci.* **2009**, *603*, 3119–3125.

[61] Li, Z.; Chen, H.-Y. T.; Schouteden, K.; Picot, T.; Liao, T.-W.; Seliverstov, A.; Van Haesendonck, C.; Pacchioni, G.; Janssens, E.; Lievens, P. *Sci. Adv.* **2020**, *6*, eaay4289.

[62] Fukamori, Y.; König, M.; Yoon, B.; Wang, B.; Esch, F.; Heiz, U.; Landman, U. *ChemCatChem* **2013**, *5*, 3330–3341.

[63] Wettergren, K.; Schweinberger, F. F.; Deiana, D.; Ridge, C. J.; Crampton, A. S.; Rötzer, M. D.; Hansen, T. W.; Zhdanov, V. P.; Heiz, U.; Langhammer, C. *Nano Lett.* **2014**, *14*, 5803–5809.

[64] Ostwald, W. *Z. Phys. Chem.* **1900**, *34*, 495–503.

[65] Smoluchowski, M. *Z. Phys. Chem.* **1916**, *17*, 557–585.

[66] Wan, Q.; Hu, S.; Dai, J.; Chen, C.; Li, W.-X. *J. Phys. Chem. C* **2018**, *123*, 1160–1169.

[67] Su, Y.-Q.; Liu, J.-X.; Filot, I. A.; Hensen, E. J. *Chem. Mater.* **2017**, *29*, 9456–9462.

[68] Zandkarimi, B.; Gorey, T. J.; Li, G.; Munarriz, J.; Anderson, S. L.; Alexandrova, A. N. *Chem. Mater.* **2020**, *32*, 8595–8605.

[69] Park, J. B.; Conner, S.; Chen, D. *J. Phys. Chem. C* **2008**, *112*, 5490–5500.

[70] Herzing, A. A.; Kiely, C. J.; Carley, A. F.; Landon, P.; Hutchings, G. J. *Science* **2008**, *321*, 1331–1335.

[71] Ruiz Puigdollers, A.; Schlexer, P.; Tosoni, S.; Pacchioni, G. *Acs Catal.* **2017**, *7*, 6493–6513.

[72] Helali, Z.; Jedidi, A.; Syzgantseva, O.; Calatayud, M.; Minot, C. *Theor. Chem. Acc.* **2017**, *136*, 1–16.

[73] Lapina, O. B.; Bal'zhinimaev, B. S.; Boghosian, S.; Eriksen, K. M.; Fehrmann, R. *Catal. Today* **1999**, *51*, 469–479.

[74] Christodoulakis, A.; Boghosian, S. *J. Catal.* **2003**, *215*, 139–150.

[75] Rayment, T.; Schlögl, R.; Thomas, J.; Ertl, G. *Nature* **1985**, *315*, 311–313.

[76] Ertl, G. *Angew. Chem. Int. Ed.* **2008**, *47*, 3524–3535.

[77] Goddard, W. A.; Chenoweth, K.; Pudar, S.; Van Duin, A. C.; Cheng, M.-J. *Top. Catal.* **2008**, *50*, 2–18.

[78] Pudar, S.; Oxgaard, J.; Chenoweth, K.; Van Duin, A. C.; Goddard, W. A. *J. Phys. Chem. C* **2007**, *111*, 16405–16415.

[79] Liu, W.; Flytzani-Stephanopoulos, M. *J. Catal.* **1995**, *153*, 304–316.

[80] Konsolakis, M. *Appl. Catal., B* **2016**, *198*, 49–66.

[81] Busca, G.; Lietti, L.; Ramis, G.; Berti, F. *Appl. Catal., B* **1998**, *18*, 1–36.

[82] Wang, Y.-G.; Yoon, Y.; Glezakou, V.-A.; Li, J.; Rousseau, R. *J. Am. Chem. Soc.* **2013**, *135*, 10673–10683.

[83] Pacchioni, G. *Phys. Chem. Chem. Phys.* **2013**, *15*, 1737–1757.

[84] Lykhach, Y.; Faisal, F.; Skála, T.; Neitzel, A.; Tsud, N.; Vorokhta, M.; Dvořák, F.; Beranová, K.; Kosto, Y.; Prince, K. C.; Matolín, V.; Libuda, J. *J. Mater. Chem.A* **2018**, *6*, 23078–23086.

[85] Jiang, Z.; Zhang, W.; Jin, L.; Yang, X.; Xu, F.; Zhu, J.; Huang, W. *J. Phys. Chem. C* **2007**, *111*, 12434–12439.

[86] Lykhach, Y.; Kozlov, S. M.; Skála, T.; Tovt, A.; Stetsovych, V.; Tsud, N.; Dvořák, F.; Johánek, V.; Neitzel, A.; Mysliveček, J.; et al. *Nat. Mater.* **2016**, *15*, 284–288.

[87] Wahlström, E.; Vestergaard, E. K.; Schaub, R.; Rønnau, A.; Vestergaard, M.; Lægsgaard, E.; Stensgaard, I.; Besenbacher, F. *Science* **2004**, *303*, 511–513.

[88] Karim, W.; Spreafico, C.; Kleibert, A.; Gobrecht, J.; VandeVondele, J.; Ekinci, Y.; van Bokhoven, J. A. *Nature* **2017**, *541*, 68–71.

[89] Beck, A.; Kazazis, D.; Ekinci, Y.; Li, X.; Müller Gubler, E. A.; Kleibert, A.; Willinger, M.-G.; Artiglia, L.; van Bokhoven, J. A. *ACS nano* **2022**, *17*, 1091–1099.

[90] Walenta, C. A.; Kollmannsberger, S. L.; Courtois, C.; Pereira, R. N.; Stutzmann, M.; Tschurl, M.; Heiz, U. *Phys. Chem. Chem. Phys.* **2019**, *21*, 1491–1496.

[91] Walenta, C. A.; Courtois, C.; Kollmannsberger, S. L.; Eder, M.; Tschurl, M.; Heiz, U. *ACS Catal.* **2020**, *10*, 4080–4091.

[92] Courtois, C.; Eder, M.; Schnabl, K.; Walenta, C. A.; Tschurl, M.; Heiz, U. *Angew. Chem. Int. Ed.* **2019**, *58*, 14255–14259.

[93] Schlexer, P.; Ruiz Puigdollers, A.; Pacchioni, G. *Top. Catal.* **2019**, *62*, 1192–1201.

[94] Ammal, S. C.; Heyden, A. *J. Chem. Phys.* **2010**, *133*, 164703.

[95] Mars, P.; Van Krevelen, D. W. *Chem. Eng. Sci.* **1954**, *3*, 41–59.

[96] Widmann, D.; Behm, R. J. *Acc. Chem. Res.* **2014**, *47*, 740–749.

[97] Kotobuki, M.; Leppelt, R.; Hansgen, D. A.; Widmann, D.; Behm, R. J. *J. Catal.* **2009**, *264*, 67–76.

[98] Widmann, D.; Liu, Y.; Schüth, F.; Behm, R. J. *J. Catal.* **2010**, *276*, 292–305.

[99] Puigdollers, A. R.; Pacchioni, G. *ChemCatChem* **2017**, *9*, 1119–1127.

[100] Barbier Jr, J.; Duprez, D. *Appl. Catal., B* **1993**, *3*, 61–83.

[101] Kalamaras, C. M.; Panagiotopoulou, P.; Kondarides, D. I.; Efstathiou, A. M. *J. Catal.* **2009**, *264*, 117–129.

[102] Ammal, S. C.; Heyden, A. *J. Phys. Chem. C* **2011**, *115*, 19246–19259.

[103] Ammal, S. C.; Heyden, A. *J. Catal.* **2013**, *306*, 78–90.

[104] Zafiris, G.; Gorte, R. J. *J. Catal.* **1993**, *139*, 561–567.

[105] Lykhach, Y.; Kubát, J.; Neitzel, A.; Tsud, N.; Vorokhta, M.; Skála, T.; Dvořák, F.; Kosto, Y.; Prince, K. C.; Matolín, V.; Johánek, V.; Mysliveček, J.; Libuda, J. *J. Chem. Phys.* **2019**, *151*, 204703.

[106] Ševčíková, K.; Kolářová, T.; Skála, T.; Tsud, N.; Václavů, M.; Lykhach, Y.; Matolín, V.; Nehasil, V. *Appl. Surf. Sci.* **2015**, *332*, 747–755.

[107] Happel, M.; Mysliveček, J.; Johánek, V.; Dvořák, F.; Stetsovych, O.; Lykhach, Y.; Matolín, V.; Libuda, J. *J. Catal.* **2012**, *289*, 118–126.

[108] Vayssilov, G. N.; Lykhach, Y.; Migani, A.; Staudt, T.; Petrova, G. P.; Tsud, N.; Skála, T.; Bruix, A.; Illas, F.; Prince, K. C.; Matolín, V.; Neymann, K. M.; Libuda, J. *Nat. Mater.* **2011**, *10*, 310–315.

[109] Bruix, A.; Migani, A.; Vayssilov, G. N.; Neyman, K. M.; Libuda, J.; Illas, F. *Phys. Chem. Chem. Phys.* **2011**, *13*, 11384–11392.

[110] Negreiros, F. R.; Fabris, S. *J. Phys. Chem. C* **2014**, *118*, 21014–21020.

[111] Tosoni, S.; Chen, H.-Y. T.; Pacchioni, G. *Surf. Sci.* **2016**, *646*, 230–238.

[112] Chen, H.-Y. T.; Tosoni, S.; Pacchioni, G. *J. Phys. Chem. C* **2015**, *119*, 10856–10868.

[113] Men, Y.; Gnaser, H.; Zapf, R.; Hessel, V.; Ziegler, C. *Catal. Commun.* **2004**, *5*, 671–675.

[114] Men, Y.; Gnaser, H.; Zapf, R.; Hessel, V.; Ziegler, C.; Kolb, G. *Appl. Catal., A* **2004**, *277*, 83–90.

[115] Zhou, Y.; Ren, S.; Yang, J.; Liu, W.; Su, Z.; Chen, Z.; Wang, M.; Chen, L. *J. Environ. Chem. Eng.* **2021**, *9*, 106218.

[116] Chen, B.; Ma, Y.; Ding, L.; Xu, L.; Wu, Z.; Yuan, Q.; Huang, W. *J. Phys. Chem. C* **2013**, *117*, 5800–5810.

[117] Calaza, F. C.; Xu, Y.; Mullins, D. R.; Overbury, S. H. *J. Am. Chem. Soc.* **2012**, *134*, 18034–18045.

[118] Bowker, M.; Bennett, R. A. *J. Phys.: Condens. Matter* **2009**, *21*, 474224.

[119] Diebold, U. *Surf. Sci. Rep.* **2003**, *48*, 53–229.

[120] Walenta, C. A.; Kollmannsberger, S. L.; Kiermaier, J.; Winbauer, A.; Tschurl, M.; Heiz, U. *Phys. Chem. Chem. Phys.* **2015**, *17*, 22809–22814.

[121] Parkinson, G. S. *Surf. Sci. Rep.* **2016**, *71*, 272–365.

[122] Gamba, O.; Hulva, J.; Pavelec, J.; Bliem, R.; Schmid, M.; Diebold, U.; Parkinson, G. S. *Top. Catal.* **2017**, *60*, 420–430.

[123] Bourgund, A.; Lechner, B. A. J.; Meier, M.; Franchini, C.; Parkinson, G. S.; Heiz, U.; Esch, F. *J. Phys. Chem. C* **2019**, *123*, 19742–19747.

[124] Tauster, S.; Fung, S.; Garten, R. L. *J. Am. Chem. Soc.* **1978**, *100*, 170–175.

[125] Tauster, S. *Acc. Chem. Res.* **1987**, *20*, 389–394.

[126] Dulub, O.; Hebenstreit, W.; Diebold, U. *Phys. Rev. Lett.* **2000**, *84*, 3646.

[127] Braunschweig, E. J.; Logan, A. D.; Datye, A. K.; Smith, D. J. *J. Catal.* **1989**, *118*, 227–237.

[128] Anderson, J.; Burch, R.; Cairns, J. *Appl. Catal.* **1986**, *25*, 173–180.

[129] Petzoldt, P.; Eder, M.; Mackewicz, S.; Blum, M.; Kratky, T.; Günther, S.; Tschurl, M.; Heiz, U.; Lechner, B. A. J. *J. Phys. Chem. C* **2022**, *126*, 16127–16139.

[130] Beck, A.; Huang, X.; Artiglia, L.; Zabilskiy, M.; Wang, X.; Rzepka, P.; Palagin, D.; Willinger, M.-G.; van Bokhoven, J. A. *Nat. Commun.* **2020**, *11*, 3220.

[131] Naitabdi, A.; Fagiewicz, R.; Boucly, A.; Olivieri, G.; Bournel, F.; Tissot, H.; Xu, Y.; Benbalagh, R.; Silly, M. G.; Sirotti, F.; Gallet, J.-J.; Rochet, F. *Top. Catal.* **2016**, *59*, 550–563.

[132] Pu, T.; Zhang, W.; Zhu, M. *Angew. Chem. Int. Ed.* **2023**, *62*, e202212278.

[133] Spencer, M. *J. Catal.* **1985**, *93*, 216–223.

[134] Fu, Q.; Wagner, T.; Olliges, S.; Carstanjen, H.-D. *J. Phys. Chem. B* **2005**, *109*, 944–951.

[135] Sá, J.; Bernardi, J.; Anderson, J. A. *Catal. Lett.* **2007**, *114*, 91–95.

[136] Tang, H.; et al. *Sci. Adv.* **2017**, *3*, e1700231.

[137] Yu, L.; Sato, K.; Toriyama, T.; Yamamoto, T.; Matsumura, S.; Nagaoka, K. *Chem.–Eur. J.* **2018**, *24*, 8742–8746.

[138] Tang, M.; Li, S.; Chen, S.; Ou, Y.; Hiroaki, M.; Yuan, W.; Zhu, B.; Yang, H.; Gao, Y.; Zhang, Z.; Wang, Y. *Angew. Chem. Int. Ed.* **2021**, *60*, 22339–22344.

[139] Zhang, K.; Shaikhutdinov, S.; Freund, H.-J. *ChemCatChem* **2015**, *7*, 3725–3730.

[140] Qin, Z.-H.; Lewandowski, M.; Sun, Y.-N.; Shaikhutdinov, S.; Freund, H.-J. *J. Phys. Chem. C* **2008**, *112*, 10209–10213.

[141] Figueiredo, W. T.; Della Mea, G. B.; Segala, M.; Baptista, D. L.; Escudero, C.; Pérez-Dieste, V.; Bernardi, F. *ACS Appl. Nano Mater.* **2019**, *2*, 2559–2573.

[142] Huang, R.; Kwon, O.; Lin, C.; Gorte, R. J. *J. Catal.* **2021**, *398*, 102–108.

[143] Cagnoli, M. V.; Alvarez, A. M.; Gallegos, N. G.; Bengoa, J. F.; de Souza, C. D.; Schmal, M.; Marchetti, S. G. *Appl. Catal., A* **2007**, *326*, 113–119.

[144] Hoang-Van, C.; Zegaoui, O. *Appl. Catal., A* **1997**, *164*, 91–103.

[145] Xin, H.; Lin, L.; Li, R.; Li, D.; Song, T.; Mu, R.; Fu, Q.; Bao, X. *J. Am. Chem. Soc.* **2022**, *144*, 4874–4882.

[146] Yang, F.; Zhao, H.; Wang, W.; Wang, L.; Zhang, L.; Liu, T.; Sheng, J.; Zhu, S.; He, D.; Lin, L.; He, J.; Wang, R.; Li, Y. *Chem. Sci.* **2021**, *12*, 12651–12660.

[147] Wang, J.; Lu, A.-H.; Li, M.; Zhang, W.; Chen, Y.-S.; Tian, D.-X.; Li, W.-C. *ACS nano* **2013**, *7*, 4902–4910.

[148] Wang, H.; Wang, L.; Lin, D.; Feng, X.; Niu, Y.; Zhang, B.; Xiao, F.-S. *Nat. Catal.* **2021**, *4*, 418–424.

[149] Kaden, W. E.; Kunkel, W. A.; Roberts, F. S.; Kane, M.; Anderson, S. L. *Surf. Sci.* **2014**, *621*, 40–50.

[150] Wu, Z.; Li, Y.; Huang, W. *J. Phys. Chem. Lett.* **2020**, *11*, 4603–4607.

[151] Frey, H.; Beck, A.; Huang, X.; van Bokhoven, J. A.; Willinger, M.-G. *Science* **2022**, *376*, 982–987.

[152] Lunkenbein, T.; Schumann, J.; Behrens, M.; Schlögl, R.; Willinger, M. G. *Angew. Chem.* **2015**, *127*, 4627–4631.

[153] Luo, Z.; Zhao, G.; Pan, H.; Sun, W. *Adv. Energy Mater.* **2022**, *12*, 2201395.

[154] Zhu, M.; Tian, P.; Kurtz, R.; Lunkenbein, T.; Xu, J.; Schlögl, R.; Wachs, I. E.; Han, Y.-F. *Angew. Chem.* **2019**, *131*, 9181–9185.

[155] Sun, Y.-N.; Qin, Z.-H.; Lewandowski, M.; Carrasco, E.; Sterrer, M.; Shaikhutdinov, S.; Freund, H.-J. *J. Catal.* **2009**, *266*, 359–368.

[156] Stühmeier, B. M.; Selve, S.; Patel, M. U.; Geppert, T. N.; Gasteiger, H. A.; El-Sayed, H. A. *ACS Appl. Energy Mater.* **2019**, *2*, 5534–5539.

[157] Geppert, T. N.; Bosund, M.; Putkonen, M.; Stühmeier, B. M.; Pasanen, A. T.; Heikkilä, P.; Gasteiger, H. A.; El-Sayed, H. A. *J. Electrochem. Soc.* **2020**, *167*, 084517.

[158] d'Alnoncourt, R. N.; Friedrich, M.; Kunkes, E.; Rosenthal, D.; Girgsdies, F.; Zhang, B.; Shao, L.; Schuster, M.; Behrens, M.; Schlögl, R. *J. Catal.* **2014**, *317*, 220–228.

[159] Li, H.; Weng, X.; Tang, Z.; Zhang, H.; Ding, D.; Chen, M.; Wan, H. *ACS Catal.* **2018**, *8*, 10156–10163.

[160] Zhang, Y.; Yang, X.; Yang, X.; Duan, H.; Qi, H.; Su, Y.; Liang, B.; Tao, H.; Liu, B.; Chen, D.; Su, X.; Huang, Y.; Zhang, T. *Nat. Commun.* **2020**, *11*, 3185.

[161] Hernández Mejía, C.; van Deelen, T. W.; de Jong, K. P. *Nat. Commun.* **2018**, *9*, 4459.

[162] Li, S.; Xu, Y.; Chen, Y.; Li, W.; Lin, L.; Li, M.; Deng, Y.; Wang, X.; Ge, B.; Yang, C.; Yao, S.; Xie, J.; Li, Y.; Liu, X.; Ma, D. *Angew. Chem.* **2017**, *129*, 10901–10905.

[163] Zhang, Y.; Zhang, Z.; Yang, X.; Wang, R.; Duan, H.; Shen, Z.; Li, L.; Su, Y.; Yang, R.; Zhang, Y.; Su, X.; Huang, Y.; Zhang, T. *Green Chem.* **2020**, *22*, 6855–6861.

[164] Guo, Y.; Li, Y.; Du, X.; Li, L.; Jiang, Q.; Qiao, B. *Nano Res.* **2022**, *15*, 10037–10043.

[165] Guo, Y.; Huang, Y.; Zeng, B.; Han, B.; Akri, M.; Shi, M.; Zhao, Y.; Li, Q.; Su, Y.; Li, L.; et al. *Nat. Commun.* **2022**, *13*, 2648.

[166] Lide, D. R. *CRC handbook of chemistry and physics*; CRC press, **2004**; Vol. 85.

[167] Fleet, M. E. *Acta Crystallogr. B: Struct. Sci. Cryst. Eng. Mater.* **1981**, *37*, 917–920.

[168] Verwey, E.; Haayman, P.; Romeijn, F. *J. Chem. Phys.* **1947**, *15*, 181–187.

[169] Taskin, M.; Novotny, Z.; Hengsberger, M.; Osterwalder, J. *Phys. Rev. Materials* **2023**, *7*, 055801.

[170] Kündig, W.; Hargrove, R. S. *Solid State Commun.* **1969**, *7*, 223–227.

[171] Verwey, E. J. *Nature* **1939**, *144*, 327–328.

[172] Piekarz, P.; Parlinski, K.; Oleś, A. M. *Phys. Rev. Lett.* **2006**, *97*, 156402.

[173] Rozenberg, G. K.; Pasternak, M.; Xu, W.; Amiel, Y.; Hanfland, M.; Amboage, M.; Taylor, R.; Jeanloz, R. *Phys. Rev. Lett.* **2006**, *96*, 045705.

[174] Néel, L. In *Annales de physique*; pp 137–198.

[175] Zhang, Z.; Satpathy, S. *Phys. Rev. B* **1991**, *44*, 13319.

[176] Tober, S.; Creutzburg, M.; Arndt, B.; Krausert, K.; Mattauch, S.; Koutsioubas, A.; Pütter, S.; Mohd, A. S.; Volgger, L.; Hutter, H.; Noei, H.; Vonk, V.; Lott, D.; Andreas, S. *Phys. Rev. Research* **2020**, *2*, 023406.

[177] Bliem, R.; McDermott, E.; Ferstl, P.; Setvin, M.; Gamba, O.; Pavelec, J.; Schneider, M.; Schmid, M.; Diebold, U.; Blaha, P.; Hammer, L.; Parkinson, G. S. *Science* **2014**, *346*, 1215–1218.

[178] Bartelt, N. C.; Nie, S.; Starodub, E.; Bernal-Villamil, I.; Gallego, S.; Vergara, L.; McCarty, K. F.; de la Figuera, J. *Phys. Rev. B* **2013**, *88*, 235436.

[179] Arndt, B.; Lechner, B. A. J.; Bourgund, A.; Grånäs, E.; Creutzburg, M.; Krausert, K.; Hulva, J.; Parkinson, G. S.; Schmid, M.; Vonk, V.; Esch, F.; Stierle, A. *Phys. Chem. Chem. Phys.* **2020**, *22*, 8336–8343.

[180] Parkinson, G. S.; Manz, T. A.; Novotnỳ, Z.; Sprunger, P. T.; Kurtz, R. L.; Schmid, M.; Sholl, D. S.; Diebold, U. *Phys. Rev. B* **2012**, *85*, 195450.

[181] Meier, M.; Hulva, J.; Jakub, Z.; Pavelec, J.; Setvin, M.; Bliem, R.; Schmid, M.; Diebold, U.; Franchini, C.; Parkinson, G. S. *Proc. Natl. Acad. Sci.* **2018**, *115*, E5642–E5650.

[182] Marcinkowski, M. D.; Adamsen, K. C.; Doudin, N.; Sharp, M. A.; Smith, R. S.; Wang, Y.; Wendt, S.; Lauritsen, J. V.; Parkinson, G. S.; Kay, B. D.; Dohnálek, Z. *J. Chem. Phys.* **2020**, *152*, 064703.

[183] Pavelec, J.; Hulva, J.; Halwidl, D.; Bliem, R.; Gamba, O.; Jakub, Z.; Brunbauer, F.; Schmid, M.; Diebold, U.; Parkinson, G. S. *J. Chem. Phys.* **2017**, *146*, 014701.

[184] Parkinson, G. S.; Mulakaluri, N.; Losovyj, Y.; Jacobson, P.; Pentcheva, R.; Diebold, U. *Phys. Rev. B* **2010**, *82*, 125413.

[185] Hiura, S.; Ikeuchi, A.; Shirini, S.; Subagyo, A.; Sueoka, K. *Phys. Rev. B* **2015**, *91*, 205411.

[186] Parkinson, G. S.; Novotnỳ, Z.; Jacobson, P.; Schmid, M.; Diebold, U. *J. Am. Chem. Soc.* **2011**, *133*, 12650–12655.

[187] Parkinson, G. S.; Novotnỳ, Z.; Jacobson, P.; Schmid, M.; Diebold, U. *Surf. Sci.* **2011**, *605*, L42–L45.

[188] Novotny, Z.; Mulakaluri, N.; Edes, Z.; Schmid, M.; Pentcheva, R.; Diebold, U.; Parkinson, G. S. *Phys. Rev. B* **2013**, *87*, 195410.

[189] Novotnỳ, Z.; Argentero, G.; Wang, Z.; Schmid, M.; Diebold, U.; Parkinson, G. S. *Phys. Rev. Lett.* **2012**, *108*, 216103.

[190] Parkinson, G. S.; Novotny, Z.; Argentero, G.; Schmid, M.; Pavelec, J.; Kosak, R.; Blaha, P.; Diebold, U. *Nat. Mater.* **2013**, *12*, 724–728.

[191] Bliem, R.; Kosak, R.; Perneczky, L.; Novotny, Z.; Gamba, O.; Fobes, D.; Mao, Z.; Schmid, M.; Blaha, P.; Diebold, U.; Parkinson, G. S. *Acs Nano* **2014**, *8*, 7531–7537.

[192] Bliem, R.; Pavelec, J.; Gamba, O.; McDermott, E.; Wang, Z.; Gerhold, S.; Wagner, M.; Osiecki, J.; Schulte, K.; Schmid, M.; Blaha, P.; Diebold, U.; Parkinson, G. S. *Phys. Rev. B* **2015**, *92*, 075440.

[193] Bliem, R.; van der Hoeven, J. E.; Hulva, J.; Pavelec, J.; Gamba, O.; de Jongh, P. E.; Schmid, M.; Blaha, P.; Diebold, U.; Parkinson, G. S. *Proc. Natl. Acad. Sci.* **2016**, *113*, 8921–8926.

[194] Jakub, Z.; Hulva, J.; Meier, M.; Bliem, R.; Kraushofer, F.; Setvin, M.; Schmid, M.; Diebold, U.; Franchini, C.; Parkinson, G. S. *Angew. Chem. Int. Ed.* **2019**, *58*, 13961–13968.

[195] Jakub, Z.; Hulva, J.; Ryan, P. T.; Duncan, D. A.; Payne, D. J.; Bliem, R.; Ulreich, M.; Hofegger, P.; Kraushofer, F.; Meier, M.; Schmid, M.; Diebold, U.; Parkinson, G. S. *Nanoscale* **2020**, *12*, 5866–5875.

[196] Marcinkowski, M. D.; Yuk, S. F.; Doudin, N.; Smith, R. S.; Nguyen, M.-T.; Kay, B. D.; Glezakou, V.-A.; Rousseau, R.; Dohnálek, Z. *ACS Catal.* **2019**, *9*, 10977–10982.

[197] Ryan, P. T. P.; et al. *Phys. Chem. Chem. Phys.* **2018**, *20*, 16469–16476.

[198] Sharp, M. A.; Lee, C. J.; Mahapatra, M.; Smith, R. S.; Kay, B. D.; Dohnalek, Z. *J. Phys. Chem. C* **2022**, *126*, 14448–14459.

[199] Gargallo-Caballero, R.; Martín-García, L.; Quesada, A.; Granados-Miralles, C.; Foerster, M.; Aballe, L.; Bliem, R.; Parkinson, G. S.; Blaha, P.; Marco, J. F.; de la Figuera, J. *J. Chem. Phys.* **2016**, *144*, 094704.

[200] Hulva, J.; Meier, M.; Bliem, R.; Jakub, Z.; Kraushofer, F.; Schmid, M.; Diebold, U.; Franchini, C.; Parkinson, G. S. *Science* **2021**, *371*, 375–379.

[201] Qin, Z.-H.; Lewandowski, M.; Sun, Y.-N.; Shaikhutdinov, S.; Freund, H.-J. *J. Phys. Chem. C* **2008**, *112*, 10209–10213.

[202] Sun, Y.-N.; Qin, Z.-H.; Lewandowski, M.; Shaikhutdinov, S.; Freund, H.-J. *Surf. Sci.* **2009**, *603*, 3099–3103.

[203] Lewandowski, M.; Sun, Y.-N.; Qin, Z.-H.; Shaikhutdinov, S.; Freund, H.-J. *Appl. Catal., A* **2011**, *391*, 407–410.

[204] Meier, M.; Hulva, J.; Jakub, Z.; Kraushofer, F.; Bobić, M.; Bliem, R.; Setvin, M.; Schmid, M.; Diebold, U.; Franchini, C.; Parkinson, G. S. *Sci. Adv.* **2022**, *8*, eabn4580.

[205] Bieletzki, M.; *Charakterisierung dünner MgO-Filme auf Ag(001) und massenselektierter Cluster auf HOPG mittels Rastersondentechnik*; **2009**.

[206] Dri, C.; Panighel, M.; Tiemann, D.; Patera, L. L.; Troiano, G.; Fukamori, Y.; Knoller, F.; Lechner, B. A. J.; Cautero, G.; Giuressi, D.; Comelli, G.; Fraxedas, J.; Africh, F., Christina ande Esch *Ultramicroscopy* **2019**, *205*, 49–56.

[207] Heiz, U.; Vanolli, F.; Trento, L.; Schneider, W.-D. *Rev. Sci. Instrum.* **1997**, *68*, 1986–1994.

[208] Smalley, R. *Laser Chem.* **1983**, *2*, 167–184.

[209] Binnig, G.; Rohrer, H. *Surf. Sci.* **1983**, *126*, 236–244.

[210] Butt, H.-J.; Graf, K.; Kappl, M. *Physics and chemistry of interfaces*, 3rd ed.; John Wiley & Sons, **2013**.

[211] Kolasinski, K. W. *Surface Science: Foundations of Catalysis and Nanoscience*, 3rd ed.; John Wiley & Sons, **2012**.

[212] Voigtländer, B. *Scanning probe microscopy: Atomic force microscopy and scanning tunneling microscopy*; Springer Nature, **2015**.

[213] Esch, F.; Dri, C.; Spessot, A.; Africh, C.; Cautero, G.; Giuressi, D.; Sergo, R.; Tommasini, R.; Comelli, G. *Rev. Sci. Instrum.* **2011**, *82*, 053702.

[214] Nečas, D.; Klapetek, P. *Open Phys.* **2012**, *10*, 181–188.

[215] Kaiser, S.; Master's thesis; Technical University of Munich; **2019**.

[216] Bonanni, S.; Aït-Mansour, K.; Hugentobler, M.; Brune, H.; Harbich, W. *Eur. Phys. J. D* **2011**, *63*, 241–249.

[217] Bourgund, A.; *Defect Dynamics at the Fe₃O₄(001) Surface under the Fast Scanning Tunnelling Microscope: Real-Time Studies on an Oxide Catalyst*; **2020**.

[218] Zehr, R. T.; Henderson, M. A. *Surf. Sci.* **2008**, *602*, 1507–1516.

[219] Chorkendorff, I.; Niemantsverdriet, J. W. *Concepts of modern catalysis and kinetics*; John Wiley & Sons, **2017**.

[220] Yates Jr, J. T. *Experimental innovations in surface science*, 2nd ed.; Springer, **1998**.

[221] Feulner, P. *J. Vac. Sci. Technol.* **1980**, *17*, 662.

[222] Dubois, L.; Somorjai, G. *Surf. Sci.* **1980**, *91*, 514–532.

[223] King, D. A. *Surf. Sci.* **1975**, *47*, 384–402.

[224] Bonanni, S.; Aït-Mansour, K.; Brune, H.; Harbich, W. *Acs Catal.* **2011**, *1*, 385–389.

[225] Bonanni, S.; Aït-Mansour, K.; Harbich, W.; Brune, H. *J. Am. Chem. Soc.* **2012**, *134*, 3445–3450.

[226] Niemantsverdriet, J. W. *Spectroscopy in catalysis: an introduction*, 3rd ed.; John Wiley & Sons, **2007**.

[227] Hofmann, S. *Auger-and X-ray photoelectron spectroscopy in materials science: a user-oriented guide*; Springer Science & Business Media, **2012**.

[228] Baer, D. R.; Artyushkova, K.; Richard Brundle, C.; Castle, J. E.; Engelhard, M. H.; Gaskell, K. J.; Grant, J. T.; Haasch, R. T.; Linford, M. R.; Powell, C. J.; Shard, A. G.; Sherwood, P. M. A. a. V. S. *J. Vac. Sci. Technol. A* **2019**, *37*.

[229] Powell, C. J. *J. Vac. Sci. Technol. A: Vac. Surf. Films* **2020**, *38*, 023209.

[230] Stöhr, J. *NEXAFS spectroscopy*; Springer Berlin Heidelberg, **1992**.

[231] Ertl, G.; Küppers, J. *Low energy electrons and surface chemistry*; Vch Weinheim, **1985**.

[232] Moulder, J. F.; Stickle, W. F.; Sobol, P. E.; Bomben, K. D. *Handbook of X-ray photoelectron spectroscopy*; Perkin-Elmer Corporation Physical Electronics Division, **1992**.

[233] Tanuma, S.; Powell, C. J.; Penn, D. R. *Surf. Interface Anal.* **1993**, *20*, 77–89.

[234] Libra, J. **2015**.

[235] Bennett, R.; Stone, P.; Bowker, M. *Catal. Lett.* **1999**, *59*, 99–105.

[236] Moulijn, J. A.; Van Diepen, A.; Kapteijn, F. *Appl. Catal., A* **2001**, *212*, 3–16.

[237] Swartzentruber, B. *Phys. Rev. Lett.* **1996**, *76*, 459.

Appendices

1 Further Publication: On-Surface Carbon Nitride Growth from Polymerization of 2,5,8-Triazido-s-heptazine

Title	On-Surface Carbon Nitride Growth from Polymerization of 2,5,8-Triazido-s-heptazine
Authors	Matthias Krinninger, Nicolas Bock, **Sebastian Kaiser**, Johanna Reich, Tobias Bruhm, Felix Haag, Francesco Allegretti, Ueli Heiz, Klaus Köhler, Barbara A. J. Lechner, Friedrich Esch
Journal	*Chemistry of Materials* **Article ASAP**
DOI	10.1021/acs.chemmater.3c01030
Status	published online August 23, 2023

Contributions

Matthias Krinninger	TAH synthesis, UHV and air experiments, data analysis and visualization, writing
Nicolas Bock	Air experiments, data analysis
Sebastian Kaiser	UHV experiments, data analysis
Johanna Reich	UHV experiments, data analysis
Tobias Bruhm	TAH Synthesis
Felix Haag	XPS experiments
Francesco Allegretti	Laboratory resources
Ueli Heiz	Funding acquisition, discussions
Klaus Köhler	Laboratory resources, discussions
Barbara A. J. Lechner	Supervision, funding acquisition, discussions, writing
Friedrich Esch	Supervision, funding acquisition, discussions, writing

On-Surface Carbon Nitride Growth from Polymerization of 2,5,8-Triazido-*s*-heptazine

Matthias Krinninger, Nicolas Bock, Sebastian Kaiser, Johanna Reich, Tobias Bruhm, Felix Haag,
Francesco Allegretti, Ueli Heiz, Klaus Köhler, Barbara A. J. Lechner, and Friedrich Esch*

ACCESS | Metrics & More | Article Recommendations | SI Supporting Information

ABSTRACT: Carbon nitrides have recently come into focus for photo- and thermal catalysis, both as support materials for metal nanoparticles as well as photocatalysts themselves. While many approaches for the synthesis of three-dimensional carbon nitride materials are available, only top-down approaches by exfoliation of powders lead to thin-film flakes of this inherently two-dimensional material. Here, we describe an in situ on-surface synthesis of monolayer 2D carbon nitride films as a first step toward precise combination with other 2D materials. Starting with a single monomer precursor, we show that 2,5,8-triazido-*s*-heptazine can be evaporated intact, deposited on a single crystalline Au(111) or graphite support, and activated via azide decomposition and subsequent coupling to form a covalent polyheptazine network. We demonstrate that the activation can occur in three pathways, via electrons (X-ray illumination), via photons (UV illumination), and thermally. Our work paves the way to coat materials with extended carbon nitride networks that are, as we show, stable under ambient conditions.
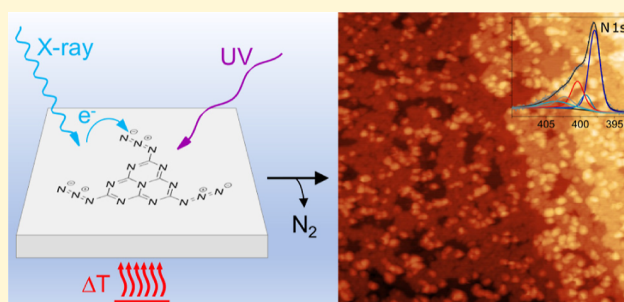
INTRODUCTION

The long-established carbon nitrides, consisting of the earth-abundant elements carbon and nitrogen, have recently moved into the focus of research for their potential as (photo)catalysts in water splitting or carbon dioxide photoreduction.[1−3] The term carbon nitride generally describes polymers consisting predominantly of C and N species. More specifically, (graphitic) carbon nitrides (g-C_3N_4) are categorized as 1D or 2D networks based on the *s*-triazine and *s*-heptazine building blocks, in line with Lau and Lotsch.[4] Networks consisting of heptazine building blocks can be connected via tertiary amine links, forming true g-C_3N_4 sheets where nitrogen atoms provide a coordination environment in the pores. Alternatively, connection via secondary amines leads to the formation of hydrogen-containing chains (melon) or cyclic arrangements in 2D poly(heptazine imides). Beyond the ideal structure of g-C_3N_4, defective modifications have been designed to tune the electronic properties.[4−6]

Besides their direct application for metal-free catalysis,[5,7] the porous nanostructures provide binding sites for catalytically active metal ions or particles. The coordination of metals to the nitrogen atoms of the carbon nitride pores is flexible enough to provide access for reactants while also immobilizing the active sites efficiently against dissolution and sintering. As the group of Ramirez showed, Suzuki coupling can be sustainably performed even on single Pd ions that remain coordinated in the carbon nitride pores throughout the

involved redox process.[8] Furthermore, the addition of metal and metal oxide cocatalysts into the pores has been shown to overcome sluggish charge transfer kinetics in the photo-(electro)catalytic water splitting by carbon nitrides.[4] More generally, the ability to bind catalyst particles from single atoms to entire clusters in an ordered manner[9] could provide a platform to systematically access size effects in the catalysis on small clusters at the non-scalable limit.[10,11]

Synthesis of purely 2D-linked, hydrogen-free g-C_3N_4 networks is experimentally highly challenging.[4] Starting from a variety of precursors,[12] the thermal condensation of melamine typically leads to the formation of only 1D melon chains, while a guided synthesis mediated by salt melts or on crystalline salt surfaces induces the 2D order via formation of poly(heptazine imides) without terminating primary amines.[4,13] A variety of more complex approaches have been reported toward a 2D preparation of g-C_3N_4, namely laser-electric discharge methods,[14] chemical vapor deposition,[15] electrodeposition,[16] spray deposition,[17] liquid−gas interface separation,[18] and exfoliation.[19] Furthermore, in an alternative

A

synthetic approach, Gillan and later the Kroke groups demonstrated that extended networks can be formed starting from single triazine or heptazine azide precursors.[20−24] Here, via thermal activation, without the need for a catalyst, powders of carbon nitride networks form. This route proceeds in the solid state via the intermediate formation of a highly reactive nitrene species; upon reaction, the sp^2 ring character is maintained. The authors showed that the final hydrogen content and thus the degree of interlinking strongly depend on pressure conditions, humidity, exposure time, and especially on heating rate upon thermal activation. This autocatalytic one-pot reaction is highly exothermic and occurs in a temperature range where the background slope of the thermogravimetric analysis might be interpreted as the onset of evaporation. The various products that can be envisaged are summarized in Supporting Information Figure S1—from primary, secondary, and tertiary amines to azo coupling, introducing hydrogen to the reactive nitrene sites of the network that is picked up from the ambient environment. Interestingly, the authors discuss only amine linking as the final connection motif.

The challenge now is to bring the polymerization reactions known for powders of carbon nitride networks onto a highly defined 2D support in order to obtain single-layer carbon nitrides as controllable interfaces. Since the formation of single atomic layers is still hardly accessible with current methods,[25] we chose the catalyst-free Gillan approach as the most promising one for the translation of a powder to an on-surface synthesis. In this work, we present an azide-based polymerization route on two highly defined, atomically flat materials, i.e., Au(111) and highly oriented pyrolytic graphite (HOPG), that have the potential to be used as model electrodes for more applied future studies. As the single precursor, we opted for the hydrogen-free 2,5,8-triazido-s-heptazine (TAH, see Figure S1) where three −N$_3$ azide groups can react both thermally[21,22] and light-induced[26,27] and, as we will show, also induced by electrons. For similar azides, a tradeoff between volatility and reactivity has been demonstrated to allow intact sublimation and deposition,[28,29] maintaining the azide reactivity, for example, for a "click" reaction.[28] The TAH precursor forms layered, close-packed crystals that indicate the feasibility of co-planar adsorption and flat 2D coupling on the surface.[21] The decomposition, under the formation of gaseous nitrogen as the only byproduct, leads to the formation of planar, rigid building blocks with directional, active nitrene linkers and therefore represents one of three reaction stimuli discussed to prepare ordered covalent organic frameworks (COFs, via the "single reaction pathway" in ref 30).

We base the discussion of our results on two recent ultrahigh vacuum (UHV) studies on on-surface reactions of similarly functionalized molecules: A first study on the thermally induced reactivity of single azide-functionalized phenanthrenes by highly resolving, cryogenic non-contact atomic force microscopy could discern three different reaction channels on Ag(111). Starting from a postulated silver-nitrenoid intermediate, the authors observed either the nitrene insertion into a C−H bond, its dimerization, or hydrogenation.[29] In comparison, our choice of the TAH precursor is free of hydrogen, allowing us to exclude the C−H insertion pathway, which would lead to heptazine ring modifications, and thus we expect linking predominantly via azo bonds. In a second, rare example of surface-bound azide photochemistry, Luo et al. postulate a mechanism for 4-methoxyphenyl azide on Cu(100) that proceeds via an upright arylnitrene-intermediate where the

reactive nitrene is stabilized by a bond to the support before coupling among the molecules to form a planar azoarene.[31]

In this paper, we focus on the various non-catalytic methods to activate the TAH azide groups, namely thermally, by photons, and by electrons, and characterize the resulting films with a particular view on density, flatness, homogeneity, and composition. Furthermore, we show the stability of the resulting film in air, thus presenting a universal approach to anchoring catalytically active particles in highly controlled interfaces of porous carbon nitride networks on supports or in 2D-layered heterostructures.[32,33]

■ EXPERIMENTAL SECTION

The carbon nitride precursor TAH was synthesized from melamine over melem and 2,5,8-trihydrazino-s-heptazine.[23,34] Au(111) single-crystal samples were prepared by several cycles of sputtering (Ar$^+$, 4 × 10^{-5} mbar, 2.0 keV, 15 min) and subsequent annealing (900 K, 10 min). For heating, a boron nitride heater located in the sample holder was used. The temperature was measured via a thermocouple (type K) attached to the crystal. For scanning tunneling microscopy (STM) measurements in air, we used Au(111) laminated on mica samples (Georg Albert PVD-Beschichtungen) which were flame-annealed in a hydrogen flame for several seconds. Evaporation of TAH was performed with a home-built molecular evaporator consisting of a small tantalum crucible spot-welded on to a wire connected to an electrical feedthrough. Additionally, a thermocouple (type K) was spot-welded to the crucible and was heated via resistive heating. STM measurements in ultrahigh vacuum (UHV, p_{bg} < 1 × 10^{-10} mbar) were performed with an Omicron VT-SPM in constant current mode with electrochemically etched tungsten tips at room temperature (RT). STM in air was performed with an STM built by the Wandelt group,[35] equipped with the SPM 100 control electronics by RHK. Here, tips were cut from a Pt/Ir wire (80/20, Temper hard, d = 0.25 mm, R = 6.81 Ω m^{-1}). For temperature-programmed reaction (TPR) measurements, a so-called sniffer was used. A detailed description of this device can be found elsewhere.[36] In short, desorption and reaction products are guided through a quartz tube, which is in close vicinity to the sample surface (∼100−200 μm), to a differentially pumped quadrupole mass spectrometer (QMS, Pfeiffer Vacuum GmbH, QMA 200 Prisma Plus). X-ray photoelectron spectroscopy measurements were performed with the Al Kα-line of a SPECS XR 50 X-ray source and an Omicron EA 125 energy analyzer.

■ RESULTS AND DISCUSSION

A prerequisite for the clean preparation of polyheptazine films from an azide precursor is the feasibility of physical vapor deposition of the pure precursor, which was synthesized from melamine over melem and 2,5,8-trihydrazino-s-heptazine,[23,34] as described in the Supporting Information, Section S2; precursor purity and reactivity agree with the literature.[22] Hereby, two effects have to be balanced: While the high reactivity of the TAH azide functional groups calls for the lowest possible evaporation temperature, considerable inter-molecular interactions within the TAH packing, due to the C/N alternation and charge distribution, imply rather high evaporation temperatures. We thus first had to determine whether we could evaporate the molecule intact or already activated. To this purpose, a few milligrams of the substance were heated in high vacuum (p_{bg} < 5 × 10^{-8} mbar) with the crucible placed in front of a QMS while monitoring the mass scan. As seen in Figure S3, a distinct peak of intact TAH (C_6N_{16}, m/z = 296) can be detected around 470 K, as well as several fragment signals in the range between m/z = 52 and m/z = 132, most likely originating from fragmentation in the QMS. We assign the fragment m/z = 78 to s-triazine (C_3N_3),
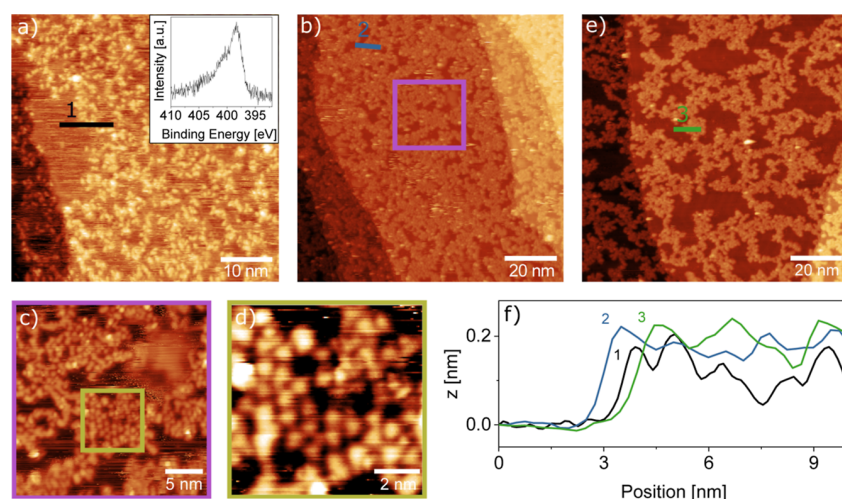
Figure 1. STM images of the on-surface synthesis of 2D carbon nitride via X-ray-induced electron activation at RT. (a) TAH molecules evaporated onto Au(111) and subsequently illuminated by an X-ray source form a disordered network of molecules which covers most of the surface, with some streaky patches of mobile species. The inset shows an XPS measurement of the N 1s region, demonstrating that the azides have already been fully reacted. (b) Annealing the same surface to 573 K leads to a less corrugated film and fewer streaks. (c,d) Zooming into the network reveals small areas of ordered molecules, which appear to remain intact upon polymerization. (e) A final annealing step to 673 K followed by further X-ray illumination opens up larger holes in the film. (f) Height profiles across the films in (a), (b), and (e) show that the overall height is similar in all three cases, corresponding to a monolayer. STM imaging parameters: U_b = 1.5 V, (a−d) I_t = 300 pA, (e) I_t = 10 pA.

which has a comparatively strong intensity due to its stabilizing π-system. Further signals are present throughout the entire temperature range and arise from residual gases in the vacuum chamber, i.e., H_2O (m/z = 18), CO (m/z = 28), and CO_2 (m/z = 44). In the entire measurement range from m/z = 1 to 600, we only observe signals from the monomer, its fragments, and residual gases.

Distinct spikes in the fragment signals around the TAH desorption maximum hint at possible molecule ejection caused by autocatalytic microexplosions at slightly hotter spots inside the crucible-located powder. Since both, the decomposition of TAH upon evaporation and the fragmentation of the evaporated TAH in the QMS, contribute to the atomic N signal (m/z = 14), we discriminate between the two by overlaying the TAH signal onto its initial rise: The polymerization reaction thus sets in at the temperature where the nitrogen curve starts to deviate from the TAH curve (indicated by a vertical dashed line in the right panel of Figure S3). We therefore deduce the ideal evaporation temperature range to be just below 445 K.

In the next step, we dosed TAH onto a clean Au(111) surface and investigated three different pathways toward on-surface polymerization: (i) via X-ray illumination (and thus secondary electron excitation), (ii) via UV illumination, and (iii) thermally.

Electron-Induced Polymerization (via X-rays). We start with the polymerization induced by X-ray photons, as shown in Figure 1. The network resulting from X-ray illumination at room temperature shows a random arrangement of bright protrusions of around 0.2 nm height from immobilized molecules, which confine similarly high streaks resulting from species that are mobile under the STM tip (Figure 1a). The quality of the network can be improved and the streaks removed by heating it to 573 K. This temperature is sufficient to desorb unreacted monomers and to complete the azide activation while avoiding further decomposition of the carbon backbone (see thermogravimetric data of TAH powder)[22] and is therefore generally chosen for annealing. The resulting

network (Figure 1b) appears more homogeneous in height (still 0.2 nm), as clearly seen in the height profiles in Figure 1f. We find that the network still covers the surface evenly, without a net preference for nucleation at steps. When zooming in successively from Figure 1b−d, we can resolve round features, which in some places form a quasi-hexagonal network. From the measured average distance of about 0.9 ± 0.1 nm, approximately matching the molecule distances when azo-bridged (0.8 nm for free-standing dimers), we assign these features to individual heptazine molecules. The increased hole size upon further heating to 673 K in Figure 1e suggests that the network contracts. Comparing height profiles shows that the corrugation within the polymer islands remains as flat as after the first annealing step.

To obtain further information on the chemical composition immediately after TAH deposition, we look at the N 1s X-ray photoelectron spectroscopy (XPS) spectrum taken right after starting the X-ray illumination (Figure 1a inset). As we will discuss in more detail below, this shape is characteristic of TAH molecules that have already lost their azide functional groups.[37] The same effect appears much slower on the less reactive HOPG surface, where we initially can record reference spectra of the intact precursor (a time-resolved XPS series on HOPG is shown in Section S4). The N 1s spectrum in Figure 1a shows that the azide reacts quasi-instantaneously upon exposure to X-rays, and only the heptazine core and the linking nitrogen species remain. This difference in reactivity suggests that secondary electrons generated in the support play a prominent role in X-ray activation.

When comparing the films that result after annealing under the STM, their different mobility is striking: under similar scanning conditions, the network on HOPG gets continuously displaced (see Figure S5), while the one on Au(111) is stable. This indicates a stronger interaction that could tentatively be assigned to a stronger charge transfer and coordination of the Au atoms with the heptazines' π-system and the central tertiary amine group, as well as to image charge interactions of the
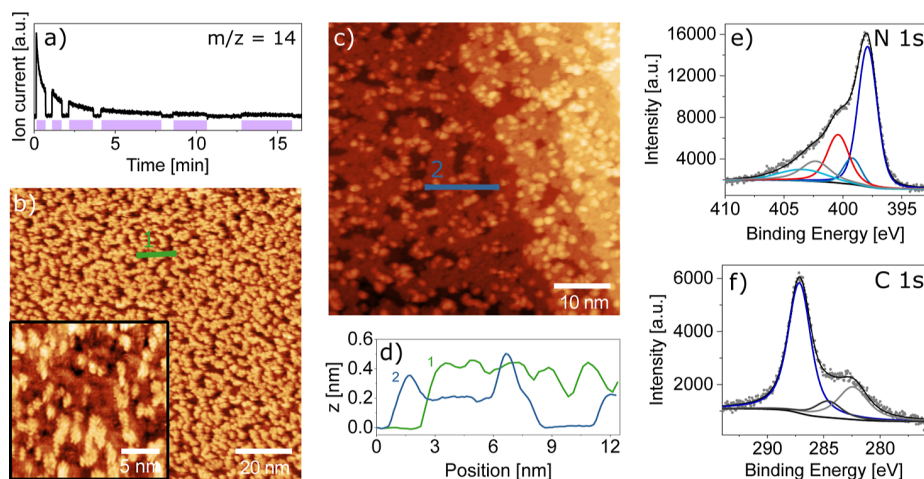
Figure 2. Room-temperature STM images and XPS data of 2D carbon nitride by photoinduced synthesis at 150 K. (a) The nitrogen ($m/z = 14$) mass trace demonstrates reproducible N_2 release concomitantly to illumination with 365 nm UV light of TAH deposited onto Au(111). The purple shading indicates when the sample was illuminated. (b) STM images of the illuminated surface show an amorphous arrangement of molecules. The zoomed-in region in the inset reveals a fern-like appearance of molecule assemblies, which we interpret as stacked, upright-standing molecules. (c) Annealing the same surface to 573 K leads to a flat, nearly complete monolayer with individual molecules in the second layer. (d) Height profiles of the images in (b,c) show that the fern-like structure appears of a similar height as the second-layer molecules. (e) XPS data in the N 1s region of the preparation shown in (c) reveal the unchanged heptazine unit, represented by the conjugated heptazine peak (dark blue), the central tertiary amine (blue), and a red peak at the position of linking amines and azo components (for the XPS analysis, see Section S5). Characteristic peaks of the azide groups are absent. In analogy to the literature, we assign the light-blue peak to π-excitation, while the gray peak is an unidentified component. (f) The corresponding C 1s peak contains components of heptazine (dark blue), adventitious carbon (black), and an unknown component (gray). STM imaging parameters: $U_b = 1.5$ V, $I_t = 300$ pA.

polar C−N bonds in the heterocycle with the highly polarizable Au support.

Photoinduced Polymerization (UV Light). Next, we look at the photoinduced synthesis by UV illumination with an LED at 365 nm, as shown in Figure 2. Turning the UV lamp on and off in front of a mass spectrometer shows the release of nitrogen only during illumination (Figure 2a). To avoid competing thermal reaction channels, we performed this activation at 150 K and found that the reaction proceeds with an exponentially decaying rate that becomes negligible after a total illumination time of 10 min. The resulting film shown in Figure 2b appears at first sight to be similarly holey to that in Figure 1. However, height profiles across the structures show a film thickness that is up to twice as high, and zooming in reveals fern-like details at different apparent heights. These parallel stripes at a distance of some Å appear as though heptazine molecules standing upright are stacked in vertical sheets. Such upright geometries have previously been reported on Cu(111) for nitrenoids[31] and for thermally activated melamine molecules,[38] while the sheet stacking recalls the layered 3D crystal structure (0.3 nm interlayer distance).[21] This interpretation would suggest that we do not have a fully polymerized film at this stage. While we found that the as-deposited molecules are bound too weakly for stable STM imaging, here we now have only a partially reacted precursor state that we can image successfully, most likely thanks to direct nitrene-gold bonds. Indeed, a subsequent annealing step to 573 K leads to a flat, nearly complete single-layer polymer with additional individual molecules or small agglomerates in the second layer. The height profile shown in Figure 2d shows almost no corrugation within the monolayer areas of this annealed film. The single flat layer shows an apparent height of 0.2 nm, similar to the values observed in Figure 1, while second-layer molecules have roughly twice the apparent height.

XPS measurements of the annealed film in the N 1s and C 1s regions indicate that the heptazine core remains unmodified by the polymerization reaction (blue peaks in Figure 2e,f), while an additional smaller peak at 400.4 eV (red peak) indicates amine and/or azo groups. These include bridging amine and azo linkers as well as chain-terminating primary amines. Note that the hydrogenation of nitrenoid compounds to amines most likely occurs by reaction with residual hydrogen and water. The precise assignment based on the literature (ref 37 and references therein) and the relative peak intensities are given in Section S5 (Table S3).

Thermal Polymerization. In order to better understand the chemical reaction occurring during the polymerization, we performed highly sensitive TPR measurements using our sniffer setup.[36,39] In the N_2 temperature-programmed desorption (TPD) spectrum, we observe four components. We discuss the N_2 TPD by comparing the overall N_2 formation ($m/z = 28$ trace) with molecular desorption (using the most intense accessible TAH fragment, $m/z = 78$). We use HOPG as a reference for intact desorption (Figure 3a). Here, we find that the $m/z = 28$ and 78 signals have precisely the same shape, implying that they arise from fragmentation of the intact, desorbed TAH molecule in the QMS. By overlaying the two traces, we determine a sensitivity multiplication factor of 3800. Notably, the onset of desorption just beyond room temperature implies that the interaction of TAH with the HOPG support is substantially weaker than within the bulk material.

Applying the same scaling factor to a sub-monolayer sample on Au(111), shown in Figure 3b, we observe that about 50% of the molecules desorb intact, while the remaining molecules react. To better illustrate the different components in the TPD curve, we show the difference spectra of the $m/z = 28$ and the scaled $m/z = 78$ signals in red in the right panels of Figure 3. The difference curve for sub-ML/Au(111) shows a reactivity maximum of around 450 K, which corresponds to the
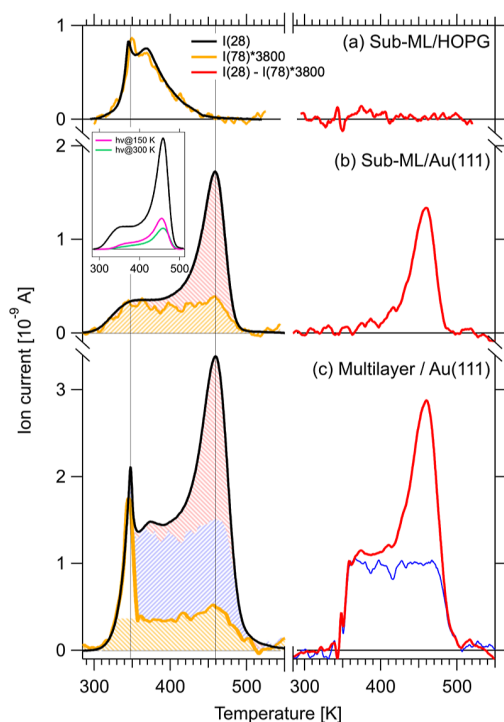
Figure 3. TPD measurements during thermal on-surface carbon nitride synthesis. For each experiment, the mass traces for TAH molecules (m/z = 78) and for N_2 from azide decomposition (m/z = 28) are shown in orange and black, respectively (left panels), and the difference between the two traces in red (right panels). (a) By studying the desorption from HOPG, where no reaction but only multi- and monolayer desorption takes place, we calibrate the intensity difference to be a factor of 3800, which we apply to the m/z = 78 traces on Au(111) in (b,c). (b) Desorption of a sub-ML coverage preparation on Au(111) shows two components: intact molecules desorbing in a broad peak between 300 and 500 K (orange) and reaction products from network formation around 450 K (red shaded area and difference trace). The inset compares the purely thermally treated sample with two that were previously illuminated for photoreaction at 150 (pink) and 300 K (green). Each spectrum starts from a similar TAH coverage. (c) At a higher TAH coverage, molecules desorb from multilayer sites around 350 K (white area in orange trace) and in the same broad peak again. Reaction products are now observed not only in the 450 K peak but an additional broad component also appears (the blue curve is a difference between the red curve in (c) and the red curve from (b) scaled by a factor of 1.4, resulting in the blue shaded area).

decomposition temperature of the pure powder precursor. In the m/z = 28 curve (left), we can thus distinguish two components: intact desorption (shaded in orange) and reacted precursors (shaded in red), respectively. Notably, the orange component has a tabletop-like shape corresponding to a wide range of activation energies of desorption, thus indicating a wide range of binding configurations (e.g., unspecific adsorption sites or varying intermolecular interactions). Once again, the molecular desorption from the surface starts well below the temperature observed for powders.

When increasing the dosed TAH coverage to a multilayer equivalent, two more components appear in the TPD (Figure 3c): A sharp peak at 350 K (white area in the orange trace) is observed in both traces with intensities that match the scaling factor determined on HOPG. Note that the same peak is also apparent in the HOPG trace. We tentatively assign this peak to

weakly, van der Waals-bound molecules in a highly disordered multilayer. The remaining yellow contribution is likely comparable to that of the sub-monolayer preparation, i.e., the desorption of intact molecules. When subtracting both traces from each other, the same reaction peak at 450 K (red) is again observed, but with a slightly higher intensity and on a tabletop background. To shade the different components in the multilayer TPD trace, we further subtracted the red curve in Figure 3b, scaled by a factor of 1.4, from the red curve in Figure 3c and thus obtained the fourth component, i.e., the blue curve and the blue shaded area, respectively. The blue component shows a similar behavior as the yellow one and originates therefore most probably also from the desorption of intact molecules. The reason for the missing signature in the m/z = 78 trace remains unclear at this point.

From our TPD experiments, we conclude that the polymerization reaction can indeed be quantitatively confirmed for up to 50% of the deposited molecules by comparison of the peak areas of the different components. Surprisingly, the temperature where the reaction reaches a maximum coincides with the reaction onset for TAH in powder form (see Figure S3). The catalytic contribution of Au(111) to the polymerization reaction is thus minimal, suggesting that the film growth presented here is not support-specific and thus likely translatable. However, for purely thermal activation, the support must bind the TAH molecules sufficiently strongly to prevent complete desorption before the reaction temperature (as observed on HOPG).

Such films formed on Au(111) by thermal synthesis are only shown in Figure 4. At very low coverages (Figure 4a), small monolayer islands are formed that seem to follow the herringbone reconstruction by occupying preferentially fcc areas. Interestingly, at higher coverages (Figure 4b), second-layer molecules and agglomerates are observed before the first layer is completed, reflected in a highly corrugated line profile (Figure 4c) similar to that observed for the photochemical activation followed by annealing. The height levels of the monolayer and second-layer molecules correspond to those observed for the other activation methods. The XPS spectra in the N 1s and C 1s regions also appear similar to those in Figure 2. The main peaks arising from the heptazine ring and core (and their shake-up peak labeled "π-excitation"[37]), as well as the combined side group signal of bridging and terminal nitrogen atoms, from here on called N (side) atoms, correspond in their intensities (see Section S5 and Table S3 therein).

A direct, quantitative evaluation of the nitrogen species present in the N 1s spectra (Section S5) can help elucidate the carbon nitride stoichiometry and hence the type of network linking. In Table S3, we calculate the ratio of N (side) atoms per heptazine unit as the ratio of the relative intensities of the N (side) peak—that takes into account azo and amine linker species—to the heptazine core and ring N 1s signals, which together represent 7 N atoms or one heptazine unit. For both, the thermal and the photochemical + thermal preparations discussed in Figures 2 and 4, we obtain similar values in the range of 2.0−2.5 N (side) atoms per heptazine unit. We can compare these values with the numbers expected for different linking motifs (Table S2) and conclude that the obtained network contains more linking nitrogen atoms per heptazine unit than expected for a perfect 2D network formed by tertiary (1.0) or secondary amine nodes (1.5)—the linking motifs postulated, e.g., by Gillan for TAH-derived carbon nitride
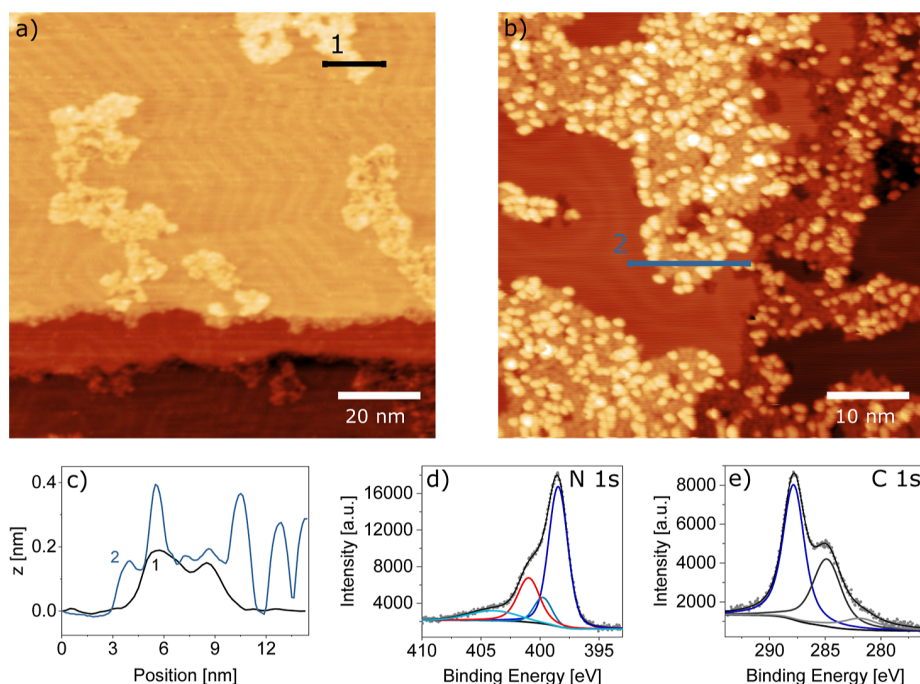
Figure 4. Thermal on-surface synthesis of carbon nitride films. (a) At a low coverage, it becomes apparent that the network grows in small islands which are constrained predominantly into the fcc areas of the Au(111) herringbone reconstruction. (b) At a higher coverage, the island area increases. Again, second-layer molecules are observed and reveal an inherent tendency of the molecules to stack. Both STM images were recorded after thermal polymerization. (c) Height profiles from (a,b) show single-layer islands for the low-coverage and single-layer islands with second-layer molecules on top for the higher coverage preparation. (d,e) XPS data in the N 1s and C 1s regions, respectively, show that the film formed by the thermal reaction is comparable to that from photoreaction shown in Figure 2. Peak colors are assigned as before: Conjugated heptazine ring (dark blue), central tertiary amine (blue), π-excitation (light blue), and linking amines and azo components (red). The corresponding C 1s peak contains components of the heptazine (dark blue), adventitious carbon (black), and an unknown component (gray). STM imaging parameters: U_b = 1.5 V; (a) I_t = 300 pA and (b) I_t = 200 pA.

powders.[22] Azo groups, instead, and terminal amines have more N (side) atoms per heptazine unit (3.0). Thus, we can as well exclude that our networks are exclusively azo-linked. The irreversible covalent bond formation upon polymerization favors rather amorphous and defect-rich networks with a high amount of terminal amines. Without their separate quantification, a clear attribution of the linking motifs remains elusive.

The N_2 TPD traces resulting from these two preparation pathways (see inset in Figure 3b) indicate that after the photoreaction—UV illumination at 150 (pink), resp. 300 K (green)—a third of the azide groups still remains intact. This intensity ratio supports the hypothesis that two of the three azide groups per molecule have reacted to a nitrene. If their reactivity is quenched by a direct nitrenoid bond to the gold support, this would point to an upright adsorption geometry of the molecules, as hypothesized for the striped patterns observed via STM in Figure 2b and in analogy to the structures discussed in the literature by Luo et al.[31] and Lin et al.[38] Furthermore, we note a slight difference in the shape of the TPD traces concerning the onset of the table-top desorption signal that occurs at slightly higher temperatures for the previously illuminated sample.

In the final step, we evaluated the stability of the carbon nitride film on Au(111) in air. For this purpose, the as-evaporated TAH film was transported through air and subsequently exposed to UV light in a tube furnace under vacuum. The resulting surface observed by ambient STM shown in Figure 5a exhibits a remarkably flat film with a similarly holey network as the films prepared under UHV
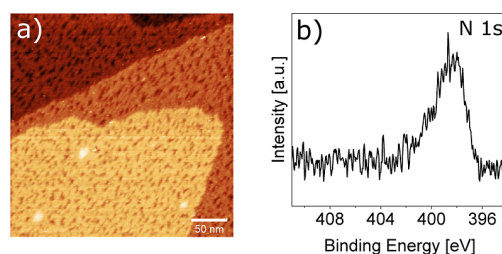

Figure 5. Stability of the carbon nitride film in air. (a) STM image of the film under ambient conditions (air, RT) after evaporation in a high vacuum setup, transport through air, and subsequent illumination with UV light (385 nm) at RT in an evacuated quartz tube with a background pressure of 1×10^{-2} mbar. STM imaging parameters: U_b = −215 mV, I_t = 200 pA. (b) XPS N 1s region after equivalent preparation conditions.

conditions. The N 1s spectrum taken after transferring back into a UHV chamber agrees well with the equivalent measurements in Figures 1−4, but we refrain from fitting the spectrum due to a poorer signal-to-noise ratio. The interpretation of the C 1s region is more difficult due to the presence of a large adventitious carbon peak from air-borne adsorbates. Nevertheless, we can conclude that the obtained carbon nitride films are stable in air and can thus be used as supports for ambient pressure experiments.

◼ CONCLUSIONS

In conclusion, we have demonstrated several pathways for on-surface synthesis of carbon nitride films starting from a single,

azide-functionalized precursor with a heptazine core, namely TAH. The simplicity of our approach lies in this particular, highly reactive precursor that has previously already been explored in powder chemistry. Here, we showed that we can successfully evaporate this relatively large molecule just before thermal activation of the azide occurs. We successfully polymerized the deposited TAH molecules by (a) X-ray illumination (and concomitant secondary electron emission), (b) UV light illumination and subsequent annealing, and (c) purely thermal activation. All three pathways lead to a similar, somewhat holey, 2D film that is stable in UHV and ambient conditions. We demonstrate that the created amorphous film is largely homogeneous, its stoichiometry pointing to various linking motifs. The UV-illuminated film provides an interesting insight into a partially reacted intermediate state before full polymerization by thermal annealing. We interpret the intermediates as upright-standing nitrenoids with strong direct nitrene−gold bonds. While gold thus stabilizes intermediates, it does not have a catalytic role in the thermal polymerization reaction.

The presented synthesis route constitutes a highly versatile tool for preparing thin 2D carbon nitride films, which can be included in stacked 2D materials or utilized as supports for nanoparticle experiments in vacuum, gas phase, and likely also liquid environments. Similar preparations have been shown to successfully immobilize even single metal ions for catalytic applications. Here, we anticipate particularly their use as highly stable confining pores for supported nanoparticles in harsh (electro)catalytic environments. Specifically, we envisage the combination of the on-surface synthesis of 2D carbon nitride films with our recently demonstrated approach to deposit size-selected clusters from polyoxometalate precursors in situ to be highly promising for atomic-scale studies on photo(electro)-catalytic water splitting environments.

■ ASSOCIATED CONTENT

Ⓢ Supporting Information

The Supporting Information is available free of charge at https://pubs.acs.org/doi/10.1021/acs.chemmater.3c01030.

> Reaction scheme of the polymerization reaction; description of the TAH synthesis and characterization of its purity; mass spectra of the TAH evaporation process; XPS and STM reference measurements on the TAH azide activation on HOPG via X-ray-induced electron activation; and XPS analysis of the heptazine network on Au(111), as formed by the photo + thermal and the purely thermal reaction (PDF)

■ AUTHOR INFORMATION

Corresponding Author

Friedrich Esch − *TUM School of Natural Sciences, Department of Chemistry, Chair of Physical Chemistry, Technical University of Munich, Garching D-85748, Germany; Catalysis Research Center, Technical University of Munich, Garching D-85748, Germany;* ⓘ orcid.org/0000-0001-7793-3341; Email: friedrich.esch@tum.de

Authors

Matthias Krinninger − *TUM School of Natural Sciences, Department of Chemistry, Chair of Physical Chemistry and TUM School of Natural Sciences, Department of Chemistry, Functional Nanomaterials Group, Technical University of Munich, Garching D-85748, Germany; Catalysis Research Center, Technical University of Munich, Garching D-85748, Germany;* ⓘ orcid.org/0000-0002-8357-9323

Nicolas Bock − *TUM School of Natural Sciences, Department of Chemistry, Chair of Physical Chemistry, Technical University of Munich, Garching D-85748, Germany; Catalysis Research Center, Technical University of Munich, Garching D-85748, Germany;* ⓘ orcid.org/0000-0002-4990-8533

Sebastian Kaiser − *TUM School of Natural Sciences, Department of Chemistry, Chair of Physical Chemistry, Technical University of Munich, Garching D-85748, Germany; Catalysis Research Center, Technical University of Munich, Garching D-85748, Germany;* ⓘ orcid.org/0000-0001-8474-6261

Johanna Reich − *TUM School of Natural Sciences, Department of Chemistry, Functional Nanomaterials Group, Technical University of Munich, Garching D-85748, Germany; Catalysis Research Center, Technical University of Munich, Garching D-85748, Germany;* ⓘ orcid.org/0000-0001-5065-5871

Tobias Bruhm − *TUM School of Natural Sciences, Department of Chemistry, Professorship of Inorganic Chemistry, Technical University of Munich, Garching D-85748, Germany; Catalysis Research Center, Technical University of Munich, Garching D-85748, Germany*

Felix Haag − *TUM School of Natural Sciences, Department of Physics, Chair of Experimental Physics (E20), Technical University of Munich, Garching D-85748, Germany*

Francesco Allegretti − *TUM School of Natural Sciences, Department of Physics, Chair of Experimental Physics (E20), Technical University of Munich, Garching D-85748, Germany;* ⓘ orcid.org/0000-0001-6141-7166

Ueli Heiz − *TUM School of Natural Sciences, Department of Chemistry, Chair of Physical Chemistry, Technical University of Munich, Garching D-85748, Germany; Catalysis Research Center, Technical University of Munich, Garching D-85748, Germany;* ⓘ orcid.org/0000-0002-9403-1486

Klaus Köhler − *TUM School of Natural Sciences, Department of Chemistry, Professorship of Inorganic Chemistry, Technical University of Munich, Garching D-85748, Germany; Catalysis Research Center, Technical University of Munich, Garching D-85748, Germany;* ⓘ orcid.org/0000-0003-3008-7875

Barbara A. J. Lechner − *TUM School of Natural Sciences, Department of Chemistry, Functional Nanomaterials Group, Technical University of Munich, Garching D-85748, Germany; Catalysis Research Center, Technical University of Munich, Garching D-85748, Germany; Institute for Advanced Study, Technical University of Munich, Garching D-85748, Germany;* ⓘ orcid.org/0000-0001-9974-1738

Complete contact information is available at:
https://pubs.acs.org/10.1021/acs.chemmater.3c01030

Notes

The authors declare no competing financial interest.

■ ACKNOWLEDGMENTS

■ REFERENCES

(1) Wang, X.; Blechert, S.; Antonietti, M. Polymeric graphitic carbon nitride for heterogeneous photocatalysis. *ACS Catal.* **2012**, *2*, 1596−1606.

(2) Kumar, P.; Vahidzadeh, E.; Thakur, U. K.; Kar, P.; Alam, K. M.; Goswami, A.; Mahdi, N.; Cui, K.; Bernard, G. M.; Michaelis, V. K.; Shankar, K. C3N5: a low bandgap semiconductor containing an azo-linked carbon nitride framework for photocatalytic, photovoltaic and adsorbent applications. *J. Am. Chem. Soc.* **2019**, *141*, 5415−5436.

(3) Schlomberg, H.; Kröger, J.; Savasci, G.; Terban, M. W.; Bette, S.; Moudrakovski, I.; Duppel, V.; Podjaski, F.; Siegel, R.; Senker, J.; Dinnebier, R. E.; Ochsenfeld, C.; Lotsch, B. V. Structural insights into poly (heptazine imides): a light-storing carbon nitride material for dark photocatalysis. *Chem. Mater.* **2019**, *31*, 7478−7486.

(4) Lau, V. W.-h.; Lotsch, B. V. A Tour-Guide through Carbon Nitride-Land: Structure-and Dimensionality-Dependent Properties for Photo (Electro) Chemical Energy Conversion and Storage. *Adv. Energy Mater.* **2022**, *12*, 2101078.

(5) Wang, X.; Maeda, K.; Thomas, A.; Takanabe, K.; Xin, G.; Carlsson, J. M.; Domen, K.; Antonietti, M. A metal-free polymeric photocatalyst for hydrogen production from water under visible light. *Nat. Mater.* **2009**, *8*, 76−80.

(6) Yu, X.; Ng, S.-F.; Putri, L. K.; Tan, L.-L.; Mohamed, A. R.; Ong, W.-J. Point-defect engineering: leveraging imperfections in graphitic carbon nitride (g-C3N4) photocatalysts toward artificial photosynthesis. *Small* **2021**, *17*, 2006851.

(7) Li, Y.-Y.; Si, Y.; Zhou, B.-X.; Huang, W.-Q.; Hu, W.; Pan, A.; Fan, X.; Huang, G.-F. Strategy to boost catalytic activity of polymeric carbon nitride: synergistic effect of controllable in situ surface engineering and morphology. *Nanoscale* **2019**, *11*, 16393−16405.

(8) Chen, Z.; Vorobyeva, E.; Mitchell, S.; Fako, E.; Ortuño, M. A.; López, N.; Collins, S. M.; Midgley, P. A.; Richard, S.; Vilé, G.; Pérez-Ramírez, J. A heterogeneous single-atom palladium catalyst surpassing homogeneous systems for Suzuki coupling. *Nat. Nanotechnol.* **2018**, *13*, 702−707.

(9) Hosseini, S. M.; Ghiaci, M.; Farrokhpour, H. The adsorption of small size Pd clusters on a g-C3N4 quantum dot: DFT and TD-DFT study. *Mater. Res. Express* **2019**, *6*, 105079.

(10) Crampton, A. S.; Rötzer, M. D.; Landman, U.; Heiz, U. Can support acidity predict sub-nanometer catalyst activity trends? *ACS Catal.* **2017**, *7*, 6738−6744.

(11) Fukamori, Y.; König, M.; Yoon, B.; Wang, B.; Esch, F.; Heiz, U.; Landman, U. Fundamental insight into the substrate-dependent ripening of monodisperse clusters. *ChemCatChem* **2013**, *5*, 3330−3341.

(12) Kessler, F. K.; Zheng, Y.; Schwarz, D.; Merschjann, C.; Schnick, W.; Wang, X.; Bojdys, M. J. Functional carbon nitride materials—design strategies for electrochemical devices. *Nat. Rev. Mater.* **2017**, *2*, 17030−17117.

(13) Guo, F.; Hu, B.; Yang, C.; Zhang, J.; Hou, Y.; Wang, X. On-surface polymerization of in-plane highly ordered carbon nitride nanosheets toward photocatalytic mineralization of mercaptan gas. *Adv. Mater.* **2021**, *33*, 2101466.

(14) Burdina, K. P.; Zorov, N. B.; Kravchenko, O. V.; Kuzyakov, Y. Y.; Kim, J. I.; Kulinich, S. A. Synthesis of crystalline carbon nitride. *Mendeleev Commun.* **2000**, *10*, 207−208.

(15) Kouvetakis, J.; Todd, M.; Wilkens, B.; Bandari, A.; Cave, N. Novel synthetic routes to carbon-nitrogen thin films. *Chem. Mater.* **1994**, *6*, 811−814.

(16) Li, C.; Cao, C.-B.; Zhu, H.-S. Graphitic carbon nitride thin films deposited by electrodeposition. *Mater. Lett.* **2004**, *58*, 1903−1906.

(17) Sima, M.; Vasile, E.; Sima, A.; Preda, N.; Logofatu, C. Graphitic carbon nitride based photoanodes prepared by spray coating method. *Int. J. Hydrogen Energy* **2019**, *44*, 24430−24440.

(18) Algara-Siller, G.; Severin, N.; Chong, S. Y.; Björkman, T.; Palgrave, R. G.; Laybourn, A.; Antonietti, M.; Khimyak, Y. Z.; Krasheninnikov, A. V.; Rabe, J. P.; Kaiser, U.; Cooper, A. I.; Thomas, A.; Bojdys, M. J. Triazine-based graphitic carbon nitride: a two-dimensional semiconductor. *Angew. Chem., Int. Ed.* **2014**, *53*, 7450−7455.

(19) Bojdys, M. J.; Severin, N.; Rabe, J. P.; Cooper, A. I.; Thomas, A.; Antonietti, M. Exfoliation of crystalline 2D carbon nitride: thin sheets, scrolls and bundles via mechanical and chemical routes. *Macromol. Rapid Commun.* **2013**, *34*, 850−854.

(20) Gillan, E. G. Synthesis of nitrogen-rich carbon nitride networks from an energetic molecular azide precursor. *Chem. Mater.* **2000**, *12*, 3906−3912.

(21) Miller, D. R.; Swenson, D. C.; Gillan, E. G. Synthesis and structure of 2, 5, 8-triazido-s-heptazine: An energetic and luminescent precursor to nitrogen-rich carbon nitrides. *J. Am. Chem. Soc.* **2004**, *126*, 5372−5373.

(22) Miller, D. R.; Holst, J. R.; Gillan, E. G. Nitrogen-rich carbon nitride network materials via the thermal decomposition of 2, 5, 8-triazido-s-heptazine. *Inorg. Chem.* **2007**, *46*, 2767−2774.

(23) Saplinova, T.; Bakumov, V.; Gmeiner, T.; Wagler, J.; Schwarz, M.; Kroke, E. 2,5,8-Trihydrazino-s-heptazine: A precursor for heptazine-based iminophosphoranes. *Z. Anorg. Allg. Chem.* **2009**, *635*, 2480−2487.

(24) Schwarzer, A.; Saplinova, T.; Kroke, E. Tri-s-triazines (s-heptazines)-From a "mystery molecule" to industrially relevant carbon nitride materials. *Coord. Chem. Rev.* **2013**, *257*, 2032−2062.

(25) Jiang, J.; Ou-yang, L.; Zhu, L.; Zheng, A.; Zou, J.; Yi, X.; Tang, H. Dependence of electronic structure of g-C3N4 on the layer number of its nanosheets: a study by Raman spectroscopy coupled with first-principles calculations. *Carbon* **2014**, *80*, 213−221.

(26) Zheng, W.; Wong, N.-B.; Wang, W.; Zhou, G.; Tian, A. Theoretical study of 1, 3, 4, 6, 7, 9, 9b-heptaazaphenalene and its ten derivatives. *J. Phys. Chem. A* **2004**, *108*, 97−106.

(27) L'abbe, G. Decomposition and addition reactions of organic azides. *Chem. Rev.* **1969**, *69*, 345−363.

(28) Diaz Arado, O.; Mönig, H.; Wagner, H.; Franke, J.-H.; Langewisch, G.; Held, P. A.; Studer, A.; Fuchs, H. On-surface azide−alkyne cycloaddition on Au (111). *ACS Nano* **2013**, *7*, 8509−8515.

(29) Hellerstedt, J.; Cahlík, A.; Stetsovych, O.; Švec, M.; Shimizu, T. K.; Mutombo, P.; Klívar, J.; Stará, I. G.; Jelínek, P.; Starý, I. Aromatic azide transformation on the Ag (111) surface studied by scanning probe microscopy. *Angew. Chem.* **2019**, *131*, 2288−2293.

(30) Haase, F.; Lotsch, B. V. Solving the COF trilemma: towards crystalline, stable and functional covalent organic frameworks. *Chem. Soc. Rev.* **2020**, *49*, 8469−8500.

(31) Luo, Y.-W.; Chou, C.-H.; Lin, P.-C.; Chiang, C.-M. Photo-chemical Synthesis of Azoarenes from Aryl Azides on Cu (100): A Mechanism Unraveled. *J. Phys. Chem. C* **2019**, *123*, 12195−12202.

(32) Yan, G.; Feng, X.; Xiao, L.; Xi, W.; Tan, H.; Shi, H.; Wang, Y.; Li, Y. Tuning of the photocatalytic performance of gC 3 N 4 by polyoxometalates under visible light. *Dalton Trans.* **2017**, *46*, 16019−16024.

(33) Bock, N.; De Clercq, A.; Seidl, L.; Kratky, T.; Ma, T.; Günther, S.; Kortz, U.; Heiz, U.; Esch, F. Towards Size-Controlled Deposition of Palladium Nanoparticles from Polyoxometalate Precursors: An

Electrochemical Scanning Tunneling Microscopy Study. *ChemElectroChem* **2021**, *8*, 1280−1288.

(34) Sattler, A. Investigations into s-Heptazine-Based Carbon Nitride Precursors. Ph.D. Thesis, Ludwig-Maximilians-Universität (LMU), Munich, 2010.

(35) Wilms, M.; Kruft, M.; Bermes, G.; Wandelt, K. A new and sophisticated electrochemical scanning tunneling microscope design for the investigation of potentiodynamic processes. *Rev. Sci. Instrum.* **1999**, *70*, 3641−3650.

(36) Kaiser, S.; Maleki, F.; Zhang, K.; Harbich, W.; Heiz, U.; Tosoni, S.; Lechner, B. A.; Pacchioni, G.; Esch, F. Cluster catalysis with lattice oxygen: Tracing oxygen transport from a magnetite (001) support onto small Pt clusters. *ACS Catal.* **2021**, *11*, 9519−9529.

(37) Zhang, J. R.; Ma, Y.; Wang, S. Y.; Ding, J.; Gao, B.; Kan, E.; Hua, W. Accurate K-edge X-ray photoelectron and absorption spectra of g-C3N4 nanosheets by first-principles simulations and reinterpretations. *Phys. Chem. Chem. Phys.* **2019**, *21*, 22819−22830.

(38) Lin, Y.-P.; Ourdjini, O.; Giovanelli, L.; Clair, S.; Faury, T.; Ksari, Y.; Themlin, J.-M.; Porte, L.; Abel, M. Self-assembled melamine monolayer on Cu (111). *J. Phys. Chem. C* **2013**, *117*, 9895−9902.

(39) Bonanni, S.; Aït-Mansour, K.; Hugentobler, M.; Brune, H.; Harbich, W. An experimental setup combining a highly sensitive detector for reaction products with a mass-selected cluster source and a low-temperature STM for advanced nanocatalysis measurements. *Eur. Phys. J. D* **2011**, *63*, 241−249.

Supporting Information for

On-Surface Carbon Nitride Growth from

Polymerization of 2,5,8-Triazido-*s*-heptazine

Matthias Krinninger,[†,‡,¶] Nicolas Bock,[†,‡] Sebastian Kaiser,[†,‡] Johanna Reich,[¶,‡]

Tobias Bruhm,[§,‡] Felix Haag,[‖] Francesco Allegretti,[‖] Ueli Heiz,[†,‡] Klaus Köhler,[§,‡]

Barbara A.J. Lechner,[¶,‡,⊥] and Friedrich Esch[*,†,‡]

†*Technical University of Munich, TUM School of Natural Sciences, Department of*
Chemistry, Chair of Physical Chemistry, Lichtenbergstr. 4,D-85748 Garching, Germany

‡*Catalysis Research Center, Technical University of Munich, Ernst-Otto-Fischer-Str. 1,*
D-85748 Garching, Germany

¶*Technical University of Munich, TUM School of Natural Sciences, Department of*
Chemistry, Functional Nanomaterials Group, Lichtenbergstr. 4, D-85748 Garching,
Germany

§*Technical University of Munich, TUM School of Natural Sciences, Department of*
Chemistry, Professorship of Inorganic Chemistry, Lichtenbergstr. 4, D-85748 Garching,
Germany

‖*Technical University of Munich, TUM School of Natural Sciences, Department of Physics,*
Chair of Experimental Physics (E20), James-Franck Str. 1, D-85748 Garching, Germany

⊥*Institute for Advanced Study, Technical University of Munich, Lichtenbergstr. 2a,*
D-85748 Garching, Germany

E-mail: friedrich.esch@tum.de

S1. Polymerization reaction
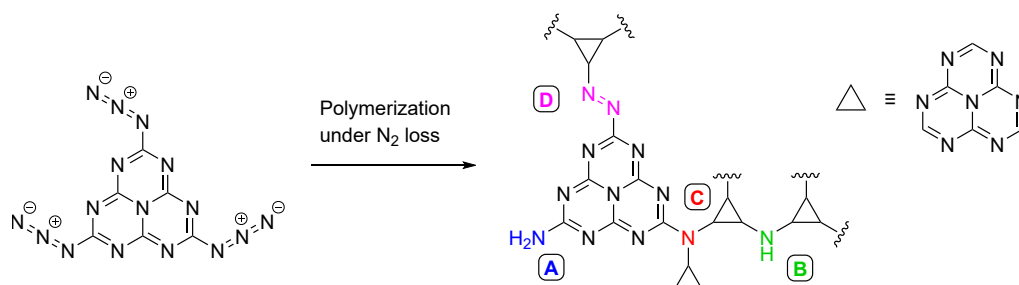
Figure S1: Reaction scheme showing the suggested pathway from 2,5,8-triazido-s-heptazine (TAH) to the 2D polyheptazine-based network. The azide groups decompose under nitrogen loss, forming nitrene intermediates. Their coupling, assuming that the π-bonded core remains intact, is discussed in the literature to proceed to the indicated products: terminal primary amines (A), linking via secondary amines - leading to poly(heptazine imides) - (B), 2D linking via tertiary amines (C) or via azo groups (D). Tertiary amines, found in the polymerization of TAH powders, might be formed by the sequential nitrene attack of azo-coupled nitrogens, under N_2 loss.

S2. TAH synthesis and characterization of purity

The synthesis of 2,5,8-triazido-s-heptazine (TAH) followed the reports of Sattler et al.[1] and Saplinova et al.[2] In a first step, melamine was heated to 663 K in a porcelain crucible, covered with a lid, in a muffle furnace for 24 hours. In order to remove undesired side products, the raw product was then heated under reflux in acetic acid for 3 hours to get the s-heptazine based melem (2,5,8-triamino-s-heptazine).

In the next step, the amino groups of melem were converted into hydrazine groups. To that purpose, the suspension of melem in hydrazine monohydrate was heated to 413 K for 24 hours in a glass lined stainless steel autoclave. The reaction mixture was purified by repetitive dissolution in hydrochloric acid, filtration and precipitation by addition of sodium hydroxide solution. The thus obtained product, 2,5,8-trihydrazino-s-heptazine was suspended in hydrochloric acid and dropped into a 278 K cold solution of $NaNO_2$ in hydrochloric acid. After stirring for 3 hours, the solid was filtered off, washed with water and ethanol to yield the final product TAH.

To characterize the purity of the obtained TAH precursor, we performed ^{13}C-NMR, ATR-FTIR and Raman spectroscopy (see Fig. S2), as well as elemental analysis, and compared to the characterization by Miller.[3,4] While both ^{13}C-NMR spectra show only two carbon signals, as expected for a pure precursor, our elemental analysis contains much less residual hydrogen (0.13 wt% as compared to 0.88 wt% in ref.[3]).

The ATR-FTIR spectrum of TAH in Fig. S2a shows the characteristic peak at 817 cm^{-1}, representative for triazine and heptazine ring breathing modes, a bunch of vibrational C$-$N and C$=$N modes in the $1200 - 1700$ cm^{-1} region and the characteristic azide modes at $2144 - 2229$ cm^{-1}, while N$-$H stretching mode in the range between 3300 and 3500 cm^{-1} are missing. Most of these peaks are also found in the Raman spectrum of the TAH precursor in Fig. S2b.

When reacting the powder at the indicated temperatures in vacuum or in argon (upper spectra in Fig. S2a), one observes the disappearance of the azide peaks, while the heptazine
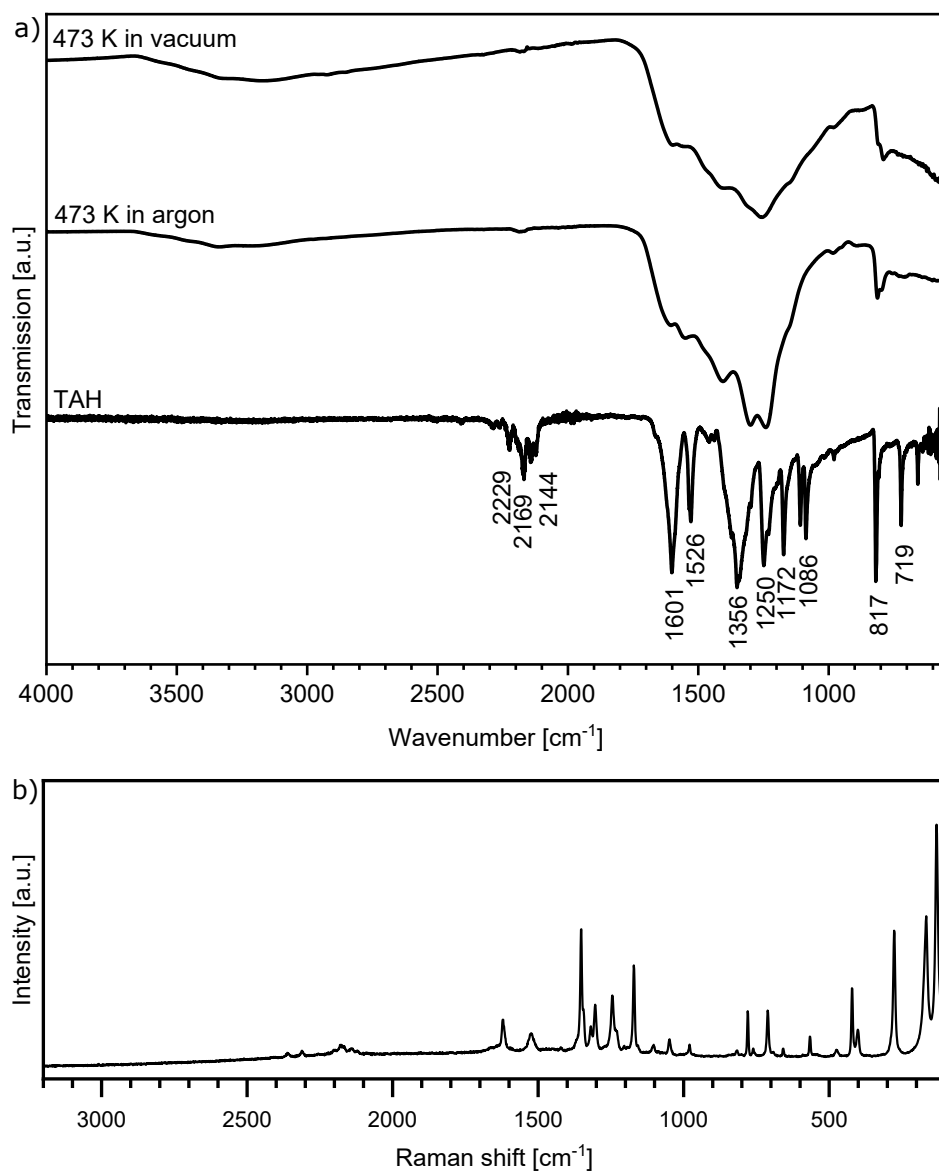
Figure S2: Characterization of the TAH precursor powder and its annealing products by vibrational spectroscopy: (a) ATR-FTIR spectra of TAH (bottom spectrum) and reaction products after heating to 473 K under argon (center) or in vacuum conditions (top spectrum). The TAH molecule can be identified by the s-heptazine, triazine and azide vibrations (see text and detailed list below). The azide contribution at $2144 - 2229$ cm^{-1} disappears for the reacted carbon nitride, while N$-$H species form. (b) Raman spectrum of TAH.

ring breathing mode at 817 cm^{-1} persists, although as a broader feature, indicating that the conjugated ring structure remains intact. In the azide peak region, a small peak at 2190 cm^{-1} remains that Miller et al. assign to the possible formation of imine side products (=C=NH, nitrile $-$C$\equiv$N, or diimide $-$N=C=N$-$.[4]

^{13}C-NMR (101 MHz, DMSO-d6) δ(ppm) = 158.8 (s, N=C$-$N), 171.5 (s, C$-$N$_3$).

Elemental analysis (wt%): Calc. C (24.33), N (75.67); Found C (24.15), N (73.64), H (0.13).

FTIR (ATR, 25 °C, cm^{-1}): 2406 (w), 2284 (w), 2229 (w), 2169 (m), 2144 (w), 2118 (w), 1601 (s), 1526 (m), 1356 (s), 1250 (s), 1172 (s), 1106 (s), 1086 (s), 977 (w), 817 (s), 719 (s), 657 (m).

Raman (785 nm, 25 °C, cm^{-1}): 2361 (w), 2310 (w), 2176 (w), 2141 (w), 2121 (w), 1621 (w), 1522 (w), 1353 (s), 1318 (w), 1304 (m), 1246 (m), 1170 (m), 1102 (w), 1050 (w), 978 (w), 815 (w), 776 (m), 757 (w), 711 (m), 660 (w), 566 (w), 476 (w), 422 (m), 401 (w), 280 (s), 168 (s), 130 (s).

S3. TAH evaporation process
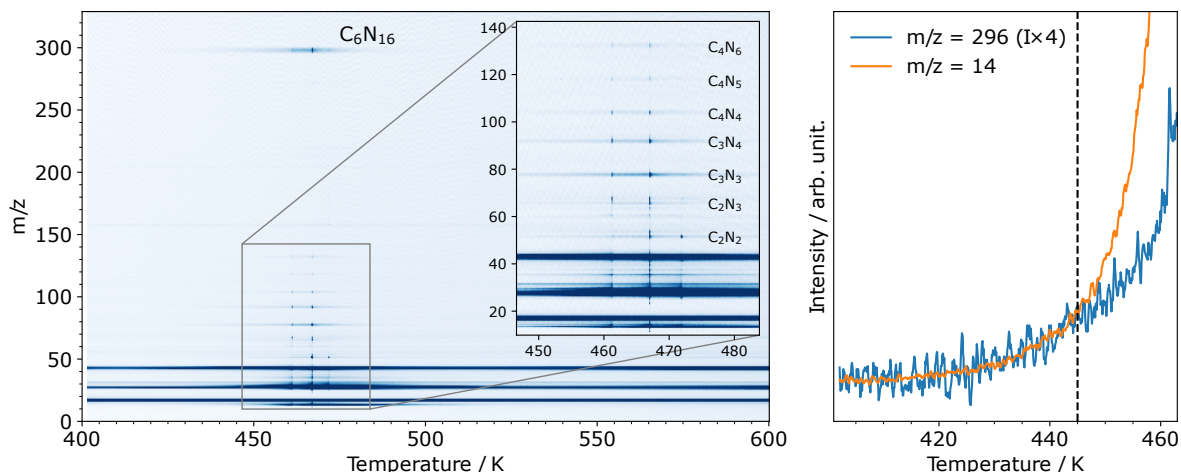
Figure S3: Thermal desorption of TAH powder from a crucible mounted in front of a quadrupole mass spectrometer. The mass spectra were measured from $m/z = 1$ to 600, by heating in high vacuum ($p_{\mathrm{bg}} < 5 \times 10^{-8}$ mbar) with a temperature ramp of 0.05 K/s.

(left) The overview scan that displays mass traces up to $m/z = 300$ clearly indicates a distinct peak of intact TAH (C_6N_{16}, $m/z = 296$), detected around 470 K, as well as several fragment signals in the range between $m/z = 52$ and $m/z = 132$, most likely originating from fragmentation in the QMS. We assign the fragment $m/z = 78$ to s-triazine (C_3N_3), which has a comparatively strong intensity thanks to its conjugated π-system. Further signals are present throughout the entire temperature range and arise from residual gases in the vacuum chamber, i.e. H_2O ($m/z = 18$), CO ($m/z = 28$) and CO_2 ($m/z = 44$). Distinct spikes in the fragment signals around the TAH desorption maximum hint at possible molecule ejection caused by autocatalytic microexplosions at slightly hotter spots inside the crucible-located powder. No polymerization products with $m/z > 300$ are detected.

(right) The signal $m/z = 14$ relates to nitrogen that stems from two processes: The decomposition of TAH in the crucible and the fragmentation of evaporated TAH in the QMS. We discriminate the two by overlaying the TAH signal ($m/z = 296$) onto the initial $m/z = 14$ rise. TAH decomposition in the powder and hence polymerization thus sets in at the temperature where the nitrogen curve starts to deviate from the TAH curve (indicated by a vertical dashed line). We therefore deduce the ideal evaporation temperature range to be just below 445 K.

S4. Reference measurements on HOPG

As illustrated in the thermal desorption spectra in Fig. 3a, the interaction of TAH with an HOPG support is substantially weaker than within the powder: TAH is not bound sufficiently strongly to activate the thermal decomposition before desorption. TAH on HOPG can, however, be activated by X-ray illumination. While TAH decomposes almost immediately on Au(111), making it impossible to trace the azide functionality in the N 1s XPS spectra, the activation on HOPG is less immediate. This difference in reactivity points to the involvement of secondary electrons in X-ray activation. It allows to prove intact azide adsorption on the HOPG support and its subsequent decomposition (Fig. S4) and to image the network that forms upon polymerization and subsequent annealing (Fig. S5).
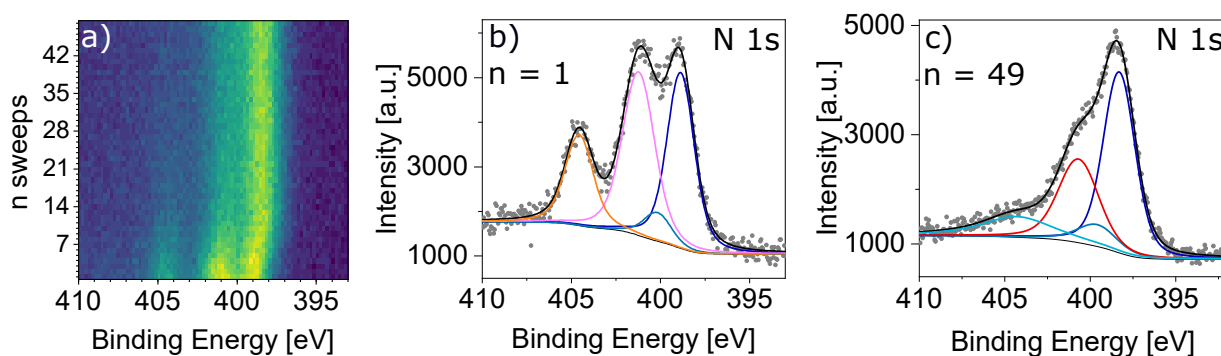
Figure S4: Series of N 1s XPS sweeps of a sub-ML TAH on HOPG (49 sweeps, time/sweep=3:49 min; n=1 after 8 min X-ray illumination, n=49 after 190 min). (a) The 2D plot of the sweeps indicates the azide loss, the transformation into amino or azo side groups and a concomitant shift in the heptazine nitrogen peaks that might be related to reordering on the support. (b) and (c) show detailed spectra for sweep n=1 and n=49 with peak fits by Voigt functions on a Shirley background. Binding energies, intensities and assignments are indicated in Table S1. While the first sweep can be described consistently as an azide layer with two azide and two heptazine nitrogen species (intensity ratio 3:6:1:6), the last sweep, n=49, consists in majority of a reacted heptazine layer with amino or azo side groups, while some intact azide groups are still present.

Table S1: N 1s XPS binding energies and relative peak intensities for the XPS data shown in Fig. S4b and c, with the color code that maps the respective fitted peaks. The obtained binding energies are altogether slightly shifted by about 0.6 eV with respect to those obtained on Au(111) (see Section S5), probably due to enhanced core hole shielding on the metal support. The π-excitation peak is relevant only for polymerized heptazine units. The ratio N (side) atoms per heptazine unit is calculated as ratio of the relative intensities (indicated by the colored bullets) and taking into account that the heptazine ring contains 7 N atoms. The indication of a range reflects exclusion, resp. inclusion of the π-excitation into the sum of heptazine relative peak intensities.

Peak	E_B [eV]		rel. intensity	
	n = 1	n = 49	n = 1	n = 49
● N (heptazine ring)	398.9	398.3	≡6	5.9
● N (heptazine core)	400.2	399.6	≡1	1.0
● N (π-excitation)	-	404.3	-	1.9
● N (azide - outer N's)	401.2	-	6.5	0
● N (azide - central N)	404.6	-	3.3	0
● N (side)	-	400.7	–	3.5
N (side) atoms (●)	–	–	–	$2.8 - 3.5$
per heptazine unit (●●/●)				

The XPS data allows us to estimate the average type of linking that results from the X-ray activation on HOPG. By comparing the obtained value of ≥ 2.8 N (side) atoms per heptazine unit with the values expected for different linking motifs in Table S2, we conclude that the obtained network contains more linking nitrogen atoms per heptazine unit than expected for a perfect 2D network formed by tertiary or secondary amine nodes. Note that the N (side) atom ratio is only indicative, since calculated from single sweeps.

Our values point rather to linear networks predominantly formed by azo groups or secondary amines, with a considerable presence of terminal amine groups that cannot be quantified separately. This is consistent with our observations in the STM images in Fig. S5: The loosely connected network, observed after short annealing to 676 K to remove residual azide groups and increase the surface order, is highly mobile and gets displaced by the scanning tip as seen in subsequent images.

Table S2: Number of N (side) atoms per heptazine unit for different types of linkers

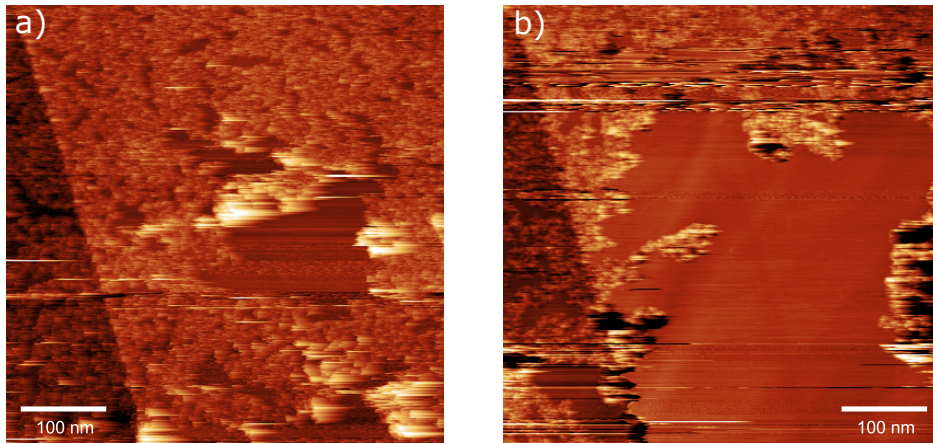| Type of side group	Number N (side) per ring	Carbon nitride stoichiometry
Tertiary amine	1	C_3N_4
Secondary amine	1.5	$C_3N_{4.5}$
Primary (terminal) amine or azo group	3	C_3N_5

Figure S5: Two subsequent STM images of the heptazine network obtained by X-ray induced electron activation on HOPG and subsequent annealing to 676 K. The scanning tip continuously displaces the loosely connected molecule carpet, opening up large areas of the bare support especially where streaky, bright (strongly interacting) patches have been observed previously. *STM imaging parameters*: (a) $U_b = 3$ V, $I_t = 300$ pA, (b) $U_b = 2$ V, $I_t = 300$ pA.

S5. XPS analysis of the heptazine network on Au(111)

Table S3: XPS binding energies and relative peak intensities for the XPS data shown in the main text: a) after photochemical reaction of TAH with subsequent annealing (Fig. 2), b) after thermal reaction (Fig. 4). The color code maps the respective fitted peaks in the figures: Two nitrogen peaks fit the heptazine, one for the six ring atoms and one for the central tertiary amine atom, as well as a third broad peak that represents the π-excitation shake-up satellite related to the conjugated ring system. Linking or terminal amine or azo side groups appear all at similar binding energies and are represented by a single N (side) peak. This peak assignment and the relative binding energy values are in line with the compilation of experimental carbon nitride powder XPS spectra and their simulation by Zhang et al.,[5] although our observed binding energy values are lower by up to 1 eV, which might be related to the interaction with the support. The ratio N (side) atoms per heptazine unit is calculated as ratio of the relative intensities (indicated by the colored bullets) and taking into account that the heptazine ring contains 7 N atoms. The indication of a range reflects exclusion, resp. inclusion of the π-excitation into the sum of heptazine relative peak intensities. Contaminant peaks stemming from the deposition process are marked in grey: Adventitious carbon, also found for powder samples, as well as an unknown carbon species with very low, carbide-like binding energy, and an unknown nitrogen species with rather high binding energy that does not belong to amorphous carbon nitride.[6]

Peak	E_B [eV]	a) photo-+thermal reaction rel. intensity	b) thermal reaction rel. intensity
● N (heptazine ring)	397.9	≡6	≡6
● N (heptazine core)	399.2	≡1	≡1
● N (π-excitation)	403.4	1.6	1.0
● N (side)	400.4	2.5	2.3
● N (unknown)	402.3	1.1	–
N (side) atoms (●) per heptazine unit (●●/●)	–	$2.0 - 2.5$	$2.0 - 2.3$
● C (heptazine)	287.2	≡6	≡6
● C (adventitious carbon)	284.6	0.9	4.0
● C (unknown)	282.4	2.2	1.1

As the XPS analysis demonstrates, both preparation approaches lead to similar values of $2.0 - 2.3$ and $2.0 - 2.5$ N (side) atoms per heptazine unit, depending on whether or not the π-excitation is included. Comparing with the numbers expected for different linking motifs in Table S2, we can exclude that our networks are exclusively azo-linked. The irreversible

covalent bond formation upon polymerization favours rather amorphous and defect-rich networks with a high amount of terminal amines. Without their separate quantification, a clear attribution of the linking motifs remains elusive. The network is, however, more interconnected than on HOPG ($\geq$ 2.8 N (side) atoms per heptazine unit and high mobility in STM).

References

(1) Sattler, A. Investigations into s-Heptazine-Based Carbon Nitride Precursors. Ph.D. thesis, Ludwig-Maximilians-Universität (LMU), Munich, 2010.

(2) Saplinova, T.; Bakumov, V.; Gmeiner, T.; Wagler, J.; Schwarz, M.; Kroke, E. 2,5,8-Trihydrazino-s-heptazine: A precursor for heptazine-based iminophosphoranes. *Zeitschrift fur Anorganische und Allgemeine Chemie* **2009**, *635*, 2480–2487.

(3) Miller, D. R.; Swenson, D. C.; Gillan, E. G. Synthesis and structure of 2, 5, 8-triazido-s-heptazine: An energetic and luminescent precursor to nitrogen-rich carbon nitrides. *Journal of the American Chemical Society* **2004**, *126*, 5372–5373.

(4) Miller, D. R.; Holst, J. R.; Gillan, E. G. Nitrogen-rich carbon nitride network materials via the thermal decomposition of 2, 5, 8-triazido-s-heptazine. *Inorganic chemistry* **2007**, *46*, 2767–2774.

(5) Zhang, J. R.; Ma, Y.; Wang, S. Y.; Ding, J.; Gao, B.; Kan, E.; Hua, W. Accurate K-edge X-ray photoelectron and absorption spectra of g-C_3N_4 nanosheets by first-principles simulations and reinterpretations. *Physical Chemistry Chemical Physics* **2019**, *21*, 22819–22830.

(6) Titantah, J.; Lamoen, D. Carbon and nitrogen 1s energy levels in amorphous carbon nitride systems: XPS interpretation using first-principles. *Diamond and related materials* **2007**, *16*, 581–588.

2 Reprint Permissions

Cluster Catalysis with Lattice Oxygen: Tracing Oxygen Transport from a Magnetite (001) Support onto Small Pt Clusters

ACS Publications
Most Trusted. Most Cited. Most Read.

Cluster Catalysis with Lattice Oxygen: Tracing Oxygen Transport from a Magnetite (001) Support onto Small Pt Clusters

Author: Sebastian Kaiser, Farahnaz Maleki, Ke Zhang, et al
Publication: ACS Catalysis
Publisher: American Chemical Society
Date: Aug 1, 2021

Copyright © 2021, American Chemical Society

Does Cluster Encapsulation Inhibit Sintering? Stabilization of Size-Selected Pt Clusters on Fe₃O₄(001)by SMSI

ACS Publications
Most Trusted. Most Cited. Most Read.

Does Cluster Encapsulation Inhibit Sintering? Stabilization of Size-Selected Pt Clusters on Fe3O4(001) by SMSI

Author: Sebastian Kaiser, Johanna Plansky, Matthias Krinninger, et al
Publication: ACS Catalysis
Publisher: American Chemical Society
Date: May 1, 2023

Copyright © 2023, American Chemical Society

BACK   CLOSE WINDOW